EFFECTS OF LANTHANUM DOPING ON THE MICROSTRUCTURE AND MECHANICAL BEHAVIOR OF A SnAg ALLOY

A Dissertation
Presented to
The Academic Faculty

by

Min Pei

In Partial Fulfillment
of the Requirements for the Degree
Doctor of Philosophy in the
George W. Woodruff School of Mechanical Engineering

Georgia Institute of Technology
May, 2007

EFFECTS OF LANTHANUM DOPING ON THE MICROSTRUCTURE AND MECHANICAL BEHAVIOR OF A SnAg ALLOY

Approved by:

Dr. Jianmin Qu, Advisor
School of Mechanical Engineering
Georgia Institute of Technology

Dr. Thomas H. Sanders, Jr.
School of Materials Science and Engineering
Georgia Institute of Technology

Dr. David L. McDowell
School of Mechanical Engineering
Georgia Institute of Technology

Dr. C. P. Wong
School of Materials Science and Engineering
Georgia Institute of Technology

Dr. Richard W. Neu
School of Mechanical Engineering
Georgia Institute of Technology

Date Approved: March 27, 2007

ACKNOWLEDGEMENTS

I wish to express my sincere thanks to my thesis advisor, Dr. Jianmin Qu for his teaching, guidance, encouragement throughout the course of this research. I also wish to express my gratitude to Dr. David L. McDowell, Dr. Richard W. Neu, Dr. Thomas H. Sanders Jr. and Dr. C.P. Wong for their invaluable suggestions, readings and comments on this thesis.

I wish to especially thank Dr. C.P. Wong, Dr. Yangyang Sun and Dr. Haiying Li in the School of Material Science at Georgia Tech for their advice on material handling techniques. Without their help, this research could not be finished.

Another special thanks to Dr. Richard Neu and Dr. Michael Woodmansee in Mechanical Engineering at Georgia Tech. I obtained great benefit from their experience on the solder material.

TABLE OF CONTENTS

LIST OF TABLES

LIST OF FIGURES

Page

SUMMARY

SnAg and SnAgCu lead-free solders are used extensively as replacements for SnPb solders in microelectronics packaging. Extensive studies have been conducted to understand the electrical and thermomechanical behaviors of these Sn-based lead-free solders, and they have been found to have issues such as formation of intermetallic compounds (IMC) and poor wetting abilities. Work is therefore needed to modify the current lead-free compositions to further improve their performance. In this work, the effects of doping with rare earth elements (REs) on SnAg alloys are investigated. REs are well recognized as surface-active agents and previous researchers have found that RE doping can dramatically increase the wetting property of solder. It can reduce IMCs and their growth on solder/pad interfaces and also refine the microstructure of the alloy which results in improved mechanical properties of the solder.

This work systematically studied Lanthanum (La) doping on the microstructure and mechanical behavior of 96.5Sn3.5Ag wt% alloy. Quantitative relations were established not only for initial as-cast conditions, but also for thermal aged conditions.

A quantitative microstructure study has been performed on multiple scales. It was found that doping greatly reduces the grain size as well as the size of the intermetallic particles Ag_3Sn. However, the inter-particle spacing remains relatively unaffected by the La doping amount and because of stoichiometry, decreasing Ag_3Sn particles size increases the total number of Ag_3Sn particles. A higher La doping level, therefore, leads to higher volume fraction of the eutectic region and lower volume fraction of the Sn dendrite phase in the solder alloy.

Creep tests at various temperatures and strain rates were conducted. A strain rate jump test was performed on the specimen of all conditions to cover the strain rate from 2×10^{-6}/s to 2×10^{-2}/s range and these tests were performed in a constant temperature

environment from -55°C to 125°C. The results show that La doping increases creep resistance of the SnAg alloy by approximate 15%.

The creep test result can be fit into a modified microstructure dependent Anand model, which is based on a uniform plastic-creep constitutive model with the modification of a particle-size dependent term. A one step data fitting method was developed to facilitate constant extraction from the complex nonlinear constitutive model.

A new constitutive law was also proposed to account for the hierarchal microstructure over multiple length scales. Specifically, at the smaller scale of the sub-micrometer level, the SnAg eutectic region was treated as a two-phase composite with the Ag_3Sn being the particle and Sn as the matrix. At the larger length scale of the micrometer level, the solder alloy was treated as a two-phase composite with the Sn dendrite as the particle and the SnAg eutectic region as the matrix.

At the small scale, a micromechanics composite material model was used to calculate the creep properties of the eutectic region and the results are used as the phase properties for large scale. Several methods were used in this scale including micromechanics composite material model and a FEM based digital image (DIB) model and these models found that although the material has local anisotropic pattern, the overall behavior is close to isotropic. A good match was found between the models and tensile creep test result.

Finally, a fatigue test was performed on bulk samples. It was found that La doping increases the fatigue life of SnAn alloy by a factor of about 5. A 3D FEM model was established and validated with the fatigue test specimen. A fatigue model was established by combining the fatigue life from test, with the local deformation obtained from 3D FEM model.

CHAPTER 1

INTRODUCTION

SnPb solders were used extensively as electrical interconnects in microelectronics packaging. Eutectic or near eutectic tin-lead solders were the most widely used solder materials due to their low melting temperature, high ductility and good wettability with other metals, but due to increasing concerns regarding the toxicity and environmental impacts of lead, major interest in lead-free solder materials has developed in the last several years. The European Union and Japan have already adopted legislation to reduce and phase out lead usage in the electronics industry, and in the United States, the Environmental Protection Agency has encouraged manufacturers to take voluntary steps to reduce hazardous waste stream volumes as well [1].

Among the lead-free solders, the most studied and widely used solder materials are SnAg and SnAgCu based alloys. Several standard organizations such JEITA, NEMI and EOLDERTEC are all recommending near eutectic SnAgCu solders [2]. Compared with tin-lead solders, these lead-free solders have some draw backs such as poor wetting ability during the reflow process and pores are more often seen in solder joints. In addition, formation of intermetallic compounds (IMC) which embrittle the solder/pad and solder/UBM interfaces makes the package prone to shock and vibration failure.

In modern surface mounting technology, the solder joint serves as both the electronic connection and the mechanical support for the chips. The coefficient of thermal extension mismatch in electronic packaging produces shear loading on solder connections and the thermomechanical reliability of modern electronic devices depends on, to a large extent, the fatigue and creep behavior of the solder joints. Depending upon the specific packages and application environments, these lead-free solders could perform thermomechanically either much better or much worse than the SnPb eutectic solder.

It is imperative to understand the fatigue and creep behaviors of these new lead-free solders and to formulate new alloy compositions that will have equal or better performance than the traditional lead-based solders. Attempts have been made by many researchers to improve solder's material properties by introducing additives to it, and rare element (RE) is one of the approaches that have been shown to be effective.

Rare earth elements have been successfully used in the steel industry [3] and it is a reasonable guess that the RE has similar effects in solder materials. As a result, a rare earth element was chosen to serve as enforcement agent to SnAg lead-free solder materials.

From the available research results, the benefit of rare earth elements has many forms. Rare earth elements were found to dramatically increase the wetting property of solder, even expanding the usability of solder to ceramic surfaces [4]-[6]. This ability is critical to lead-free solder materials because it is commonly recognized that lead-free solder has poor wetting ability compares with tin lead solders. Another benefit is to reduce the intermetallic compound (IMC) growth and greatly increase the reliability of solder [7]. More benefits include refining the microstructure of solder [8] and thus improving the mechanical properties of the solder material.

Objective

With the known benefit of rare earth elements on lead-free solder materials, this composite material is expected to be widely used in industry. Further study on this material is necessary to understand its behavior better and the objective of this study is to provide a quantitatively understanding of the effect of RE doping on the lead-free solder materials. In this study, RE element Lanthanum (La) doping effect in 96.5Sn3.5Ag lead-free solder will be studied. This main objective includes two aspects:

First, the percentage of La put in lead-free solder material needs to be optimized. Usually very small amount of rare earth element will be necessary to dramatically

improve the properties of solder material. Over doping with rare earth element can deteriorate solder's material properties [3] and an optimized point was sought for the rare earth element additives. Second, interaction of La doping effect with thermal aging effect needed to be studied. Currently, all the attention is focused on the RE doping effect on IMC growth during thermal aging[7] but the aging of lead-free solder material itself under the influence of RE doping is also important.

To fulfill these two goals, the material properties studied in this work include two major areas: microstructure and mechanical properties. Quantitative microstructure characterization will be conducted at multiple length scales, as available age coarsening data for lead-free solders is rare at this point, let alone that with the effect of rare earth element additives. To study the mechanical properties of bulk material, both monotonic tensile and fatigue test will be preformed. The monotonic tensile test can provide elastic and creep properties of the material and eventually constitutive laws with La doping and thermal aging effect. Fatigue is the major failure mechanism for solder joint in electronic packaging and therefore a fatigue test is critical to fully understand La doing effect on material behavior.

Chapter Structure

Chapter 1 is the introduction of the whole project, including the objective of the project.

Chapter 2 is the background, which contains the literature review of enhancing lead-free solder material by introducing additives. Literature reviews of other related topics are put in the relevant chapters. The experimental design for this research is also discussed. Factors that are considered in this study are listed.

Chapter 3 contains the microstructure study of the La doped SnAg solder materials under different thermal treatment. Quantitative microstructure study results at multiple length scales are included.

Chapter 4 is the particle coarsening model data fitting. Particle size data obtained from Chapter 3 was fit to an existing coarsening model, and the La doping dependence of this model is discussed.

Chapter 5 elaborates on the method and the result of tensile creep tests. Specially designed specimens and test system setups were used for the soft solder alloy and the effects of La doping and thermal aging on the creep resistance of solder material are discussed.

Chapter 6 contains methods and results of constitutive law constant extraction. A modified Anand model is proposed in this chapter to capture the creep behavior of La doped solder material.

Chapter 7 is the hieratical modeling study. This newly proposed constitutive law considers the solder alloys as composite materials at different length scales and models were established accordingly.

Chapter 8 contains the fatigue study of La doped solder material. In the fatigue test, bulk samples were used and the mechanical shear fatigue loading was applied. A FEM model was also developed to simulation the fatigue loading. Finally, a fatigue model was established.

Chapter 9 draws the conclusions of the whole project. Recommendations for future works are also provided.

CHAPTER 2

BACKGROUND

As introduced in Chapter 1, SnAg solder has become the dominant lead-free replacement of SnPb solder, but this solder alloy has several draw backs. Attempts have been made by many researchers to improve solder material properties by introducing additives to it.

It is well known that metals and alloys can be strengthened by the presence of fine second-phase particles [9], which can be introduced to the material by precipitation from super saturated liquid, as in eutectic composition. The Ag_3Sn particles in SnAg solder, for example, is considered to be this kind of particle [10]. Other materials that can be found in tin based solder are Cu, Ni, Fe and their intermetallic with Sn, to name a few. The disadvantage with this kind of material is that the particles coarsen with time and deformation, especially under high homologous temperature, such as the working temperature of solder material.

As an alternative, some external addition can be introduced in as the strengthening phase. This kind of particle is usually insoluble, having minimum diffusivity, interfacial energy, and solubility in the matrix. Oxide particles are usually used as this type [10], such as Al_2O_3 and TiO_2. Another example of this kind of external addition is the nano-size Polyhedral Oligomeric Silsesquioxanes (POSS) particles [11]. POSS can be seen as an inert Si-O core covered with active organic bonds which can form Si-O-Sn bonds with solder. The particles with this chemical bond can be mixed with solder uniformly. This kind of material does not coarsen easily and can serve as obstacles to grain growth and coarsening of solders [9].

The process of mixing these external particles into solder alloy, however, is not straight forward. Usually these particles cannot form chemical bonds with SnAg solder,

or the chemical bound will be destroyed by high reflow temperature. Even though the particles can be mechanically mixed in the solder in solid form by either mixing with solder paste or put in bulk solder through repeat work [10], these composite solders are not stable during reflow. The particles expelled from liquid solder will also harm the wetting.

Enhance Solder Material with Rare Earth Element Additives

Rare earth elements are another approach that has been shown to be effective. Rare earth elements are a collection of sixteen chemical elements in the periodic table, namely scandium, yttrium, and fourteen of the fifteen lanthanides (excluding promethium), which naturally occur on the Earth [12]. Despite their relative abundance in Earth's crust, they are difficult to mine and extract, making them relative expensive [12].

Rare earth elements have been recognized as surface-active agents because they can lower the surface/interface tension or energy, and they have been successfully used in the steel industry [3]. RE can segregate at the grain/dendrite boundaries and lower the grain/dendrite boundary energy, and restrain the moving or sliding of the boundaries. Furthermore, they can remove the impurities, such as sulfur and phosphorus, in steel liquid, change the property, shape, and distribution of the inclusions and, hence, improve the performance of the steel.

Several works have also been done on solder materials and several solder alloys have been studied. For example, Ce and La have been added to Sn-9Zn system [8][14], and Lu has been added to SnAg and AuSn solders [13], *etc.*

Material Preparation

To add RE elements into solder material, some dropped solid RE into melted solder [4]-[8][14]-[18], some make Sn-RE and Pb-RE IMC first and melt them together[19] [20]. The mixing procedures are usually performed at very high

temperatures of 500~600°C and frequent stirring is necessary. At this temperature range, a vacuum or inert gas environment is needed to prevent the solder material from oxidizing. Combining the environment and stirring requirement, usually specially designed equipment is needed to manufacture RE doped solder material, and productivity is limited.

An alternate way to create protection from oxidation is to use salt. Chen, *et al*. [21] suggested using KCl+LiCl 1.3:1wt to cover the melted solder. Melted salt will float on liquid solder to prevent reaction with air and mechanical stirring equipment can be easily placed in this set up.

Benefits of Rare Earth Element in Solder Materials

The three major benefits of rare earth elements on lead-free solder materials are: improving wetting ability, reducing intermetallic growth, and refining microstructure.

Rare earth elements were found to be able to dramatically increase the wetting property of solder, which draws the attention of optical equipment researchers. Studies show that SnAg or SnAu solder with RE additives can form a direct bond to different kinds of inorganic surfaces (nitrides, carbides, oxides, *etc*.) with interfacial bond strength in excess of 6.9-13.8 MPa, without even using flux[4]-[6]. A TEM study found that when the rare earth enhanced solder comes into contact with silica, the Lu atoms move to the interface to form a layer of interface chemical bounding with Lu_2O_3[6]. Other researchers also found that the RE can improve wetting with Cu by decreasing the interfacial tension between the solder alloy and the Cu substrate due to the interaction of RE and Cu [8][14]-[18].

For solder joints, a small amount of La can reduce the intermetallic compound (IMC) growth and greatly increase the reliability of the solder [7]. As a surface activation agent, this rare earth element tends to accumulate at the solder / copper interface during reflow and provides a barrier for the formation of tin copper intermetallic. Moreover,

after high temperature aging, tin-copper intermetallic in rare earth element doped solder joint has much lower growth rate than in those joints without rare earth. IMC is harmful to the reliability of solder joint due to its brittle character, and rare earth element enhanced solder joints will have higher reliability.

RE elements can refine the microstructure of solder [7]-[20] [22]. Some models on SnPb solder showed that the RE element can change the contact angle of the three phase junction point [19][20], while others mentioned that in lead-free solder the maximum surface tension plane will grow slower during solidification by adsorbing more surface-active materials[22]. Some researchers found that the atomic radius difference between Sn and RE makes them unlikely to form replacement atom type solid-solutions, and the RE atoms will gather at defects, such as dendrite boundaries [3].

RE doping can also cause mechanical property change in solder alloys. It is common knowledge that microstructure change will affect the mechanical behavior, especially in solder materials [20]. With refined microstructure from RE doping, solder material usually shows improved creep resistance [20]. The refined grain and particles decrease the distance for dislocations to pile up, consequently the doped solders have better creep resistance, longer creep rupture time, and higher strength in tension with less elongation.

Besides refinement of microstructure, RE can also affect mechanical properties in other ways. A web-like sub-grain in Sn3.8Ag0.7Cu solder was found with lower than 0.1wt% RE element at slow cooling rate [3] [22] [23]. This structure limits the movement of the dendrites, hinders Sn diffusion and increases the creep property of the solder, but when the RE is higher than 0.1wt%, the creep rupture life drops, due to RE aggregation at the grain boundary in snow flake shape[3].

Existing Literature on La Doped SnAg Lead-free Solder

Several preliminary studies have been performed on RE/La doped SnAg/SnAgCu solder materials but no systematic work has been done, especially on the microstructure and mechanical behaviors of these materials. A detailed review of the state-of-art in this area is presented below.

Yu, *et al.* [15] doped Sn3.5Ag0.7Cu solder with mixed RE elements that mainly consist of Ce and La. In their studies, two doping levels were used at 0.1wt% and 0.25wt%. The samples were chill cast with cooling rate of ~15°C/s and polished for microstructure study. From SEM images, the RE doping was found to refine the Sn dendrite greatly. They found that the Ag_3Sn particle size was reduced from about 1~4μm for un-doped alloy to about 0.1~0.2μm for the doped alloys. In their tensile test study, the samples were aged at 100°C for 5 hours before test and the tensile test was performed with fixed strain rate of 1.5E-2/s at room temperature only. The RE doping was found to increase the tensile strength and ductility, because RE doping removed large Ag_3Sn particles which is harmful to ductile property. The shortcoming of this study is that no quantitative microstructure study was carried, and the size of Ag_3Sn particles were directly estimated from the SEM images. In addition, only one test condition was used in the tensile test, and no creep stress strain relation was recorded.

Similar to Yu, *et al.*'s work [15], Wang, *et al.* [18] also only used one test condition to evaluate the creep failure only. Wang, *et al.* [18] tested tensile property of mixed La and Ce doped Sn3.5Ag solder. Cylinder shape samples were used with a diameter of 6mm and gauge length of 20mm, but the cooling rate of the sample was not specified. The only test condition used was 4E-3/s strain rate at room temperature. Within the range of up to 1wt% RE doping, 0.5% of RE was found to maximize both strength and ductility. SEM image at fracture surfaces suggested that while RE induced micro-alloying can benefit the ductility at low doping level, excessive RE intermetallic compound will induce transganular fracture. Similar to Yu, *et al.*'s work [15], this work

is limited only the room temperature test and did not discuss the creep behavior of the doped alloys.

In a more recent paper, Wu, *et al.* [16] performed multi-temperature, multi-strain-rate creep test on RE doped SnAg solder. Test materials included Sn3.5Ag and Sn3.5Ag0.25RE where RE elements were mainly Ce and La. Samples were cast with a cooling rate of 15~20°C/s and machined to dogbone shape of 20mm gauge length and 4mm gauge diameter. The microstructure of the samples showed RE doping decreased the Sn dendrite size from 25-30μm to 10-20μm at 0.5% RE level and particle size from about 1μm to about 0.5μm at 0.25% RE level. The tensile test was performed at temperature range from 20°C to 120°C with stress level at 8-34MPa in a load controlled mode. The test showed the RE can increase steady state creep resistance and the result was fitted into the Dorn creep equation. The stress exponent at 393, 348 and 303K is found to be 9.9, 11.3 and 12.3, respectively, for SnAg solder and 9.05, 12.04 and 12.08 for SnAg0.25RE solder. Although multi-temperatures and multi-strain rates were used in this work, only one RE doping level was studied. More importantly, the temperature and strain ranges considered in their paper are not the typical conditions encountered in the accelerated fatigue test of electronic packaging, where heating and cooling thermal shock test causes high strain rate loading on solder joint.

Chen, *et al.* [3] [23] doped up to 1% of RE into Sn3.8Ag0.7Cu solder and solder joints of 0.1mm in thickness were made between two copper bars with cross section of 1mm by 1mm. The cooling rate of the solder joint sample was very low at 25°C/min and no further thermal aging was used. The creep-rupture life of the solder joints were measured with a dead load of 16.5MPa at room temperature and 11.5MPa at 65°C. The result shows that 0.1% RE was the optimal doping level to maximize the creep-rupture life and at 0.5% doping level, the creep rupture time was very close to or even lower than that un-doped. One tensile test was also performed with cylindrical samples that had a diameter of 3mm and a gauge length of 25mm. The samples were cooled at about 2°C/s

and they were aged at 100°C for 1 hour before test. Strain rate of 1E-3/s was used for the tensile test at room temperature. Again, 0.1% RE was found to be the best doping level that can maximize the elongation and fracture energy. Microstructure study on the slow cooled solder joint samples showed that, with less than 0.1% RE doping, a RE solid solution was observed to form a web at the Sn dendrite boundaries, which was concluded to be the enforcing mechanism. However, this web structure cannot form in fast cooled samples. At more than 0.1% RE doping level, the segregation of RE-Sn intermetallic along grain boundaries will reduce the ductility of the material, for all cooling rates alike. There are several shortcomings in this study. The slow cooling rate prevents results from being applied to electronic packaging industry where fast cooling rate was usually applied. Mean while, test conditions were very limited in this study and no temperature and strain rate dependence was obtained from the creep data. Furthermore, by using solder joint type of specimen, the mechanical test results consist of not only the RE doping effect on the solder material, but also the effect of reflow process, from the interface layer between copper pad and solder joint, and from the solder joint geometry. Although the solder joint samples are closer to the reality of electronic packaging than bulk sample approach, the three factors are mentioned above tend to distort the conclusions on the effect of RE doping.

The same group of researchers also performed creep test on Sn3.8Ag0.7Cu and SnAgCu0.1RE solder joints[17], based on the optimization of RE doping on creep rupture [3] [23]. The same solder joint samples were used for creep test in the rage of 25°C to 125°C with the test stress range of 4-20 MPa, and the creep test results were fitted into piecewise Dorn creep model for different stress ranges. It was found that at low stress level, the stress exponents for SnAgCu solder and SnAgCu0.1RE solder are 6.9 and 8.2, respectively, with the creep activation energy close to lattice self-diffusion energy; at high stress level, the exponent of the two alloys became 11.6 and 14.6 and the creep

activation energy is close to dislocation-pipe diffusion. Nevertheless, such creep test condition does not include low temperature and high stress conditions.

Another solder joint typed creep work comes from Dudek, *et al.* [41]. Solders Sn3.9Ag0.7Cu, SnAgCu0.1La, and SnAgCu0.5La were fabricated and quenched with water from 1000°C. The microstructure study on the as-processed samples found that Sn dendrite was refined with La doping and $LaSn_3$ particles homogeneously distributed in the material. The solders were then reflowed with copper pad to form solder joint samples of 0.5mm in thickness and 6.35×6.35mm in size. The cooling rate was 0.7°C/s and no thermal aging was used. Microstructure study on reflowed samples also found the refinement effect of La on Sn dendrite. The creep test was performed at room temperature with a shear strain rate of 1E-3/s. RE doping was found to be able to slightly decrease the ultimate shear strength from 27MPa to 18MPa, but dramatically increased the strain to failure from ~1 to 2.5. The $LaSn_3$ particles were believed to be able to nucleate void and uniformly soften the material, and thus increase the ductility of the solder joint. This result is consistent with Wang's result [18] where 0.5% RE was found to maximize the ductility of fast cooled bar shape samples, but is conflicting with Chen's result [3] [23] that 0.1% RE maximize slowly cooled solder joint creep rupture life. The cooling rate induced microstructure difference would be the main reason for this discrepancy.

In summary, to-date there has been no quantitative microstructure investigation to establish the effect of RE doping. The few studies available in the literature only present qualitative trends on the refinement effect of the RE doping in the Sn dendrites and intermetallic particles. No study available on the RE effect on grain size. Since the mechanical behavior of solder alloys depends on the microstructure, it is critically needed to conduct a systematic quantitative microstructure study at all relevant length scales.

As for the mechanical behavior, the existing results from the literature are limited to room and high temperature and low strain rate, which are not typical in electronic

packaging applications. Furthermore, no appropriate constitutive models are available to account for the effect of RE doping. In addition, there is virtually no study on the effect of RE on the fatigue behavior of solder alloys.

Based on these needs, the research presented in this thesis is aimed at conducting a comprehensive and systematic study to understand how the RE doping affect the thermomehcanical behavior of SnAg solder alloys. Specifically, systematic testing and modeling have been conducted over a wide range of temperature, strain rate, and aging conditions for both monotonic creep and cyclic fatigue. Data from such systematic tests provide useful guidelines for developing constitutive models for the design and reliability analysis of RE doped solder joints in electronic packaging. More importantly, constitutive models have been develop to account for the RE effects. To accomplish this, a quantitative study on the microstructure and its evolution was carried out at different length scales for La doped SnAg alloys. This work provides a comprehensive approach to systematically evaluate the benefits and drawbacks of La doped SnAg alloys. The same approach can be used for studding doping of other RE element in different alloys.

Experiment design

The objective of this study is to quantitatively study the effect of La and thermal aging on the properties of the SnAg lead-free solder material. It is well known that the microstructure of solder material is highly thermal-treatment dependent and the mechanical properties are decided by the microstructure, to a large extent. In this study, the factors of La doping and thermal treatment are considered for the evolution of the microstructure, and thus for mechanical properties. The mechanical loading induced microstructure change is not considered here.

For problems with multiple factors, traditionally one-factor-at-a-time experiment would be used for the research [24]. This method usually identifies the most important factor first, and investigates the factor by itself. When searching for an optimized level

for this factor, other factors will be fixed in the procedure. Only after this optimized level was found, research on other factors will carry on. This procedure will be iterated to obtain the optimization point of all the factors [24].

Different from one-factor-at-a-time experiment, a full-factorial-experimental-design experiment was used in this study [24]. In full-factorial-experimental-design, all the combinations of factors at every level are considered together. Comparing with the traditional one-factor-at-a-time experiment, the factorial-experiment-design has several advantages [24], the biggest one being that the factorial-experiment-design requests less runs for the same accuracy. In addition, all the interactions of factors can be observed from factorial-design, but not from one-factor-at-a-time method [24]. The factorial-experiment-design result, therefore, is general and optimal settings of factors cannot be missed [24]. The statistical derivation and more discussions about factorial design can be seen in Wu and Hamada's book [24].

Sample Space

In the full factorial experiment design of this research, there are three factors: La doping, thermal aging temperature and aging time.

The first factor is the La doping percentage. The base material used in this study is the 96.5Sn3.5Ag wt% lead-free solder alloy and three level of La doping were used with the final alloy compositions in weight percent are: 96.45Sn3.5Ag0.05La, 96.4Sn3.5Ag0.1La and 96.25Sn3.5Ag0.25La. Because rare earth elements cannot be separated easily, usually mixed RE of Lanthanum (La) and Cerium (Ce) are used [16]. In this study, however, La was doped in SnAg solder. No result can be found on comparison between the effect from mixed RE and pure La, but due to the similarity between La and Ce, no obvious difference could be expected. From the discussion from previous discussion, RE doping level $\geq$ 0.5wt% will negatively affect the mechanical behavior [18], so maximum of 0.25% La was used for refined material optimization. The Sn3.5Ag

solder is obtained from Indium Corporation in the form of 1Kg ingot. Other SnAgLa alloys are obtained from Atlantic Metals & Alloys Inc. in the form of 200g ingot.

The other two factors of the factorial-design are controlled during the thermal-treatment procedure. The solder material was melted and cased in an aluminum mold and quenched in water at 15°C. This quenching procedure ensures the fast cooling rate to simulate the common reflow procedure. Some of the samples were then aged isothermally in high temperature oven. Two levels of the aging temperatures were used: 100°C and 170°C. The aging time factor has three levels: 20, 100 and 300 hours. Including the as-cast specimens, there were 7 combinations of thermal treatment on the specimens and considering the 4 alloys used in this study, there were 4x7=28 test conditions.

The whole sample space is illustrated in Figure 1 in a 3D space. The three axes are La percentage, aging temperature and aging time, respectively. Each cell in the 3D sample space indicates a material with unique microstructure and mechanical behaviors. Each cell was tested independently.

The effect of La doping on melting temperature and electrical resistivity were first measured. Differential scanning calorimeter (DSC) tests found that within the range of this study, La doping does not change the solder melting temperature. The melting temperature difference between the 4 materials was less than 2°C. The electrical resistivity was also found to be unchanged with both La doping and thermal aging. The resistivity of SnAg lead-free solder material is typically around 10-15μΩcm [25] and the result of this study shows the resistivity of all the test conditions are within this range. More detailed result of melting temperature and resistivity can be found in Appendix B and C, respectively.

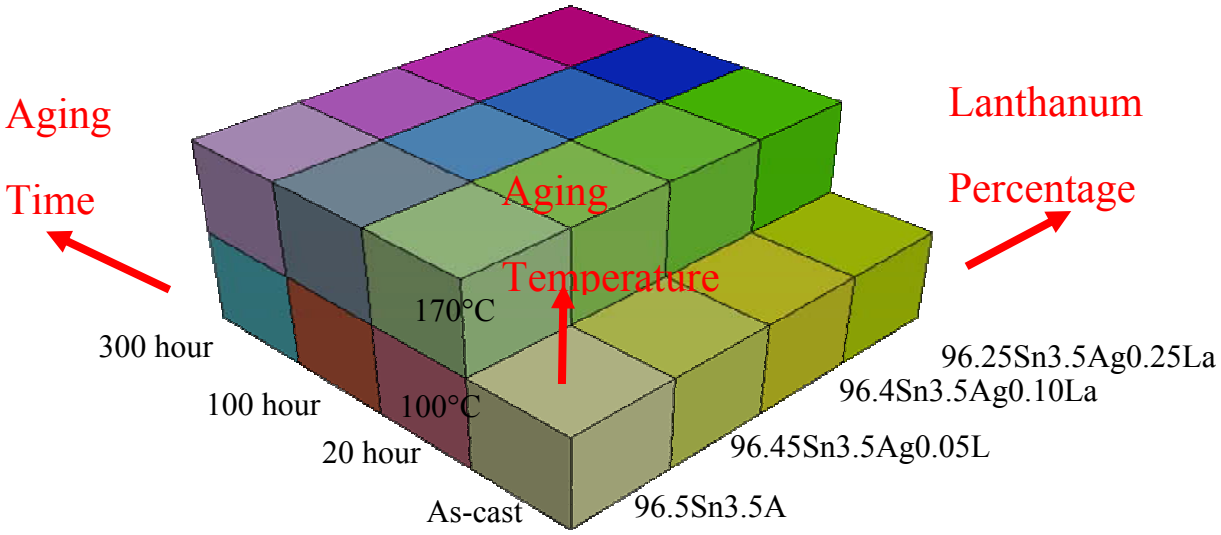

Figure 1: Experiment design sample space of this study

CHAPTER 3

MICROSTRUCTURE STUDY

Background

For the SnAg alloy, phase fraction can be estimated from phase diagrams. The calculated Ag-Sn phase diagram [26] can be seen in Figure 2. The eutectic point of this system is 96.5Sn3.5Ag. The most common phases in the SnAg alloys and their structure and prototype can be seen in Table 1.

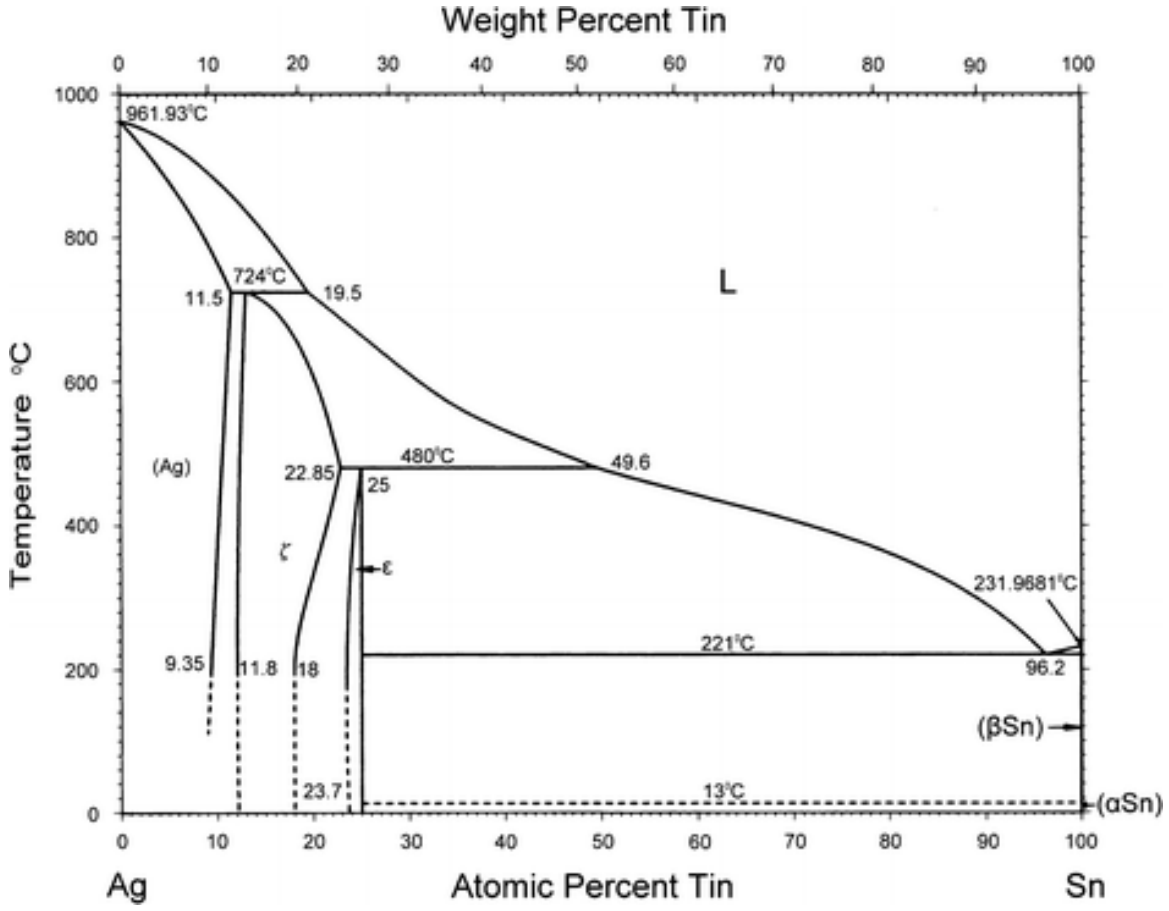

Figure 2: SnAg phase diagram [26]

Table 1: Phases crystal structures in SnAg solder [26]

Phase	Common Names	Prototype
BCT	(Sn), (beta Sn)	beta Sn
Ag_3Sn	Epsilon	beta Cu_3Ti

The typical microstructure of SnAg solder can be seen in Figure 3(a). In the eutectic SnAg solder microstructure, about 90% of the volume is β-Sn [35], which is in the form of β-Sn dendrites to be seen as the dark part of Figure 3 (a). More information about β-Sn crystal structure is collected in Appendix A. The light parts are SnAg eutectic structures of SnAg intermetallic or SnCu intermetallic embedded in Sn matrix. When stored at high temperature, the particles will coarsen.

All microstructures are highly thermal-treatment dependent. Depending on the cooling rate, the SnAg intermetallic particles can vary from needles of approximately 10 micron (slow cool) [27] to spheres of sub-micrometer diameter(fast cool). The Sn dendrites are also smaller under rapid cooling. Under slow cooling with the cooling rate less than 1.2°C/s, Ag_3Sn plate can be formed in solder material. The interfaces between the Ag_3Sn plate and β-Sn phase provide a preferential crack propagation path [28]-[30]. So the suggested cooling rate is above 1.5°C/s [28]-[30] for Ag content higher than 3wt%. The plates must dissolve back into the liquid solder and the re-solidification will decide the new microstructure [28]-[30].

Aging can also affect the properties of solder material, as can be seen from Figure 3. High temperature (above 180°C), long duration (more than 3 days) aging can even modify the characterization of SnAgCu solder[31] to allow silver to rapidly diffuse into the tin-rich crystals from the eutectic region and form new precipitates, as seen in Figure 3 (d). The Cu particles coarsen more quickly along the β-Sn particle boundary.

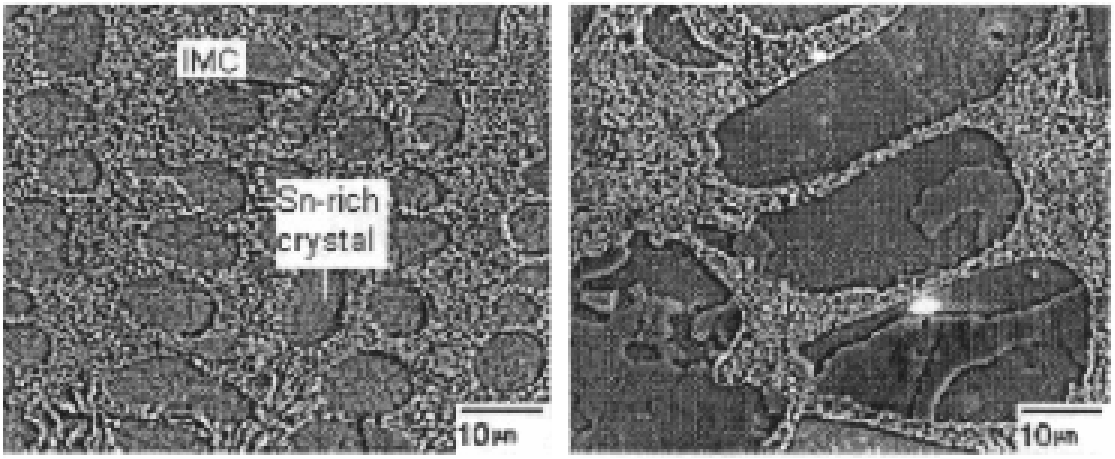

(a) As quenched (b) 35days RT

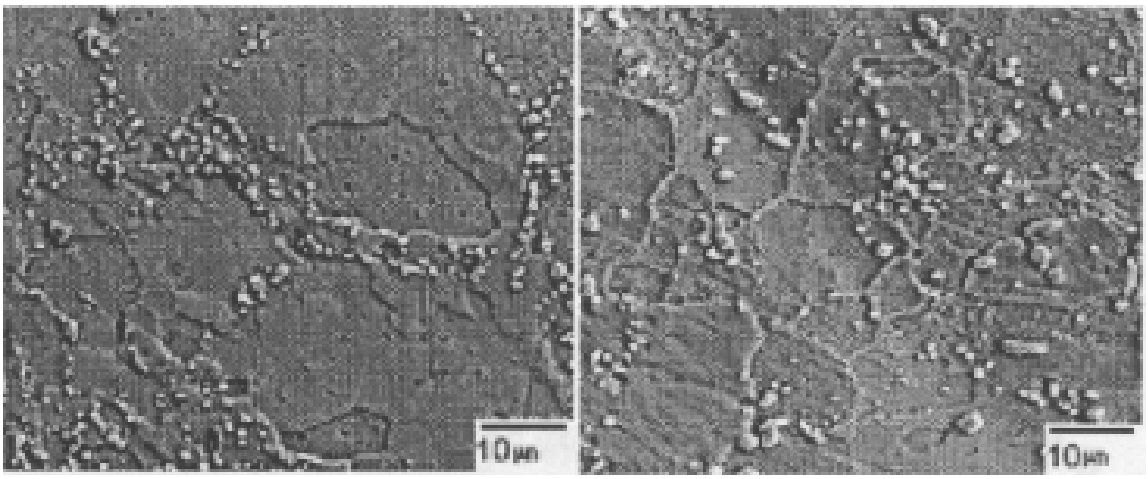

(c) 1days at 180°C (d) 3days at 180°C

Figure 3: SEM microscopies of Sn3.9Ag0.6Cu, illustrating aging effect [31]

An Orientation Imaging (OIM) with automated electron backscattered pattern (EBSP) index study found that as-fabricated joints consistently show a preferred crystal orientation with a few minority orientations with highly preferred disorientations [32]. Solidification affects crystal orientation and thus subsequent microstructural evolution. Aging can reduce the high angle disorientation grains in the SnAg solder, coarsen the Ag_3Sn particles, and reduce small grains with high –angle disorientations by forming a number of small angle boundaries.

Loading can also change the microstructure of lead-free solder. While most other researchers found fatigue coarsening of Ag_3Sn particles is not as serious as in tin lead solders and omitted this effect [27], Dutta considered coarsening in a creep model [33]. Small grains can be observed along fracture surface [34]-[36] and near the crack path region [38][39] under fatigue load, both in the Sn dendrite area and dislocation rearrangement (polygoniation) was speculated to be the cause. The Orientation Imaging study [32][37] confirmed that at a strain concentrated region, the thermomechanical fatigue causes heterogeneous refinement of the microstructure that accounts for the localized grain boundary sliding. One study of SnAgCu solder showed that after elevated temperature deformation, the β-Sn particles aligned along the maximum shear direction [31]; some even formed elongated continuous threads, as seen in Figure 4. Relations of shear band development with strain direction, crystal orientation and recrystallization phenomena are still unknown. [32][37]

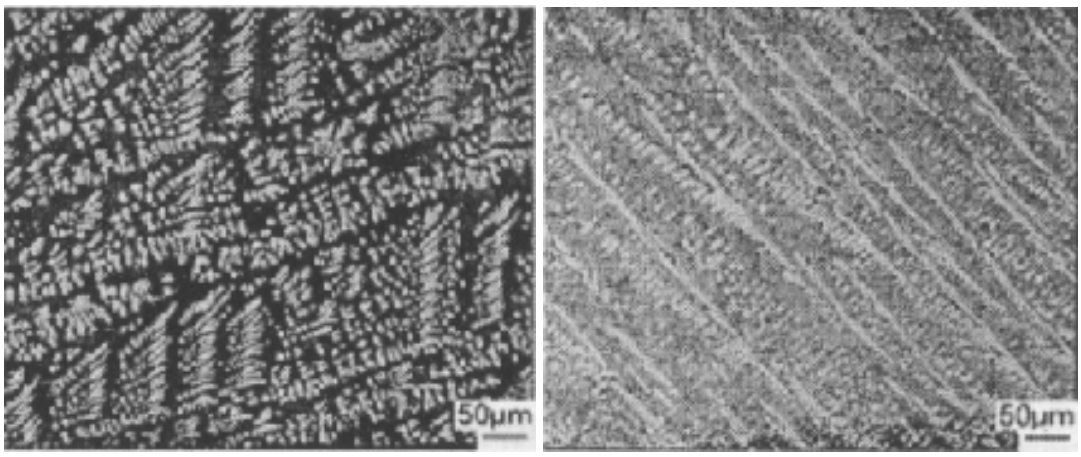

(a) As-cast (b) After crept at 115°C with 11.13MPa

Figure 4: Optical microscopy of Sn3.9Ag0.6Cu. Light phase is β-Sn. Tensile loading direction is horizontal [31]

Microstructure Study Methodology

In the microstructure study, tensile specimens were used. The sample shape is shown in Figure 5 and the thickness is 1mm. Micrographs were taken on the larger

surface of the sample. For microscopy, samples were placed into molding compound and polished to 0.05μm finish, if not otherwise stated. The polished samples were etched with HCl for different durations for different studies.

Both optical microscope and Scanning electron microscope (SEM) were used. The optical microscope used in this study is the Olympus BX40F-3 while SEM used was the LEO 1530 that equipped with Energy Dispersive X-ray Spectroscopy (EDX).

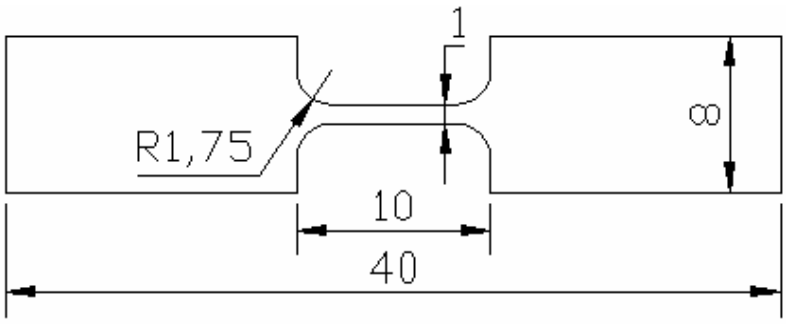

Figure 5: Mechanical drawing of tensile test specimen. Unit in mm

Quantitative Microstructure Study Methodology

Quantitative microstructure studies were performed following the instruction of ASM handbook [40]. The method can be briefly summarized here. On the cross section of the material, a set of cycloids were plotted. An example of an image overlayed with cycloid is shown in Figure 6. The test cycloid line length can be calculated from the line length in the image and the magnification of the microscopy. In Figure 6, intersections of cycloid with grain boundaries are marked with red dots.

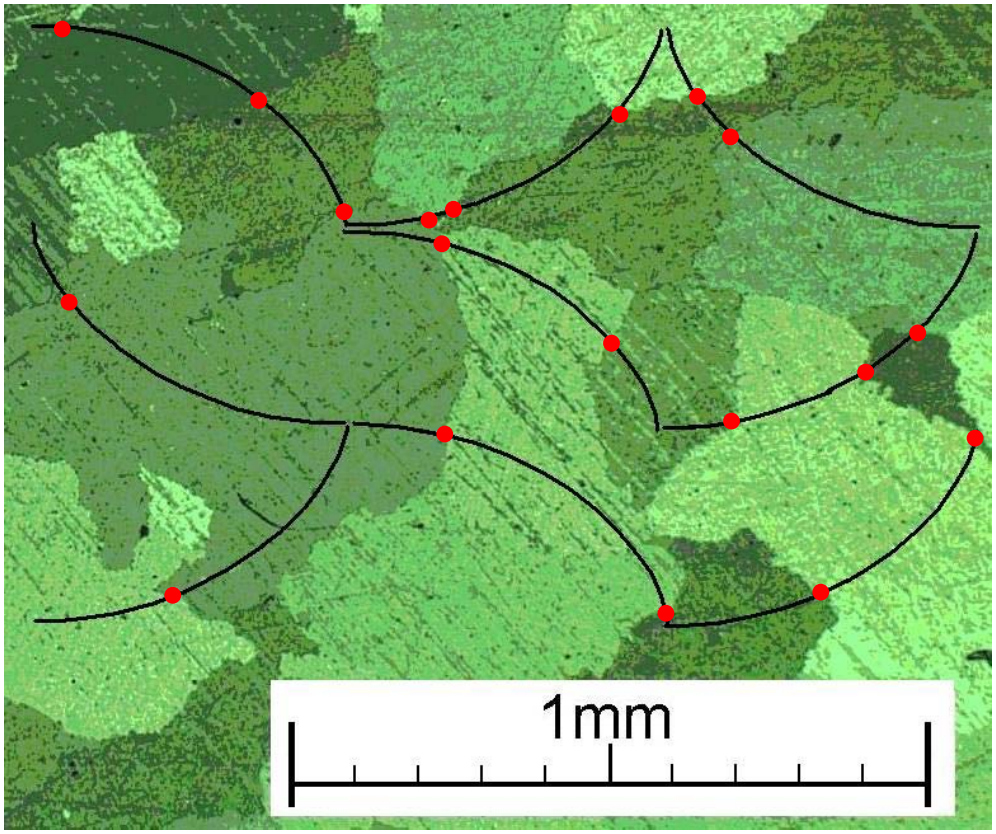

Figure 6: Illustration of calculation of intersection-per-length with cycloid lines on microscopy. Intersections are marked with red dots.

The surface area per unit volume S_V can be estimated using the stereological equation:

$$S_V = 2\langle T_L \rangle \quad (1)$$

where $\langle T_L \rangle$ is the population average value of the number of intersections of the microstructural surfaces with the cycloid shape test lines in the cross sections per unit test line length. In this study, $\langle T_L \rangle$ of a certain sample was obtained by averaging 9 cycloids per image, 10 microscopy images per sample.

For single phase polycrystalline material, grain size G can be computed using:

$$G = 2 / S_V \quad (2)$$

For the multiple phase material, there are several methods available to calculate particle size in materials. The surface-area-averaged particle size was chosen for the best accuracy within the limit of the processing method available to the author. For the multiple phase condition, such as Ag_3Sn particle size and Sn dendrite/eutectic region size in this research, surface-area-averaged particle size was used. Surface area averaged particle size d_s can be obtained with:

$$d_s = 6V_V / S_V \quad \textbf{(3)}$$

where V_V is the volume fraction of the particles. To estimate the volume fraction, a point sampling frame was also used to determine $\overline{P}^{\alpha}$, the average number of points falling within the interest regions. An example of the point sampling frame is shown in Figure 7. The volume fraction can be estimated from the ratio of $\overline{P}^{\alpha}$ to total point number.

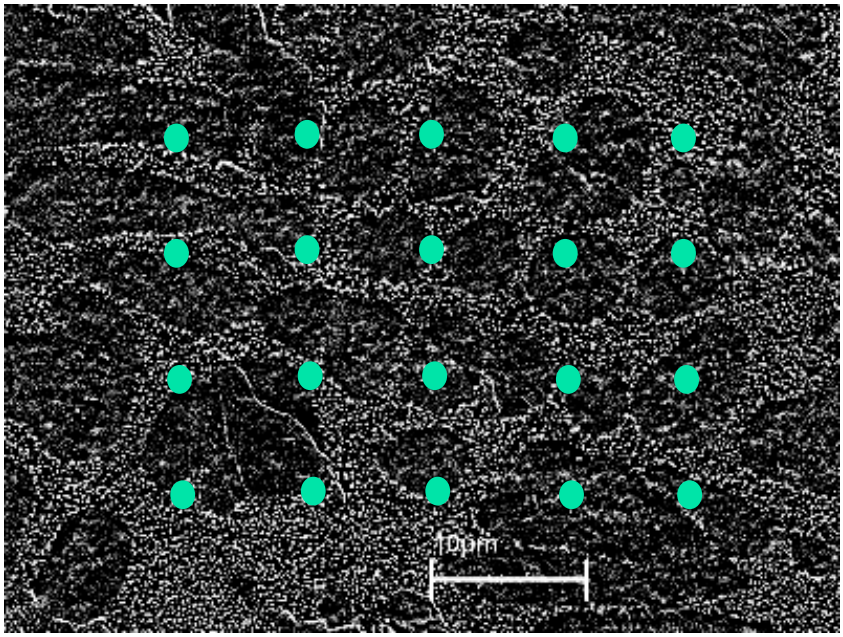

Figure 7: Illustration of point sampling method for volume fraction measurement Sn dendrite

Due to the complexity of the microstructure of the SnAg alloy and the low contract of Sn and Ag element in SEM image, most of the stereology studies reported here are done manually.

Confidence intervals were constructed for all experimental values. These intervals are expressed as sampling errors centered about the estimate,

$$error = \frac{t_{\frac{\beta}{2},(n-1)}\, s}{\sqrt{N}} \quad (4)$$

where $t_{\frac{\beta}{2},(n-1)}$ is the students t-distribution for confidence level (1-β) and N data observations and s is the sample variance of observations x as described by

$$s^2 = \sum_{i=1}^{N} \frac{\bar{x} - x_i}{N-1} \quad (5)$$

And the average value of all the sample observations is given by

$$\bar{x} = \frac{1}{N} \sum_{i=1}^{N} x_i \quad (6)$$

For a large number of observations (about 25 or so) $t_{\frac{\beta}{2},(n-1)} \approx 1.75$ at 95% confidence (β=0.05). When using a point counting frame to determine volume fraction, the sampling relative error decreases with increasing number of sampling points in the frame such that

$$error_{V_V,\,relative} = \frac{1.75s}{\bar{P}^{\alpha}\sqrt{N}} \quad (7)$$

where $\bar{P}^{\alpha}$ is the average number of points on the counting frame which lie in the phase of interest.

Distribution of Rare Earth Element

EDX study found that the La exists in lead-free solder materials in two forms: at the natural surface or in the form of La-Sn intermetallic.

Specimen Surface

As the surface agent, some of the La element will move to the surface during solidification. Comparing with no doped condition, micron size pores are seen on the unpolished surface at doped sample, as in Figure 8(a). EDX study detected much higher

concentration of La on the unpolished, as-cast natural surface. Element maps were acquired using EDX on the surface of the La doped solder material, as shown in Figure 8. Figure 8 (d) shows that the La element is uniformly distributed on the surface.

The effects of higher concentrations of La element on the surface have two folds. When the material is used as solder joint, the RE element at interface will help to improve the wetting ability of the joint, because the La element at the natural surface of the bulk solder will form chemical bound with other materials. On the other hand, higher concentration on the surface means less La within the bulk.

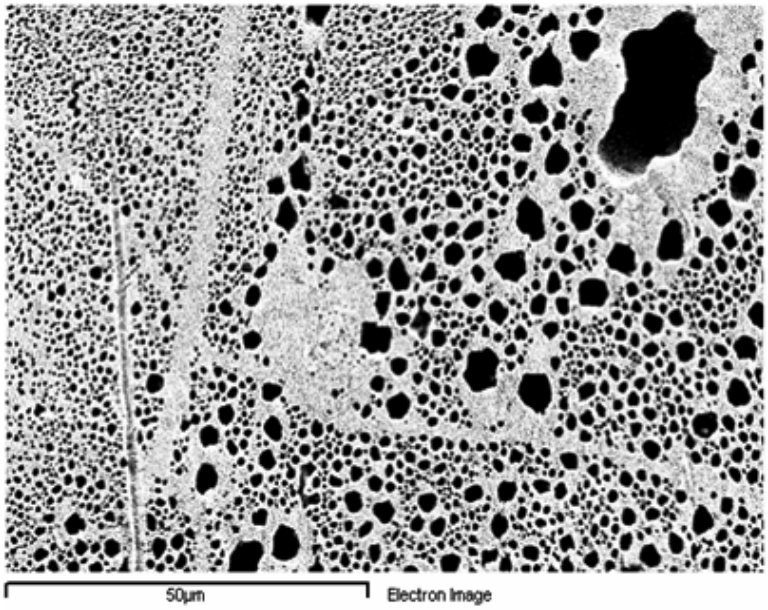

(a) Original SEM image

Figure 8: EDX element maps of the natural surface of a sample

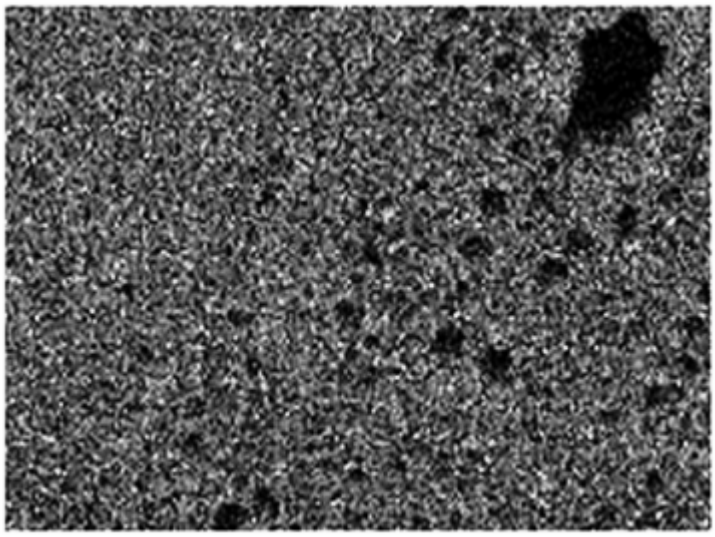

Tin

(b) Tin

Silver

(c) Silver

Figure 8: EDX element maps of the natural surface (continue)

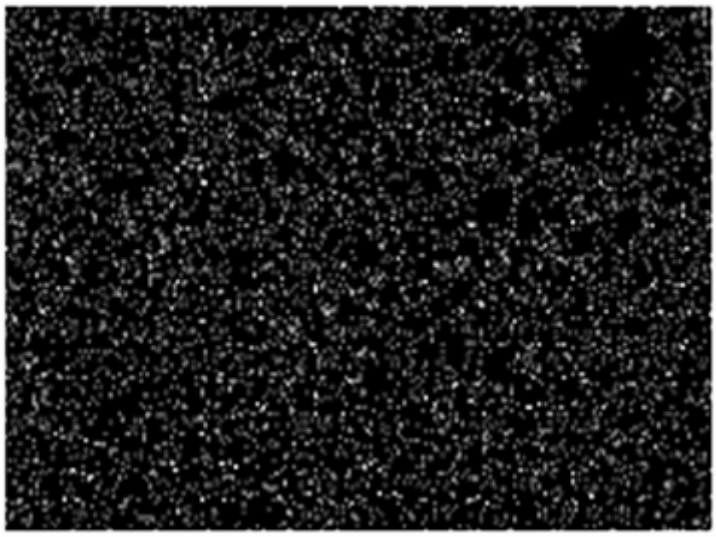

(d) Lanthanum

Figure 8: EDX element maps of the natural surface (continue)

Rare Earth Intermetallic

Within the bulk, RE exists as a La-Sn intermetallic. As mentioned in [41], La in SAC solder will form the $LaSn_3$ alloy. The heat flow vs. temperature melting curves show that the melting temperature of this alloy is ~335°C [41]. The IMC has complex 3D branch structure [41], which is usually shown as clusters of snow flakes [3] in SEM images.

The snow flakes were also observed in this study and examples can be seen in Figure 9 and Figure 10. EDX study confirmed that there was indeed very high concentration of La in the snow flake structure. It was also observed that the amount of $LaSn_3$ IMC is dependent on RE doping. With less RE doping, the snow flakes are usually isolated small ones, as seen in Figure 9 for 0.05wt% condition; with higher RE doping, bigger snow flakes can be seen in a cluster form, as seen in Figure 10 in 0.25wt% condition.

Previous research found that high doping of La will cause $LaSn_3$ IMC flakes to aggregate along grain boundaries and adversely affect the mechanical properties of solder alloy [3][23][22]. Following these results, 0.25wt% of La was set as the upper limit of this study. This tendency, however, was not found, and the creep property was not degraded with excessive IMC, which will be discussed in a Chapter 5. Also different from the result in [3][23][22], the La-Sn IMC clusters are not necessarily located at the grain boundaries. These differences may caused by the cooling rate difference, and in stead of using slow cooling rate as in previous studies, fast water quenching was used in this work. No conclusion can be made at this time.

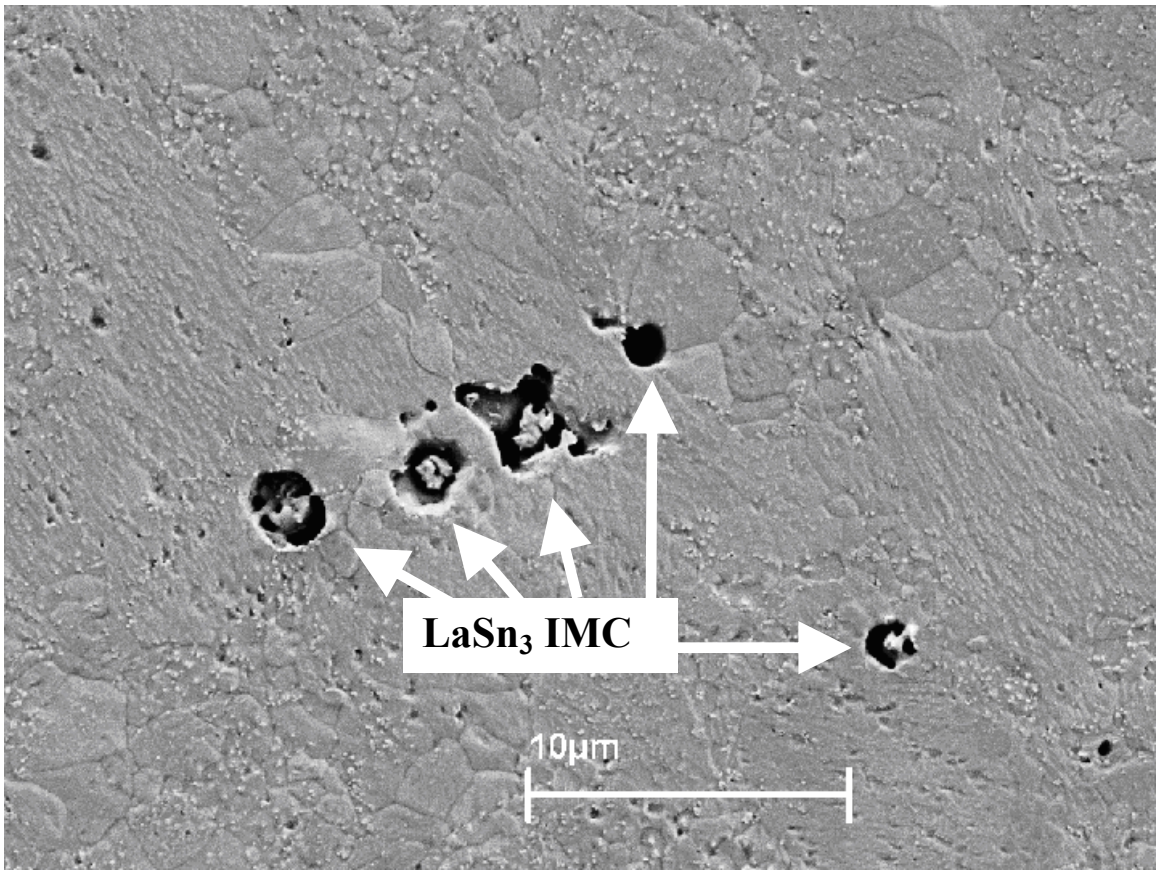

Figure 9: A $LaSn_3$ cluster in 0.05%La solder

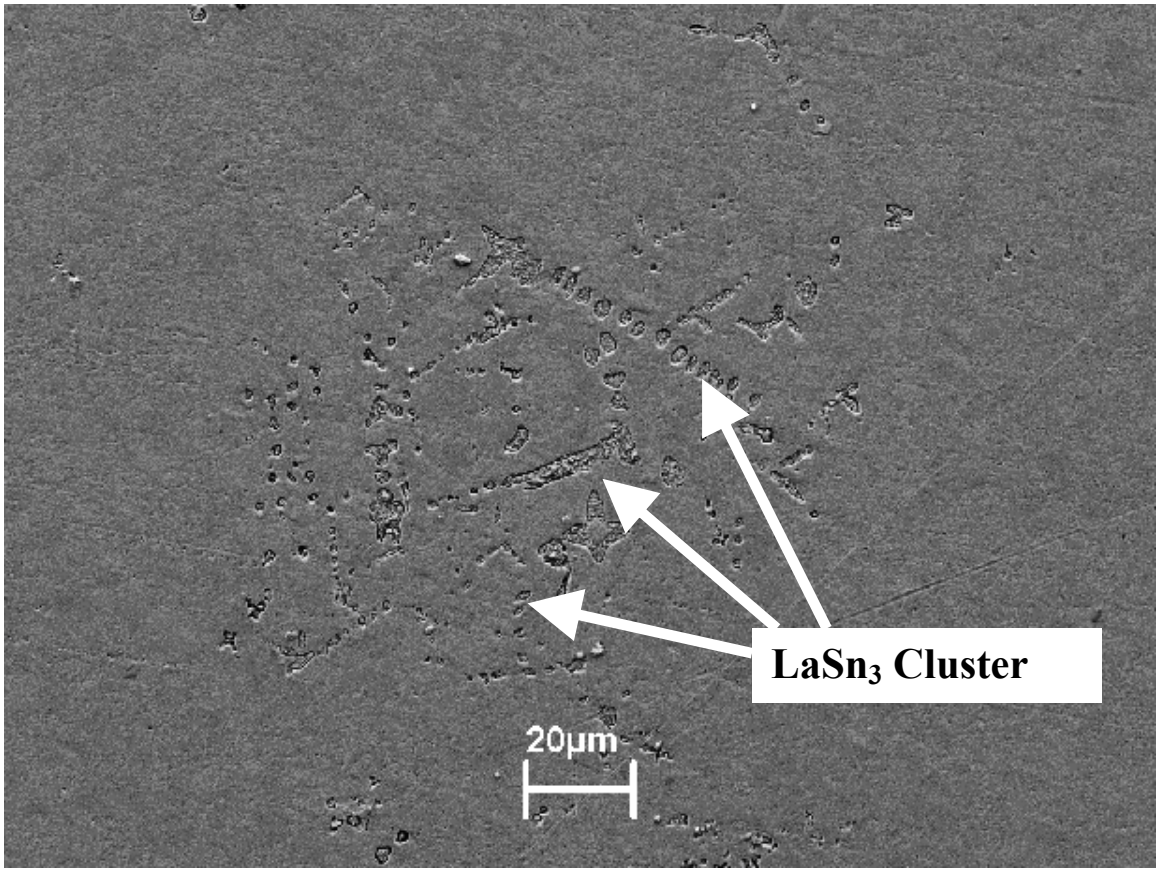

Figure 10: $LaSn_3$ clusters in 0.25%La solder

Discussion

Two forms of detectable La in SnAg solder have been discussed: the natural surface and the La-Sn IMC. Although not observed due to experimental limitation, the La may also be present in bulk alloy in an elemental form. It is postulated that such elemental form of RE dispersed through out the bulk is responsible for changing the overall microstructure of the alloy. A STEM study by Buban *et al.* observed yttrium atoms deposit at alumina boundaries [42] and its effect on enforcing interfacial bonding was proved by physical atom dynamics model [42]. No similar study has been done with La and SnAg alloy but similar situations could be expected.

Grain Size

The microstructure of the alloys was studied from multiple length scales including grain, phases and particles.

Optical microscopy with cross polarized light was used to study the microstructure of the solder material at the grain scale. With the help of cross polarized light, grains can be observed as different shade under the microscope. A typical image of an as-cast sample with no La doping is shown in Figure 11, and that of a La doped sample is shown in Figure 12. The grain size difference is obvious, and the grain sizes of samples subjected to different tests conditions are plotted in Figure 13 and Figure 14 as a function of percentage of La doping. Figure 13 illustrates the La doping effect on initial as-cast grain size only with error bars on each data point and Figure 14 contains all the test data. The errors of the data shown in Figure 14 are close to that shown in Figure 13 and thus not shown in detail. These figures show that alloys with La doping have much smaller grain size than that without La.

Note that while the grain size of the un-doped samples is very large, there is typically only one grain across the width of the sample. Therefore, the specimen width (8mm) is used as the grain size for un-doped samples, as seen in Figure and Figure 14.

Figure 13 and Figure 14 shows that the optimal La doping to minimize grain size is around 0.05%. This conclusion was obtained by collecting an additional data point with 0.02% of La which is not included in the original sample space.

The grain sizes of La doped samples are shown in Figure 15 as a function of aging time. Statistical analyses of the data shown in Figure 7 using a general linear model ANOVA [24] indicate that thermal aging do not coarsen grain size of La doped solder materials.

Previous studies have found that due to the pining effects of the Ag_3Sn particles, temperature aging dose not affect the grain size in un-doped SnAg solder alloys[32][43]. The data presented in Figure 14 and Figure 15 show that even though La doping

drastically reduced the grain size in these alloys, the much smaller grains still remain relatively unchanged during temperature aging within the range considered here.

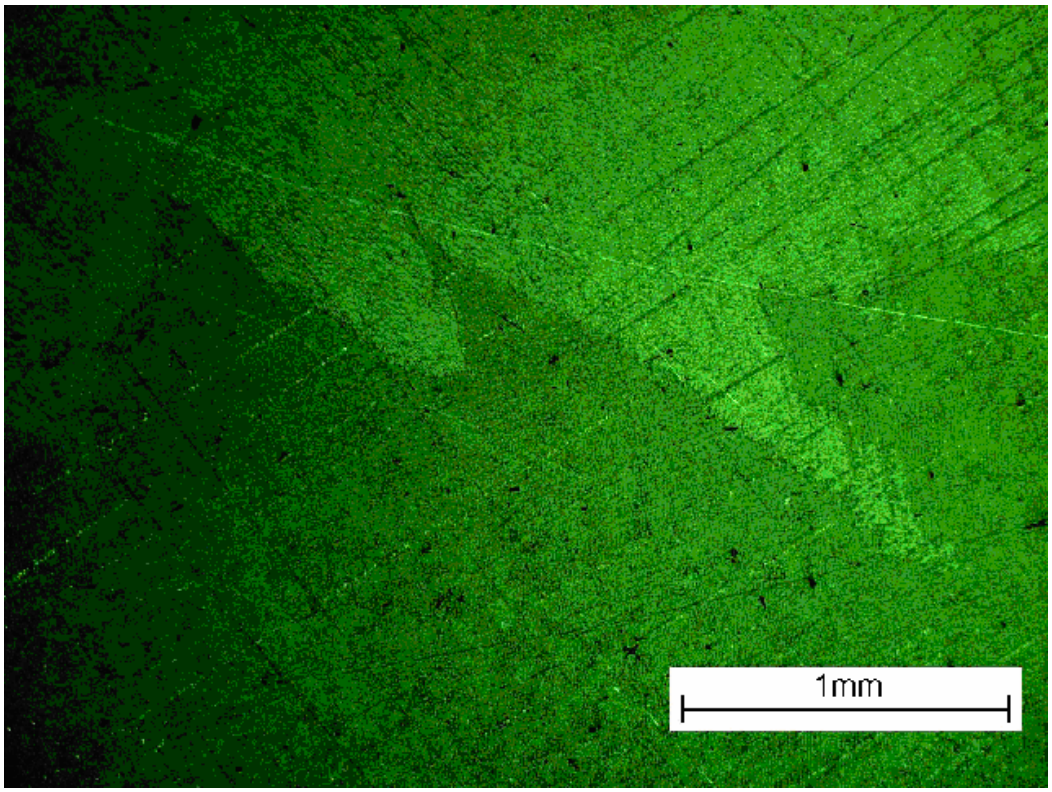

Figure 11: A grain boundary obtained with optical microscopy with cross polarized light, no La

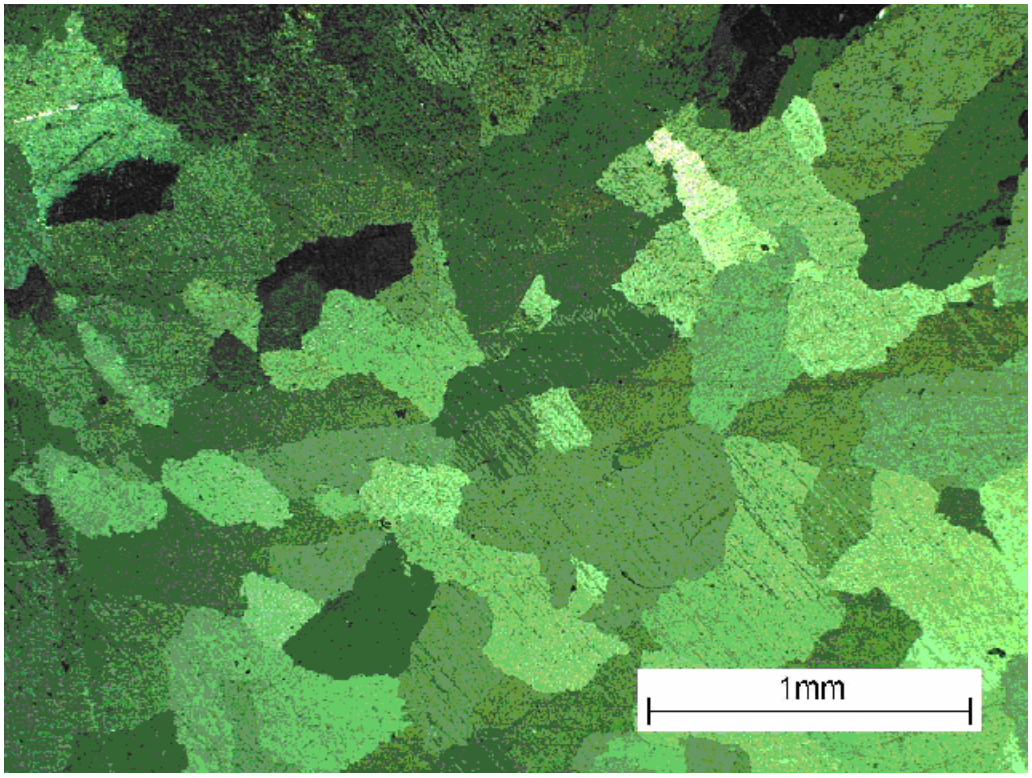

Figure 12: Grains of a 0.25%La solder sample obtained with optical microscopy with polarized light

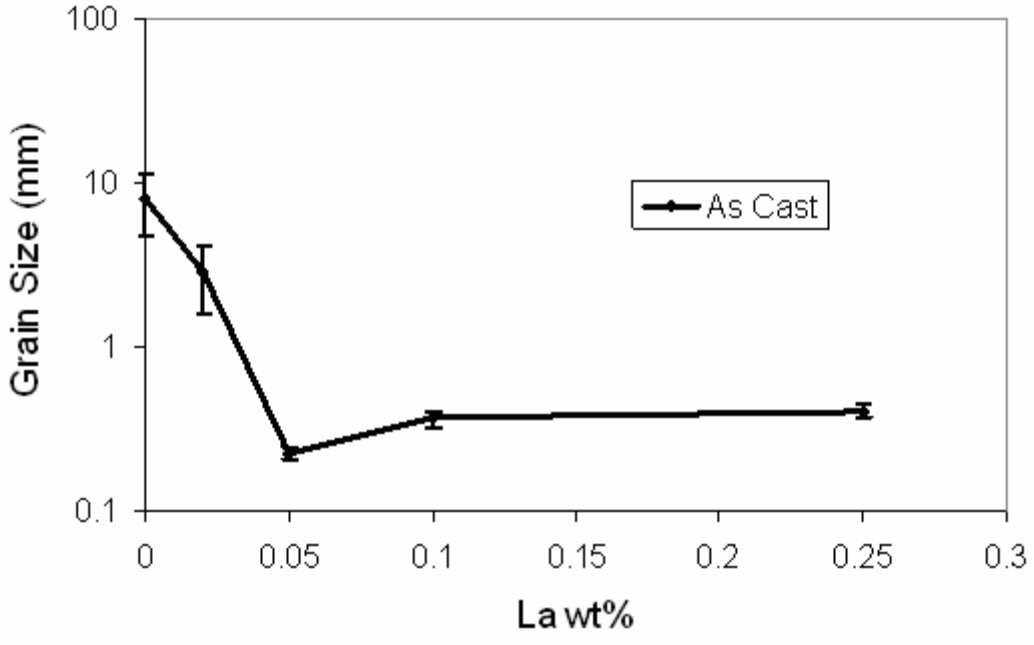

Figure 13: Grain size as a function of rare earth percentage, with error bar, as-cast condition only

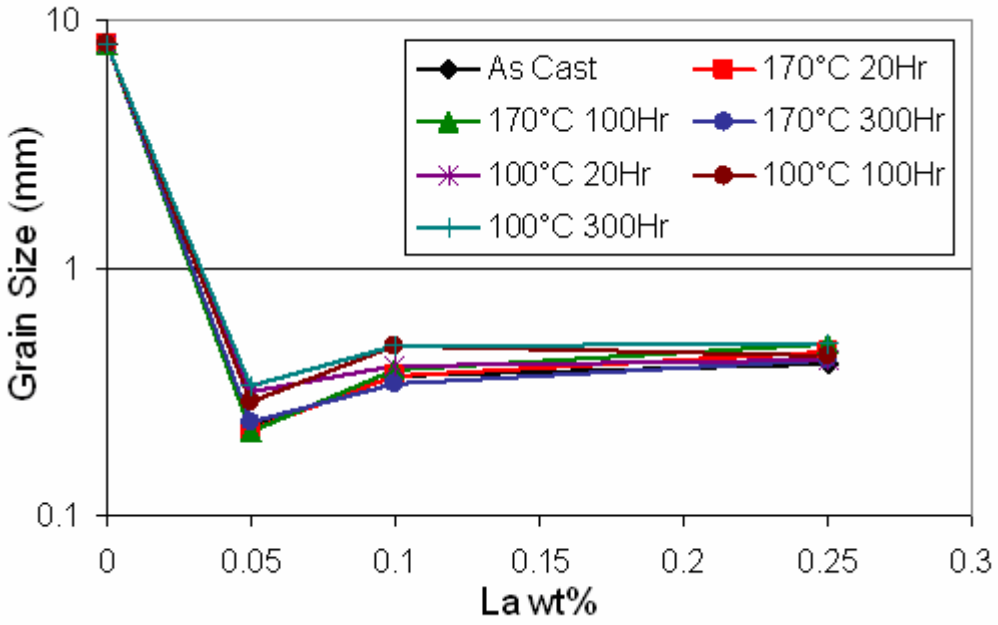

Figure 14: Grain size as a function of La percentage

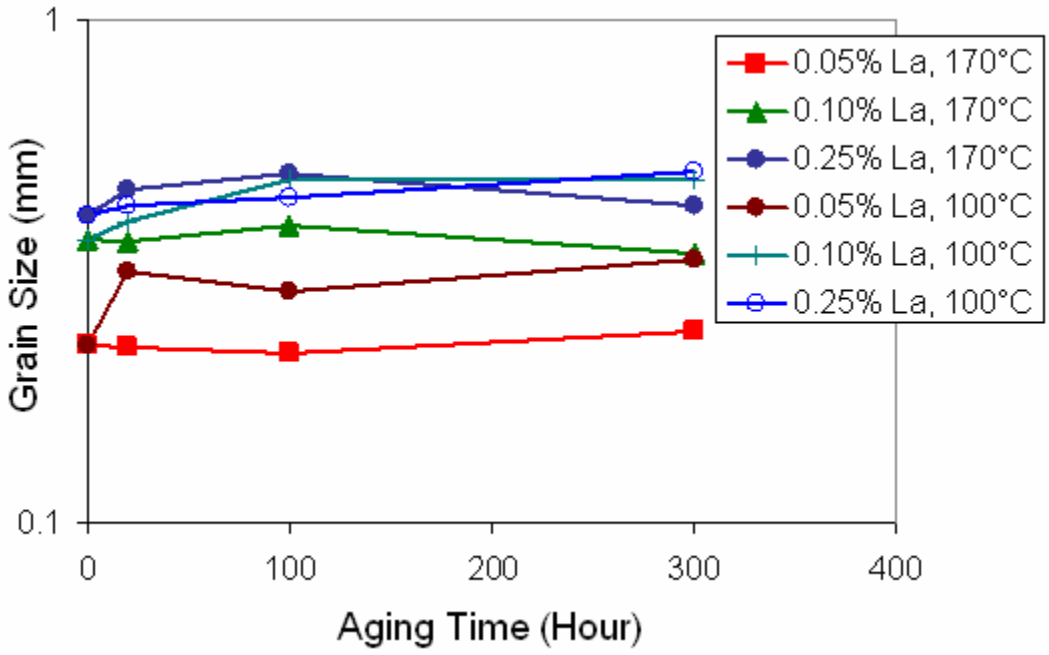

Figure 15: Grain size as a function of thermal treatment, La doped only

Dendrite/Eutectic Volume Fraction Study

The as-cast solder alloy can be viewed as a composite material comprising β-Sn dendrite and SnAg eutectic region with a very clear boundary between these two. After aging, Ag_3Sn particles in SnAg eutectic region become bigger and more uniformly distributed. In this condition, the Sn dendrite and eutectic region are not clearly defined, see Figure 17. For this reason, the volume fractions of these two regions were measured for only the as-cast samples and shortly aged samples.

The volume fractions were measured manually following the point sampling frame specified in ASM handbook [40]. Volume fractions of the regions are plotted in Figure 16 for as-cast condition only with error bar and both as-cast and shortly aged conditions are listed in Table 2. La doping enlarged the eutectic region and the material change from Sn dendrite dominated in un-doped solder to eutectic region dominated in RE doped condition. It can be seen that short aging does not change the region volume fraction.

The sizes of the dendrite and eutectic region were also measured and no obvious trend can be observed from this figure.

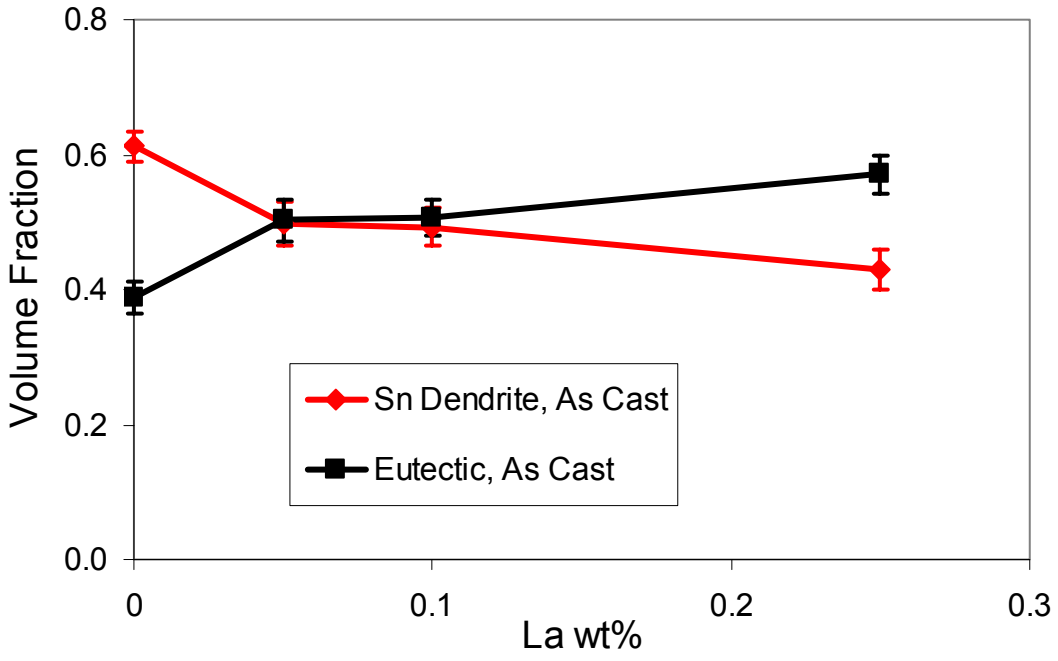

Figure 16: Volume fraction of Sn dendrite and eutectic region as a function of La percentage, with error bar, as-cast condition only

Table 2: Volume fraction distribution dendrite and SnAg eutectic region, as-cast conditions only

La wt%		0	0.05	0.1	0.25
As-cast	Sn Dendrite	0.61±0.02	0.50±0.03	0.49±0.03	0.43±0.03
	Eutectic	0.39±0.02	0.50±0.03	0.51±0.03	0.57±0.03
170°C 20 Hr	Sn Dendrite	0.61±0.03	0.53±0.04	0.49±0.03	0.45±0.04
	Eutectic	0.39±0.03	0.47±0.04	0.51±0.03	0.55±0.04

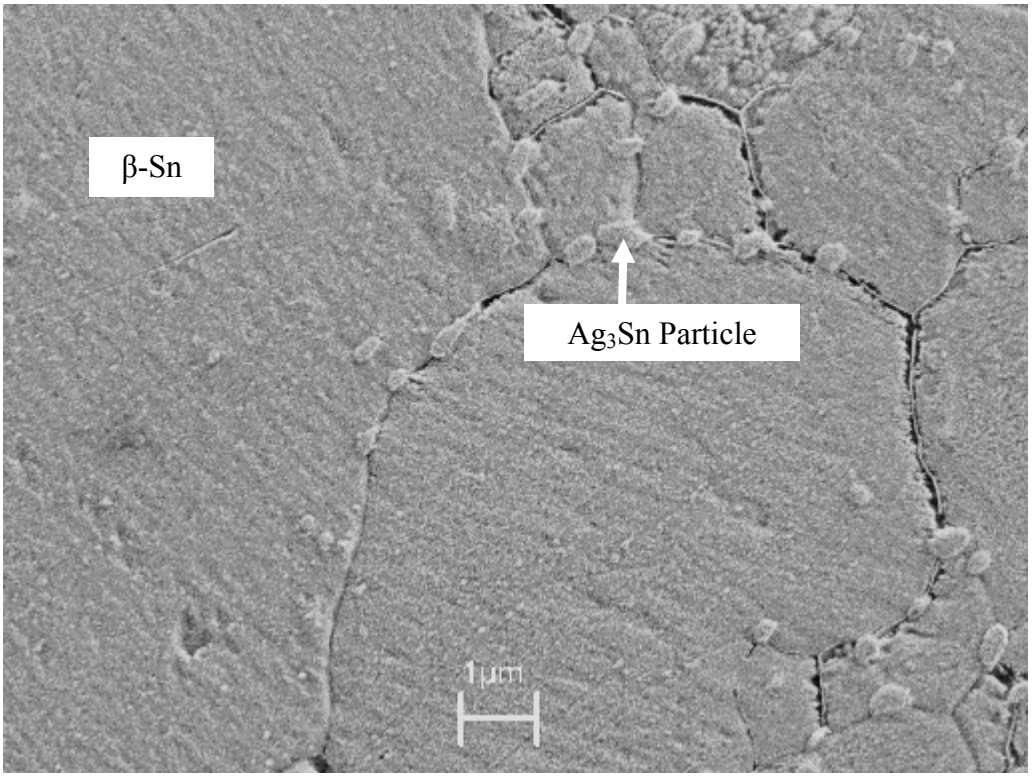

Figure 17: A thermal aged microstructure illustrating eutectic regions are not well defined after aging. 0.05% La aged at 100°C for 100 hours.

Particle Size

To study the Ag_3Sn particle size, the specimens were etched with 10% HCl for 5 minutes. The typical SEM images of alloys are shown in Figure 18 (no doping) and Figure 19 (La doped). The particle size difference is obvious.

Surface area averaged particle size of Ag_3Sn particles are manually calculated according to the ASM Handbook [40]. Ag_3Sn particle sizes are plotted in Figure 20 for initial as-cast condition only with error bars and the full data set is plotted in Figure 21 and Figure 22 as functions of La doping level and aging times, respectively. Rest of the data has similar error level as in the as-cast condition in Figure 20. The data clearly show that the La can drastically decrease the particle size. The coarsening rate is also reduced with La doping. Particles refinement will be further discussed in the Chapter 4.

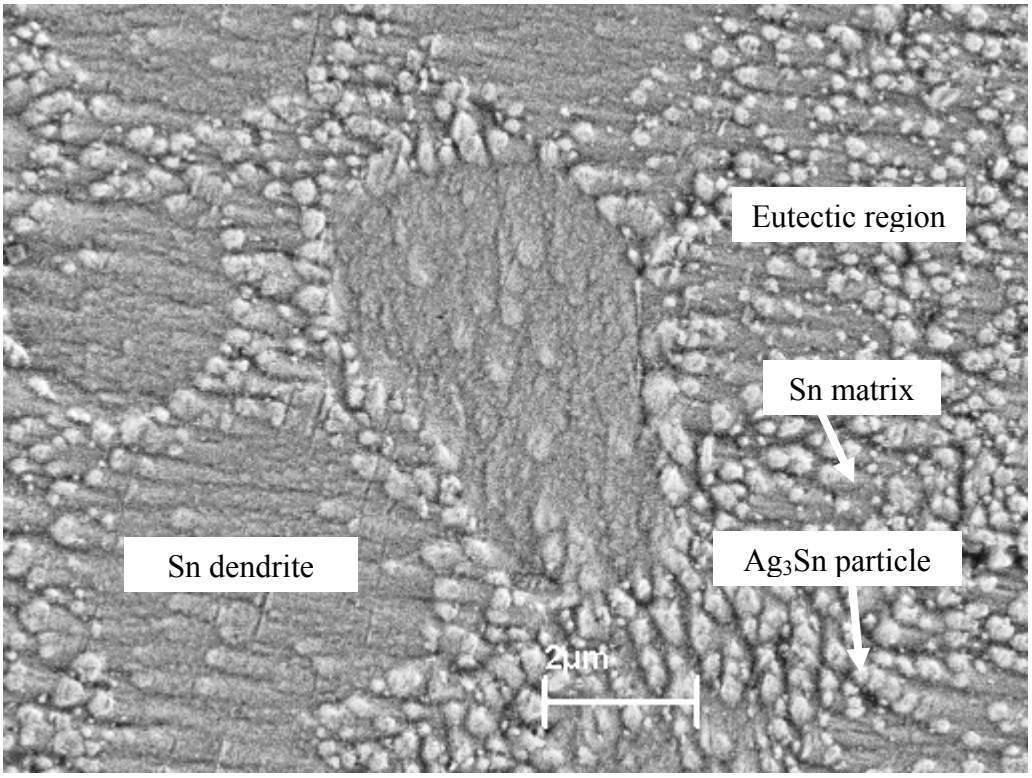

Figure 18: SEM image of SnAg solder, La free, as-cast

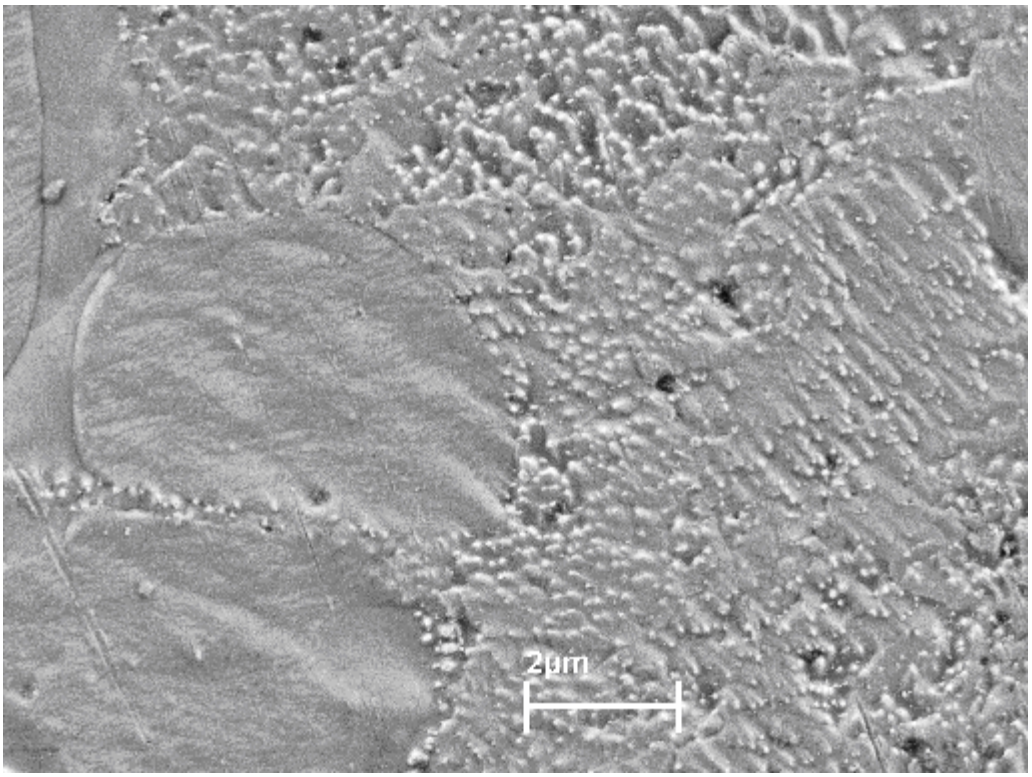

Figure 19: SEM image of SnAg solder, 0.25%La, as-cast

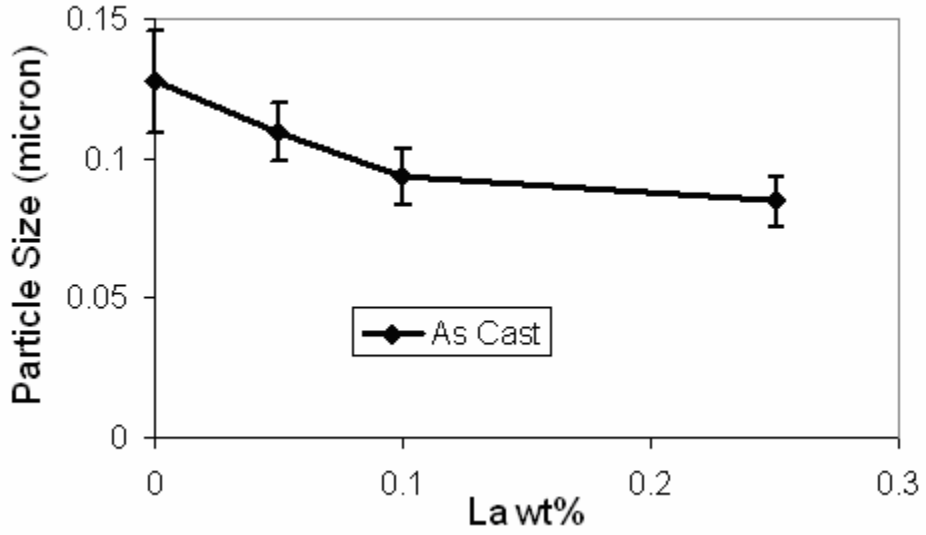

Figure 20: La doping effect on initial Ag_3Sn particle size, with error bar

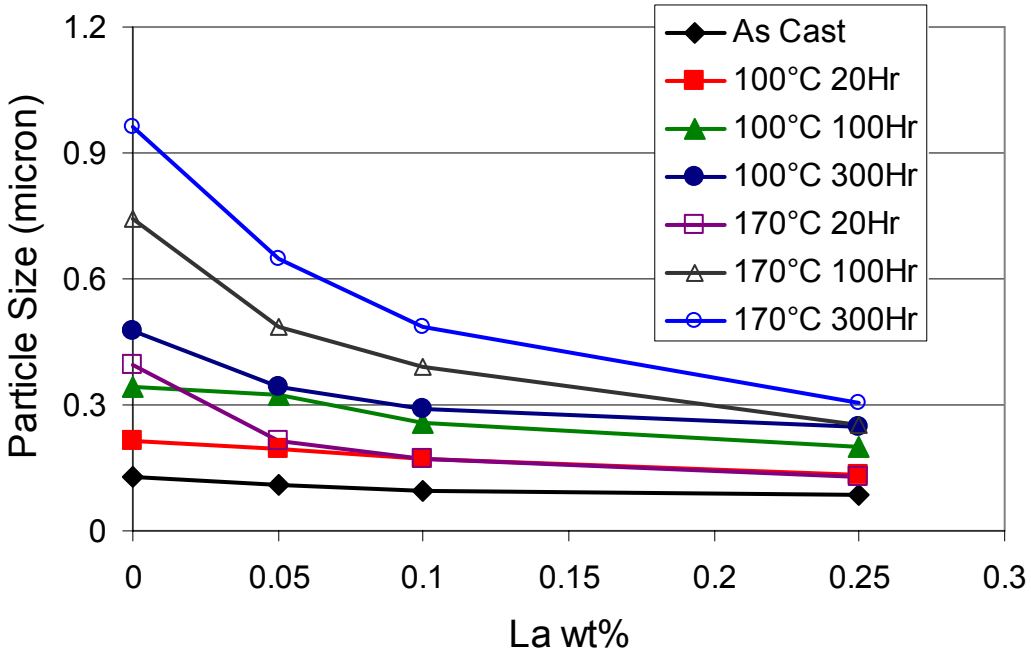

Figure 21: Particle size as a function of La percentage

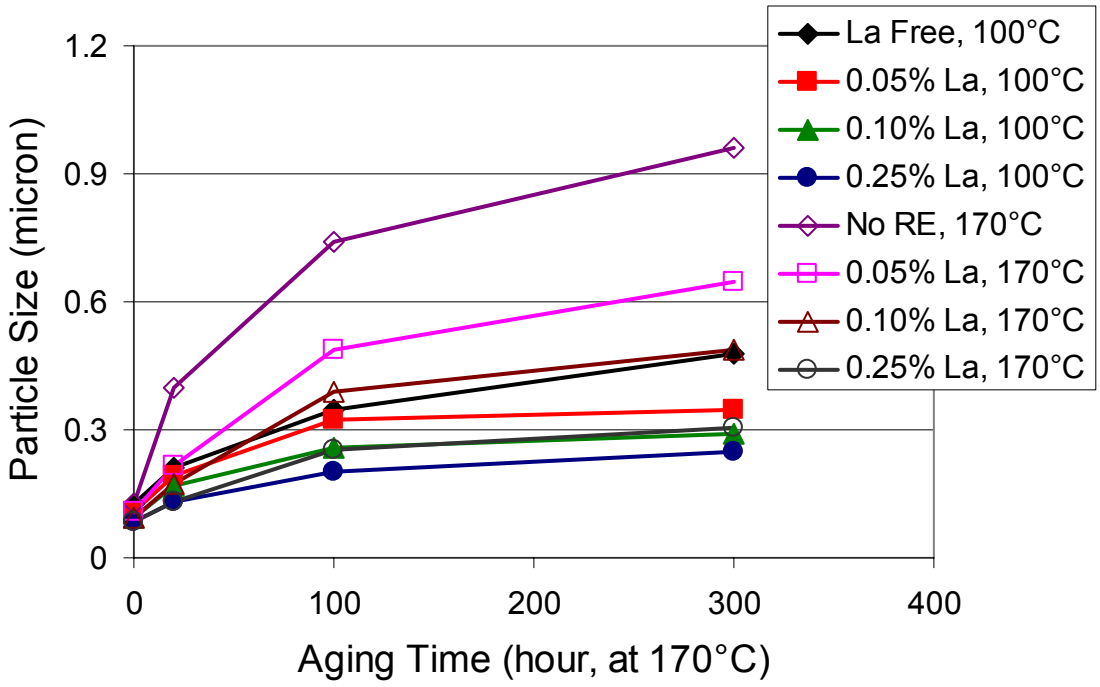

Figure 22: Particle size as a function of thermal treatment

Particle Spacing

It can be calculated from stoichiometry that the volume fraction of Ag_3Sn particles in the Sn3.5Ag should be around 0.07[33]. Since the LA doping amount was very small and Ag fraction was kept constant among the alloys, it is reasonable to assume that the Ag_3Sn volume fraction will not change with doping. If one assumes that the particles are spherical and uniformly distributed within the eutectic region, then the spacing between the particles can be calculated from the eutectic region volume fraction.

The results are shown in Table 3. Interestingly, the results show that the inter-particle spacing (side-to-side distance) remains constant (average 0.06 μm with standard derivation of 0.003 μm) even though doping drastically reduced the particle size. This is consistent with the fact that higher doping level yields smaller particles size, which inevitably increases the number of particles. If the inter-particle spacing remains unchanged, higher doping level will then leads to larger eutectic regions volume fraction.

Note that during solidification, the Ag_3Sn particles are formed first because of their low undercooling requirement. Once formed, they will be covered with small amount of tin layer before the Sn dendrites push them together to from the eutectic region. The fact that the inter-particle spacing does not change with La doping seems to indicate that the thickness of this tin layer covering Ag_3Sn particles is not affected by the La doping.

Table 3: Calculated particle spacing

RE Doping (%)	0	0.05	0.1	0.25
Particle Spacing (micron)	0.05	0.06	0.05	0.05

Summary

In this chapter, quantitative microstructure study has been performed at various length scales to investigate the effects of La doping on SnAg solder alloys. It is found that La doping (i) drastically reduces grain size, (ii) does not affect grain size coarsening, (iii) significantly reduces the Ag_3Sn particle size, (iv) does not change the inter-particle spacing, and (v) greatly reduces the particle coarsening rate.

CHAPTER 4

MICROSTRUCTURE COARSENING MODELING

Background

For many polycrystalline materials, the particle size d varies with time t according to the following relationship [44],

$$< d >^n - < d_0 >^n = Kt \quad \textbf{(8)}$$

where $<d>$ is the averaged particle size at time t, $<d_0>$is the averaged initial particle size at the time when the particles start coarsening, and K and n are time-independent constants. Depending on coarsening mechanisms, the particle size exponent n will have different values, as listed in Table 4[45]. Several studies on Ag_3Sn particle coarsening found that volume diffusion is the dominant process and 3 is used for the exponent n [45] [46] [48] [50]. This model can be rewrite into the following equation [46],

$$< d >^3 - < d_0 >^3 = B\frac{\gamma \Omega C_0 D_v}{RT} t \quad \textbf{(9)}$$

where B is the parameter depending on the volume fraction of the particles, γ is the free energy per unit area of the particle boundary, Ω is the molar volume of the particle, C_0 is equilibrium solute concentration near the particle boundary, D_v is the coefficient of solute diffusion in the matrix, R is the gas constant, and T is the absolute temperature. Equation (9) can be simplified as

$$< d >^3 - < d_0 >^3 = \frac{K_0}{T} t \exp\left(\frac{-Q}{RT}\right) \quad \textbf{(10)}$$

where K_0 is a temperature and time independent constant, Q is the activation energy for the rate-controlling process.

The activation energy (Q in equation (10) was found to be between 45kJ/mol [48] [50] and 65kJ/mol [48]. Dutta [33] also considered the effect of thermomechanical loading on coarsening. In his model, a strain rate dependent term was introduced into the constant K_0 in equation (10).

Table 4: Value of the particle size exponent *n* for coarsening processes with different rate-controlling mechanism [45]

n	Rate-controlling mechanism
2	Transfer of solute atoms across the interface between the particle and matrix
3	Volume diffusion
4	Diffusion along grain boundaries or interfaces
5	Diffusion along triple junctions or dislocations

Particle Coarsening Model Fitting

Based on the discussion above, the coarsening model shown in equation (10) was used in La doped SnAg solder particle coarsening. The constants for K_0 and Q are listed in Table 5 and comparisons of test data with model are plotted in Figure 23.

The coarsening activation energy for non-doped SnAg solder was found to be about 39kJ/mol. This is consistent with Dutta's result [48]. The activation energy decreases with the increasing of La doping. The pre-exponential constant K_0 decreases drastically with increase of La addition. Because of the low activation energy and low pre-exponential constants, it will be easier for La doped solder alloys to reach the saturated particle size, and the saturated particle size is much smaller than that of the un-doped alloys.

Table 5: Particle coarsening model constants

La doping level (wt %)	0	0.05	0.10	0.25
Q (kJ/mol)	39	31	27	15
K_0(μm^3/Hour)	4.2E4	1.6E3	2.4E2	3.2

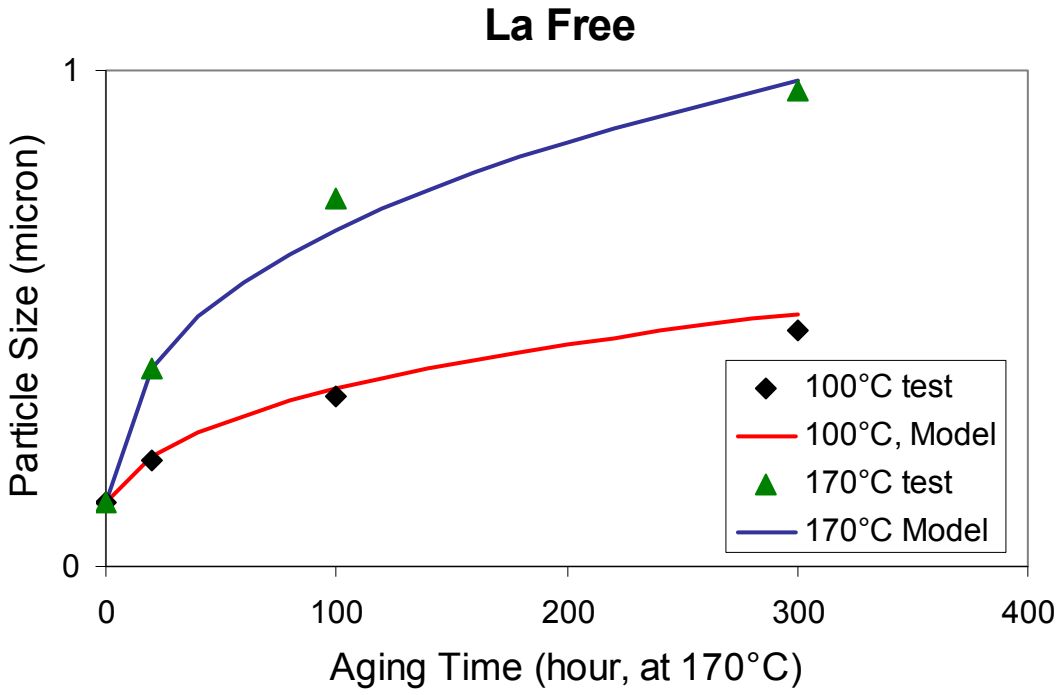

(a)

Figure 23: Comparison of particle coarsening model with test data

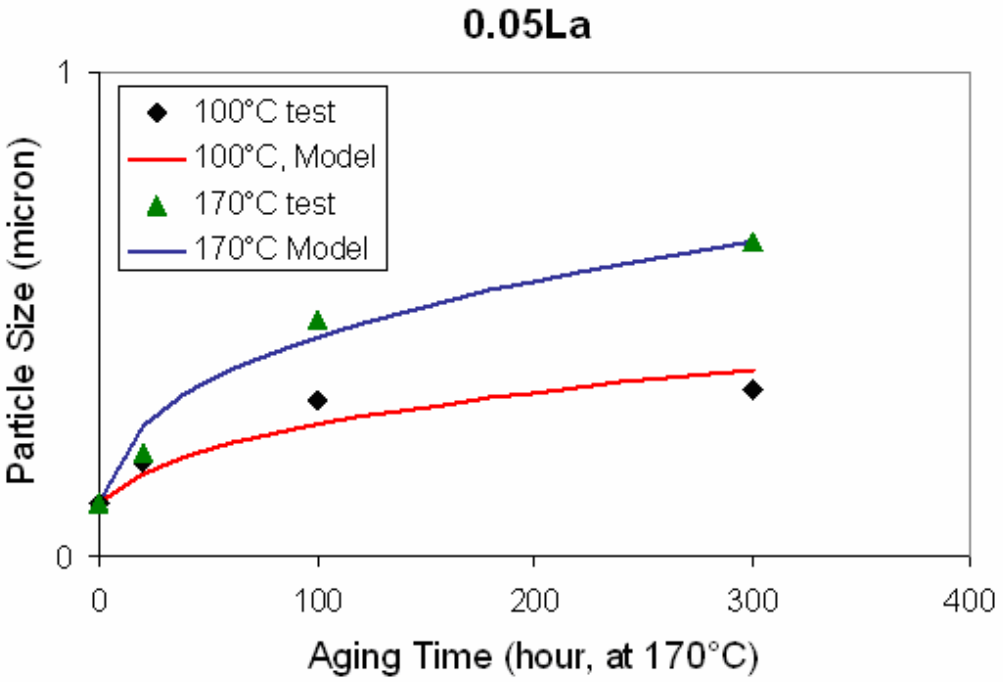

(b)

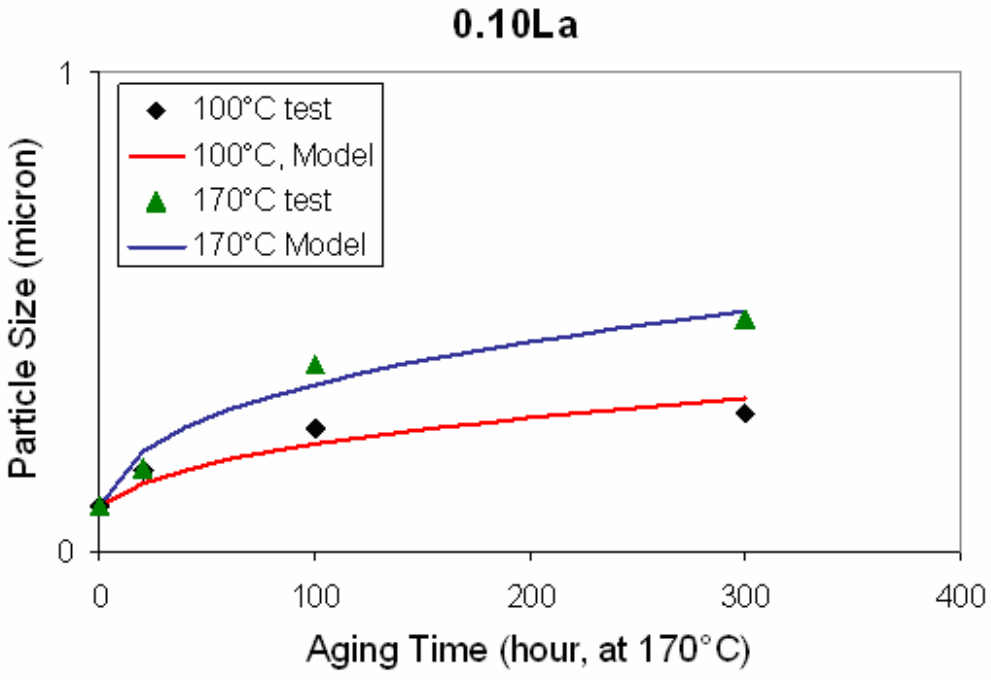

(c)

Figure 23: Comparison of particle coarsening model with test data (continue)

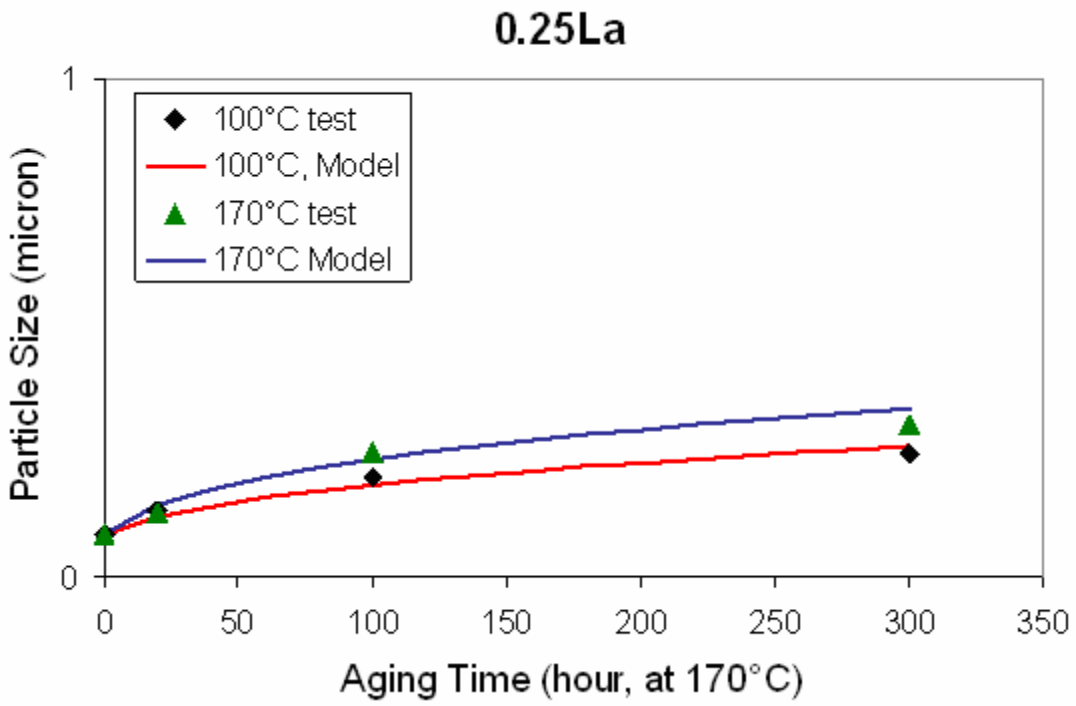

(d)

Figure 23: Comparison of particle coarsening model with test data (continue)

To account for the La doping effect, the coarsening model given by (10) can be modified to:

$$< d >^3 - < d_0^{RE} >^3 = \frac{K_0^{RE}}{T} t \exp\left(\frac{-Q^{RE}}{RT}\right) \quad \textbf{(11)}$$

where

$$< d_0^{RE} >= d_0 (1 + 28.5RE)^{-0.2}$$

$$K_0^{RE} = K_0 (1 + 11.4RE)^{-7.0} \quad \textbf{(12)}$$

$$Q^{RE} = Q(1 + 0.71RE)^{-5.5}$$

In which RE is the La doping in percentage, and d_0, K_0 and Q are the values of un-doped solder alloy, as shown in Table 5. Predictions from (11) are shown in Figure 24 and Figure 25 as a function of aging time and La doping respectively.

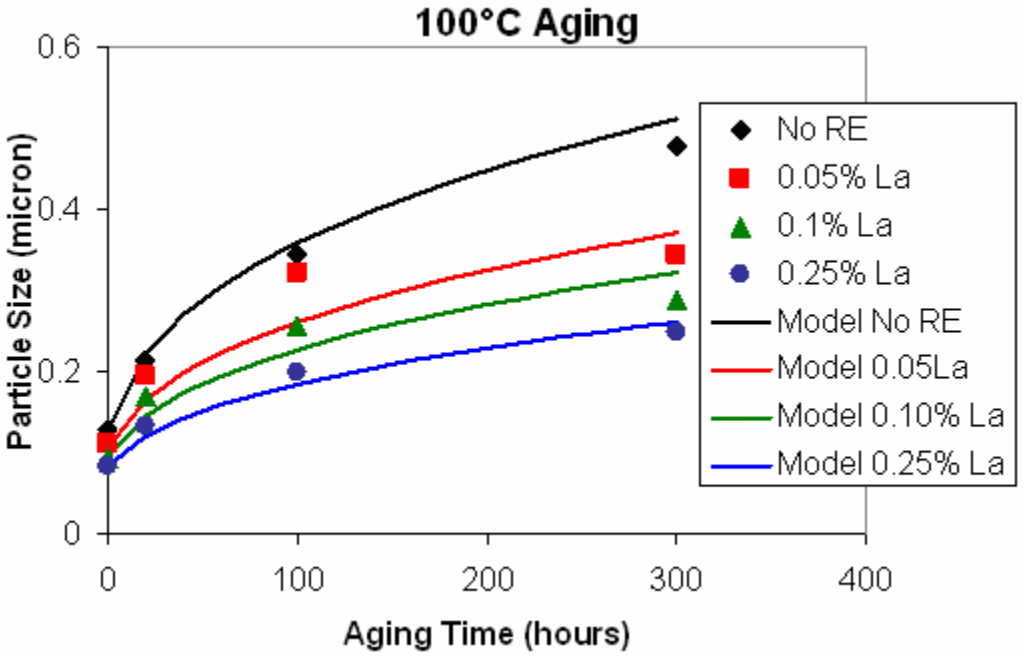

(a) 100°C aging

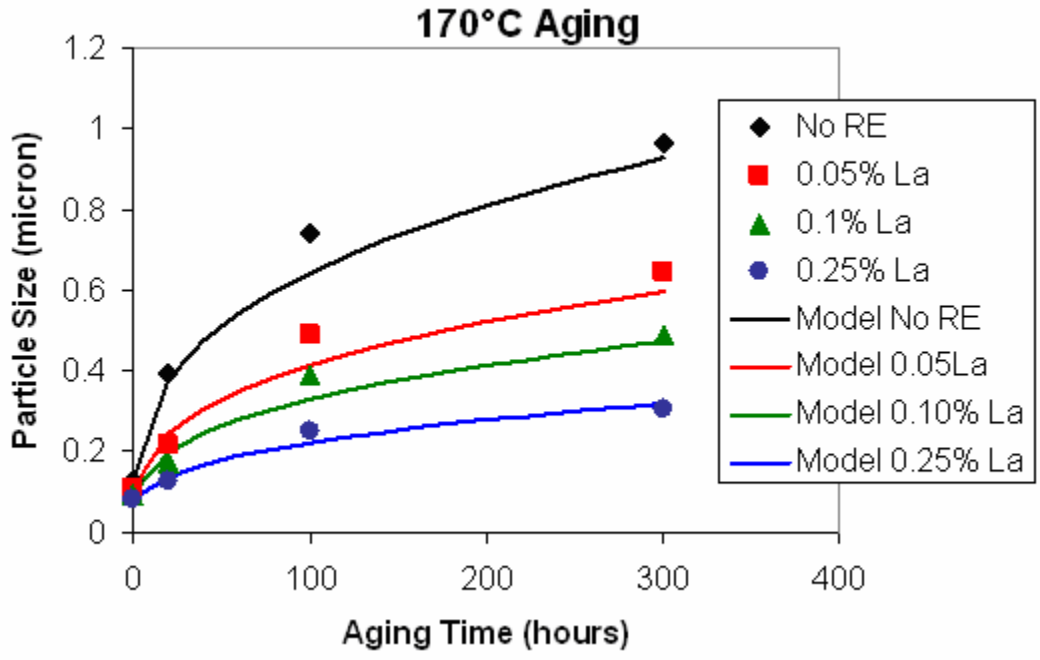

(b) 170°C aging

Figure 24: Particle coarsening modeling with La dependence, as a function of aging time

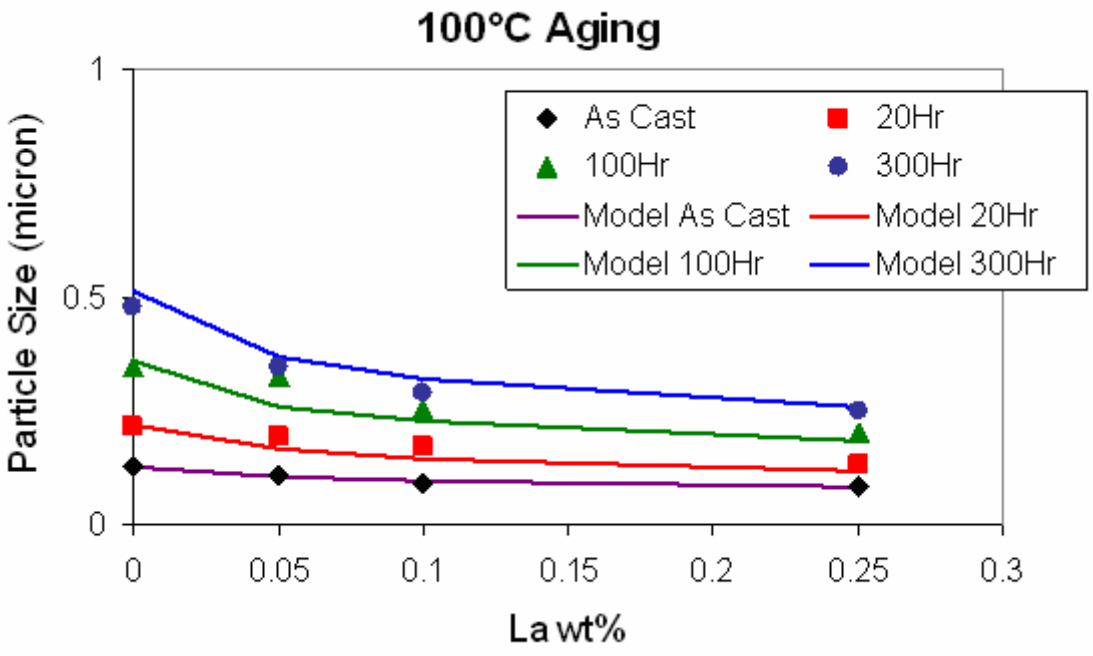

(a) 100°C

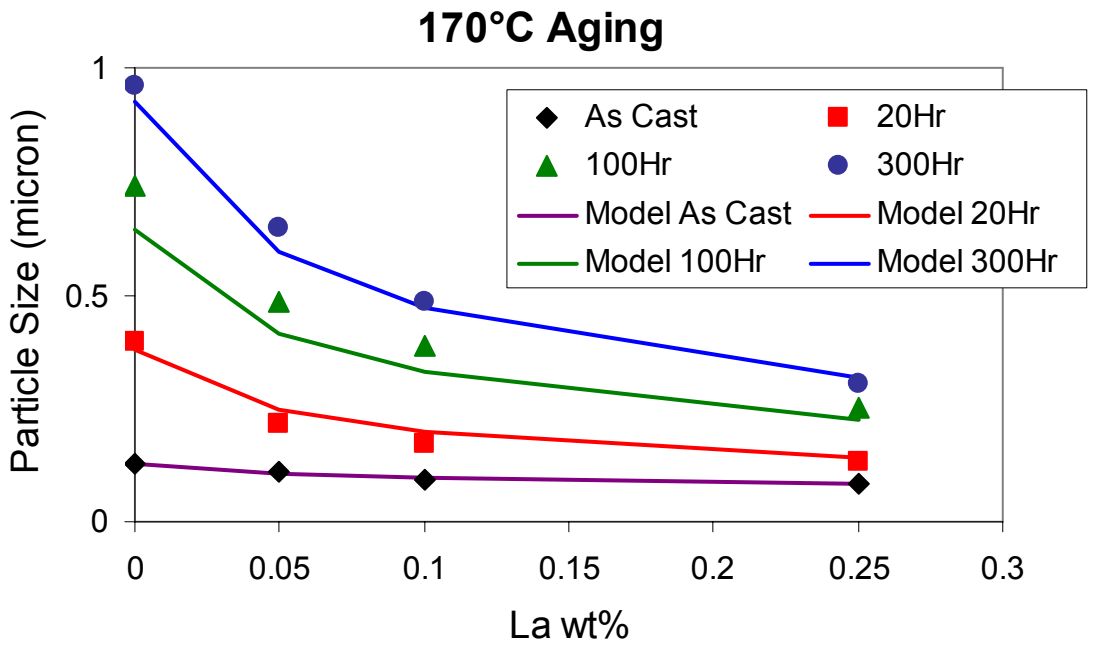

(b) 170°C aging

Figure 25: Particle coarsening modeling with La dependence, as a function as function La doping

Discussion

To close this chapter, we note that when the specimens aged at 100°C, thin lines were found along the grain/sub-grain boundary. One example of this kind of thin line is shown in Figure 17. EDX study found the lines have high concentration of Ag element. Element maps were also captured as shown in Figure 26. Vacancies are accumulated along these lines and voids can be seen after etching. It is also interesting to note that these lines were only found on 100°C aged samples, and more of them were observed in samples with higher La doping.

Although it is not clear what causes these Ag lines, it is plausible that the higher Ag concentration along the grain boundaries would effectively reduce the Ag content within the eutectic region, thus reduce the Ag_3Sn particle coarsening rate. This hypothesis is consistent with the experimental data shown in Figure 24 and Figure 25 where higher La doping tends to reduce the coarsening rate.

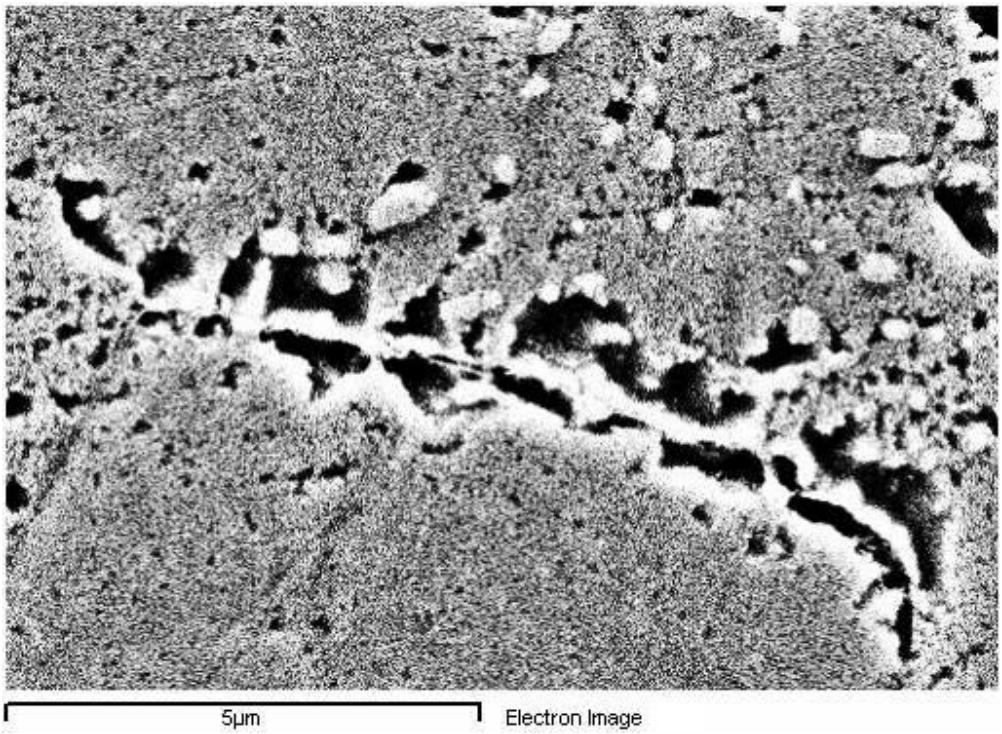

(a) Original SEM image

Figure 26: Element maps of grain boundary, SnAg0.25La, 100°C aged for 100 hours

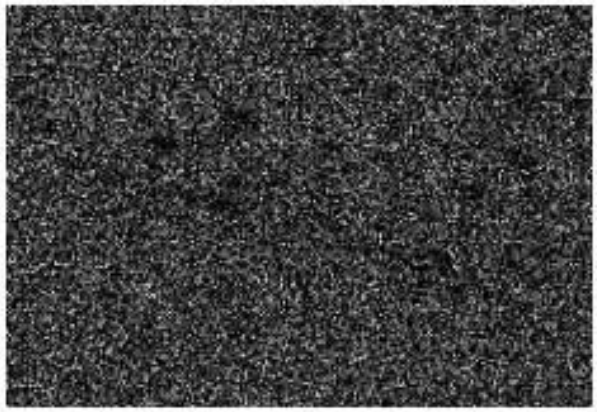

Tin

(b)

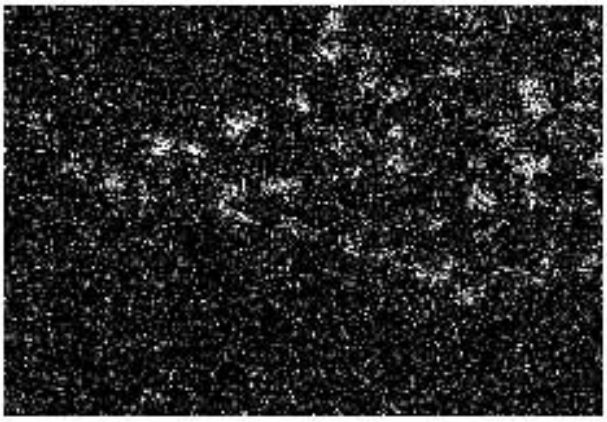

Silver

(c)

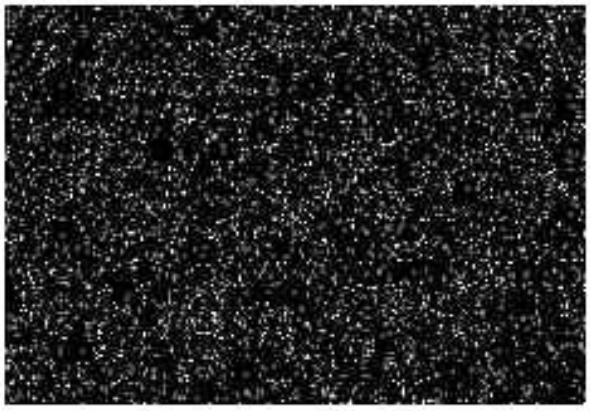

Lanthanum

(d)

Figure 26: Element maps of grain boundary, SnAg0.25La, 100°C aged for 100 hours (continue)

Summary

In this chapter, available particle coarsening models are briefly introduced and then the Ag_3Sn particle coarsening data were fitted into the power law coarsening model for each La doping level. A new coarsening model with power law La dependence was introduced and fitted. All the models obtained acceptable accuracy.

CHAPTER 5

TENSILE CREEP TEST

Tensile Test System

A tensile test was performed on an EnduraTech® ScopeTester. This tester is mechanical-shaft driven and the load cell capacity is 50lbf. An environmental chamber has been constructed to provide both high and low temperature environments and a non-contact strain measurement method was used for the tests. The detail about this strain measurement system will be discussed in Appendix D. A custom fixture has been made to apply tensile load to the dog bone shaped specimen. All the specimens used in this study are in the bulk form. The overview of the test system can be seen in Figure 27.

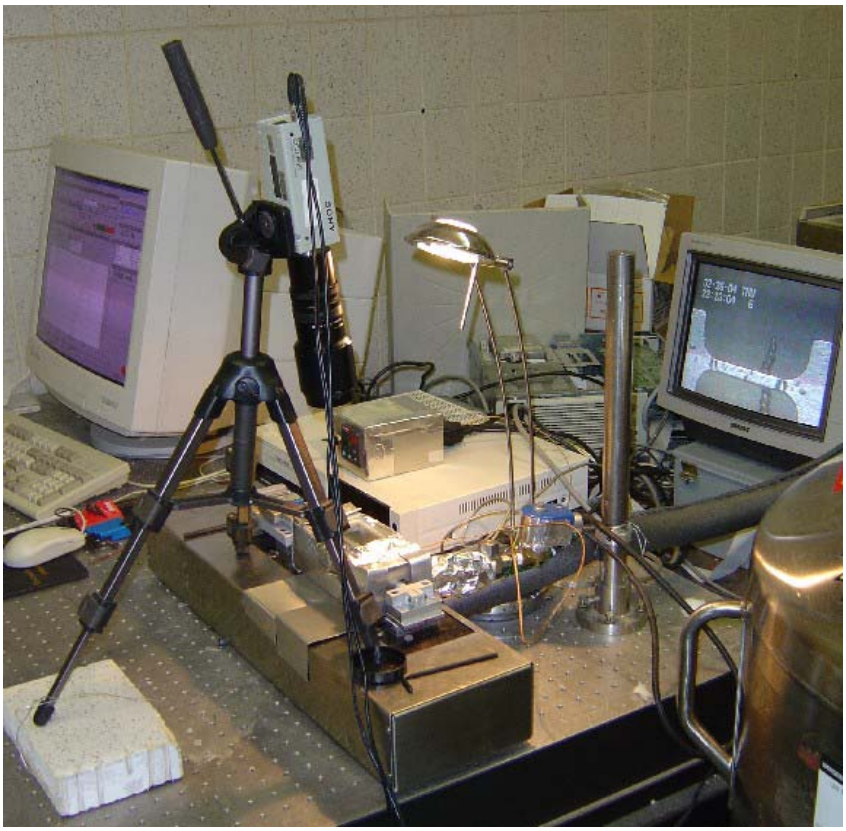

Figure 27: Tensile test system

Tensile test specimens were cast in metal mold and fast cooled to obtain refined microstructure similar to the solder joint. The casting procedure is elaborated below. Some of the specimens were aged at high temperature. The aging procedure was performed in air atmosphere.

Sample Casting

The design chart of the dog bone shaped specimen is shown in Figure 5. A three piece metal mold was made for the sample casting based on the design, as shown in Figure 28. The middle piece was machined with electrical discharge machining (EDM) from 0.036in (~0.9mm) thick stainless steel board. The thickness of the board became the thickness of the samples after casting. The two outer pieces were made by aluminum and polished with grit 2400 sand paper. The mold was designed to have thinner structure around the specimen area to reduce the thermal capacity around this area, which will enable fast cooling of the specimen during quenching. The three pieces were bolted together during the casting. The mold for the tensile test specimen is shown in Figure 28.

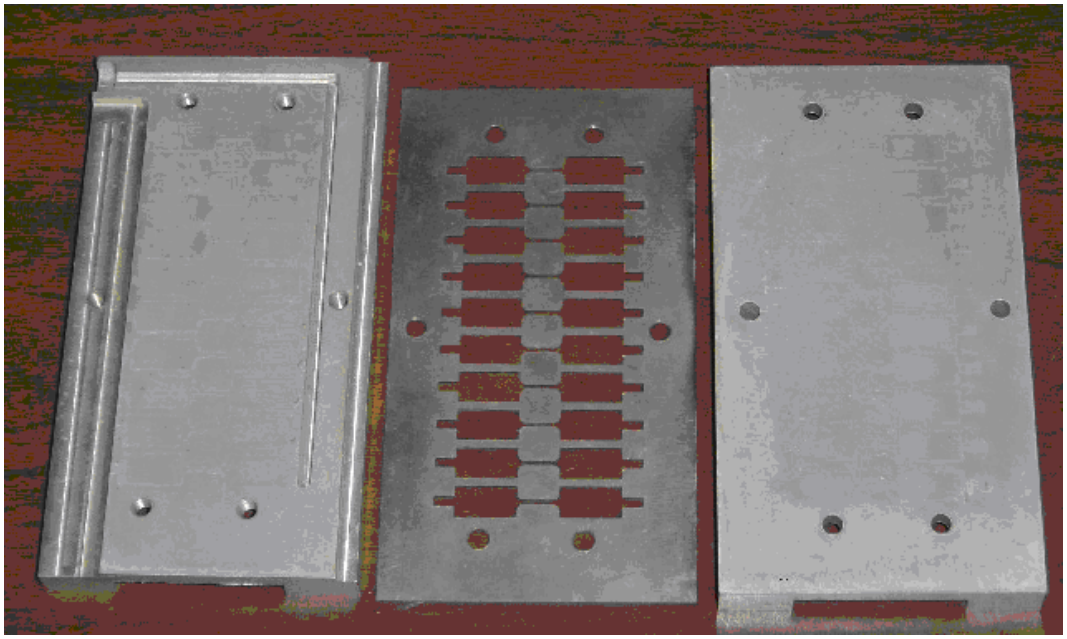

Figure 28: Metal mold for tensile test samples

The whole mold was heated in an oven to 260°C, together with a crucible, as seen in Figure 29. After pouring liquid material into the mold, the whole mold was put in 15°C water. After cooling completely, the samples were taken out from mold. The whole cast piece contained ten samples, as shown in Figure 30. After removing the extra materials, one specimen for the tensile test can be seen in Figure 31. The dog bone sample was left at room temperature (about 25°C) for one whole day to release some of the residual stress due to quenching then stored in a freezer thereafter.

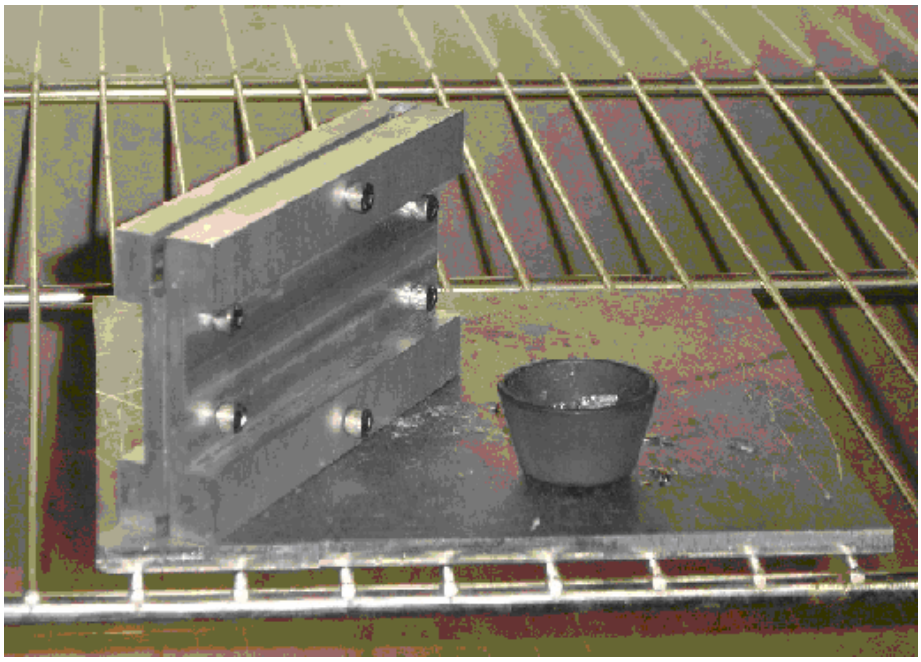

Figure 29: Casting procedure of tensile samples

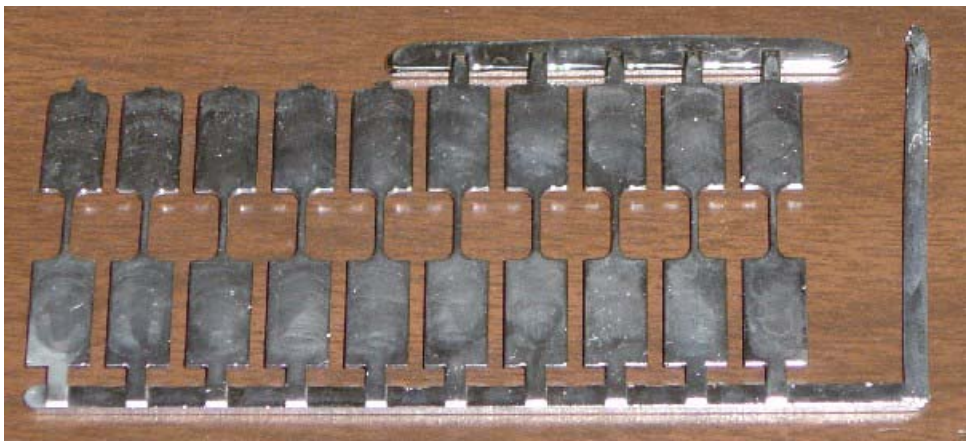

Figure 30: One batch of tensile samples

Figure 31: One tensile test specimen

The cooling rate was measured with a thermal couple attached on the mold near the specimen location during the water quenching. The temperature was measured with a Keithley® 2001Digital Multi Meter (DMM), which was connected to a computer via IEEE488 (GPIB) interface. The computer recorded the temperature reading starting from when the mold was removed from the hotplate and its history curve is shown in Figure 32.

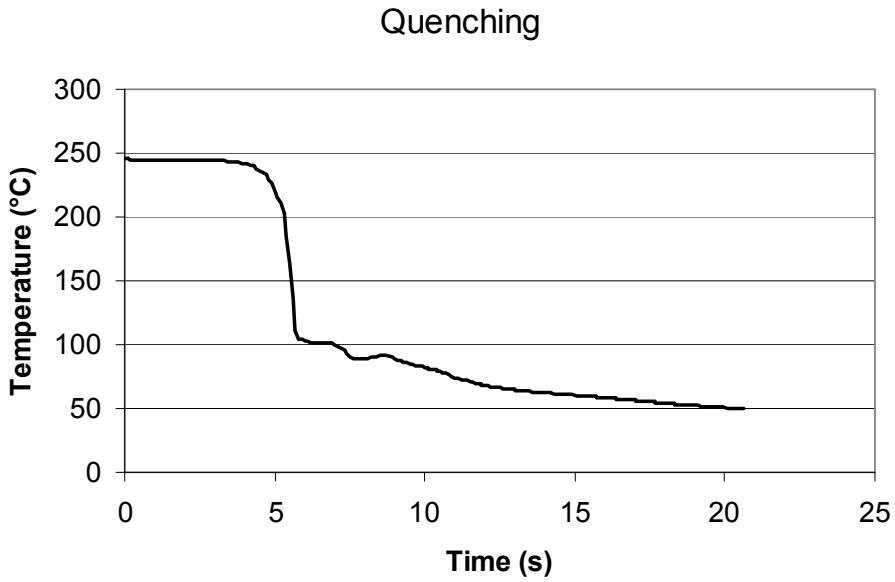

Figure 32: Temperature history of quenching procedure of sample casting

The cooling curve shows a fast cool at above 100°C and much slower cooling rate below 100°C. The fast cooling rate comes from the water vaporizing around the mold. A portion of the curve around 200°C was taken out for a linear fitting and the cooling rate was estimated to be about 100°C/sec.

To further estimate the cooling rate of the sample, a simple FEM model was established. Due to the small sample size, this model only considered part of the aluminum mold, as shown in Figure 33. The material constants of aluminum were obtained from [49]. As can be seen in Figure 33, with 100°C/s of cooling rate at both side of the mold, the middle part of the model has a cooling rate about 85°C/s. This will be the estimation of the cooling rate of the samples.

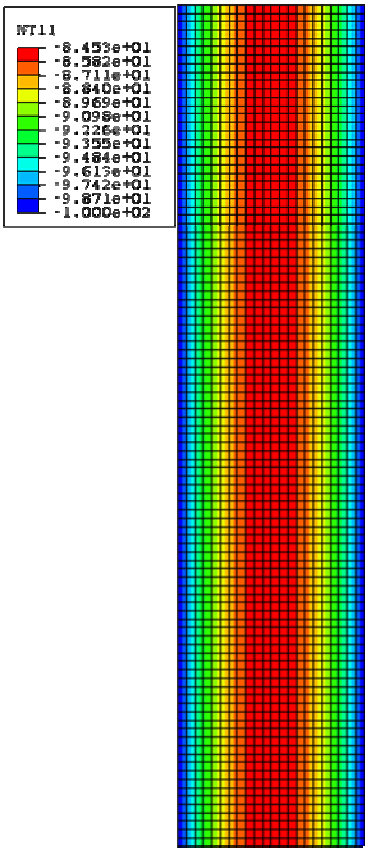

Figure 33: FEM model temperature field for sample cooling rate estimation

Environmental Control System

To facilitate the test at different temperature, an environmental control chamber was constructed. This chamber was controlled by a thermal controller and has the ability of both heating and cooling. The heating was provided by electronic heating unit and cooling was provided by spray of liquid nitrogen. The temperature feedback was

provided by K type thermal couple. The thermal couple will be in contact with the specimen during test. The opened chamber is shown in Figure 34.

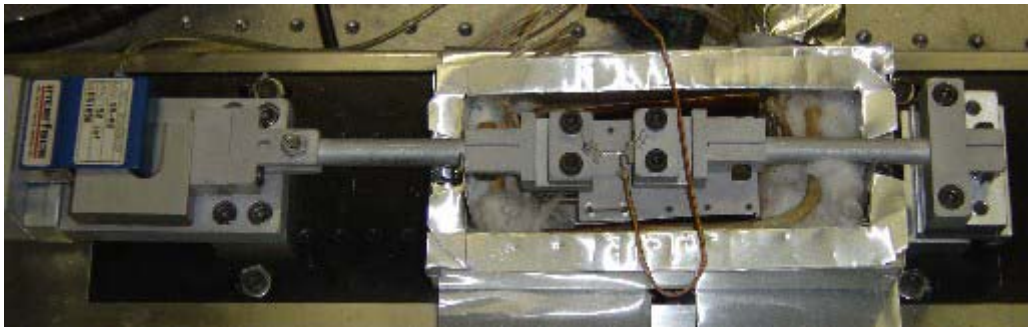

Figure 34: Custom fixture and thermal chamber for tensile test

Benchmark Test

A series of constant loading rate monotonic tensile tests have been conducted as bench mark of this test method. The materials tested were 97Pb3Sn, 96.5Sn3.5Ag and Sn3.8Ag0.7Cu solders. The maximum stress result can be seen in Figure 35. The max stress is the steady state stress at high temperature and low strain rate or is the ultimate stress if the sample break before saturation stress is reached. The results were compared with the corresponding data available in the commercial material database CINDAS [51]. Good agreement was observed.

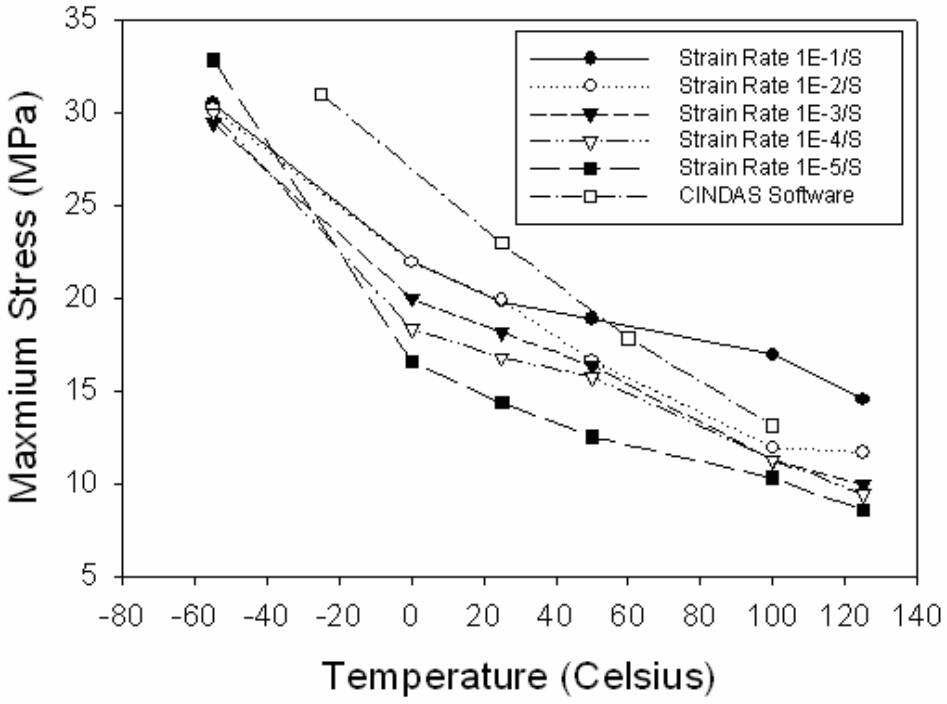

(a) 97Pb3Sn solder

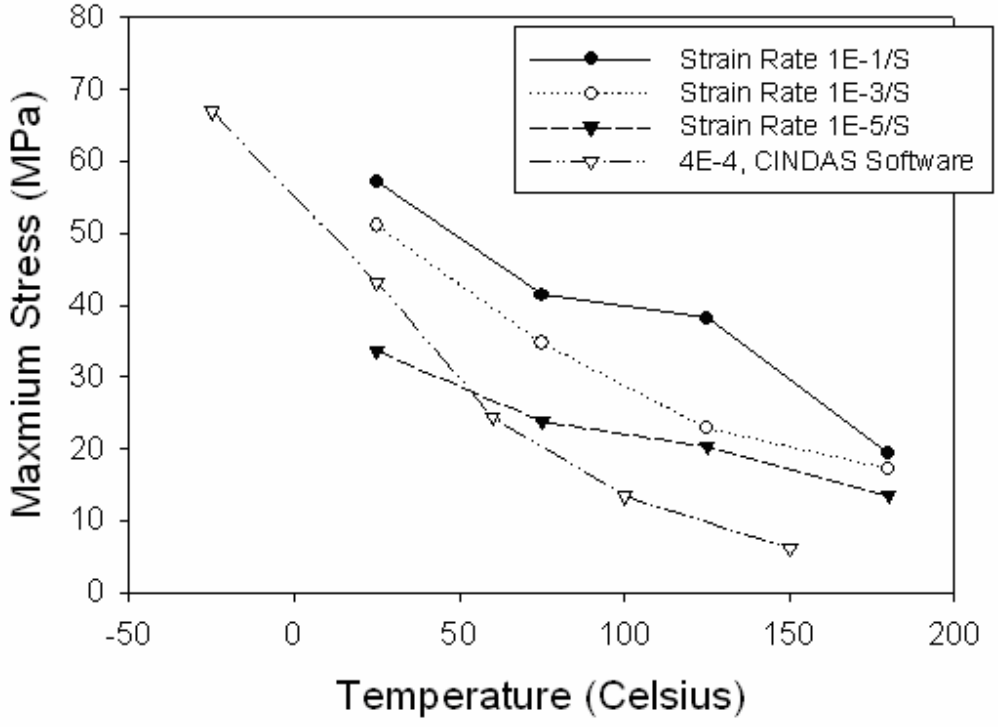

(b) 96.5Sn3.5Ag solder

Figure 35: Maximum stress vs. temperature chart of benchmark tensile tests

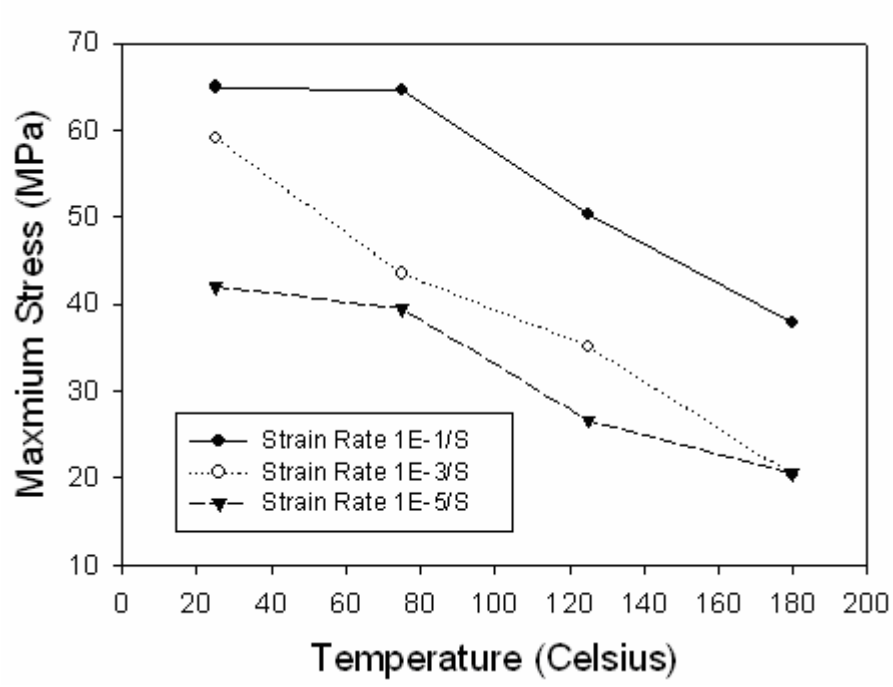

(c) Sn3.8Ag0.7Cu solder

Figure 35: Maximum stress vs. temperature chart of benchmark tensile tests (continue)

Multiple Strain Rate Loading

To investigate the effect of strain rate and temperature, monotonic tension tests were conducted at 4 different temperature of -55°C, 0°C, 50°C ,125°C. Strain rate jump test was performed as follows. The specimen was elongated to 0.9% strain at a strain rate of 2×10^{-6}/s. At this point, the strain rate was increased by factor of 10 to 2×10^{-5}/s and the specimen was elongated to 1.8%. This procedure was repeated up to a strain rate of 2×10^{-2}/s. A typical strain-stress relation curve is shown in Figure 36.

This strain rate jump test can drastically reduce the number of specimen required but the strain-stress behavior may be distorted by the loading history at a low strain rate [63]. The loading history effect on SnAg solder material was studied by comparing constant-strain-rate test results with strain-rate-jump test results, as shown in Figure 37. The close result shows that SnAg solder has little dependence on loading history dependent.

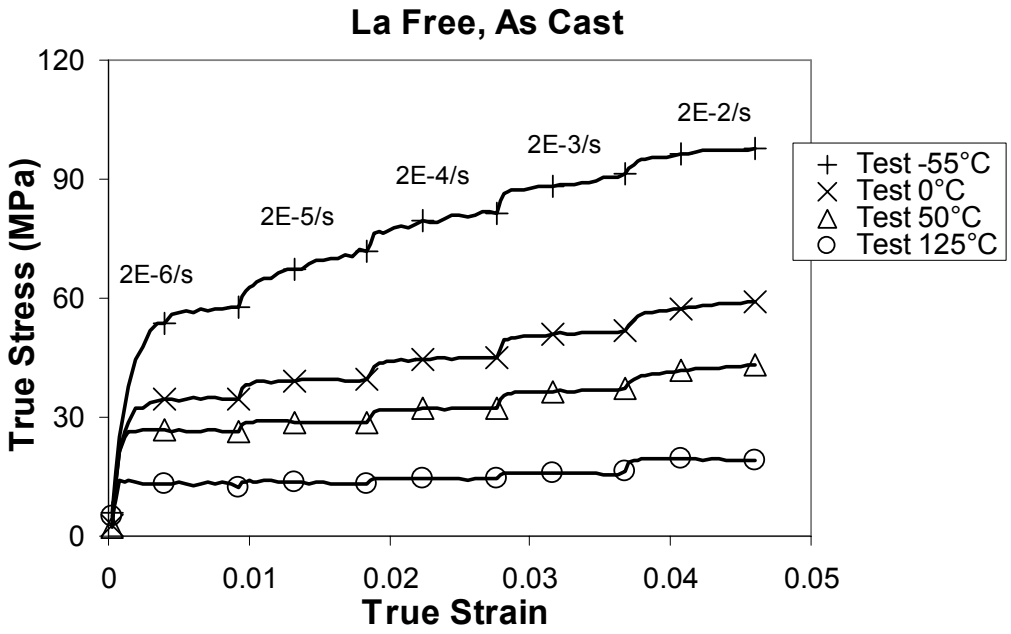

Figure 36: Typical loading curve of strain rate jump test. Different strain sections have different strain rates.

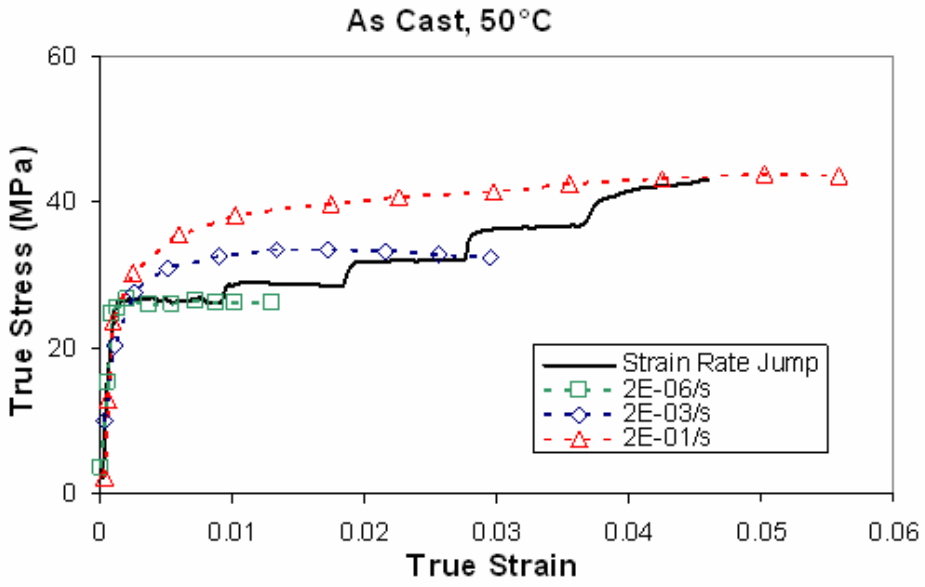

Figure 37: Comparison of constant strain rate test result with strain rate jump test result. The solid line represents the strain rate jump test result and the symbles are the result of constant strain rate test result as indicated in the lable.

Creep Test Result

Effect of La Doping

Effects of La doping on the as-cast samples and for samples subjected to 170°C for 300 hours are shown in Figure 38 and in Figure 39, respectively. From these experimental data it can be seen that La doping generally increases the stress under a given strain and strain rate, and the increase is much more pronounced at high temperature, reaching as high as 15%. This observation is consistent with existing results in several other solder alloys [14][21][52]. The steady-state creep behavior is shown in Figure 40 as a function of strain rate and in Figure 41 as a function of temperature for the as-cast samples.

One of the important characteristics of creep deformation is the steady-state (saturation) stress as a function of strain rate. To obtain this steady-state stress vs. strain rate curve from the stain rate jump test data, it is assumed that the stress at the end of each strain rate has reached its saturation, e.g., toward the end of each strain rate, the creep is becoming steady-state. The measured stress-strain curves Figure 38 and Figure 39 show that this assumption is very good at higher temperature and lower strain rate, which are the conditions most relevant to solder joints in electronic packaging. Therefore, by taking the stress at the end of each strain rate, the steady-state stress versus strain rate curves can be obtained for samples with various doping levels and aging condition at different temperature. The steady-state stresses of as-cast samples are shown in Figure 40 as the function of RE doping, and the same information is plotted in Figure 41 as a function of temperature.

From Figure 38 and Figure 40, it can be seen that at the same strain rate loading, the steady-state stress in the doped samples is about 5~10 MPa higher than that in the un-doped samples. Considering the soft nature of the solder materials, especially at high temperature, this is a significant enhancement. The improvement in creep resistance can

also be illustrated in a different way. From Figure 40 it can be seen that to reach the same steady-state stress (dead load), the corresponding strain rate of La doped samples can be an order of magnitude less than that of the un-doped samples.

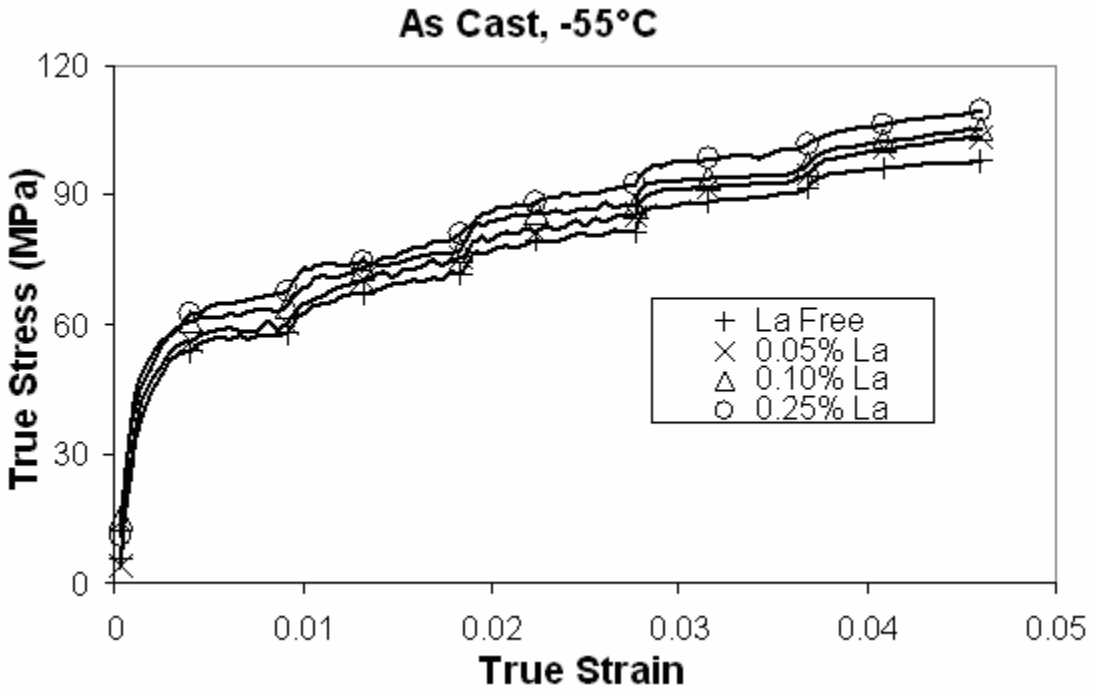

Figure 38: Strain rate jump test result of as-cast alloys, comparing La doping effect

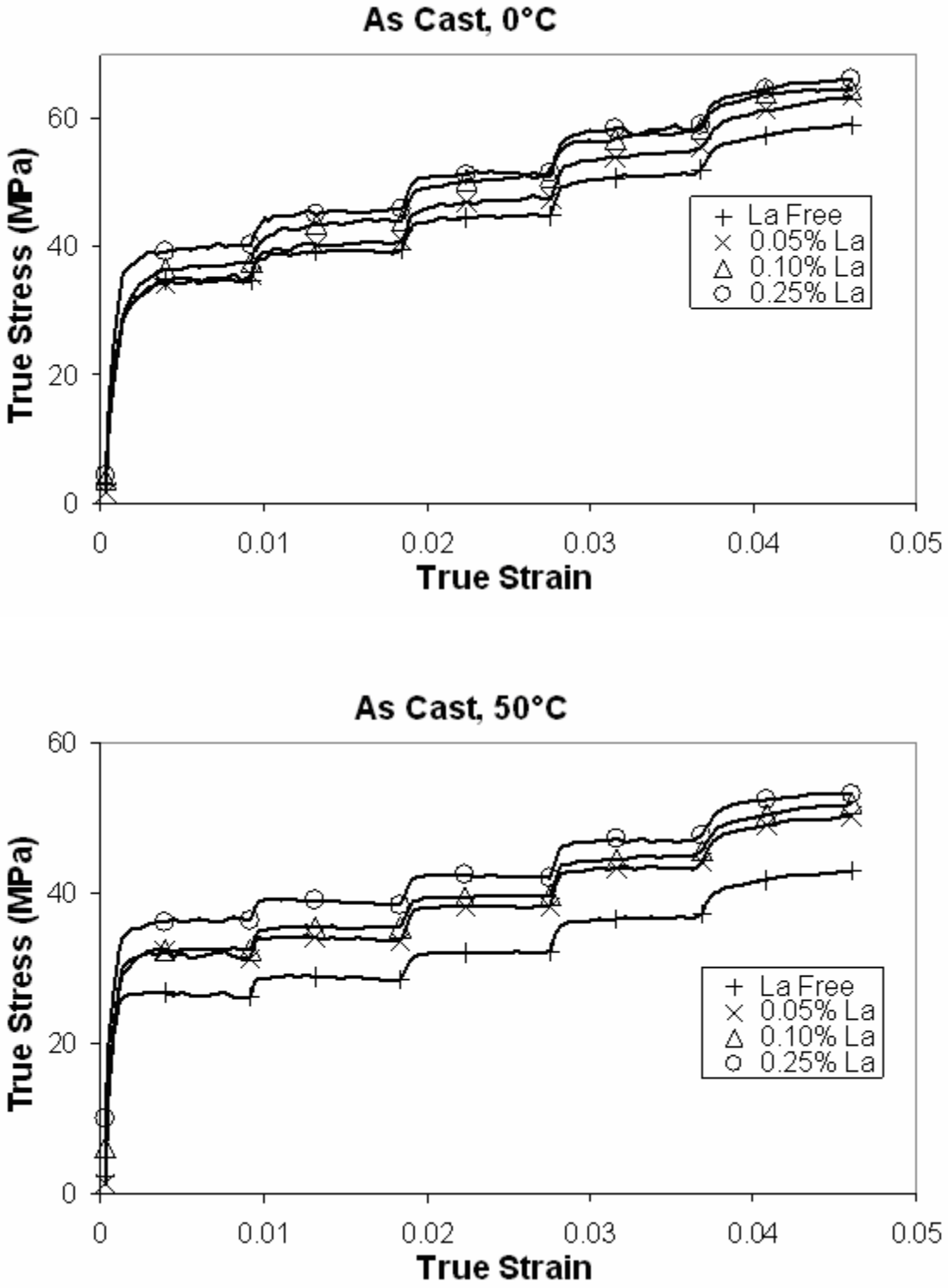

Figure 38: Strain rate jump test result of as-cast alloys, comparing La doping effect (continue)

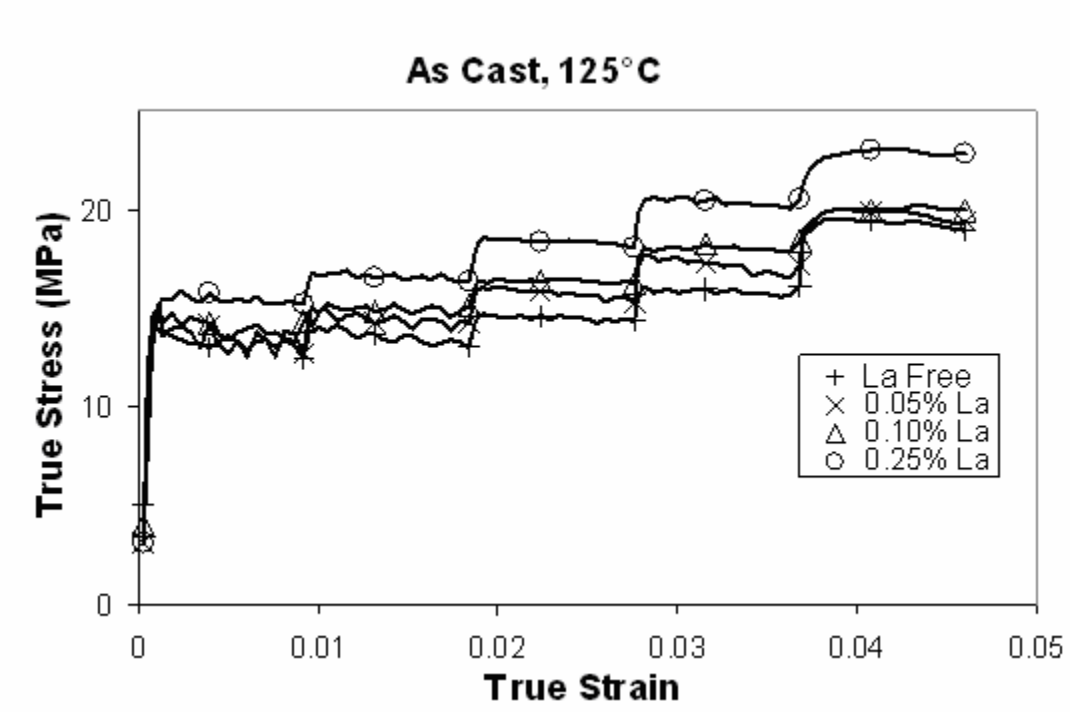

Figure 38: Strain rate jump test result of as-cast alloys, comparing La doping effect (continue)

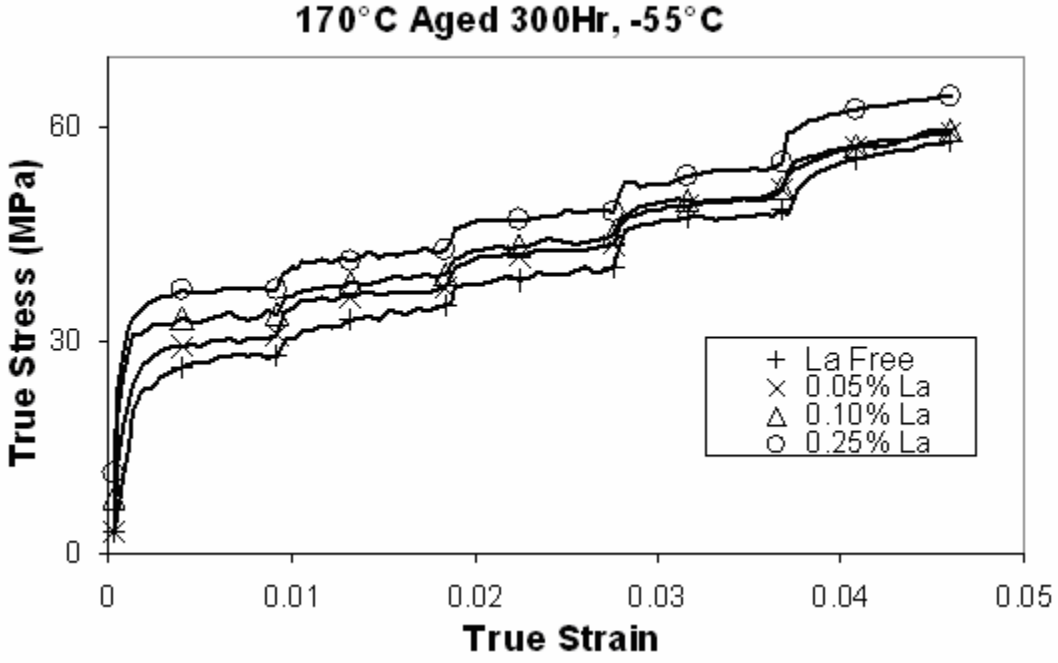

Figure 39: Strain rate tensile test result of solders aged at 170°C for 300 hours, comparing La doping effect

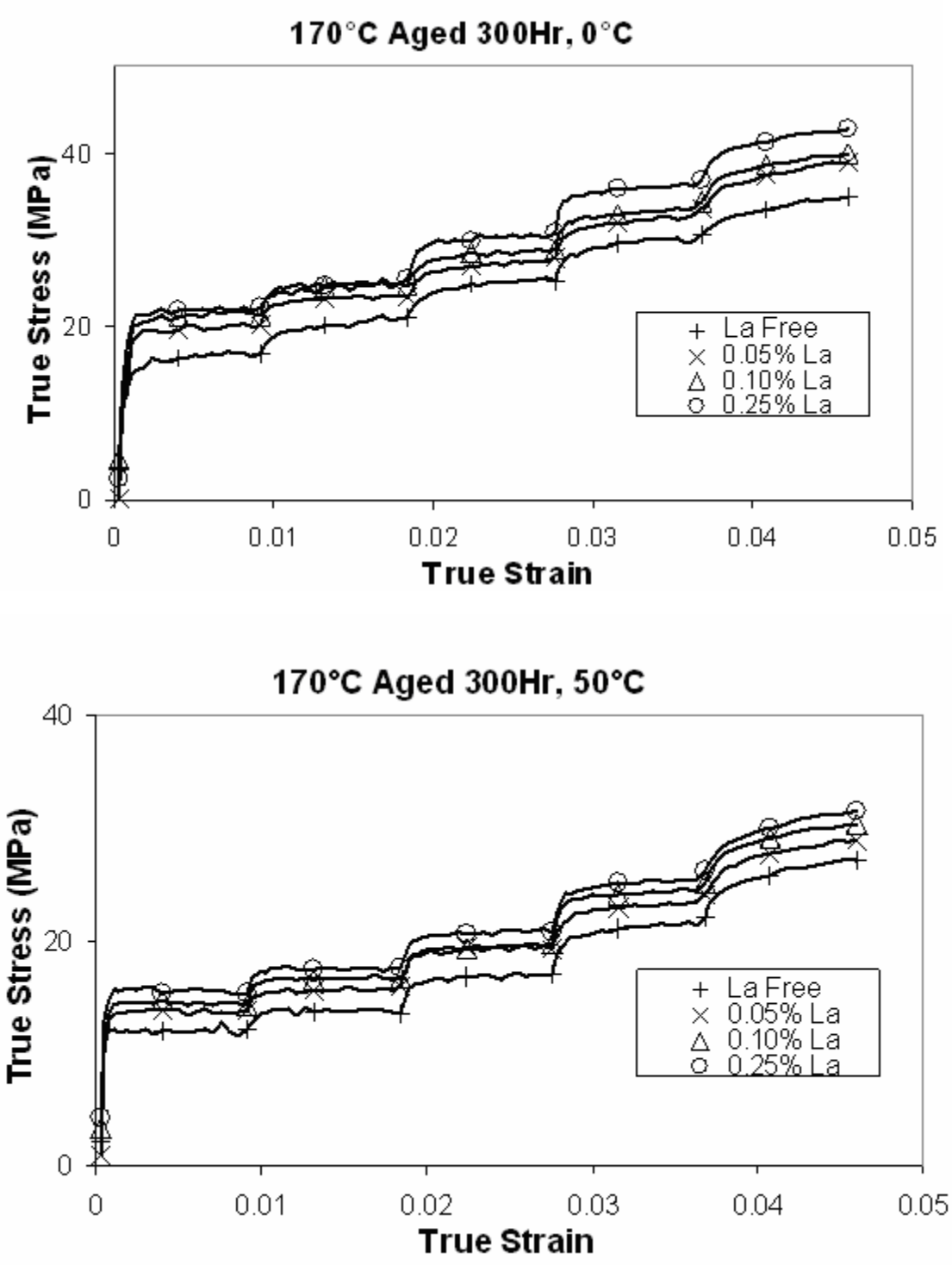

Figure 39: Strain rate tensile test result of solders aged at 170°C for 300 hours, comparing La doping effect (continue)

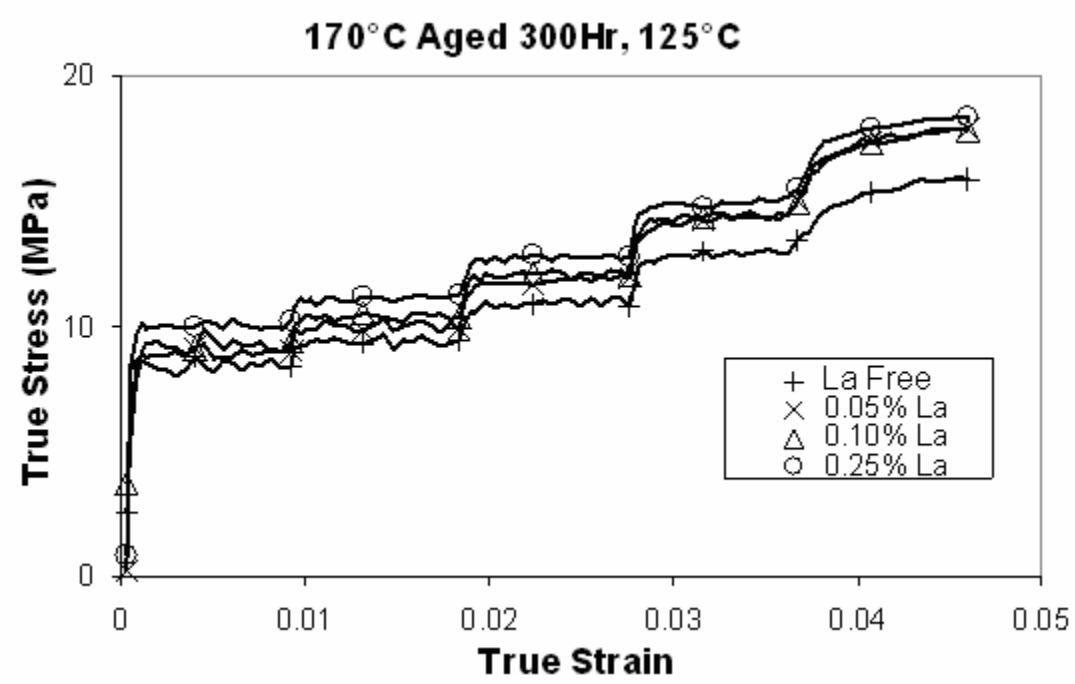

Figure 39: Strain rate tensile test result of solders aged at 170°C for 300 hours, comparing La doping effect (continue)

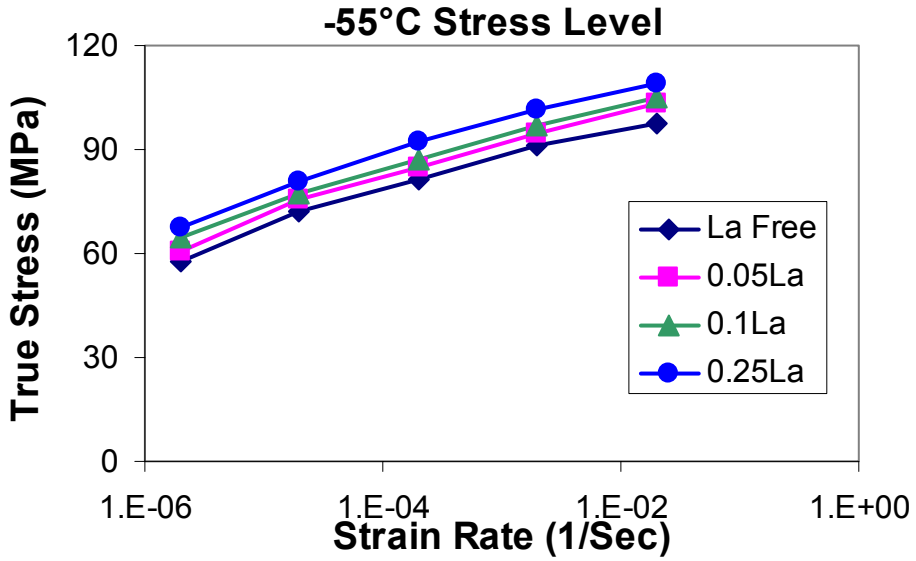

Figure 40: The steady state stress levels of as-cast condition, listed by different temperatures

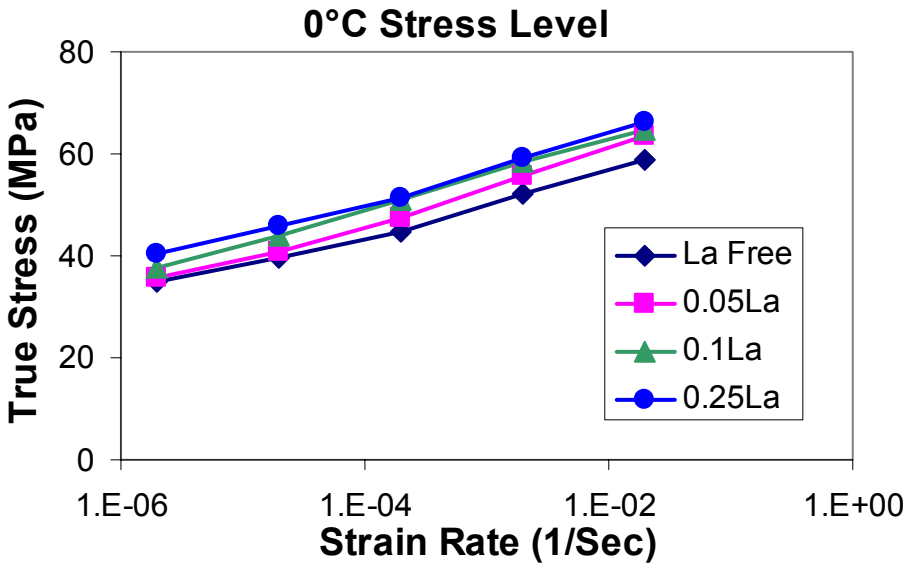

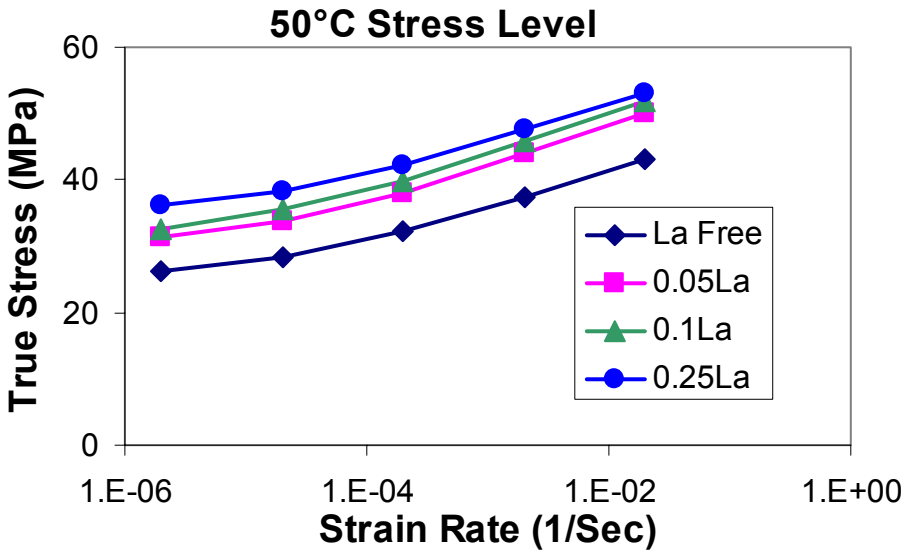

Figure 40: The steady state stress levels of as-cast condition, listed by different temperature (continue)

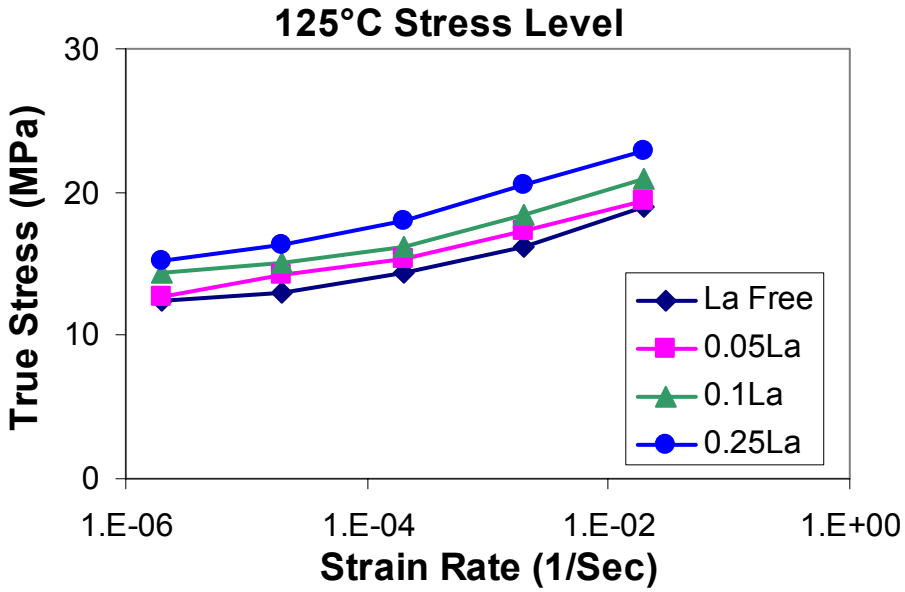

Figure 40: The steady state stress levels of as-cast condition, listed by different temperature (continue)

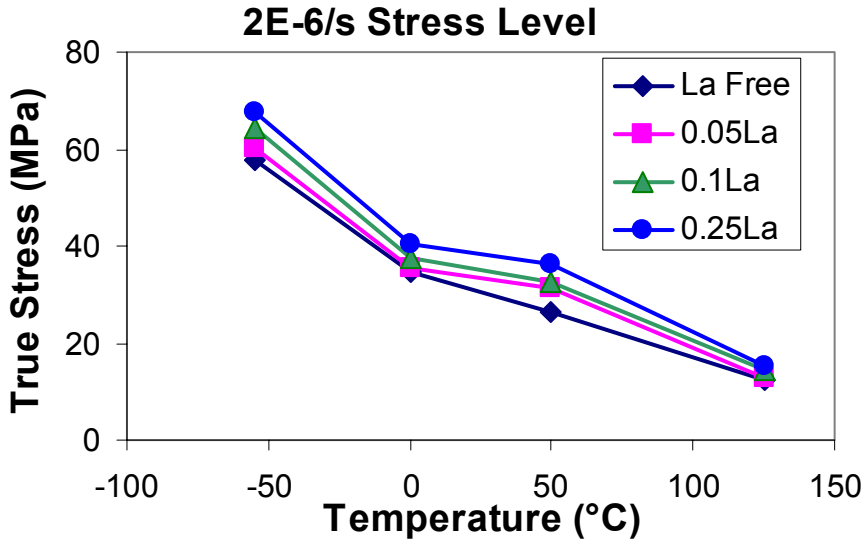

Figure 41: The steady state stress levels of as-cast condition, listed by different strain rates

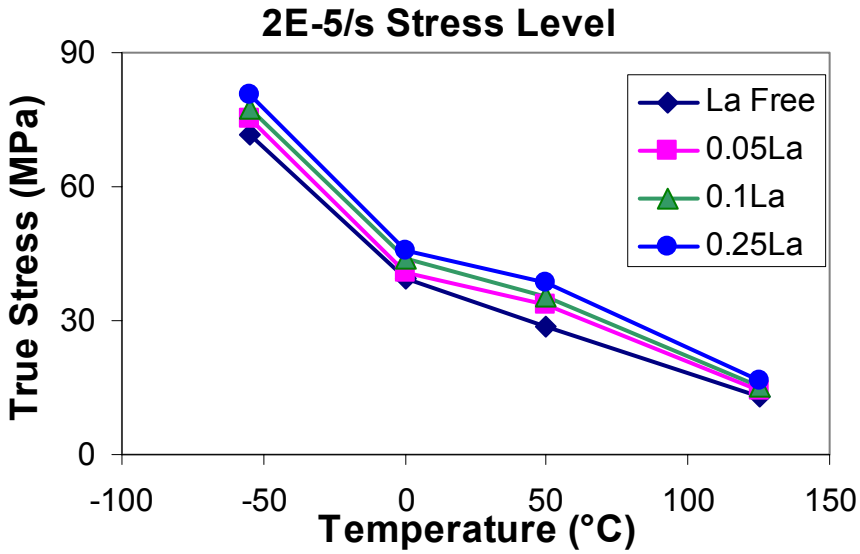

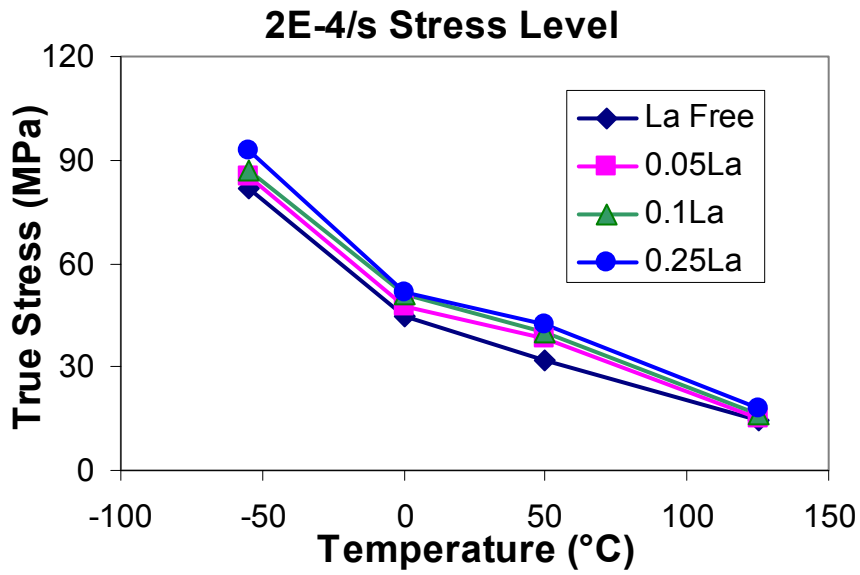

Figure 41: The steady state stress levels of as-cast condition, listed by different strain rate (continue)

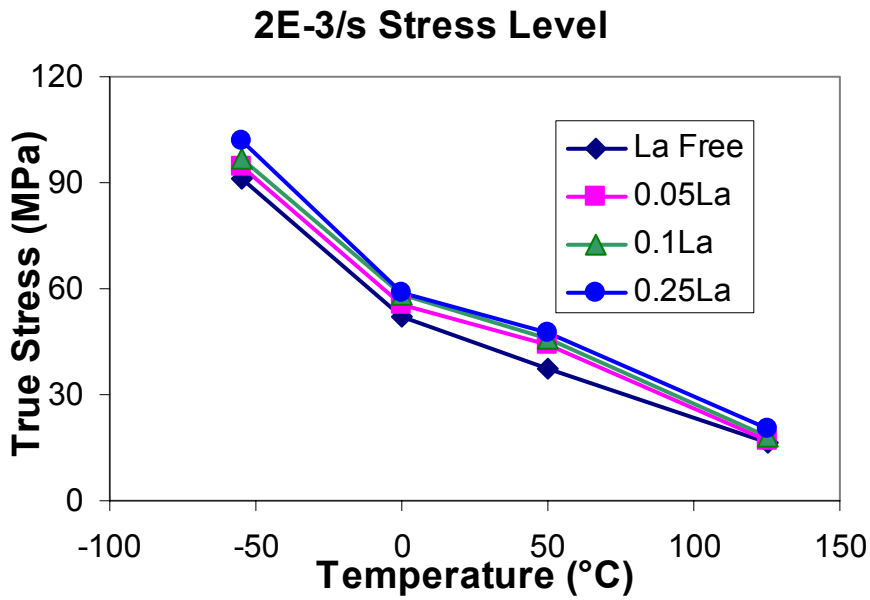

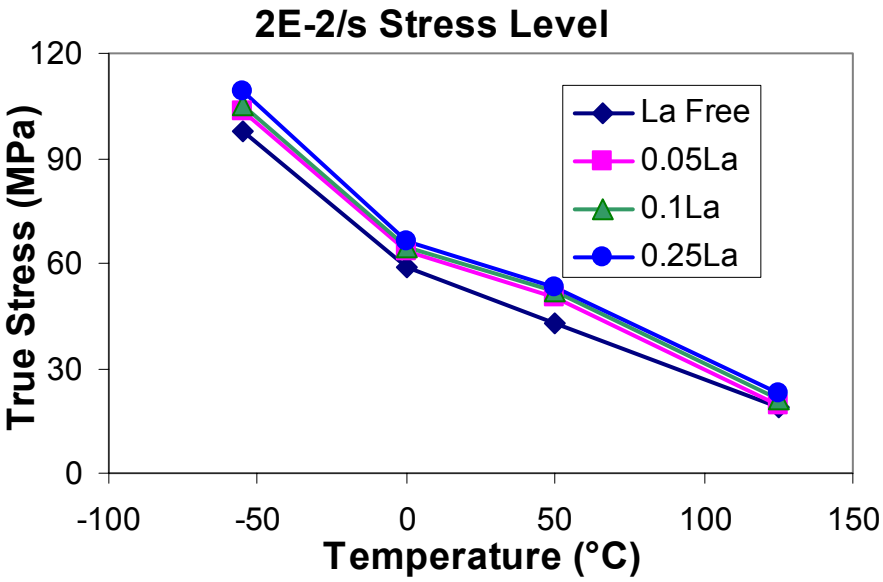

Figure 41: The steady state stress levels of as-cast condition, listed by different strain rate (continue)

Effect of Aging

After casting, samples were aged at either 100°C or 170°C for 20, 100 and 300 hours, respectively. The strain rate jump tests were then performed on these samples at

various temperatures. The steady-state stress vs. strain-rate curves were obtained using the same approach discussed in the preceding section. Results obtained at -55°C are shown in Figure 42 (a)–(b) for the un-doped and doped samples, respectively. Similarly, results obtained at 125°C are shown in Figure 42 (c) – (d). It is seen from these data that thermal aging leads to similar effect in both doped and un-doped samples indicating that La doping does not affect the aging behavior of SnAg alloy.

Showing in Figure 43 are the steady-state stress vs. temperature curves for a given strain rate. It is seen that both the doped and un-doped samples behave similarly, confirming again that La doping does not affect the aging behavior of the SnAg alloy.

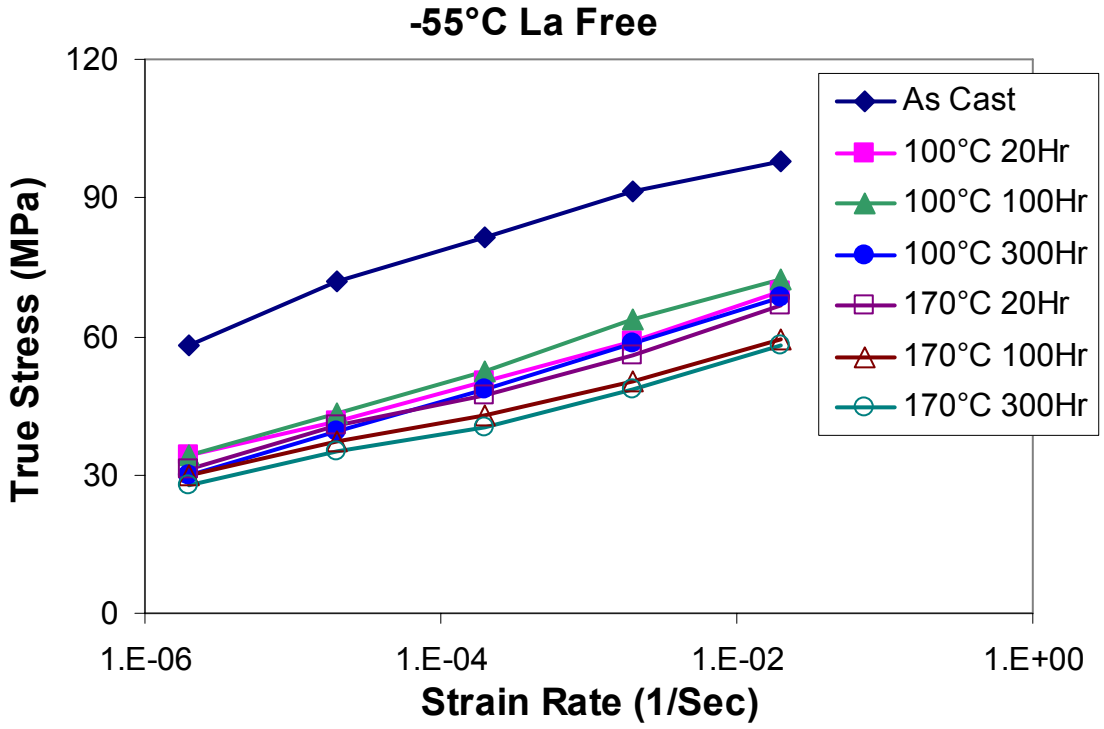

(a) SnAg solder at -55°C

Figure 42: The steady state stress levels, listed by different temperatures and materials

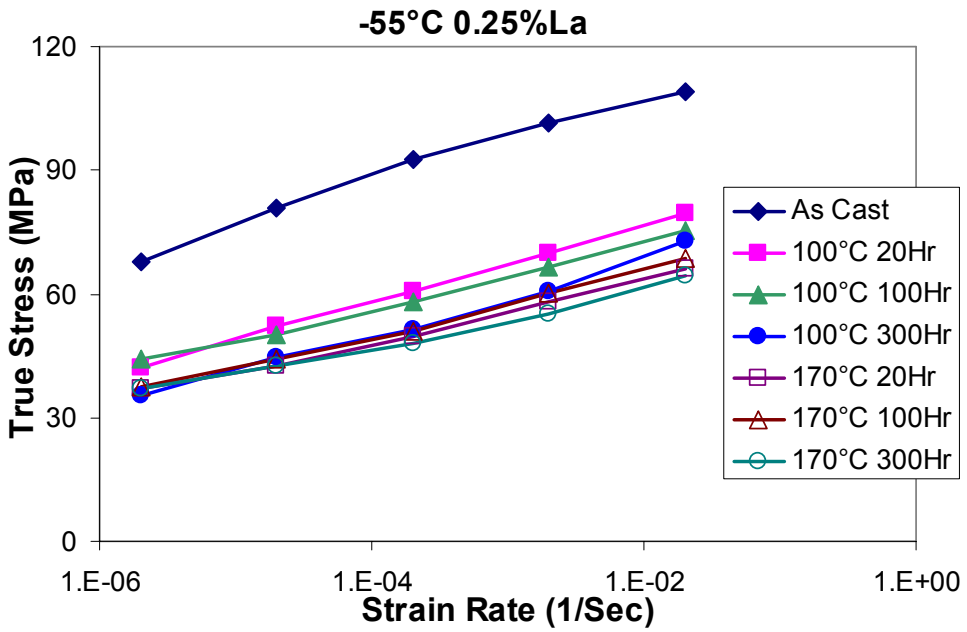

(b) SnAg0.25La solder at -55°C

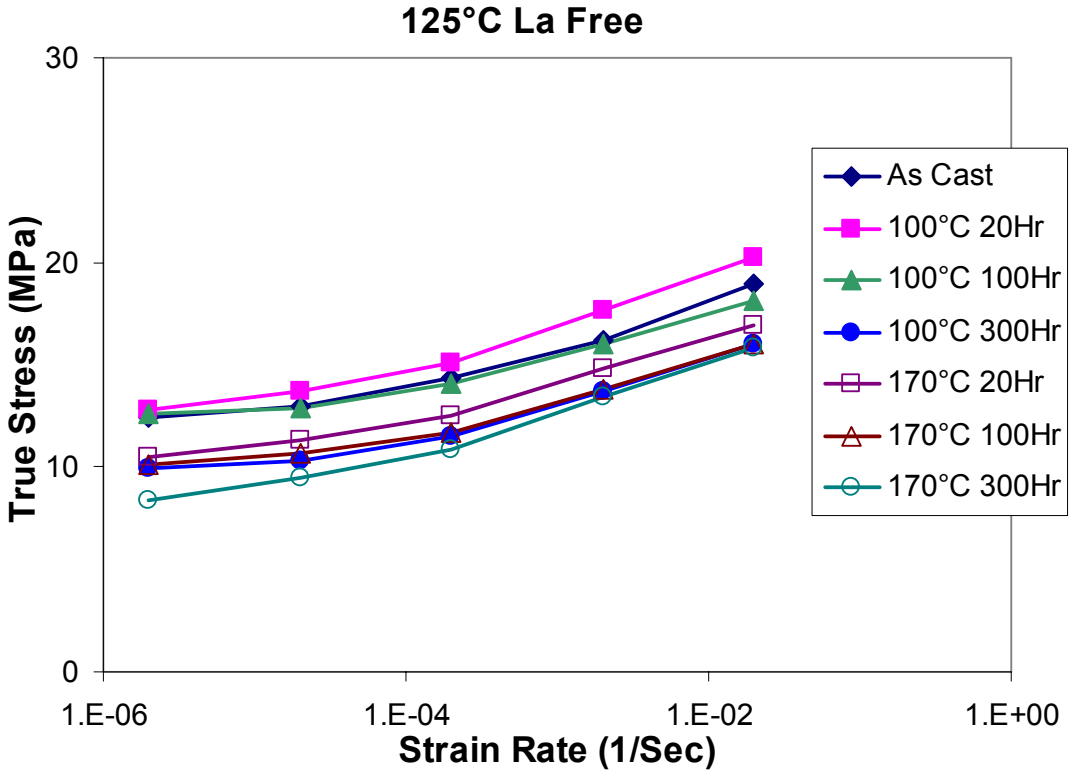

(c) SnAg solder 125°C

Figure 42: The steady state stress levels, listed by different temperature (continue)

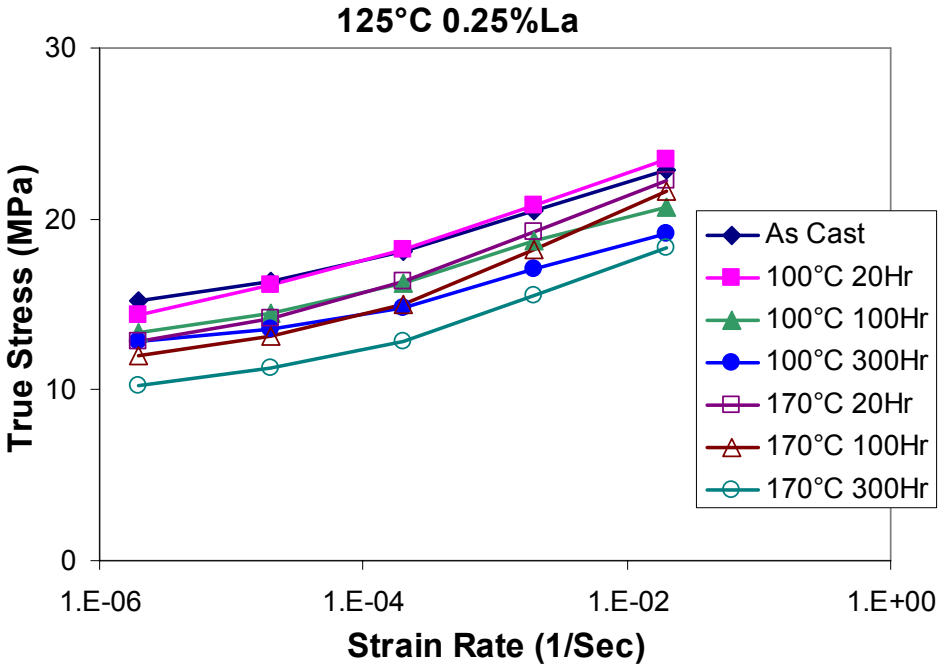

(d) SnAg0.25% 125°C

Figure 42: The steady state stress levels, listed by different temperature (continue)

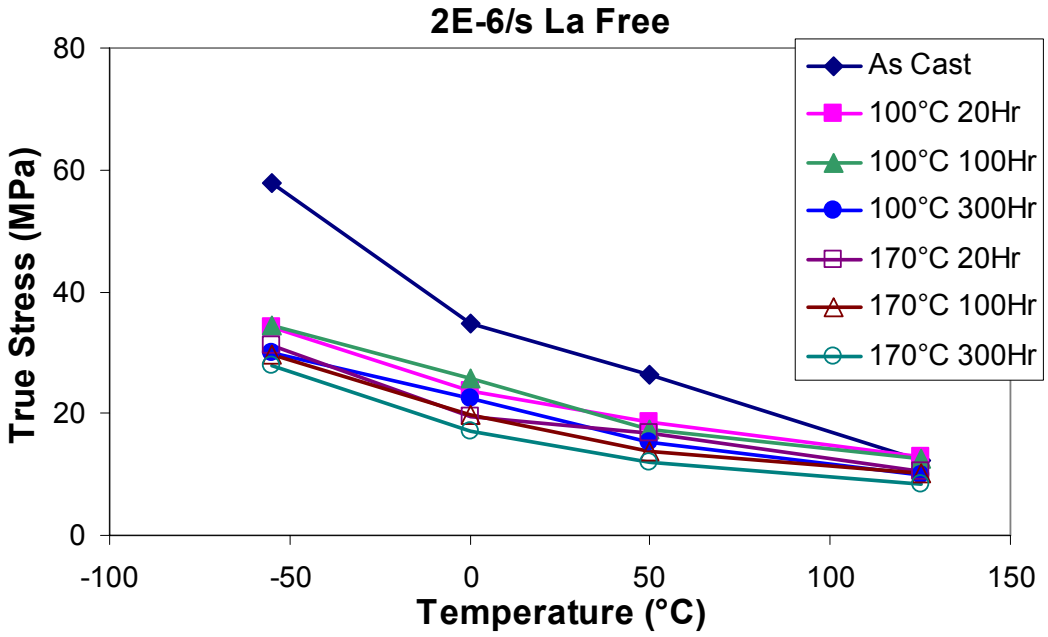

(a) SnAg solder 2E-6/s

Figure 43: The steady state stress levels, listed by different strain rates and materials

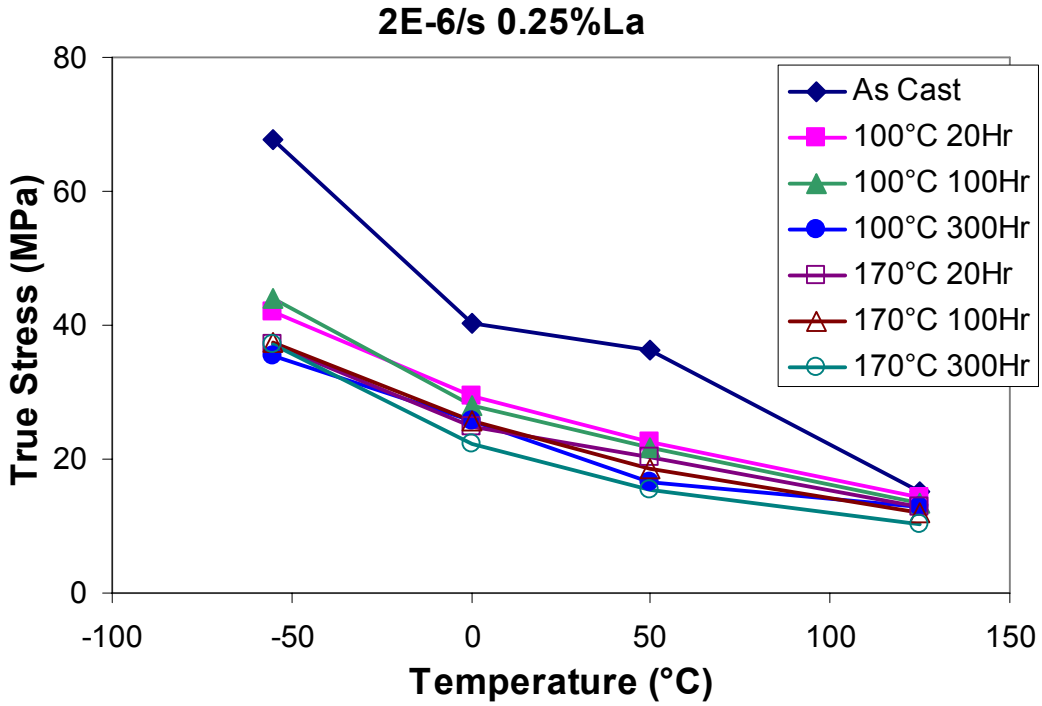

(b) SnAg0.25La solder 1E-6/s

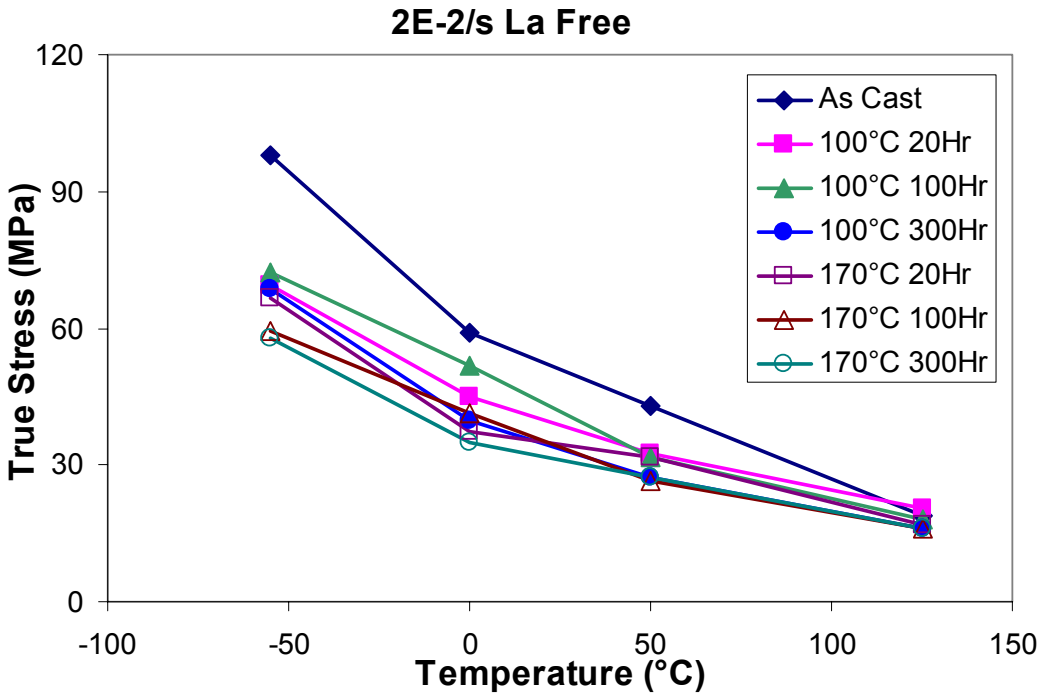

(c) SnAg solder 2E-2/s

Figure 43: The steady state stress levels, listed by different strain rate (continue)

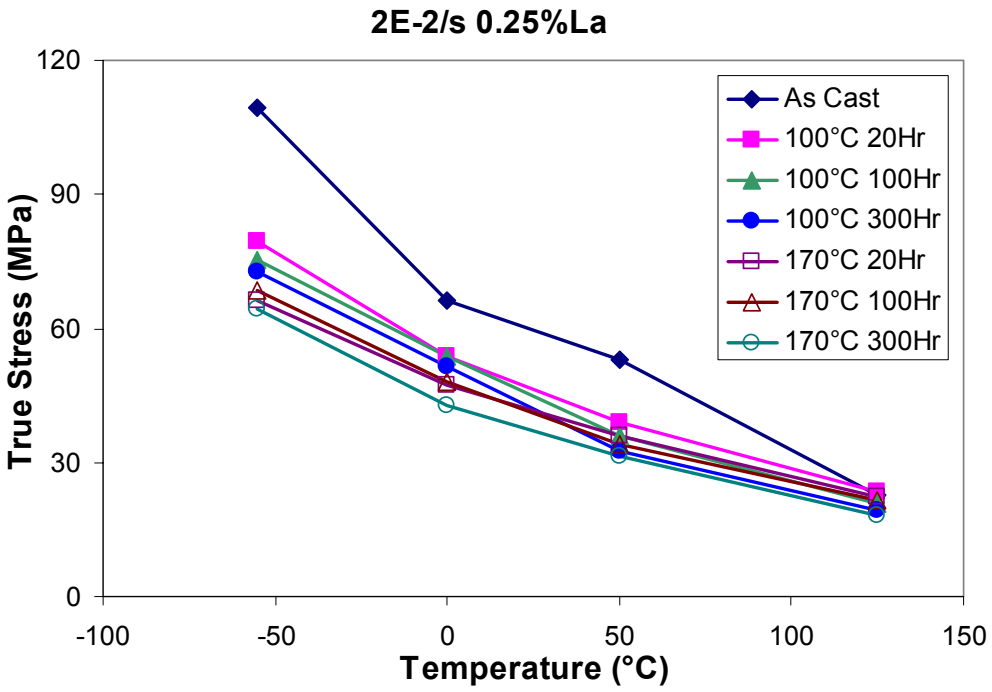

(d) SnAg0.25La solder 2E-2/s

Figure 43: The steady state stress levels, listed by different strain rate (continue)

Summary

In this chapter, the tensile creep test of solder materials was performed. With the strain rate jump test, the La doping effect and aging effect on lead-free solder were studied on wide range of strain rate and temperature.

La doping was found to increase the creep resistance. Within the range of this study (0.25% La), higher La doping will provide higher creep resistance; meanwhile, La doping does not change the aging dependent trend of solder material. With thermal aging, La doped material will still have higher creep resistance.

CHAPTER 6

CONSTITUTIVE LAW CONSTANT EXTRACTION

Background

Due to low melting temperature, the working condition of solder material is always above 0.5 of the melting temperature. As a result, creep is considered to be the most important deformation mechanism. Usually creep deformation is composed with primary (transient) creep, secondary (steady state) creep and break down. Steady state creep occupies the longest time of the material life span and it is of the highest interest.

Creep

Most of the lead-free solders used in industry are high Sn solders. Because pure tin has an exceptionally low lattice self-diffusion coefficient, dislocation pipe diffusion controls the majority of the creep part [31]. For SnAg solder, literature results differ greatly. Some of these results even have smaller activation energy than pure tin. The possible origin of such scatter is the nucleation, accumulation, and further growth of internal defects such as pores and microcracks.

Steady State Creep

The steady state creep of solder alloys usually has 4 regions [53], which can be identified as 4 straight lines in the log-log plot of stress vs. strain rate. The slopes of the lines are 3, 2, 3-7, and greater than 10 respectively.

The deformation properties of the four regions for near eutectic Pb/Sn solder have been well studied. The first region is grain size dependent and the steady state creep is generally expressed as the Weertman-Dorn equation:

$$\frac{d\gamma_s}{dt} = \frac{AGb}{kT}\left(\frac{b}{d}\right)^p \left(\frac{\tau}{G}\right)^n D_0 \exp(-Q/kT) \quad \textbf{(13)}$$

Region II is considered to be dominated by grain boundary sliding process (superplasticity) and region III is controlled by dislocation climb and glide (matrix creep). The double power law is usually used for these two regions:

$$\frac{d\varepsilon_s}{dt} = C_{II} \exp\left(\frac{-Q_{II}}{kT}\right)\sigma^{n_{II}} + C_{III} \exp\left(\frac{-Q_{III}}{kT}\right)\sigma^{n_{III}} \quad \textbf{(14)}$$

If we consider regions III and IV together, a hyperbolic sine equation can express the power law break down well:

$$\frac{d\varepsilon_s}{dt} = C_{III,IV}\left[\sinh(\alpha\sigma)\right]^n \exp\left(\frac{-Q}{kT}\right) \quad \text{or}$$

$$\frac{d\varepsilon_s}{dt} = \frac{C_{III,IV}}{T}\left[\sinh(\alpha\sigma)\right]^n \exp\left(\frac{-Q}{kT}\right) \quad \textbf{(15)}$$

All the constants in the equations above have the usual meaning.

The creep regions also exist in lead-free solders and they can be explained according to different ways that mobile dislocations escape from the hard particles in the soft β-Sn matrix [27]: 1. particle shearing, 2. bowing between particles (Orowan bowing) and 3. climbing around particles. The first two mechanisms depend little on temperature while the climbing around particles does depend on temperature because it involves diffusion mass transfer. If either of the first two mechanisms can happen, it will dominate; however, dislocations will be pinned at Ag_3Sn and Cu_6Sn_5 particles when stress level is under critical Orowan stress. As a result,the double power law is usually used to describe region II and III together. Note here that the low end of the steady state creep cannot always be observed for small samples such as real size flip chip samples [27].

Sometimes the precipitation strengthened alloys are expressed by a power law with stress threshold:

$$\dot{\varepsilon} = A\left(\frac{\sigma - \sigma_{th}}{E}\right)^{n} \exp\left(-\frac{Q}{kT}\right) \quad \textbf{(16)}$$

But it is not used in lead-free solders for two reasons. First, the σ_{th} is not a real threshold because it decreases with the strain rate [27], and second, abnormally high values of stress exponent and activation energy are not commonly seen in lead-free solders [33].

Primary Creep

The mechanism of primary creep is not very clear; consequently several phenomenological equations were proposed to describe it. Darveaux *et al*. [54] used the following equation to describe the transient creep rate:

$$\frac{d\gamma_c}{dt} = \frac{d\gamma_s}{dt}\left(1 + \gamma_T B \exp\left(-B\frac{d\gamma_s}{dt}t\right)\right) \quad \text{or}$$
$$\gamma_c = \frac{d\gamma_s}{dt}t + \gamma_T\left(1 - \exp\left(-B\frac{d\gamma_s}{dt}t\right)\right) \quad \textbf{(17)}$$

In which $\frac{d\gamma_s}{dt}$ is the steady state creep strain rate, γ_T is the transient creep and B is the transient creep coefficient. Schubertt *et al*. [55] used a form similar to the Darveaux equations with exponential changed into power law.

Zhang *et al*. [56] found the saturated transient creep has a power law relation with stress. Then the transient creep stress γ_T follows the equations below:

$$\frac{\gamma_{T-sat} - \gamma_T}{\gamma_{T-sat}} = \exp(At + B) \quad \textbf{(18)}$$

where A and B are dependent on the steady state creep rate and temperature.

Plastic Deformation

Because solder alloys are always working in high homogeneous temperatures, most researchers simply ignore the time independent plastic properties. Still, some authors want to keep this part in their constitutive laws either to describe the low strain

portion of the high strain rate, low temperature deformation [54], or to serve as an error correction term of the hyperbolic sine creep [56]. Power law hardening plastic flow is usually used:

$$\gamma_p = C\left(\frac{\tau}{G}\right)^m \quad \textbf{(19)}$$

In which the G is the shear modulus and C is a constant.

Internal Variable Method

The advantage of using the internal variable constitutive law is that this kind of method combines rate dependent creep and plastic together and there is no need to distinguish them. They are, however, usually in a complex form that includes not only the flow function but also the evolution of the internal variables.

The most commonly used internal variable model is the Anand model [57] and it has been implemented into commercial FEM software such as ANSYS [58]. The flow function of the Anand model is in hyperbolic sine shape:

$$\frac{d\varepsilon_p}{dt} = A\left[\sinh\left(\frac{\xi\sigma}{s}\right)\right]^{1/m} \exp\left(\frac{-Q}{RT}\right) \quad \textbf{(20)}$$

The evolution equations for internal variable s are

$$\frac{ds}{dt} = \left\{h_0\left(|B|\right)^a \frac{B}{|B|}\right\}\frac{d\varepsilon_p}{dt} \quad \textbf{(21)}$$

$$B = 1 - \frac{s}{s^*} \quad \textbf{(22)}$$

$$s^* = \hat{s}\left[\frac{d\varepsilon_p / dt}{A}\exp\left(\frac{Q}{RT}\right)\right]^n \quad \textbf{(23)}$$

The ANSYS theory manual explains all the constants used in the model as in Table 6. Other characters have the usual meanings. Due to the complexity of the Anand

model, the constants are not widely available for solder materials. More details of the Anand model can be found in [57].

Table 6 Anand model constants in ANSYS software [58]

Constant	Meaning	Material Property	Units
C1	s_o	initial value of deformation resistance	Stress
C2	Q/R	Q = activation energy R = universal gas constant	energy /volume energy /(volume temp)
C3	A	pre-exponential factor	1 / time
C4	ξ	multiplier of stress	Dimensionless
C5	m	strain rate sensitivity of stress	Dimensionless
C6	h_o	hardening / softening constant	Stress
C7	$\hat{s}$	coefficient for deformation resistance saturation value	Stress
C8	n	strain rate sensitivity of saturation (deformation resistance) value	Dimensionless
C9	α	strain rate sensitivity of hardening or softening	Dimensionless

However, the Anand model is not suitable for fatigue modeling of solder material due to a short of back-stress support. McDowell, *et al*. [59] proposed a sophisticated unified plastic creep constitutive law for solder materials. In their viscoplastic flow rule, they introduced both short range and long range back stresses. In the evolution rules of the back stresses, both isotropic hardening and static thermal recovery are considered. The isotropic hardening law is partitioned between the yield strength and the amplitude of the short range kinematic hardening variable. This model and modified versions are widely used on solder materials [60]-[62][64].

Constitutive Law Extraction Methodology

In this study, some complex constitutive laws such as Anand model will be applied to the solder materials. The extracting of constants of these constitutive laws brings a new challenge. Taking the Anand model as an example, due to the complexity of the constitutive model, previous researchers usually used multi-step methods to obtain the parameters of this model, although there is a trend to reduce the steps and rely on nonlinear data fitting. For example, a paper from Anand himself [57] suggested a seven step method, including one nonlinear fitting step that has 4 parameters. More recent studies usually use 4 to 5 step methods and can have up to 5 parameters in each step[64][66][67]. Usually in the first step, the constants in the flow function were obtained from the saturation creep stress, followed by other evolution parameters in other steps. These multi-step methods require manually partition the deformation curve into the elastic part, the evaluating part, and the saturated part. This partition may introduce error, especially at low temperature and high strain-rate condition, where the specimen will not reach saturation stress before failure.

Taking advantage of the recent improvements in computer speed and optimization algorithms, one-step methods were used in this study. These methods fit the whole deformation curve with a constitutive model that has both elastic and plastic/creep deformations. This method avoids the errors from manually reading the saturation stresses and Young's modulus. Traditionally, the Young's modulus was obtained by linear fitting using the initial portion of the deformation curves. The traditional method may mix inelastic deformation in the elastic modulus. The one-step data fitting methods used in this study will generate elastic properties automatically and avoid this error. The elastic part was considered to be linearly dependent on temperature, as in the equation below:

$$E = E_0 + E_1 \bullet T \quad \textbf{(24)}$$

where E_0 is the modulus at 0°C and E_1 is temperature dependent coefficient. The unit of temperature T is °C. Two one-step methods are used in this study. They are the nonlinear optimization method and the neural network method.

Nonlinear Optimization

Optimization Toolbox Version 2.2 provided by Matlab® Version 6.5.0 was used in this study. The parameters to be optimized include 2 elastic constants and 9 Anand model constants. The target of the optimization was to minimize the square error between the model simulation with the test deformation curve, and the model simulation program was written with C++. The study shows that the initial parameter has little effect on fitting result.

Neural Network Method

Neural networks have been widely used in data simulation and pattern recognition. This study used neural network to recognize the deformation curve patterns. Neural Network Toolbox Version 4.0.2 provided by Matlab® Version 6.5.0 was used. Prior to the neural network simulation, the network was trained with stress strain curves from the Anand model. A trained neural network can recognize the curve shapes and generate the model parameters. Several types of neural networks have been investigated and the best result came from the Generalized Regression Neural Network (GRNN). If properly trained, GRNN can give results very close to the nonlinear optimization result. The layer structure of GRNN network can be found in Figure 44[68].

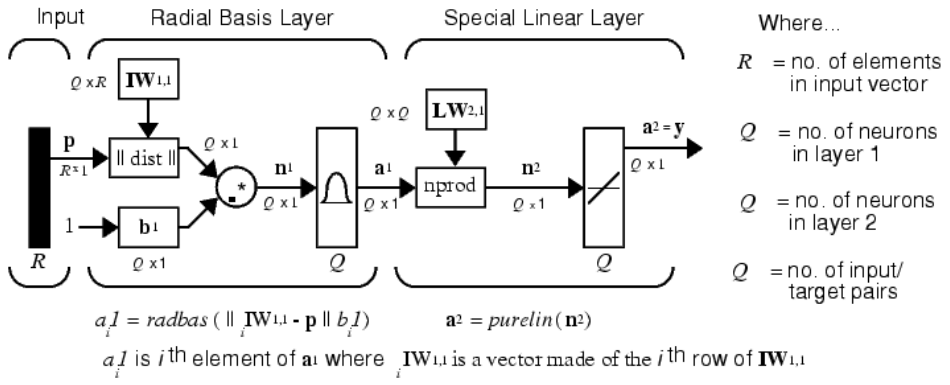

Figure 44: Generalized Regression Neural Network (GRNN) structure

Microstructure Dependent Constitutive Law

A microstructure dependence constitutive model is introduced in this paper by modifying the Anand model with a power-law particle-size dependent term introduced in the model:

$$\frac{d\varepsilon_c}{dt} = A_1\left(\frac{d_p}{d_{p0}}\right)^q\left[\sinh\left(\frac{\xi\sigma}{s}\right)\right]^{1/m}\exp\left(-\frac{Q}{RT}\right) \quad \textbf{(25)}$$

where the dimensionless term $(d_p/d_{p0})^q$ was introduced to equation (20). The diameters of the Ag_3Sn particles d_p are in units of μm and the initial particle size of un-doped alloy d_{p0} is 0.128μm. Particle sizes can be obtained from the quantitative microstructure study in Chapter 4. Meanwhile, a particle size coarsening model discussed in Chapter 5 can be used to calculate the particle size as the function of La doping and thermal aging. This model is listed in equation (11) and (12). Combining this model and equation (25) and comparing the result with (20), the constant A in the Anand model can be expressed as the following equation and can be used in FEM model according to the thermal treatment and La doping:

$$A = A_1\left(d_0^{RE^3} + \frac{K_0^{RE}}{T}t\exp\left(-\frac{Q_{ag}^{RE}}{RT_{ag}}\right)\right)^{\frac{q}{3}} \quad \textbf{(26)}$$

The evolution of internal state variable *s* in the microstructure dependent Anand model will follow the Anand model shown in equations (21)(22) and (23).

Model Fitting Result

To study the La doping effect on solder material creep behavior, the model was fitted with tensile test data from samples that have different La doping levels but with the same thermal treatment. As a result, each thermal process condition has one set of corresponding model constants, which are listed in Table 7. Two examples of the model comparing with tensile test are shown in Figure 45 for as-cast condition and in Figure 46 for 170°C 300 hour aged condition. Good fit can be observed from these two figures.

It can be seen from Table 7 that the particle size dependent exponents are around 5.5 for most of the cases. This is a very high exponent compared with existing model where 1 was used [33]. In this phenomenological model, only particle size effect on creep behavior is considered. Other creep enforcing mechanisms, such as the distribution of the particles and RE atoms' effect, are not explicitly expressed in the model. However, these mechanisms do affect the material creep behavior through the particle size in the model. For this reason, an abnormally high particle size dependent exponent can fit the test data better.

This model did not attempt to incorporate aging effect through particle size change, for the same reason, and excessive error will be introduced if the model is fitted with all the test data. As a result, one set of model constants were obtained for each thermal treatment condition.

Table 7: Microstructure dependent Anand model constants for different processing conditions

Constant	As-cast	100°C 20Hr	100°C 100Hr	100°C 300Hr	170°C 20Hr	170°C 100Hr	170°C 300Hr
s_o (MPa)	1.52E+01	1.04E+01	1.21E+01	1.18E+01	1.11E+01	1.37E+01	1.47E+01
Q/R (K)	1.19E+04	1.26E+04	1.46E+04	1.37E+04	1.33E+04	1.10E+04	1.02E+04
A_1 (1/s)	2.25E+03	1.97E+02	3.21E+03	5.99E+01	1.84E+01	4.79E+00	3.76E+02
ξ	1.91E+00	1.78E+00	2.11E+00	2.19E+00	2.06E+00	1.61E+00	1.44E+00
m	1.76E-01	1.27E-01	1.20E-01	1.15E-01	1.21E-01	9.09E-02	9.38E-02
ho(MPa)	3.17E+02	9.59E+02	3.28E+02	3.66E+02	3.16E+02	2.38E+03	3.46E+03
$\hat{s}$ (MPa)	5.73E+00	1.18E+01	5.40E+00	5.55E+00	8.19E+00	1.57E+01	1.73E+01
n	1.38E-01	3.29E-02	7.40E-02	9.56E-02	5.28E-02	3.37E-02	2.46E-02
α	5.49E+00	2.71E+00	1.38E+00	1.98E+00	1.02E+00	2.77E+00	2.50E+00
E_0	3.06E+04	3.49E+04	3.00E+04	3.00E+04	3.00E+04	3.00E+04	3.00E+04
E_1	-1.07E+02	-7.66E-02	-9.51E+01	-1.02E+02	-9.04E+01	-6.76E+01	-1.45E+02
q	4.99E+00	4.80E+00	4.42E+00	6.23E+00	6.89E+00	6.28E+00	4.36E+00

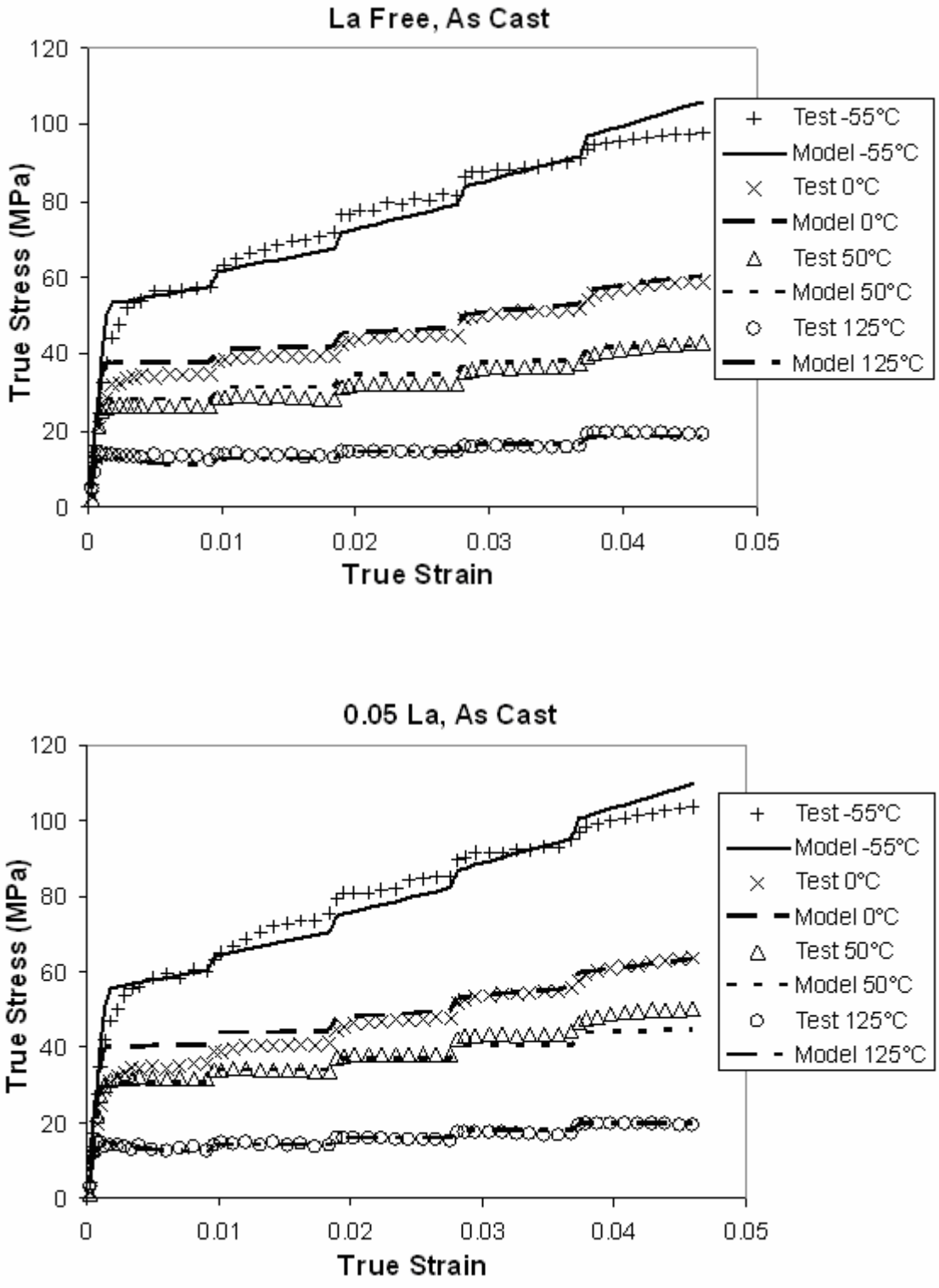

Figure 45: Modified Anand model fitting result, as-cast condition

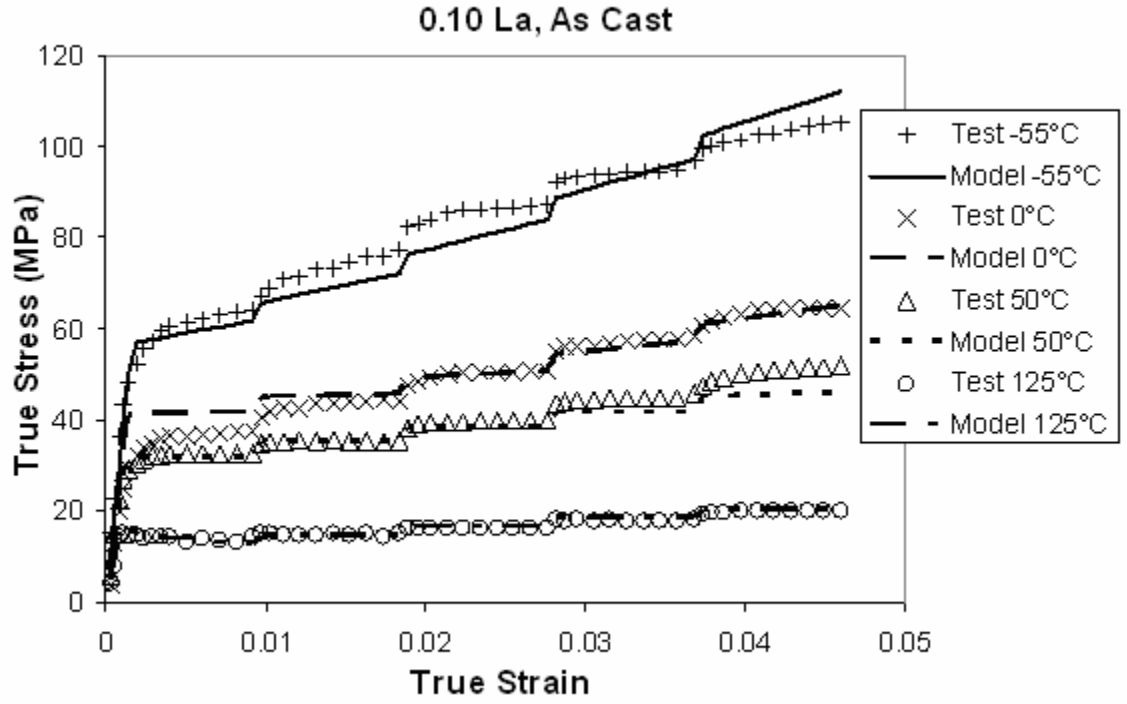

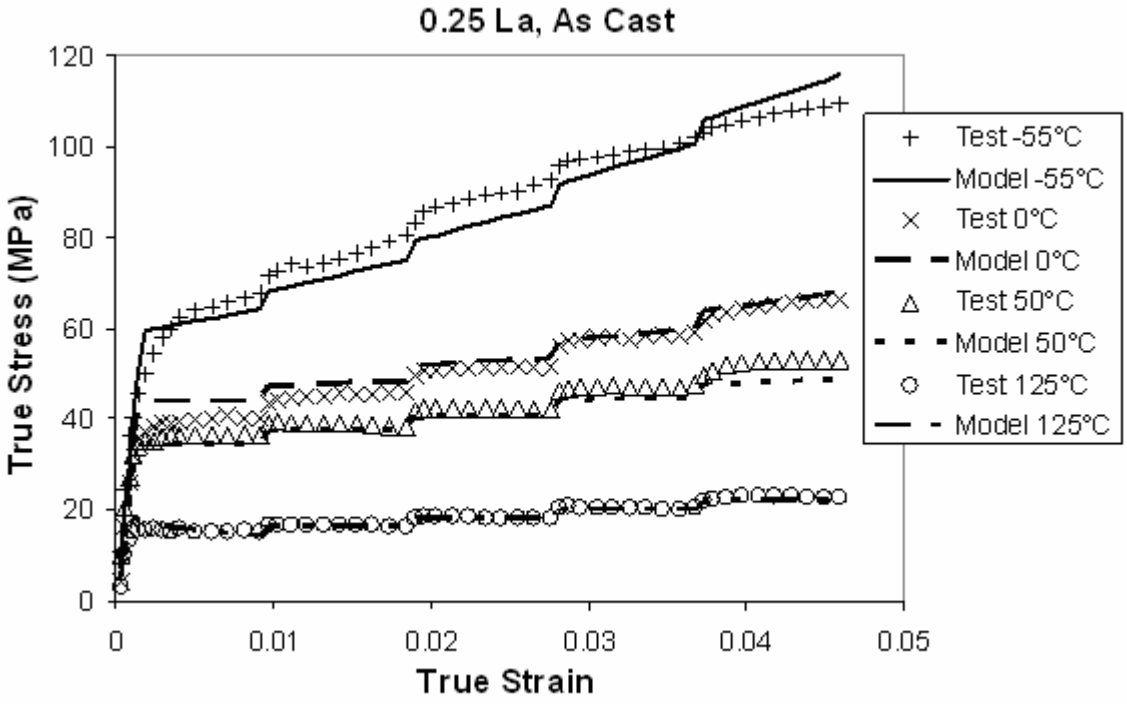

Figure 45: Modified Anand model fitting result, as-cast condition (continue)

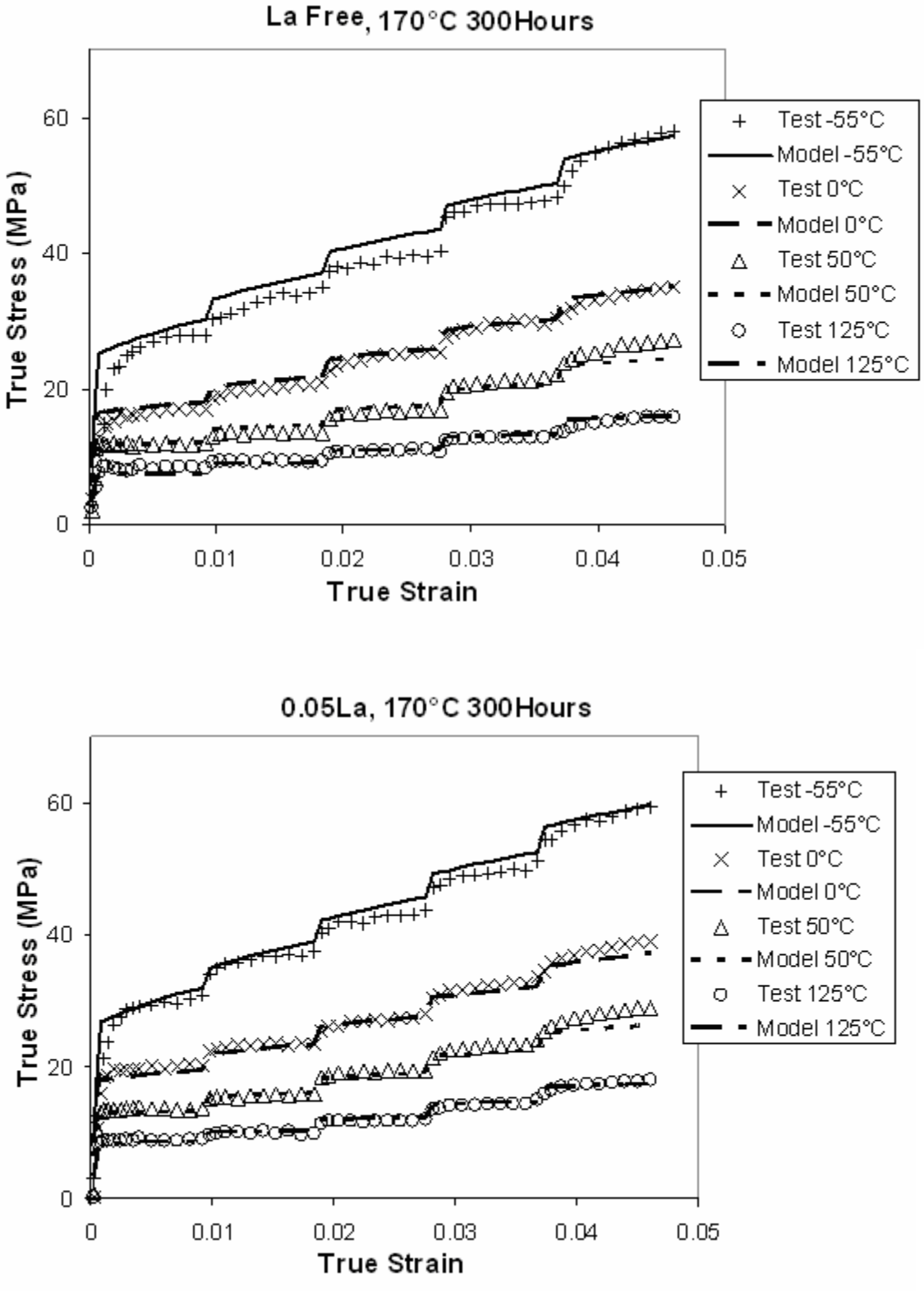

Figure 46: Modified Anand model fitting result, 170°C aged for 300 hours

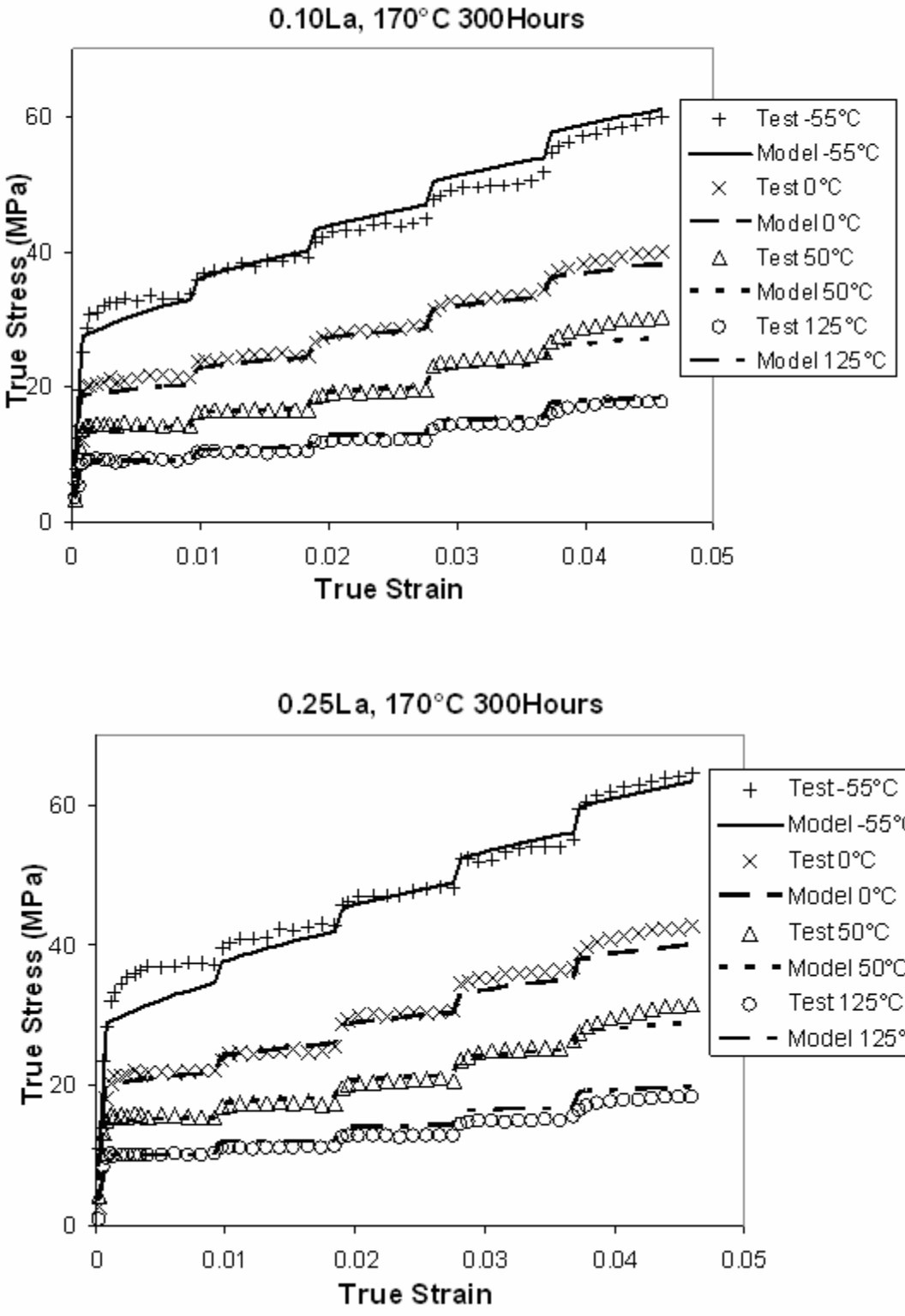

Figure 46: Modified Anand model fitting result, 170°C aged for 300 hours (continue)

Summary

In this chapter, a microstructure dependent modified Anand model was proposed after a short review of the constitutive laws used on solder materials, and a one-step data fitting method was used to extract the constant from the tensile test stress strain curves.

This model is fitted with the test result from Chapter 5 to study the La doping effect. A good fitting result was obtained.

CHAPTER 7

HIERARCHAL MODELING OF SnAg SOLDER ALLOY

To understand the relationship between microstructure and creep behavior, a constitutive law for SnAg alloys is proposed. Unlike existing models, the new constitutive law should consider the hierarchal microstructure at multiple length scales.

Specifically, at the smaller length scale, SnAg eutectic region is first treated as a particulate-enforced composite with the sub-micron-size Ag_3Sn particles embedded in Sn matrix. At this length scale, the Ag_3Sn particles are considered to be randomly dispersed in the Sn matrix. At the larger length scale, the solder alloys is treated as a two-phase composite with micron-size Sn dendrite as the particle and the SnAg eutectic region as the matrix.

Small Length Scale

The eutectic region consisting of Ag_3Sn particles and Sn matrix can be viewed as a particulate-reinforced composite. Therefore, its properties can be estimated using standard micromechanics theories. In this work, it is assumed that the Ag_3Sn particles are spherical and randomly distributed in the Sn matrix. They behave linear elastically with elastic molduli of

E = 80GPa, $\quad v$ = 0.36

The creep behavior of the Sn matrix is assumed to follow the power law,

$$\dot{\varepsilon}_c = A(\sigma)^n \exp\left(-\frac{Q}{RT}\right) \tag{27}$$

where $\dot{\varepsilon}_c$ is the creep strain rate, σ is the stress, A and n are material constants and $\exp\left(-\frac{Q}{RT}\right)$ is the temperature dependent term.

Two different solder compositions, Sn3.5Ag and 96.25Sn3.5Ag0.25La, are considered here. It has been shown in previous chapters that the La doped alloy has a much refined microstructure and better creep resistance than the standard Sn3.5Ag alloy. Therefore, they are chosen to validate the model developed here. For these two alloys, the Ag_3Sn particle volume fractions in the eutectic region are 0.18 and 0.12 for the un-doped and doped alloys, respectively.

It is assumed here that properties of the Sn matrix in the eutectic region are the same as those of the Sn dendrite. For Sn dendrite, room temperature values of the material constants in (27) were measured using nanoindentation test and are listed in Table 8. Nanoindentation tests used are discussed in the Appendix G.

To estimate the effective creep behavior of the eutectic region, a standard secant-modulus approach in conjunction with the Mori-Tanaka method [71] was used. This method is discussed in detail in Appendix H. The steady-state effective stress as a function of strain rate at room temperature were obtained and plotted in Figure 47. The material constants used in the computation were taken from Table 8.

The predicted stress-strain rate curve shown in Figure 47 was fitted to a power law function similar to (27) and the constants for the eutectic region are listed in Table 8. To validate the micromechanics model, nanoindentation tests were again conducted on the eutectic region to obtain the stead-stress versus strain rate curve. The results are also shown in Figure 47 to compare with the model prediction.

Good agreement between the model prediction and the test data was observed at lower strain rate (<2E-3/s) but some deviation was found for the doped alloy at high strain rate. In the model, it was assumed that the creep behavior of Sn matrix in eutectic region is the same as that of Sn dendrite. The derivation shows that this assumption may not hold at high strain rate in La doped solder. Considering the fact that La doping increases creep resistance of the Sn dendrite, it is conceivable that it may have even

stronger effect on Sn matrix due to the existence of much higher amount of interfaces in eutectic region.

Table 8: Power law creep model constants in small length scale

	n	$A\exp(-Q/RT)$
Sn dendrite in SnAg	15.5	4.3E-26
Sn dendrite in SnAgLa	17.0	6.8E-30
Eutectic region in SnAg	15.5	2.3E-29
Eutectic region in SnAgLa	15.5	4.3E-26

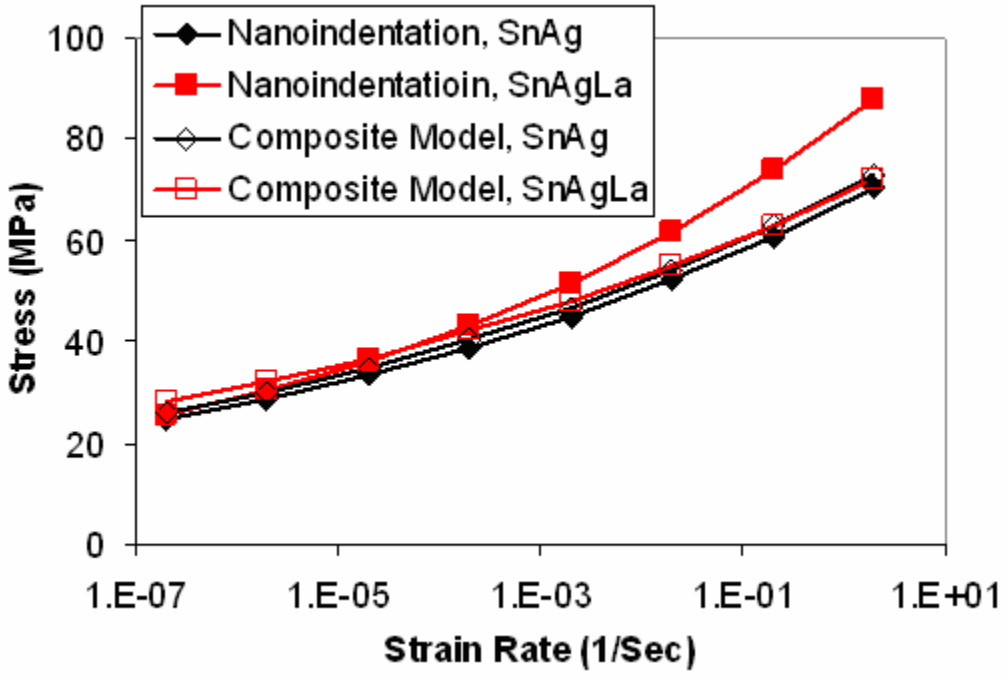

Figure 47: Comparison of smaller scale micromechanics composite model with nanoindentation result on eutectic region

Large Length Scale Model

In the large length scale model, the SnAg solder alloy was treated as a two phase composite with the homogeneous Sn dendrite as particles embedded in the eutectic region. The Sn dendrite is about ~10μm and therefore, the eutectic region, at this length scale, can be considered homogeneous with its creep properties described by the small length scale model discussed in the previous section. The results from small length scale study are listed in Table 8. From the microstructure study from Chapter 3, the volume fractions of the Sn dendrite in the alloys can be calculated to be 0.61 and 0.43 for the un-doped and doped alloys, respectively.

Again, by assuming that the Sn dendrite are spherical particles, and by using the same secant-modulus approach in conjunction with the Mori-Tanaka method [71] as discussed in Appendix H, the effective creep behavior of the solder alloys can be estimated. Room temperature results for the steady-state stress as a function of strain rate are shown in Figure 48. For comparison purpose, the Voigt upper and Reuss lower bounds are also plotted on the same figures. As expected, the micromechanics estimates are between these two bounds.

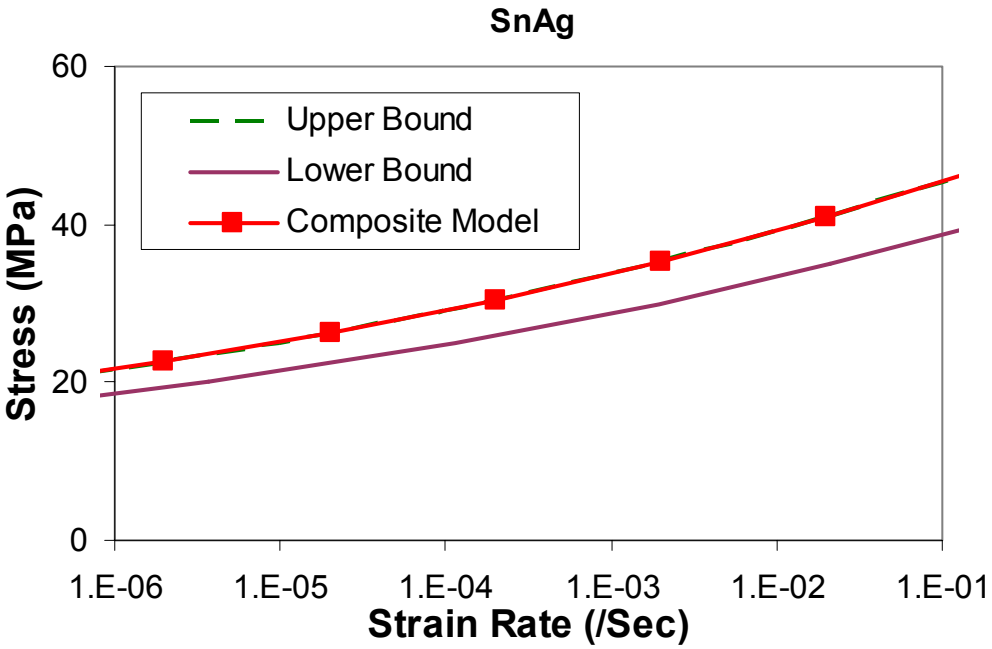

(a) un-doped solder alloy

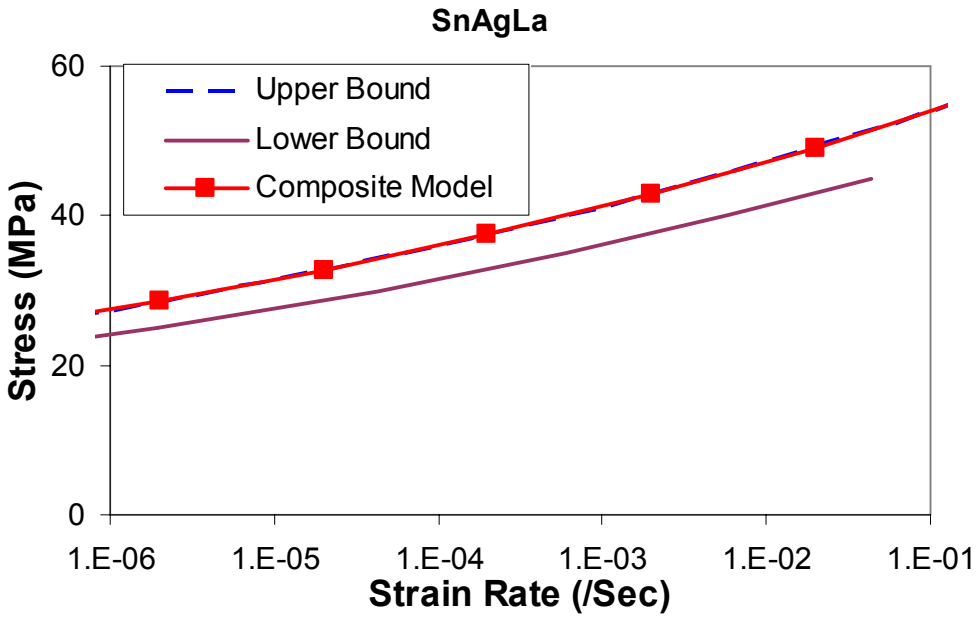

(b) RE doped solder alloy

Figure 48: Large length scale micromechanics composite model compared with upper and lower bounds

Digital Image Based FEM study

Microscopic studies indicate that the Sn dendrites are not spherical. Their shapes are rather irregular. To see whether such irregular shape would affect the model prediction, a finite element (FE) based modeling techniques were conducted on a representative volume element (RVE): digital image-based (DIB) model.

A detailed review of Digital Image-Based (DIB) modeling technique can be find in the reference [72][73]. First, a microscopic image was taken on a RVE of the alloy by a SEM. A FE mesh was then generated using the commercial software OOF2 [74]. Two sets of mashes for the Su dendrite and eutectic regions, respectively, were generated with different phase volume fractions. An example of the SEM image is shown in Figure 49, and the corresponding FE mesh using tetragonal elements are shown in Figure 50. The light color stands for Sn dendrite and dark color represents eutectic region. Shown in Figure 50(a), un-doped solder model contains 8040 elements and in Figure 50 (b), 0.25% La doped solder model contains 8350 elements.

The meshed models were then imported into ABAQUS for the stress analysis. Plane strain 8-node quadratic element with reduced integration was used in the models. A constant uniaxial velocity field was prescribed on the boundary of the RVE to simulate a constant strain rate, and the entire stress-strain curve can be obtained for any given strain rate, which is not possible using the micromechanics models discussed here. Figure 51 is an example of the entire stress-strain curve for SnAg0.25La solder under uniaxial tensile loading at 10^{-3}/s strain rate. It is clearly seen that at 1% strain, the material had already reached its state of steady-state creep region.

FEM mesh convergence study was performed by changing the element type into 4-node linear element in the model. The quadratic element is known to be able to provide better result than linear element with even higher mesh density [98]. The result shows that models with linear and quadratic element types obtained practically identical

effective creep property. As a result, the current mesh shown in Figure 50 was concluded to have sufficient mesh density. To better capture the local stress concentration, quadratic element was used in this study.

In order to ensure the RVE area selected is sufficient to represent the solder material, a convergence study was performed. Following the steps mentioned above, a model was established with about 60% area of the SEM imaged in Figure 49. The effective material creep behavior was found to have less than 2% error from the model shown in Figure 50. This result shows that the current model was satisfactory to serve as RVE of the SnAg solder.

The corresponding stress at 1% strain as a function of strain rate was recorded and plotted in Figure 52 for both the un-doped and doped alloys. The two different curves are the results of uniaxial loading in two orthogonal directions of the rectangular RVE. The fact that these two curves are so close to each other indicates that the RVE is isotropic in its creep behavior.

It is also seen that the FE results are very close to the micromechanics predictions, indicating that the assumed spherical shape for the Sn dendrite is reasonable. Furthermore, we notice that both the FE results are bounded by the upper and lower bounds.

The stress and strain fields of the RVE can also be obtained from the FE model. Shown in Figure 53 are the equivalent creep strains and in Figure 54 Von Mises stresses at 1% prescribed overall strain. It is very clear from these figures that creep strain is much higher in the Sn dendrite as expected because Sn is very prone to creep.

Deformation field of RVE under other loading conditions are listed in Appendix J. They have the similar shape with Figure 53 and Figure 54.

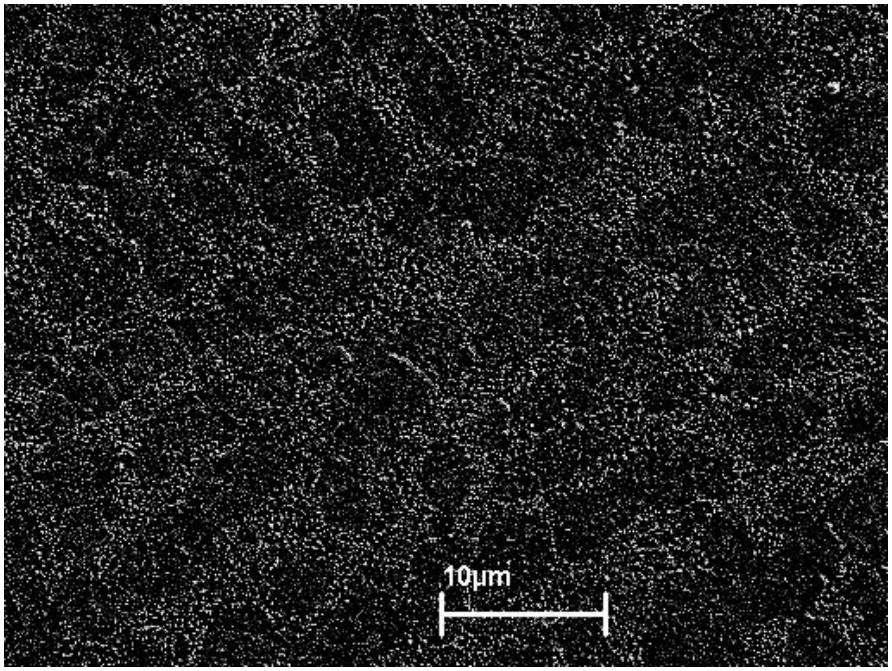

Figure 49: Original SEM image for digital image based FEM model

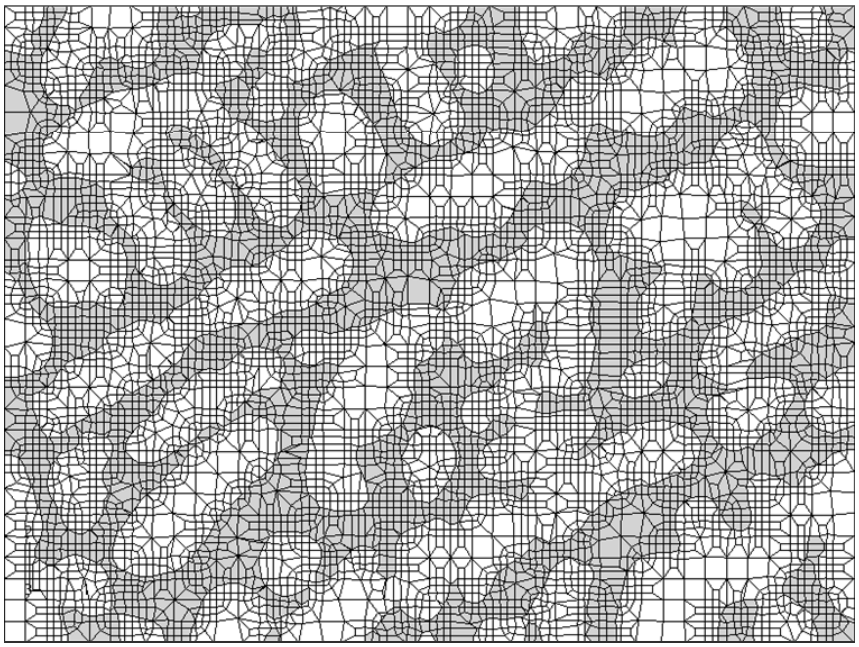

(a) Un-doped solder

Figure 50: FEM mesh of digital image based study

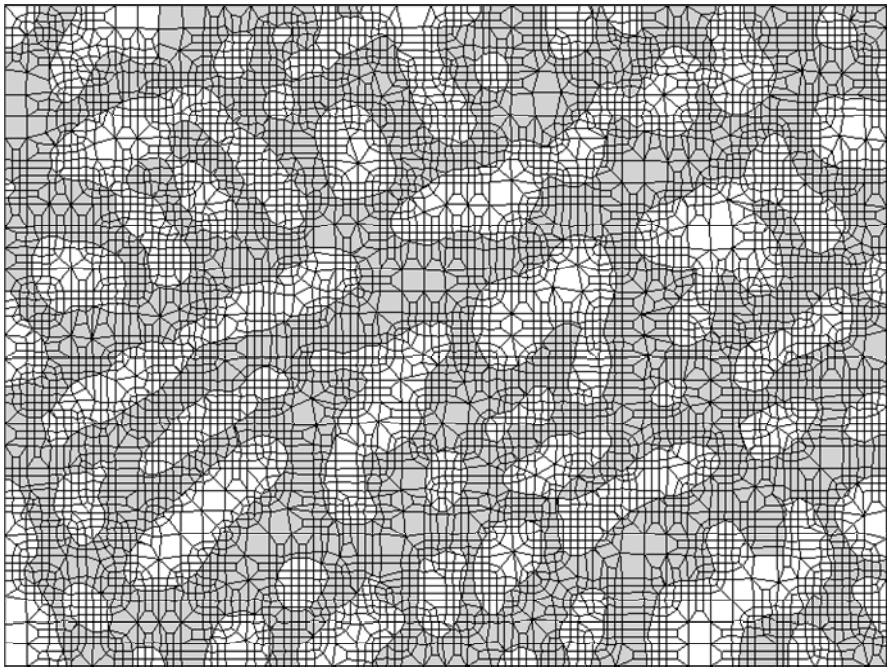

(b) RE doped

Figure 50: FEM mesh of digital image based study (continue)

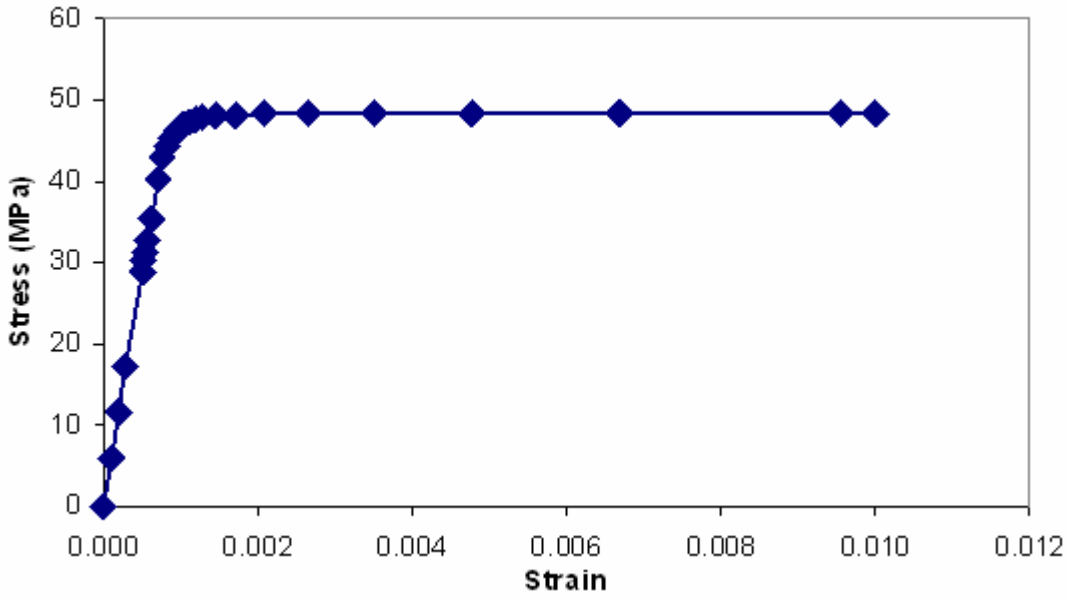

Figure 51: Stress-strain curve predicted by the FE method

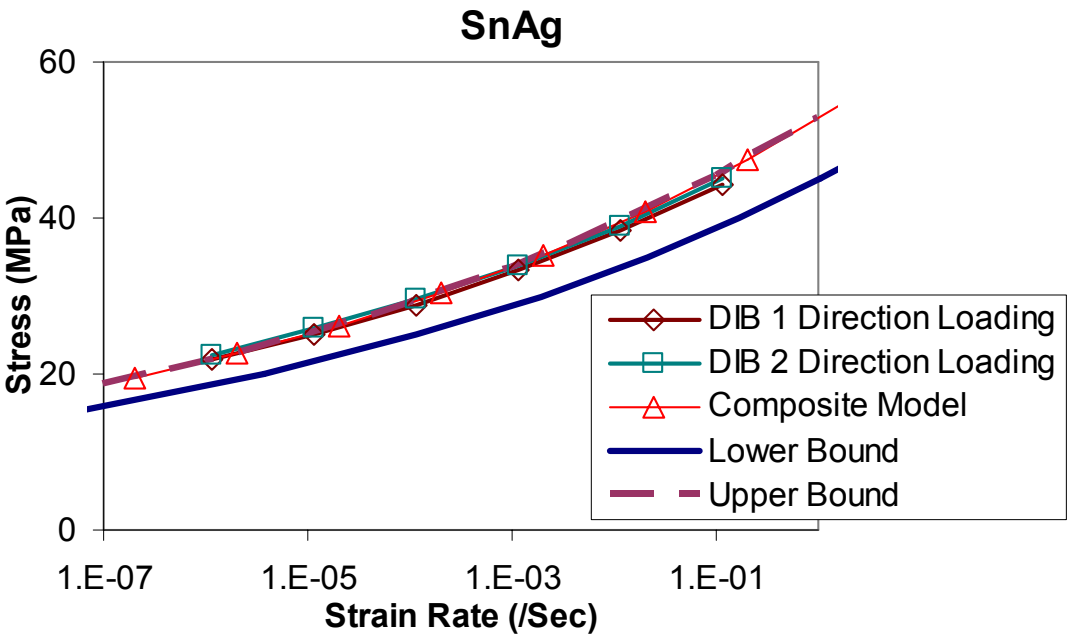

(a) Un-doped solder

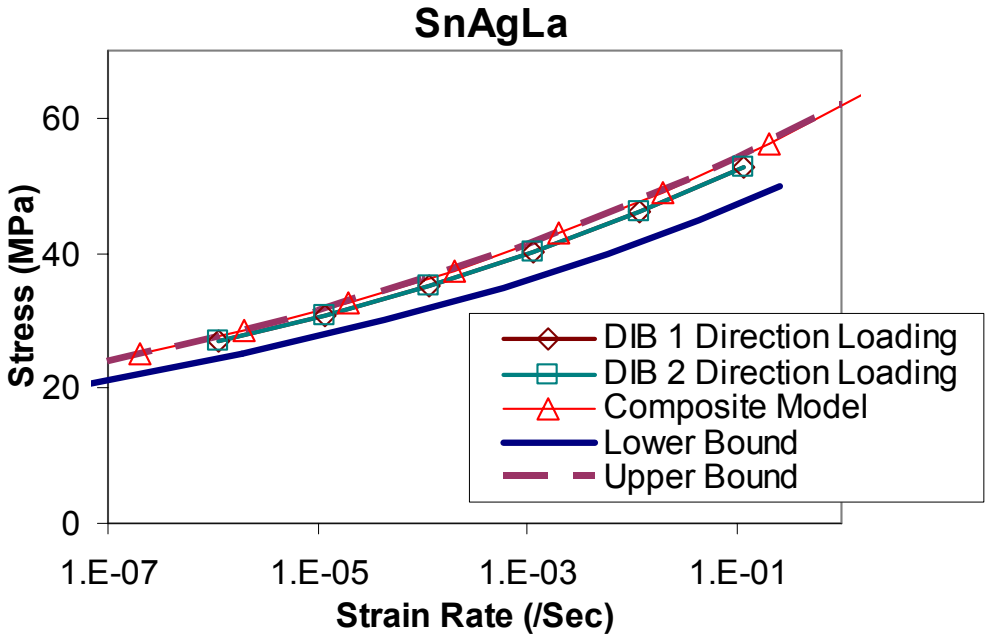

(b) RE doped solder

Figure 52: Effective stress vs. strain rate relation of DIB models compare with analytical bounds

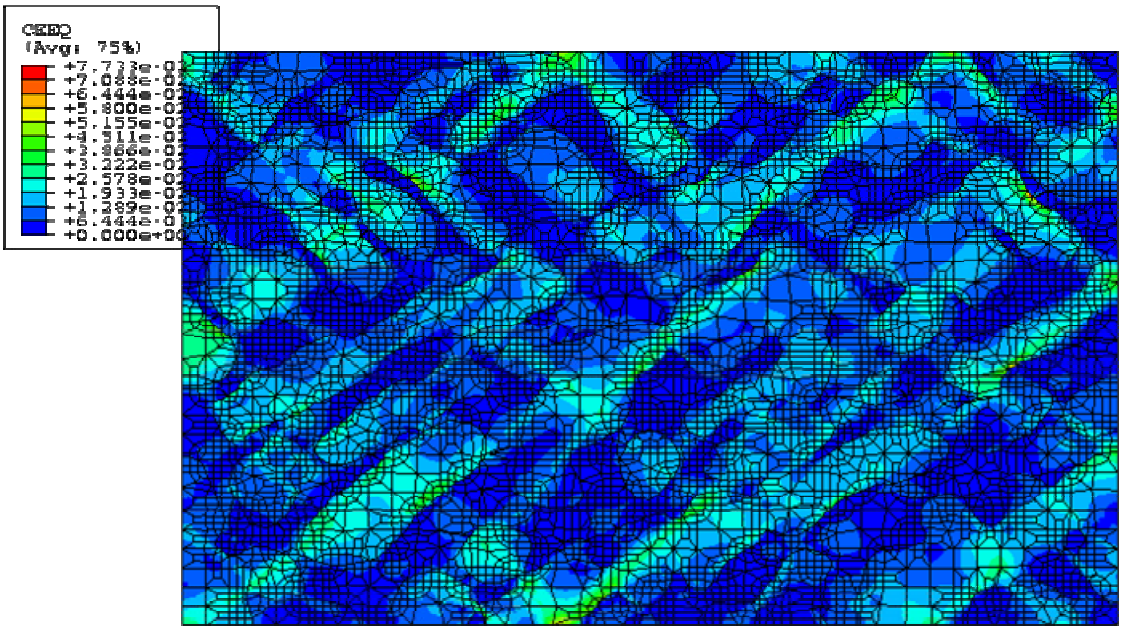

(a) 1-direction loading

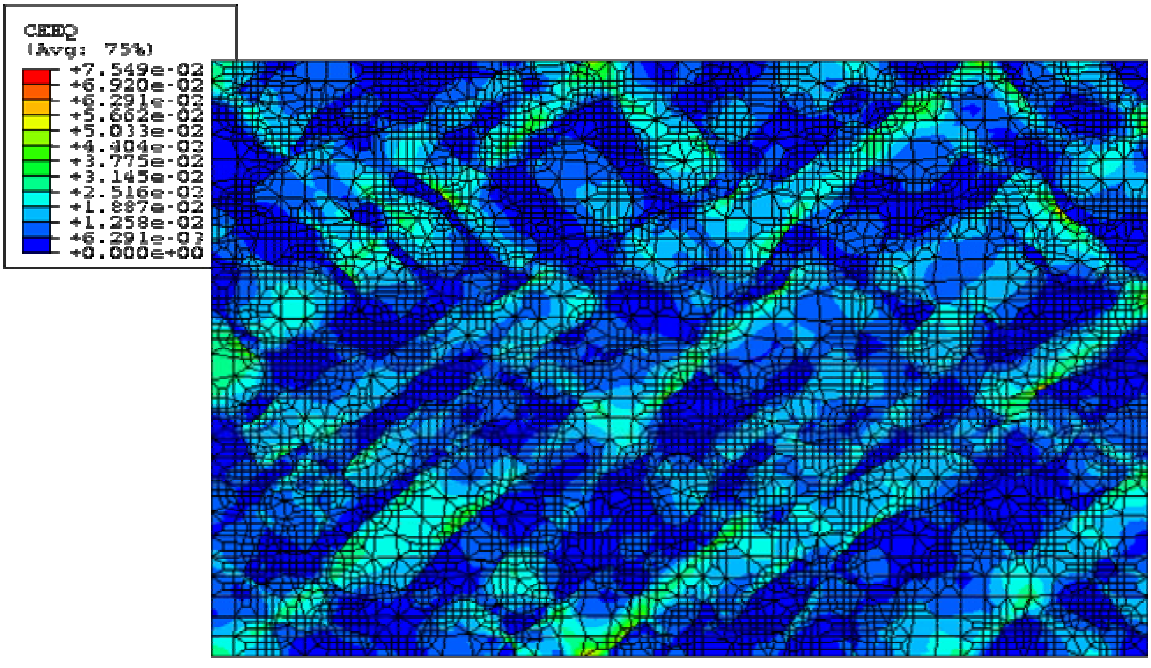

(b) 2-direction loading

Figure 53: Equivalent creep strain field of SnAg alloy from DIB model

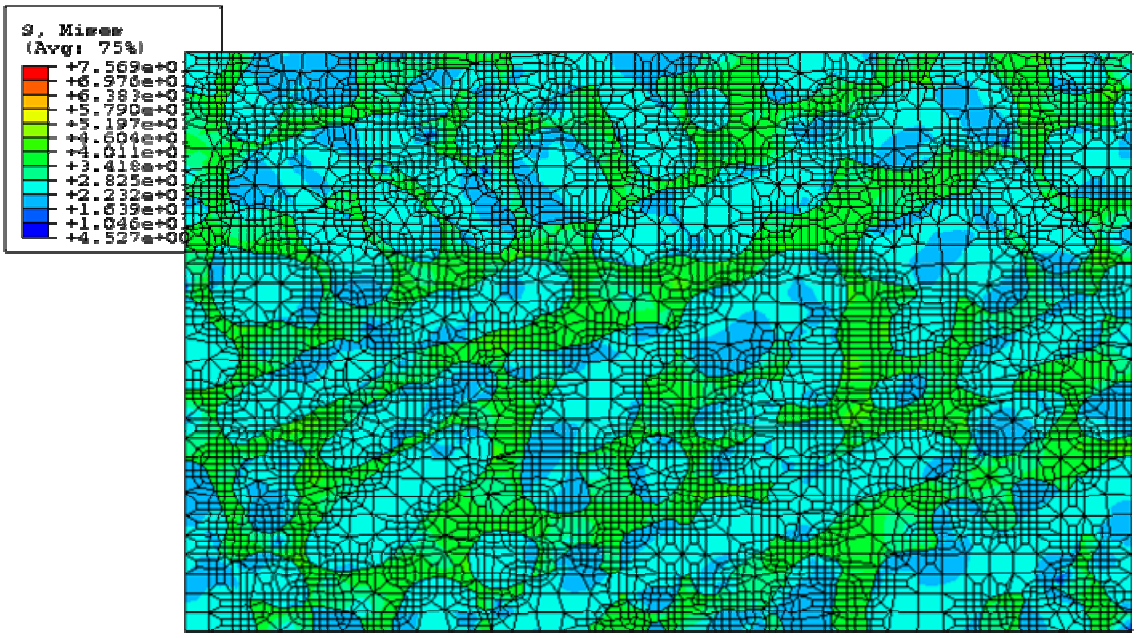

(a) 1-direction loading

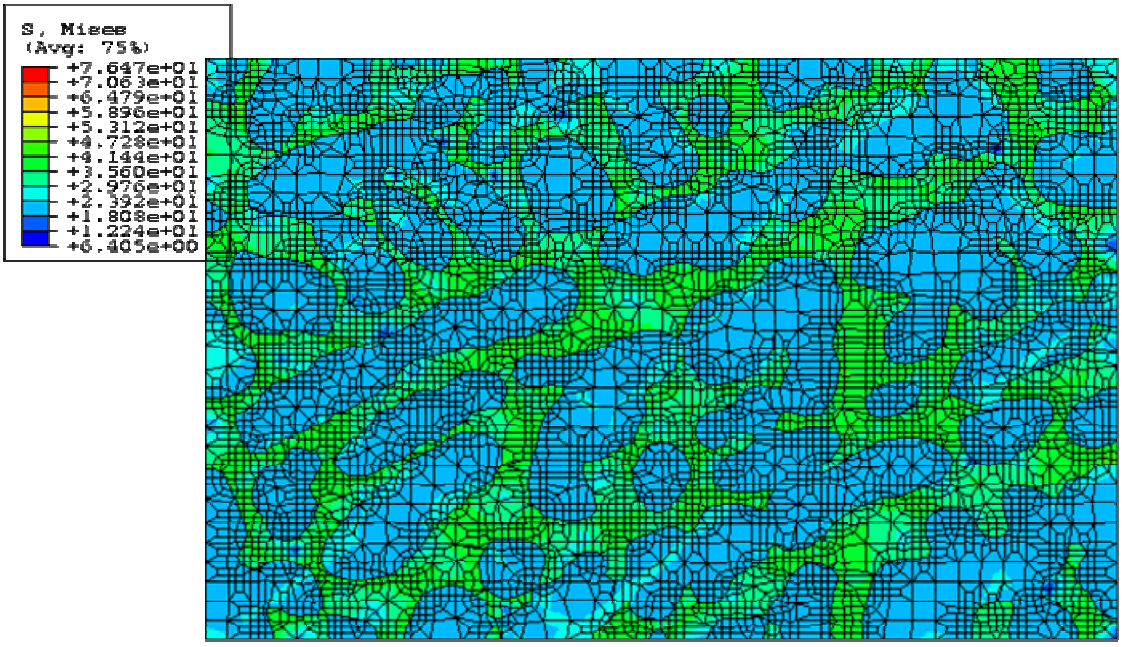

(b) 2-direction loading

Figure 54: Von Mises stress field of SnAg alloy from DIB model

Model Validation

In the large length scale, micromechanics composite model and DIB model were used. It was found that digital image based model proved the SnAg solder is isotropic in the creep behavior. With this result, it can be concluded that the less computationally intensive micromechanics composite model can provide good estimate for effective creep property for SnAg solder.

The two isotropic models, the DIB model and the composite model, are compared with tensile test result, as show in Figure 55. The creep test samples that aged at 100°C for 20 hours are picked to validate the models. It can be seen from Figure 55 that the model fit the tensile test data well.

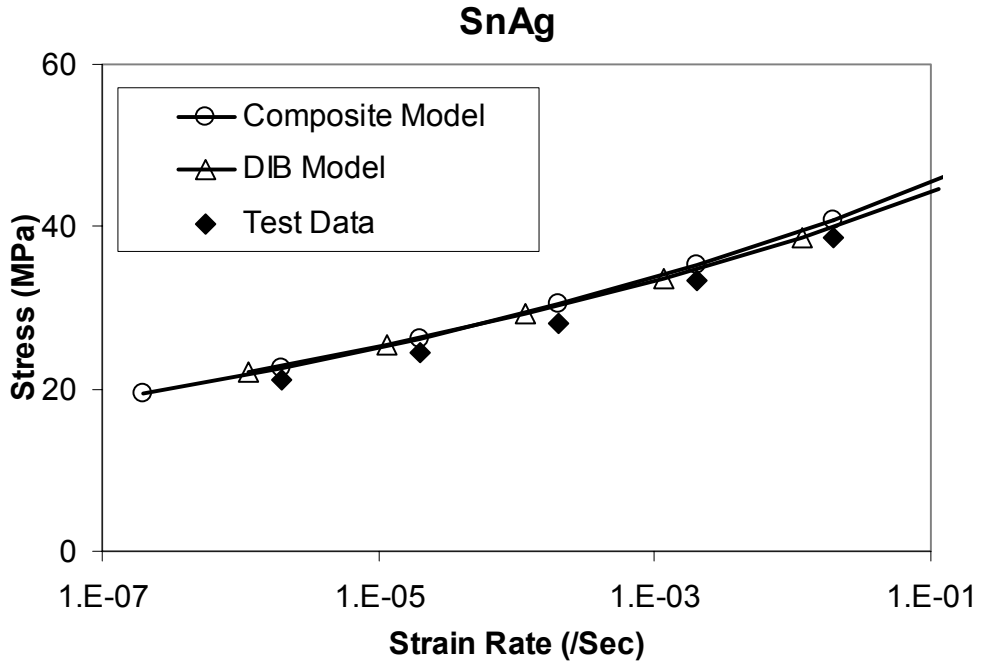

(a) Un-doped alloy

Figure 55: Comparison of model results at large length scale with test result

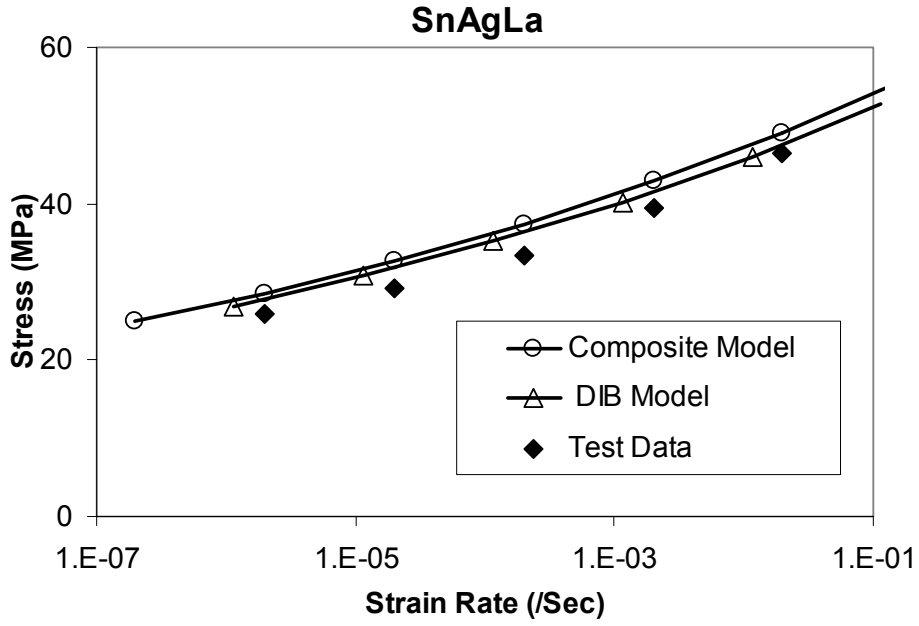

(b) RE doped

Figure 55: Comparison of model results at large length scale with test result (continue)

Summary

A hierarchal model was developed in this paper to describe the creep behavior of SnAg alloys, which accounts for the multiple lengths scales typical to lead-free solder alloys. Predictions from the model were validated by experimental measurement data.

The model developed here is simple and does not require large scale numerical computation. Moreover, this model is a physical based model that only requires the initial microstructure and the creep properties of the constituent materials which can be easily measured. For these reasons, this model can be applied to other alloys with multiple length scales in their microstructure.

CHAPTER 8

FATIGUE TEST

In electronic packaging, the thermal-mechanical fatigue failure is the major failure mechanism. Fatigue properties of lead-free solder with La doping are studied in this chapter.

Background

SnAg solder is found to be far superior to eutectic Sn/Pb at high strain amplitudes at isothermal fatigue condition, but far inferior to Sn/Pb at low strain amplitudes [75]. This is due to the resistance of SnAg alloy to fatigue crack initiation rather than to crack propagation, since this alloy has relatively low crack growth resistance compared to other solder alloys. For the thermal fatigue condition, failure is postponed because the localized microstructural coarsening that leads to failure in the Sn/Pb alloys does not occur in the SnAg alloys [75].

Coffin-Mansion Typed Fatigue Model

The Coffin-Mansion fatigue model uses a power law relation of plastic strain amplitude with the cycle life time, as in following equation:

$$\Delta\varepsilon_p N_f^{\alpha} = \theta \qquad \textbf{(28)}$$

where $\Delta\varepsilon_p$ is the inelastic strain range of one cycle, N_f is the fatigue life and α and θ are constants. This model has been used in several studies [76]-[78], and is often modified to use other criteria of fatigue loading, such as creep strain [79], and inelastic energy [55] [56] [76][78] [80] [81]. If the mechanism of fatigue damage could be distinguished from each other, the partition method can be used in fatigue life prediction. The example below uses the energy partition method [56].

$$TotalEnergy = U_e + W_p + W_c = U_{e0} N_{fe}^b + W_{p0} N_{fp}^c + W_{c0} N_{fc}^d$$

$$\frac{1}{N_f} = \frac{1}{N_{fe}} + \frac{1}{N_{fp}} + \frac{1}{N_{fc}} \quad \textbf{(29)}$$

where U_e is the elastic energy and W_p and W_c are the plastic work and creep work, respectively. b, c and d are constants.

Fracture Mechanics Based Model

Under thermal-mechanical fatigue loading, crack start from the surface and propagate into the solder [82][34]-[36]. In 96.5Sn3.5Ag solder specimen, boundary steps were observed along Sn-dendrite boundaries and microcracks were found initiated from the steps [34]-[36]. The cracks then linked up to form macroscopic cracks and propagated in a mixed manner. Figure 56(a) (b) shows the step formation along the fatigue load and the cross section of surface crack. Figure 56(c) shows the mixed manner crack propagation [35]. The crack may continue growing after the loading was stopped by the residual stress caused by the thermomechanical fatigue [82].

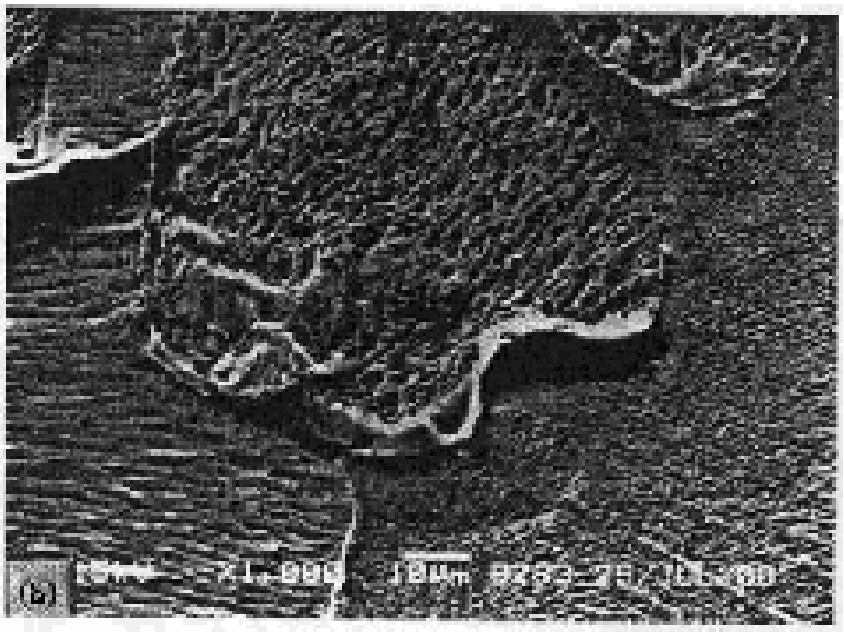

(a) 800 cycles

Figure 56: SEM image of SnAg solder under 1%Δε fatigue test, load on vertical direction [35]

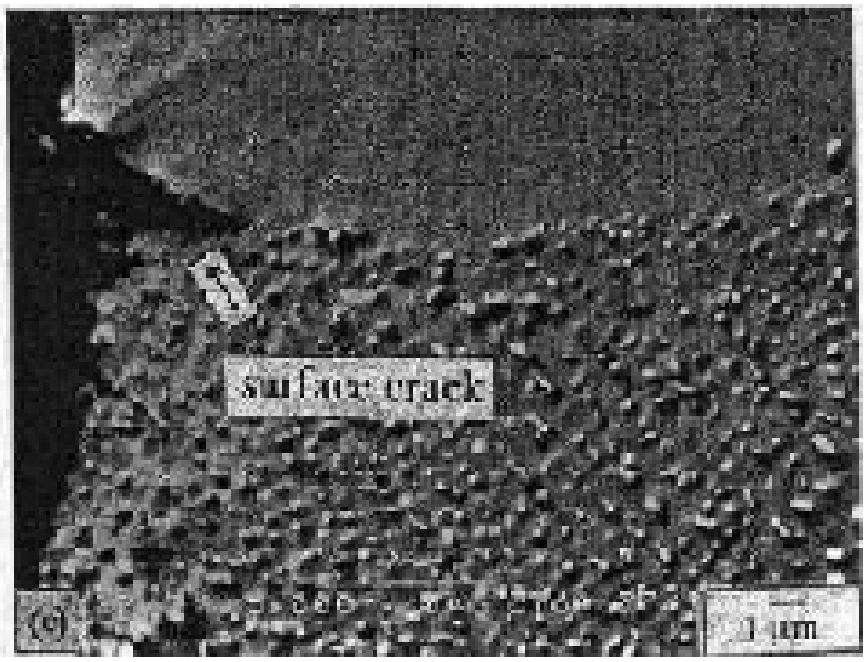

(b) Surface crack

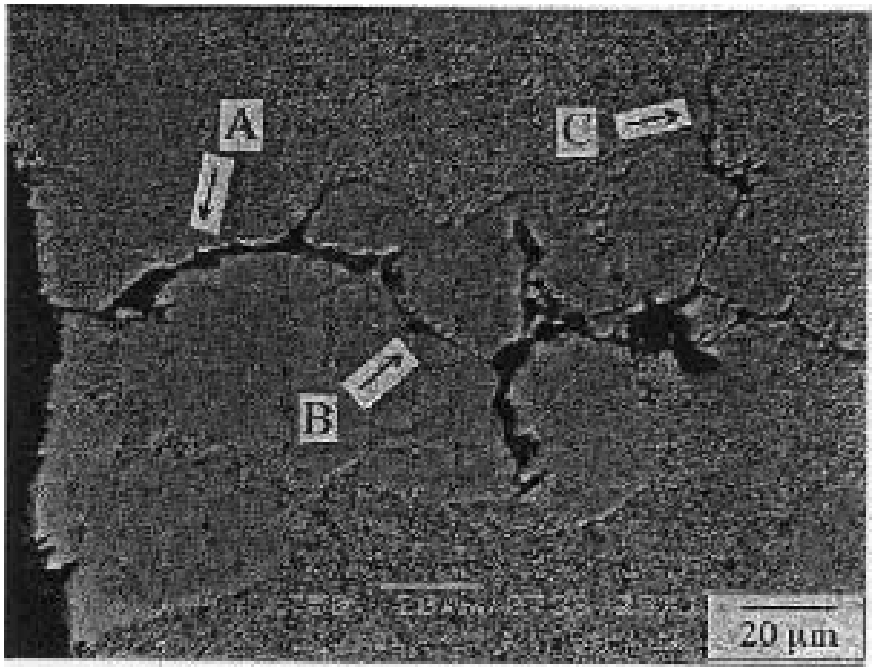

(c) Crack propagation A: integranular crack along Sn dendrite. B: transganular crack in and C: transganular crack along SnAg eutectic region

Figure 56: SEM image of SnAg solder under 1%Δε fatigue test, load on vertical direction [35] (continue)

The fracture mechanics based model partitions the fatigue life into two parts before the final failure: crack initiation and crack propagation. In electronic packaging research, a lot of researchers simply ignore the unstable crack propagation part and use the total solder joint size as the final crack length [83]. The crack initiation part is not well understood and sometimes ignored also. Some authors suggest using energy density as a criteria [84] [83] or fixing the ratio of crack initiation to total crack growth life [85]. The crack propagation part is the longest part of fatigue life and has been well studied. In high frequency, low stress ratio condition, the crack propagation is ΔJ controlled transgranularly with high crack growth resistance, while in low frequency, high stress ratio condition, it is C^* controlled intergranularly with low crack growth resistance [35][38][39]. Strain energy density is also widely used in crack propagation models [83][84]. The dye-penetration method study [86] showed that on crack growth under thermal cycle loading with BGA shaped test bed, the crack shape and propagation angle match well with dissipated creep energy densities from the FEM model.

A fatigue model using strain energy density can be seen below [83]:

$$N_a = N_0 + \frac{a}{da/dN} = C_1 \Delta W^{c_2} + \frac{a}{C_3 \Delta W^{c_4}} \quad \textbf{(30)}$$

In which, final crack length a is the total solder bump diameter. One common problem with this type of model is that when using the FEM model to obtain strain energy density, the result is often element size dependent due to the stress strain concentration of usual solder joint [83].

Damage Model

Damage can be considered as one internal variable in the constitutive laws, and its evolution is always coupled with other mechanical properties [60] [61] [87]-[89]. The definition of damage can be load drop due to the microcrack [60] [61], modulus drop [87] or entropy.

Test Setup

Mechanical fatigue test was performed on bulk solder material specimens. Bulk samples were chosen to avoid any interfacial effect in fatigue test and the pre-notched sample drawing is shown in Figure 57. The samples are 4mm wide, 0.9mm thick, with 1mm pre-notch on the each size. When in-plane shear fatigue load was applied, the shear deformation will be concentrated in the pre-notch portion of the sample.

Similar to the tensile test specimen, fatigue samples were cast in a three piece aluminum-stainless steel mold. The mold is shown in Figure 58. The mold with liquid solder will be quenched in pipe water of about 15°C. Quenched specimens were aged in room temperature for about 24 hours before test. At this stage, only as-cast specimens were used.

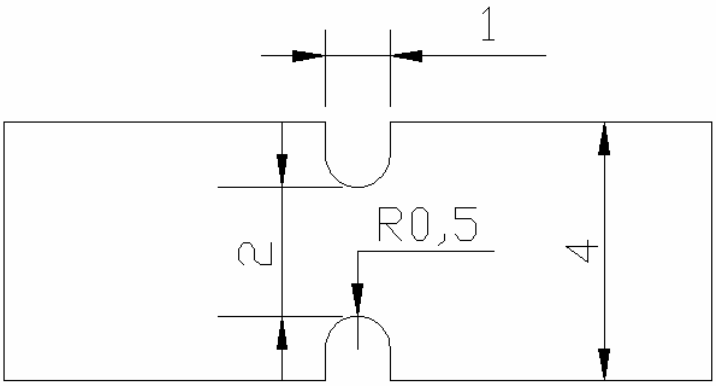

Figure 57: Mechanical drawing of fatigue test sample (unit mm)

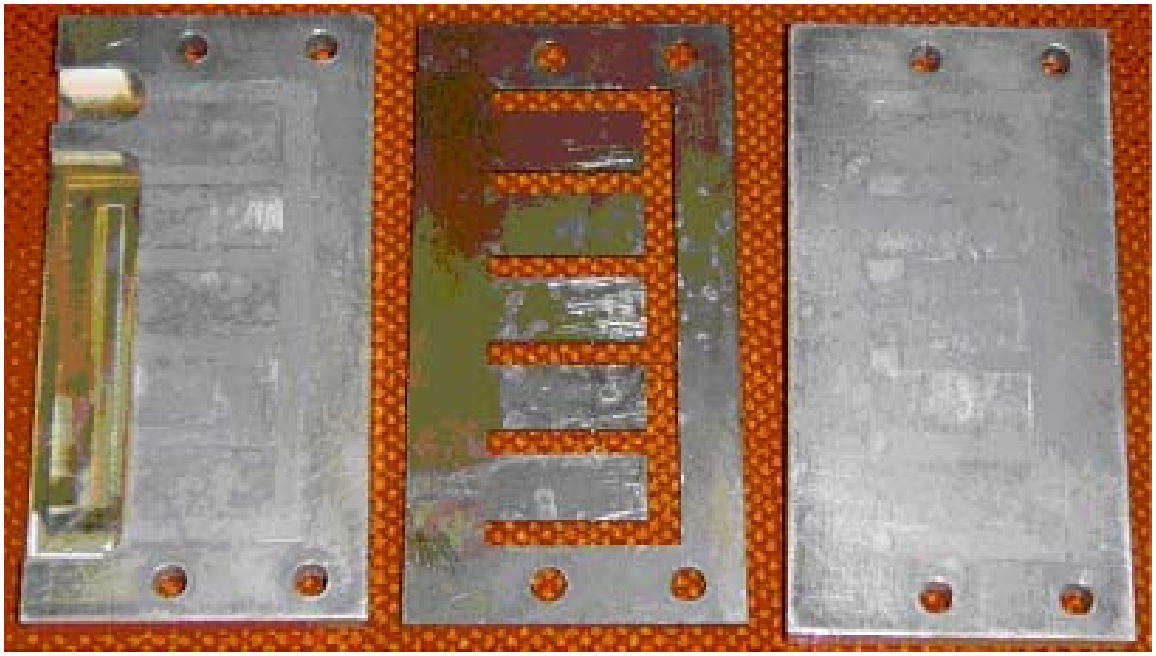

Figure 58: Fatigue specimen mold

A fixture, as seen in Figure 59, was made to clamp the sample in the EnduraTec® tester. The average shear strain applied on the sample was measured with a non-contact method. The ImageStrain software discussed in Appendix C was modified to fit fatigue condition, as shown in Figure 60, of which the software measured the displacement near the notch of the sample, as shown in Figure 60. The averaged-shear-strain γ was calculated from the relative displacements over notch width, as illustrated in Figure 61. The fatigue averaged-loading-strain-range $\Delta\gamma=2\gamma$.

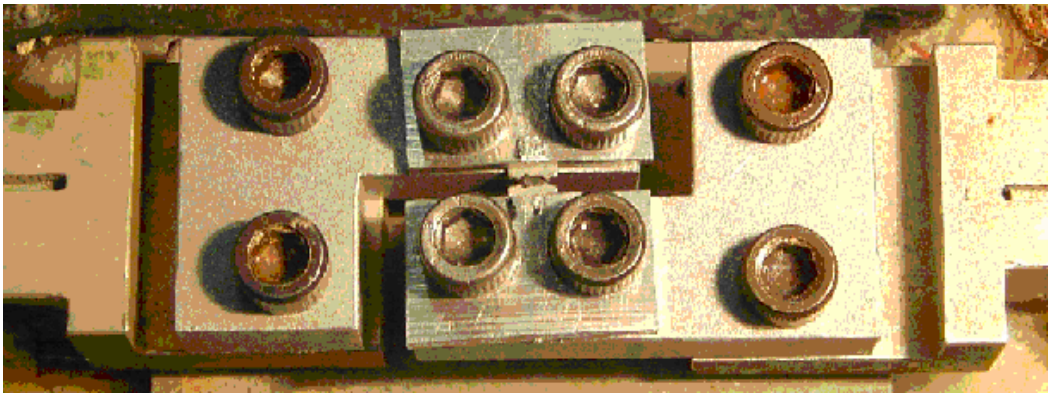

Figure 59: Fatigue loading fixture

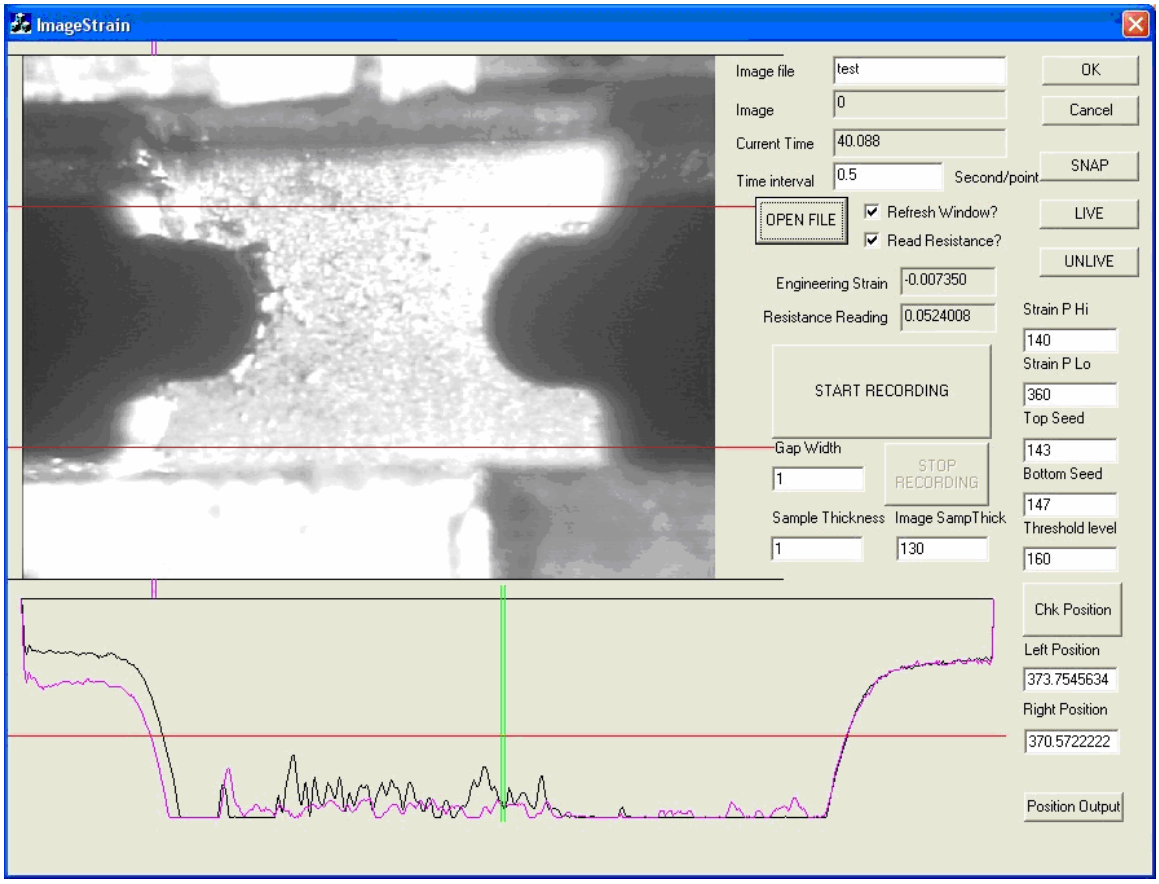

Figure 60: ImageStrain software for measurement of average shear strain of fatigue test

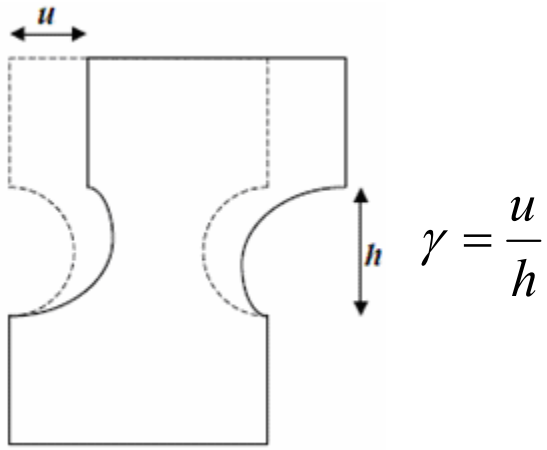

Figure 61: Definition of averaged shear strain for fatigue test

An electrical resistance measurement capability was also added to the test system. The sample's resistance was measured using the Keithley® 2001Digital Multi Meter (DMM) with Keithley® 1801 nano-volt Preamp. Using the four-point method of

resistance measurement, the accuracy is about 0.05mΩ at 200mΩ range. The accuracy can be expressed as ±(560 ppm of reading + 100 ppm of range). The measured resistance before loading is about 50mΩ, so the accuracy is ±(560 ppm x 0.05 + 100 ppm x 0.2) Ω = ±48e-6 Ω≅±0.05 mΩ. Offset compensation was used to eliminate the thermocouple effect and every reading was averaged for more than 5 power supply cycles to reduce the effect of noise.

Fatigue Test Result

Typical Fatigue Test Result

Fatigue tests were conducted at room temperatures with various loading levels and a typical fatigue test result is shown in Figure 62. In the figure, the load amplitude, the maximum and the minimum resistance reading are plotted. Resistance increase always follows significant load drop, usually significantly after the load drops to zero. The cause of the resistance change is either friction induced material loss, or non-conductive powder generated due to friction. The cracked or broken sample can still keep most of its conductivity if the broken parts kept contact. The solder joints in actual package would also behave in this manner [90].

With the observation above, load drop (half of the max mechanical load) will be used as the fatigue failure criterion in the following result.

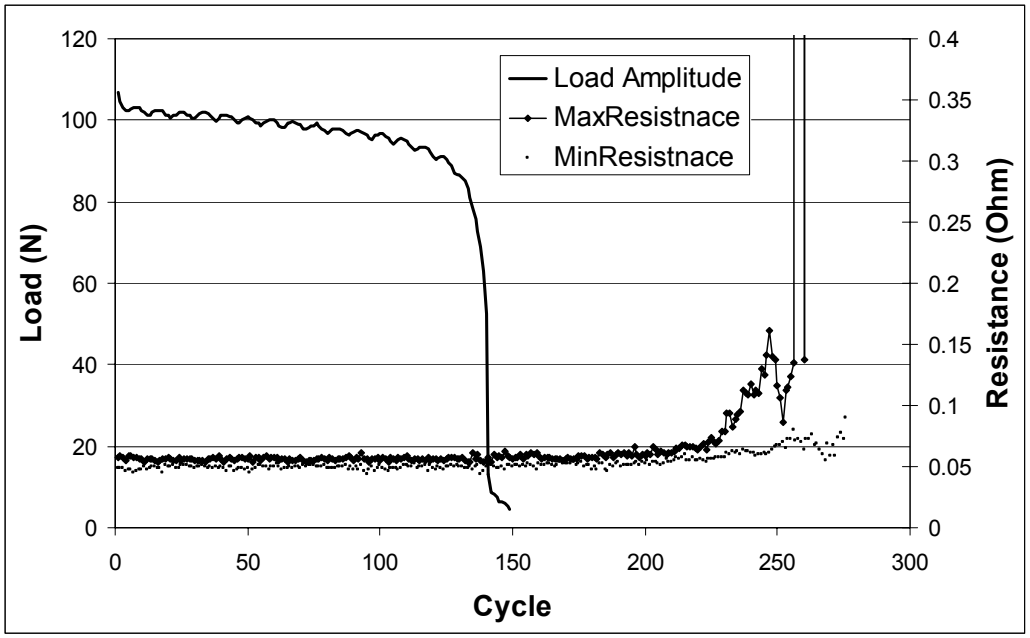

Figure 62: Typical fatigue test history of load amplitude and electrical resistance

Fatigue Test Result

At the current stage, the majority of fatigue tests were performed with the frequency of 0.1Hz (10Sec per cycle). The averaged-loading-strain-range vs. fatigue life is shown in Figure 63.

It can be seen that the La doped specimens have about 5 times longer life span than the un-doped specimens. This difference is not obvious at the high strain, low fatigue cycle conditions (200~300 cycles), but becomes obvious when fatigue cycles increase to >1000 cycles.

The most likely reason for La doping to prolong fatigue life may come from the grain / sub-grain boundaries of SnAg solder, which were found to have great importance in the fatigue behavior of SnAg solder materials. It was found that Sn3.5Ag has relatively low crack growth resistance compared to other solder alloys and the fatigue life depends on the resistance to fatigue crack initiation rather than to crack propagation [75]. Before the crack initiation, an Orientation Imaging study [32][37] confirmed that at a strain

concentrated region, thermomechanical fatigue causes heterogeneous refinement of the microstructure that accounts for the localized grain boundary sliding. Microscopy on cracked samples found that the cracks will propagate along grain / sub-grain boundaries [34]-[36]. After fatigue failure, small grains can be observed along the fracture surface [34]-[36] and near the crack path region [38][39].

As REs are surface active agents, La doping yields several benefits on solder fatigue through grain / sub-grain boundaries. First, La refinds the grain size, provids more boundaries for stress release locations to reduce the damage on each grain and prevent crack formation. In addition, the pinning effect from the La atoms helps to form stronger bonds at grain boundaries [42]. These better bonded grain boundaries will have higher resistance to damage and thus prevent cracks from initiating.

One should bear in mind that this discussion is based on bulk solder specimens. In solder joints, La doping has been proven to improve interface bonding, as discussed in Chapter 2. Combining these two effects together, the La doped solder joints can be expected to have much longer fatigue life.

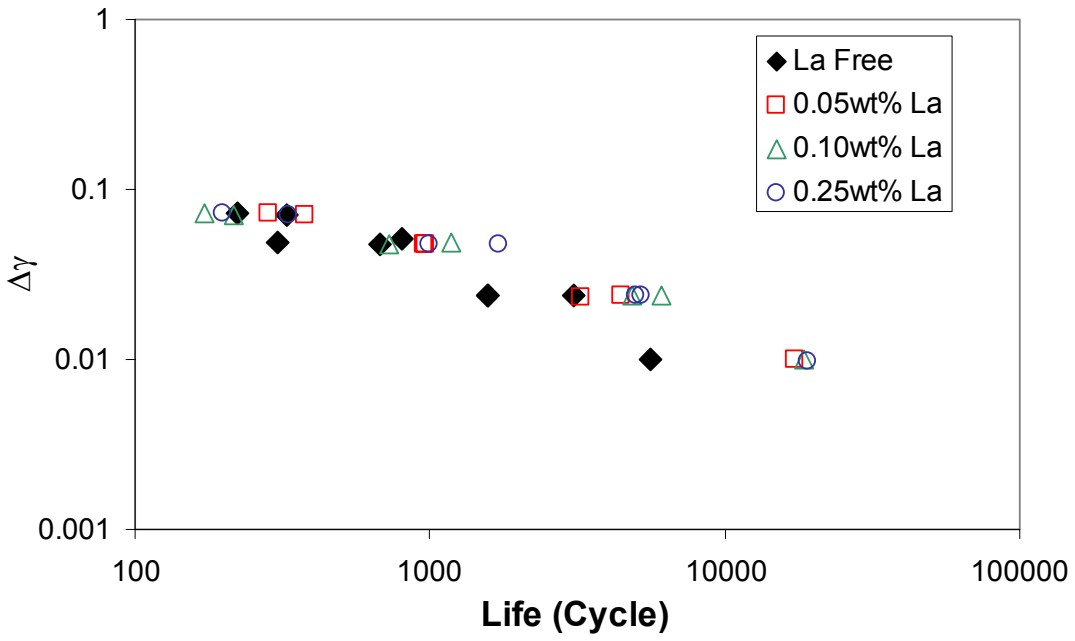

Figure 63: Fatigue test data of as-cast samples at room temperature, 0.1Hz

Fatigue Test Simulation with FEM model

Considering the complex geometry of the test specimens and loading conditions, a FEM model was built to simulate the fatigue test. The critical point with maximum deformation can be found from the structure and their deformation information will be used in fatigue model fitting.

A 3D FEM model was made with ANSYS to simulate the deformation of the fatigue samples. The model uses 8-Node element VISCO107 with large strain mode and transient ramp loading. The mesh of the model is shown in Figure 64. The displacement loading is applied by fixing the bottom of the model and setting a uniform displacement on the top. Although Anand model has some draw backs on modeling fatigue behaviors due to short of back stress support, but it is used here for the reason of simplification. The material constants for the Anand model come from the least square fitting, as shown in Chapter 6.

One of the cases will be shown here as a typical result. This specimen is loaded at room temperature with frequency of 0.01Hz. 10 cycles were simulated in this FEM model, and several contour plots of the FEM result are shown in Figure 65. These images are at the last time step, with max displacement at top to be 0.093mm. It can be seen in Figure 65 (a) that the XY shear deformation is uniformly distributed near the center of the specimen, although the most severe deformation happens at the inner corner of the notch. During fatigue shear loading, these corners were repeated with tensile and compression loading.

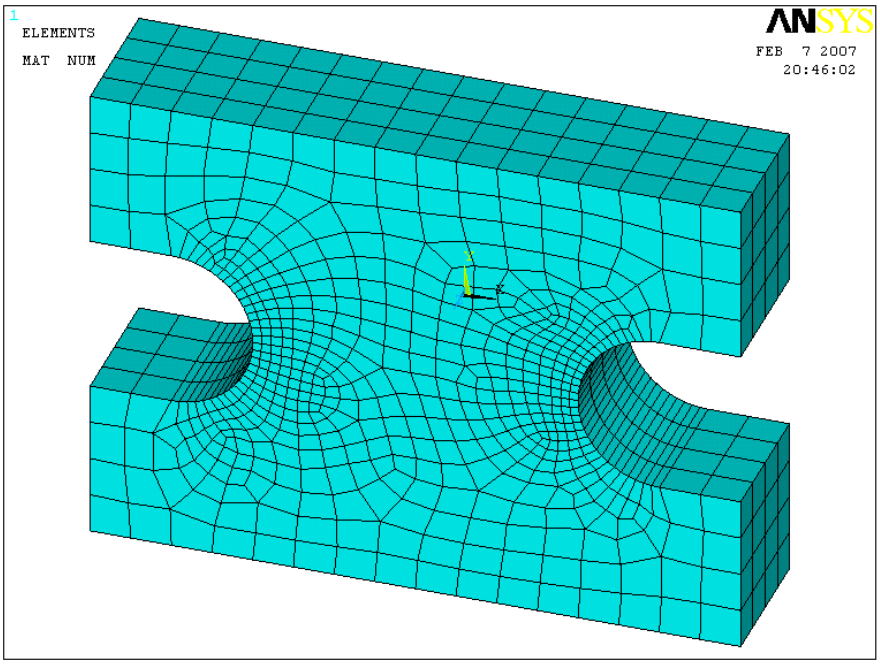

Figure 64: 3D FEM model mesh of fatigue test sample model

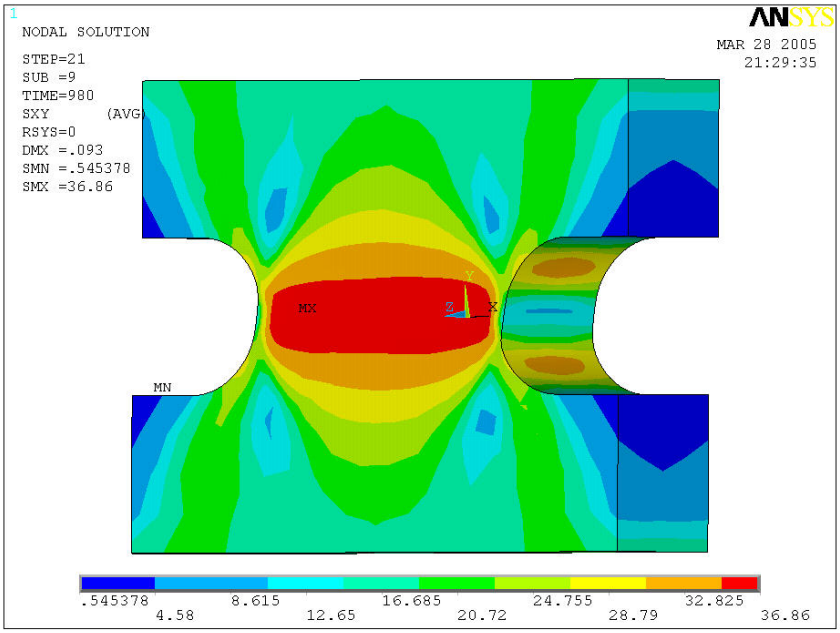

(a) XY shear stress

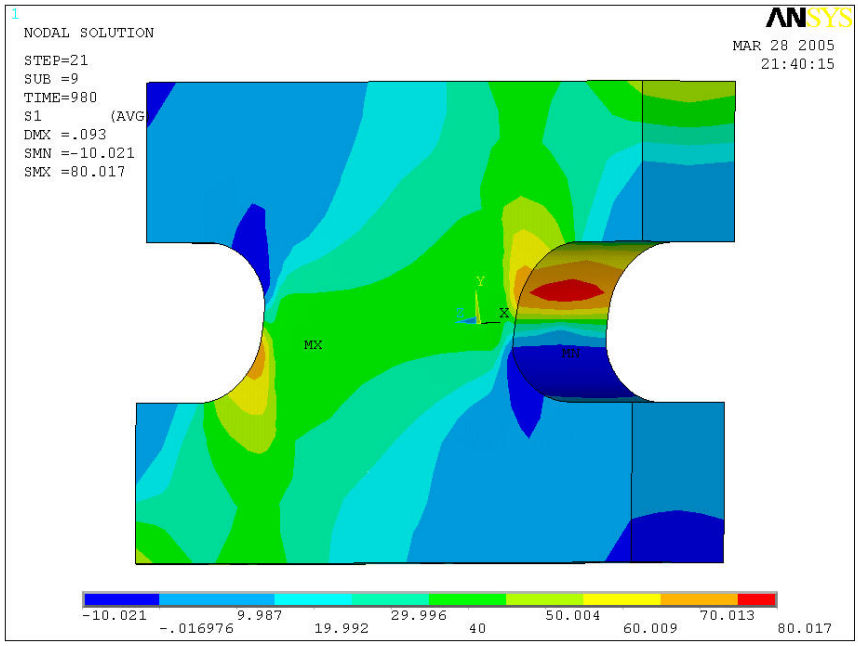

(b) 1st principal stress

Figure 65: Contour plot of FEM result simulating fatigue test

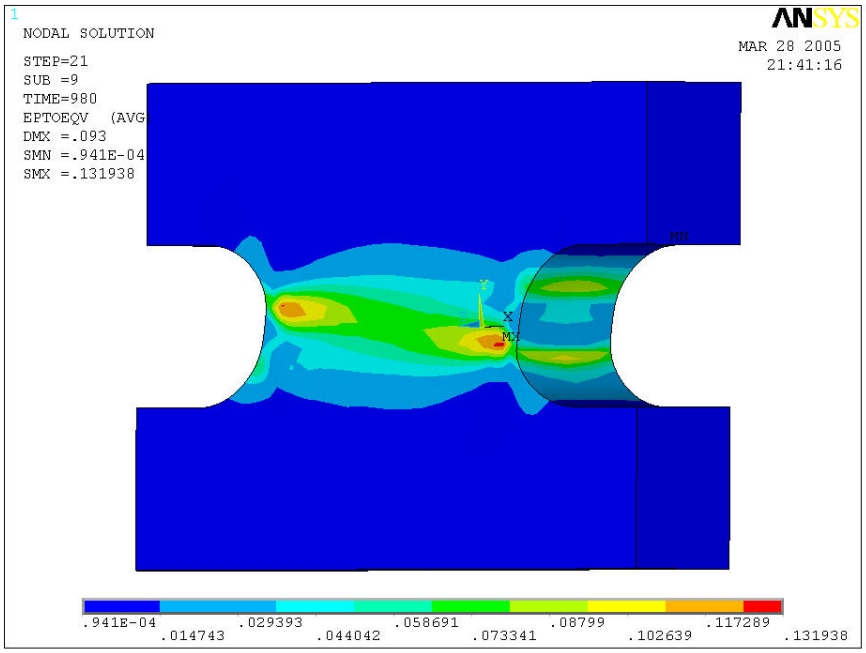

(c) Total equivalent strain

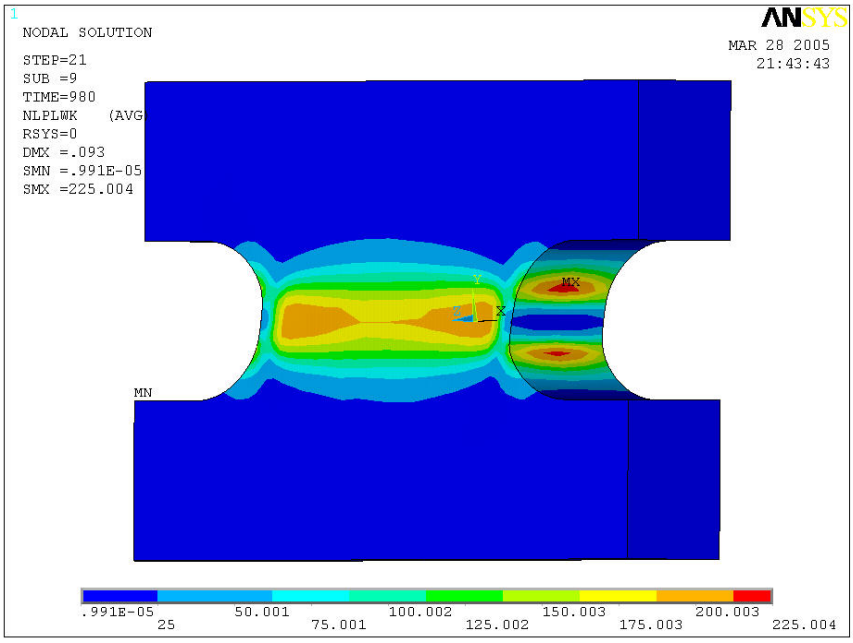

(d) Plastic work

Figure 65: Contour plot of FEM result simulating fatigue test (continue)

FEM Model Validation

With both the fatigue test and the FEM model ready, it is necessary to validate the relationship of the FEM model with the fatigue test, which can be done from several aspects. First, the deformation field was validated with a monotonic shear loading test. Second, cyclic loading was applied to the FEM model to compare with the fatigue test results.

Deformation Field Validation

To validate the deformation field, a monotonic loading test was conducted with 0.1mm/s constant crosshead movement speed loading till the specimen was broken. The averaged shear strain was recorded with ImageStrain software. The test was also video recorded and captured to as digital image with 0.25 Second intervals.

An image correlation method was used on some samples to measure the displacement fields. By comparing two images and correlating pixel movement, the image correlation algorithm can solve in-plane displacement vector fields. This work used winDac® software to complete the image correlation.

Figure 66 shows the typical displacement field. In the figure, displacement vectors are marked with yellow short lines, and one of the two images was shown in the figure.

A least square error data fitting method was used to find the closest deformation fields between the experiments with the FEM loading steps, the result is shown in Figure 67. Each data point indicates one correlated loading step. The correlation points were fit into straight lines and the factor is 1 from the figure. Because the width of the pre-notch is 1mm, the averaged shear strain γ has the same number with displacement loading. This correlation result shows that the shear deformation is concentrated in the notched part, as the specimen design expected.

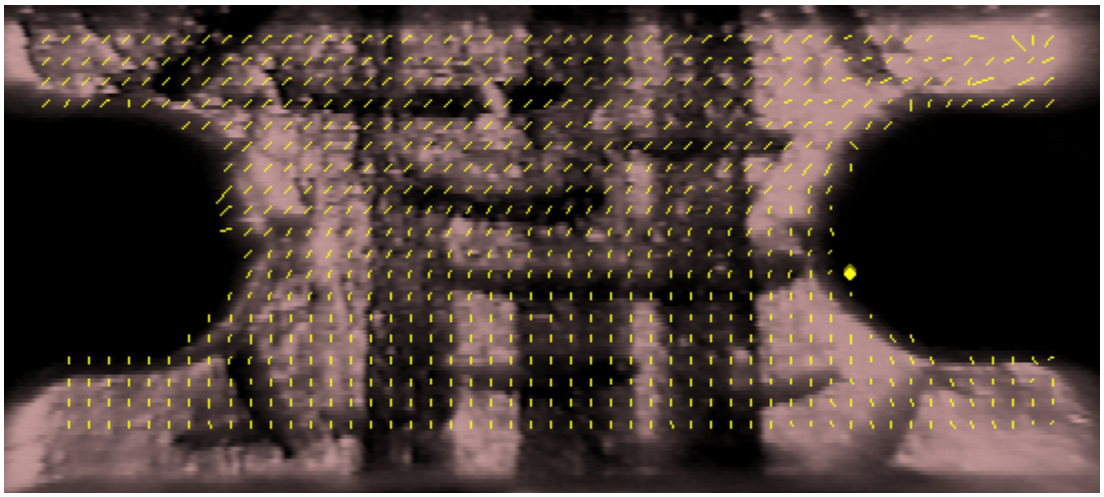

Figure 66: Typical displacement field of fatigue test sample from image correlation method

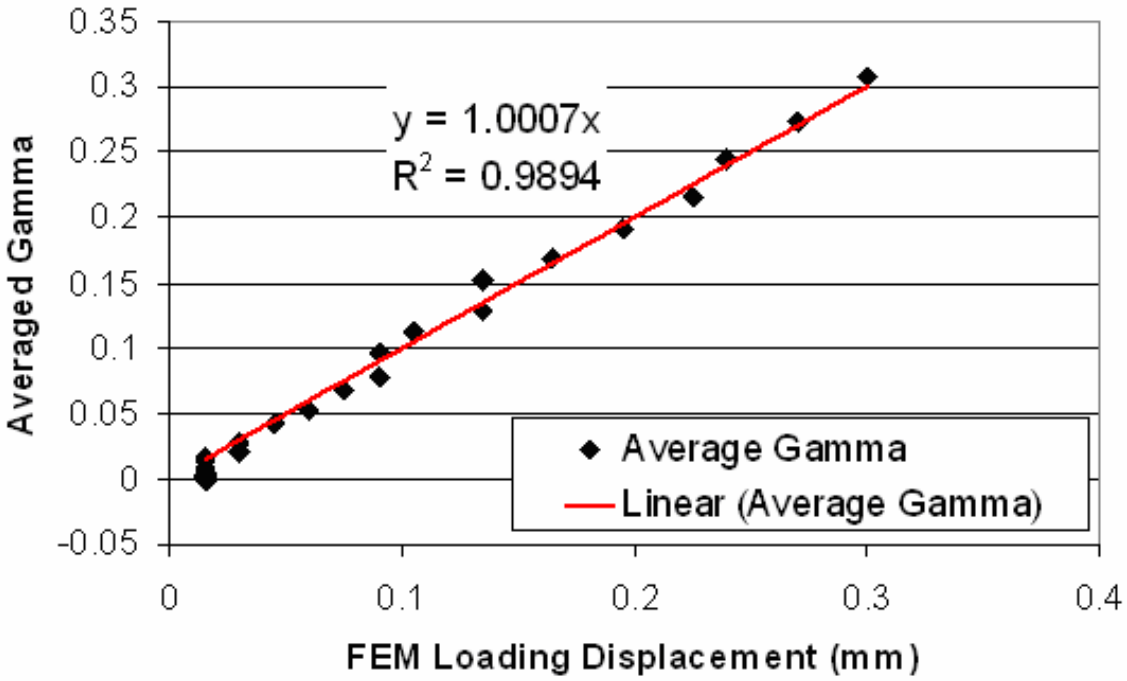

Figure 67: Correlation displacement field of FEM model with test

Validation of Reaction Force

Fatigue tests were simulated with FEM model. The average strain loading and force reading from experiment are compared with displacement loading and reaction force in the FEM model.

A typical result is shown in Figure 68 and Figure 69. Figure 68 shows the comparison of measured γ with the FEM displacement loading. In Figure 69, the reaction force of the FEM model is compared with loading force measured from the test. A very close match was found.

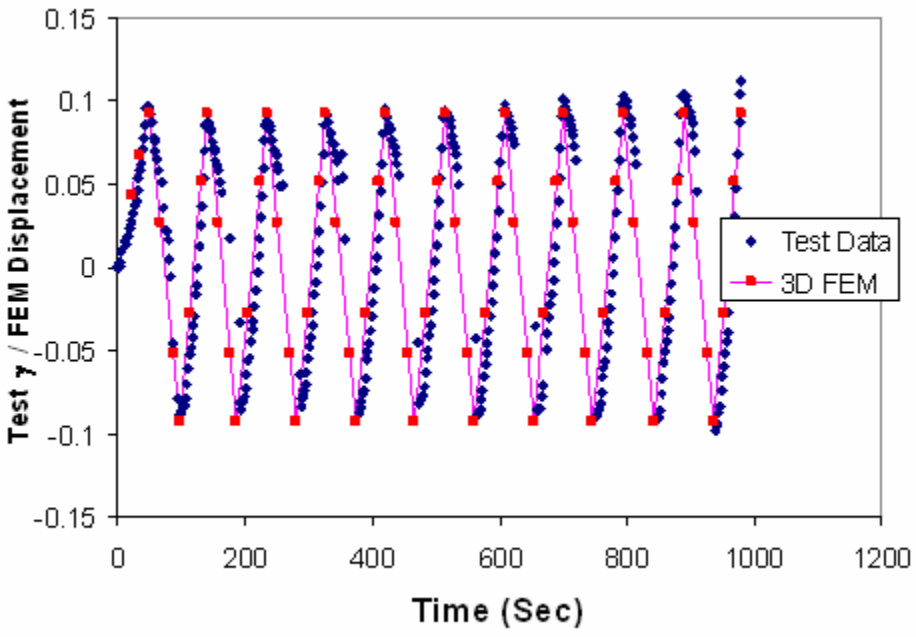

Figure 68: Comparison of test loading averaged shear strain with FEM displacement loading

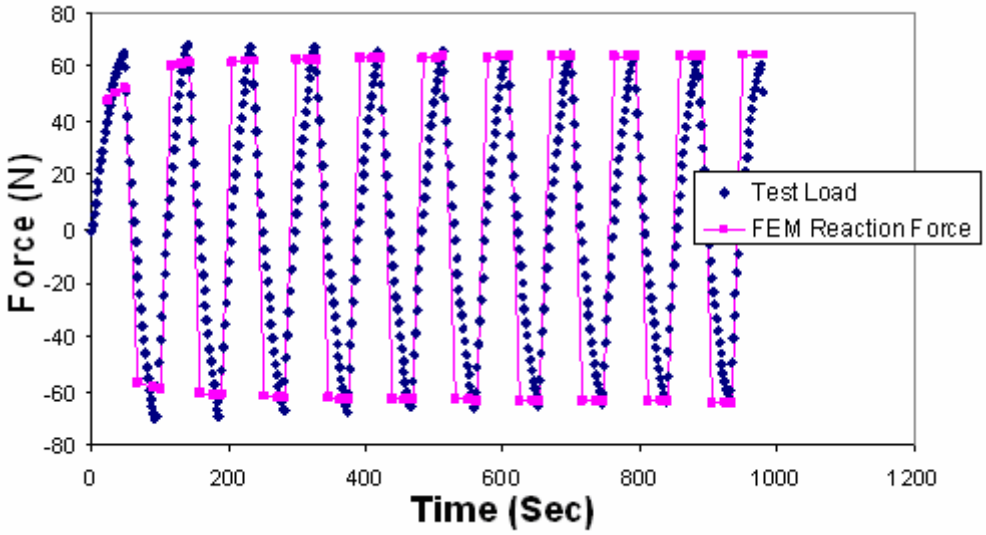

Figure 69: Comparison of test loading with FEM reaction force

After searching the result, the location of the maximum deformation is located in node 1152, which is at the corner of the notch, as shown in Figure 70(a). This result can be confirmed by the test results which show that the cracks always start from the vicinity, as shown in Figure 70 (b).

The 1st principle elastic strain, plastic strain, Von Mises stress and plastic work density of node 1152 are plotted in Figure 71. These local stress/strain deformation properties will be used in the fatigue model extractions.

From the history output of either the macroscopic result in Figure 69, it can be seen that the digital fatigue test with FEM model can reach a relatively steady state after about 3 cycles. For this reason, only 3 cycles will be used for the fatigue model study.

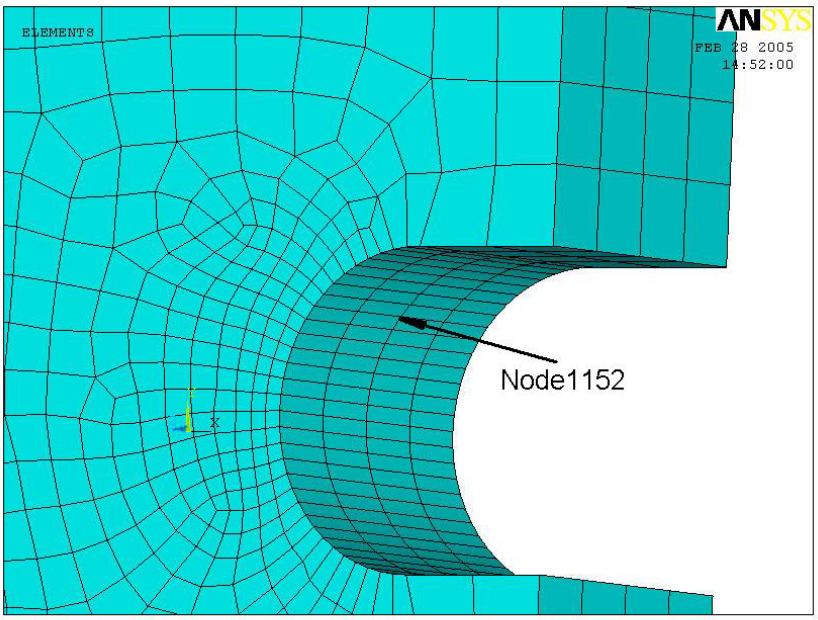

(A) node 1152 in FEM model

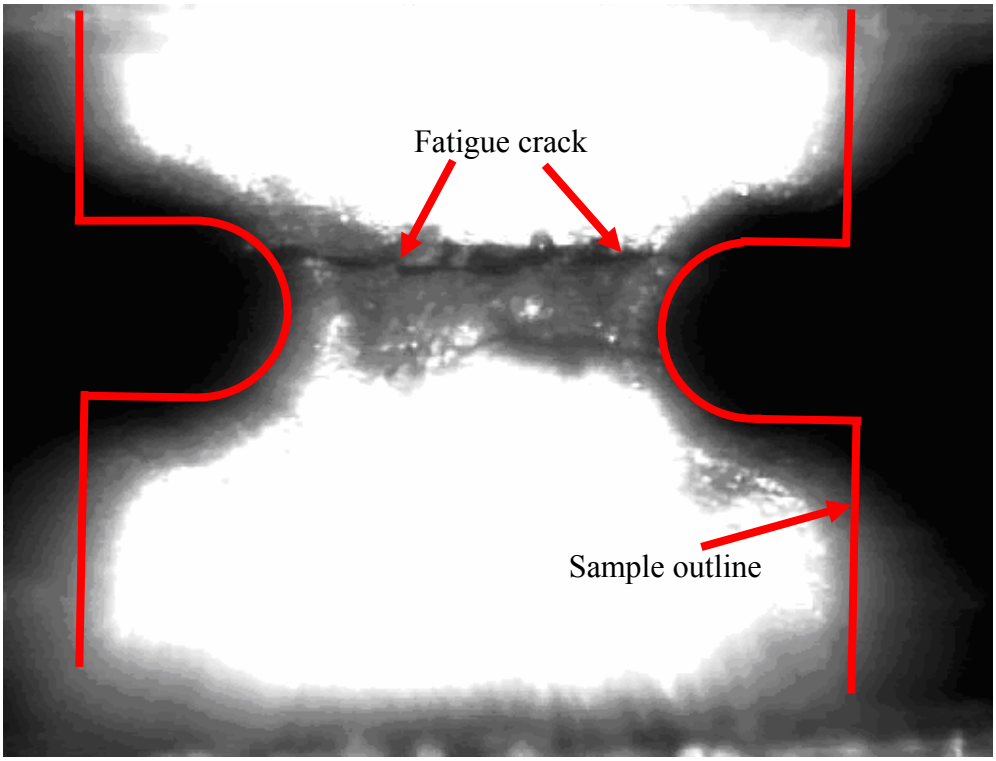

(b) Failed sample

Figure 70: Location of the maximum deformation of fatigue sample

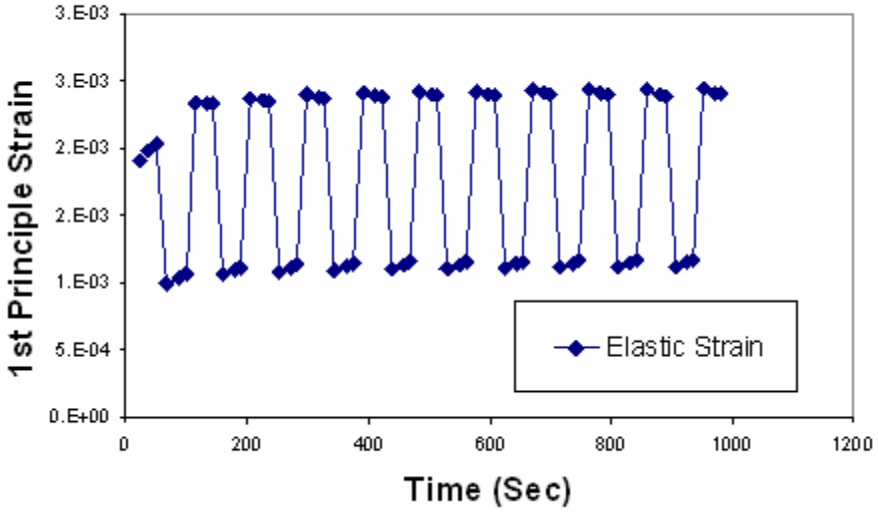

(a) 1st principal elastic strain

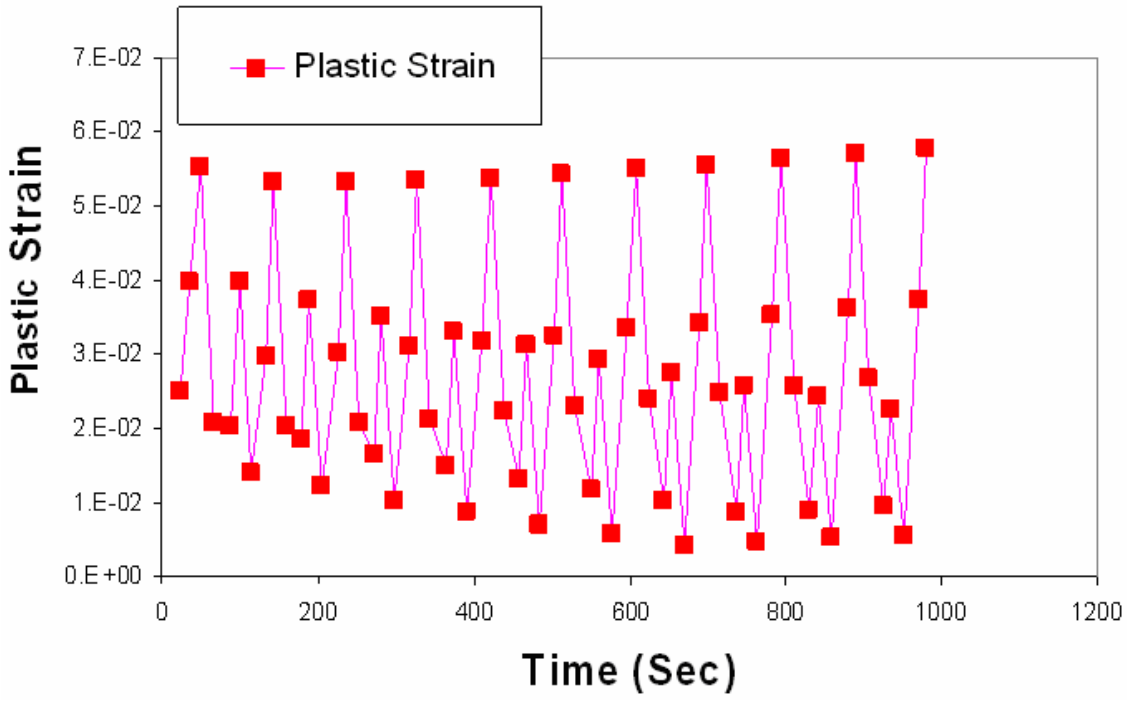

(b) 1st principal plastic strain

Figure 71: Deformation history at the notch corner from FEM fatigue simulation

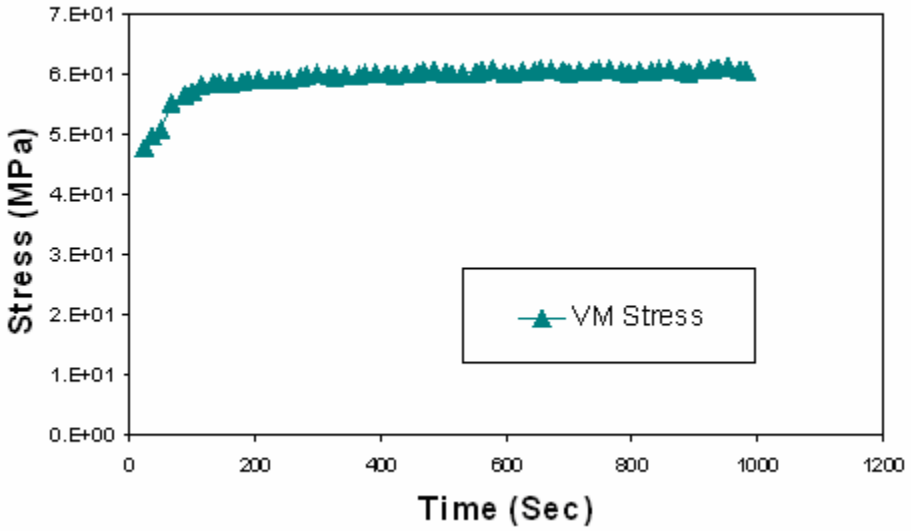

(c) Von Mises stress

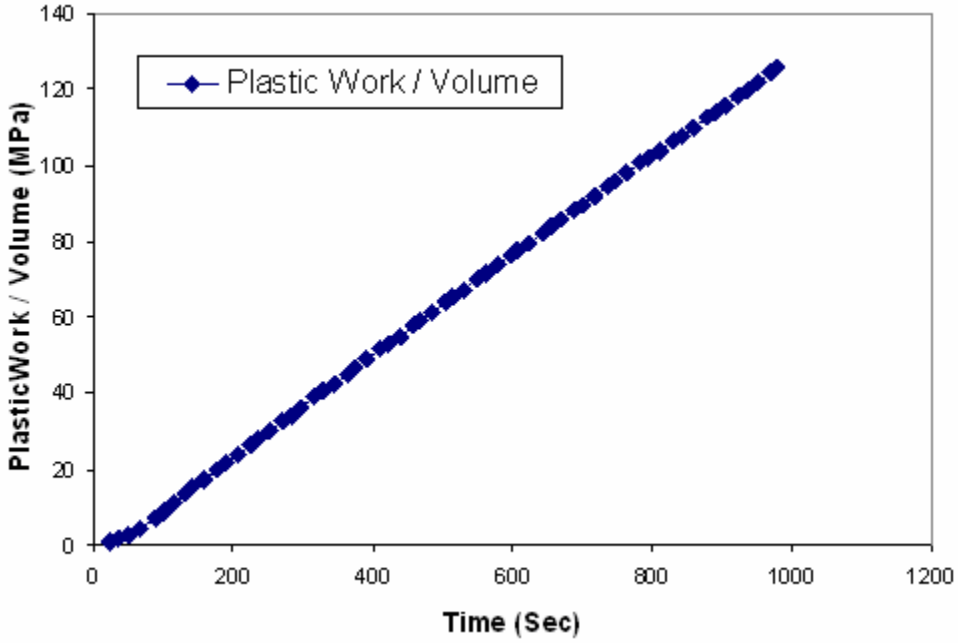

(d) Plastic work density

Figure 71: Deformation history at the notch corner from FEM fatigue simulation (continue)

Fatigue Model Extraction

The Coffin-Mansion model was used to predict the fatigue life of La doped SnAg solder. The metrics used are the plastic strain range per cycle and plastic work per cycle, all of which are from the FEM model at the critical point. The fatigue life used comes from the power law equation fitted from experimental measurements, which are listed below in equation (31)(32). The linear log-log curve fitting plot and final constants in the model are shown in Figure 72 and Table 9, respectively. The fatigue exponents of the un-doped solder are close to available models [78] [81].

$$\Delta\varepsilon_c = \theta_1 \left(N_f\right)^{-\alpha_1} \quad \textbf{(31)}$$

$$\Delta W_c = \theta_2 \left(N_f\right)^{-\alpha_2} \quad \textbf{(32)}$$

Table 9: Fatigue models constants

	$\Delta\varepsilon_c = \theta_1 \left(N_f\right)^{-\alpha_1}$		$\Delta W_c = \theta_2 \left(N_f\right)^{-\alpha_2}$	
	α_1	θ_1	α_2	θ_2
No La	0.96	3.9	1.16	4.1E3
0.05% La	0.88	3.2	0.91	1.1E3
0.10% La	0.85	2.6	1.05	3.5E3
0.25% La	0.85	2.4	1.08	4.1E3

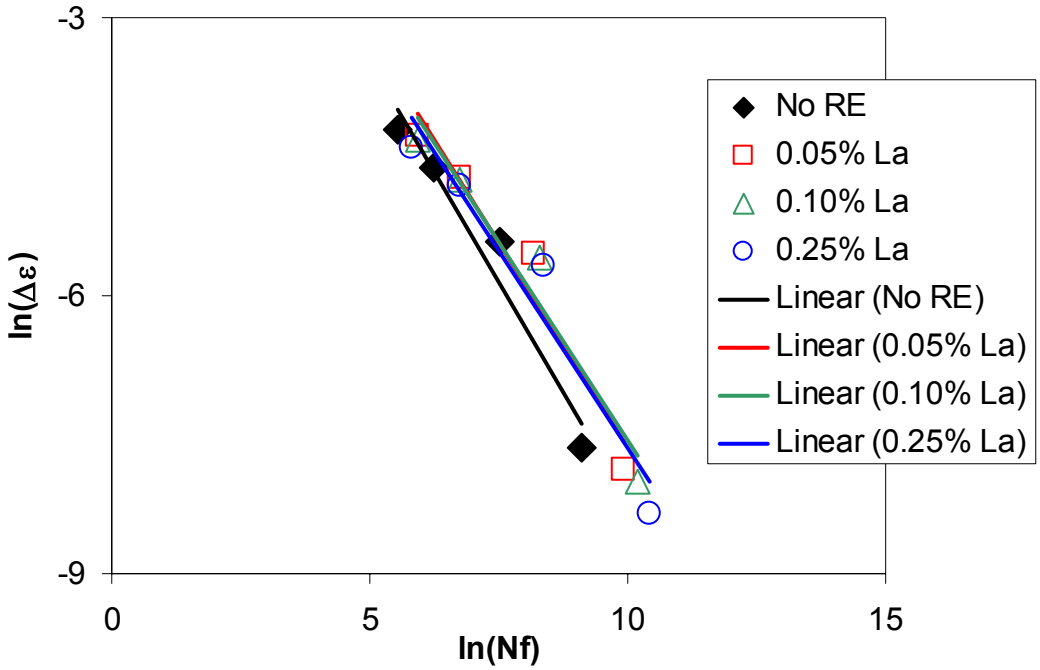

(a) Inelastic strain based

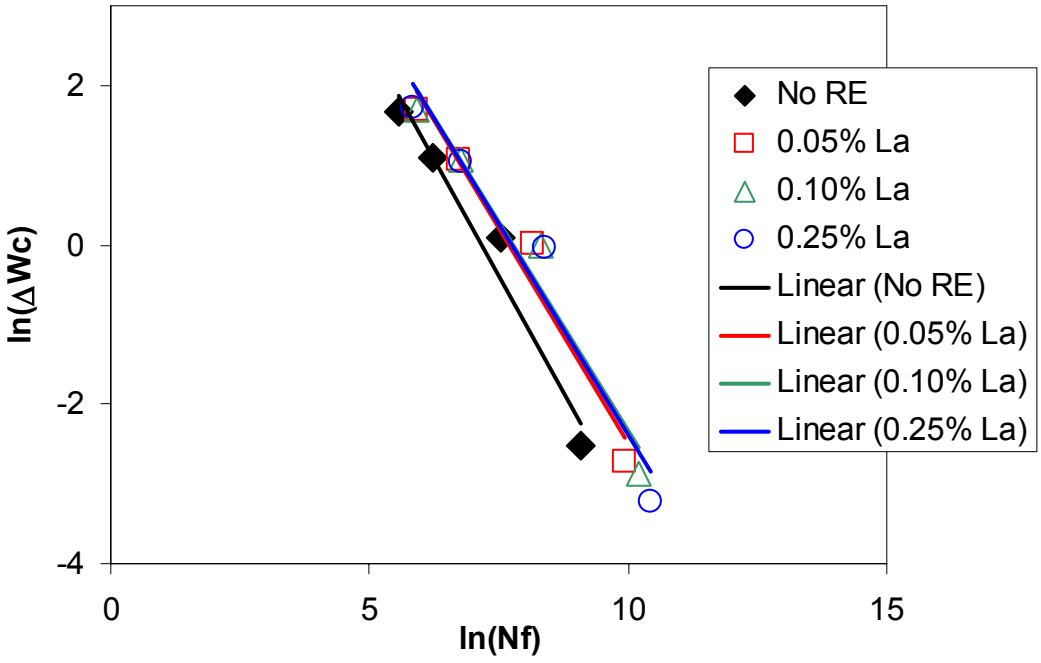

(b) Energy based

Figure 72: Curve fitting of the Coffin-Mansion type fatigue models

Microstructure Evolution during Fatigue

Several samples were applied with shear fatigue load at averaged shear strain amplitude of 0.007 level and loading stopped before breakage. An optical microscope and a SEM were used to study both the specimens' natural surfaces and the polished cross sections. The images can be seen in Figure 73 and Figure 74 for unpolished sample surfaces and in Figure 75 for polished cross sections. For all these images, the shear loading directions are vertical, as illustrated in Figure 73.

After fatigue loading, the surface of the specimen will become rough along the middle of the sample where fatigue strain was concentrated, as illustrated in Figure 73. In this rough area, groups of parallel lines can be found, as seen in Figure 74. Sometimes groups of crossed lines can be seen. The directions of the parallel lines do not necessarily have relations with the loading direction.

On the other hand, study on the polished cross sections along the sample middle line found highly deformed Sn dendrites and sometimes parallel lines of merged dendrites, as seen in Figure 75. These long dendrite directions tend to depend on the initial microstructure orientation but not on the loading direction. Similar observations were made by Xiao, *et al*. [31] on SnAgCu solder.

When considering the observations of parallel lines on un-polished surface and the parallel merged dendrite cluster on polished cross sections, it is a reasonable guess that these two observations come from the same physical phenomenon. The roughened surface could be the direct result of high concentration of inelastic deformation along Sn dendrite arrays near the surface. This high inelastic deformation will accumulate damage during fatigue loading and eventually lead to crack. In this study, this phenomenon can only be observed on fatigue samples but its effect on fatigue life needs further study.

A quantitative study was performed on the Sn dendrite of fatigued samples. The Sn dendrite volume fractions along the notch line are shown in Figure 76 and the dendrite sizes are shown in Figure 77. It is found that the volume fraction of the dendrite is not

affected by fatigue loading. No obvious trend can be seen from the dendrite size and no effect can be found by La doping.

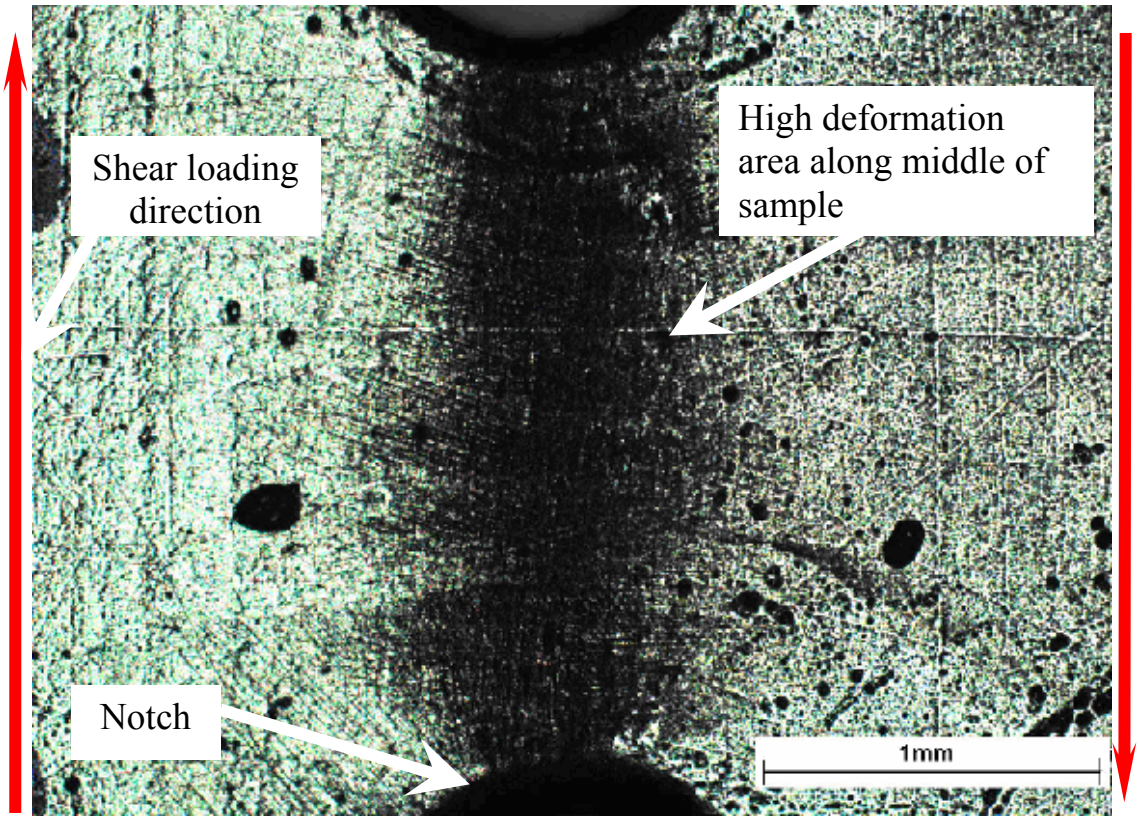

Figure 73: Optical image of SnAg solder after 2000cycles. Red arrows show the shear loading direction. Sample surface roughen at high deformed area at the middle of the sample.

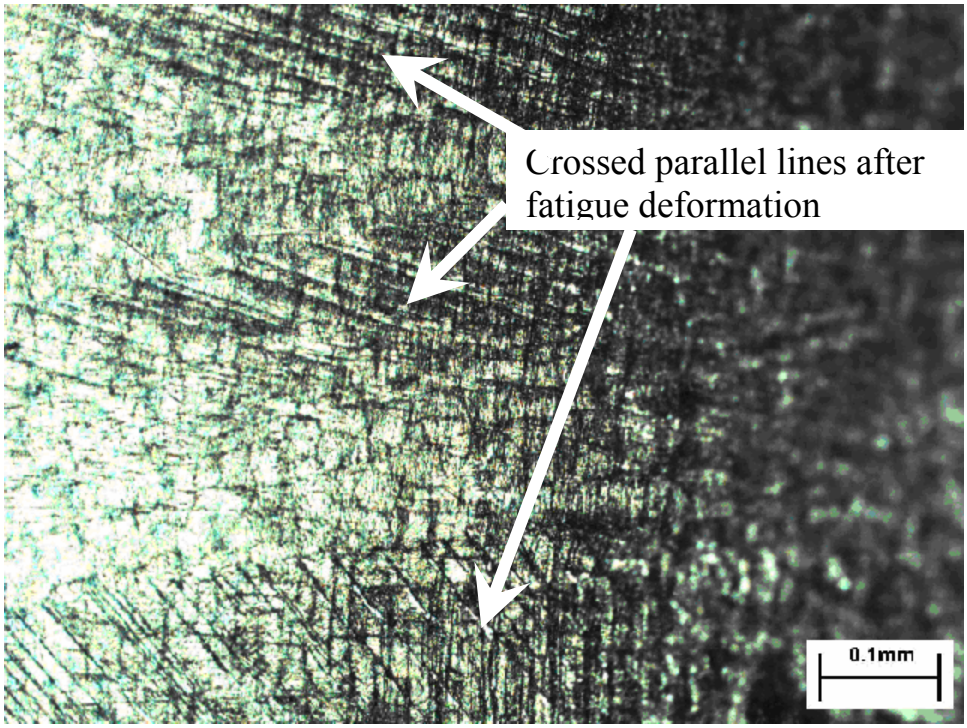

(a) La free, 2000 cycle, optical image, unpolished surface

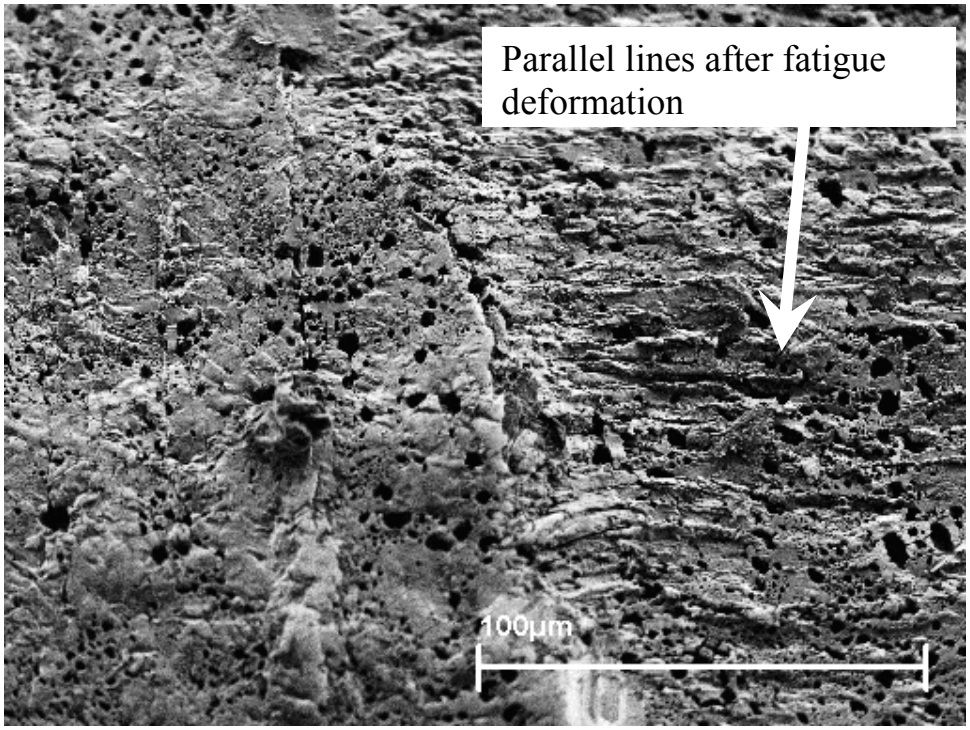

(b) 25wt% La, 3000 cycle, SEM. unpolished surface

Figure 74: High magnification images of roghen sample natural surface after fatigue. Groups of parallels lines can be found, indicating high deformation along Sn dendrite clusters.

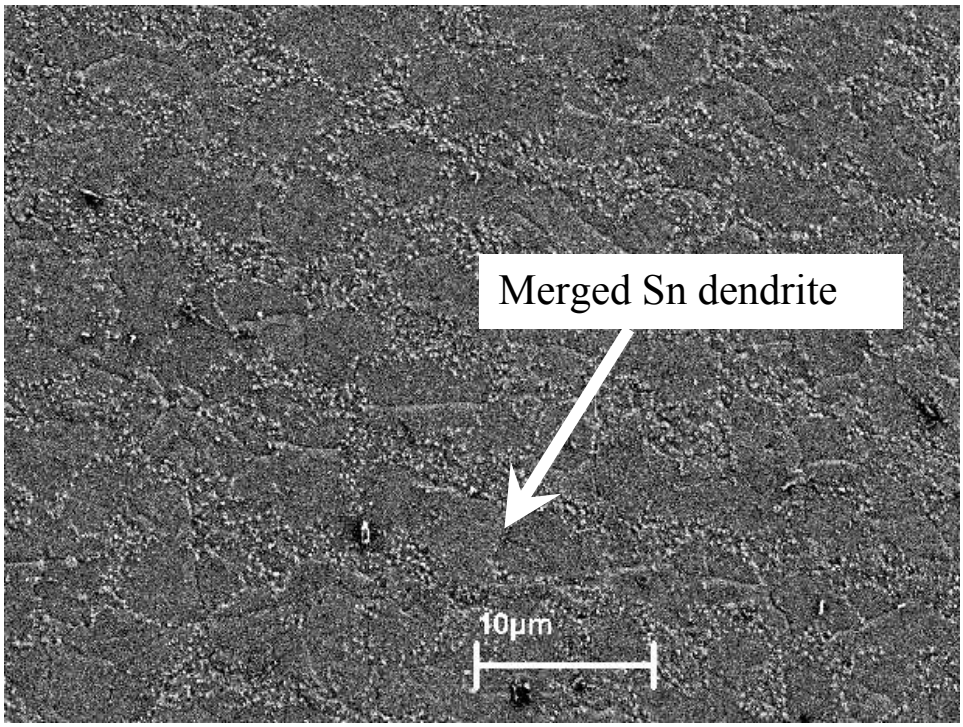

(a) No La, 2000 cycle. SEM polished

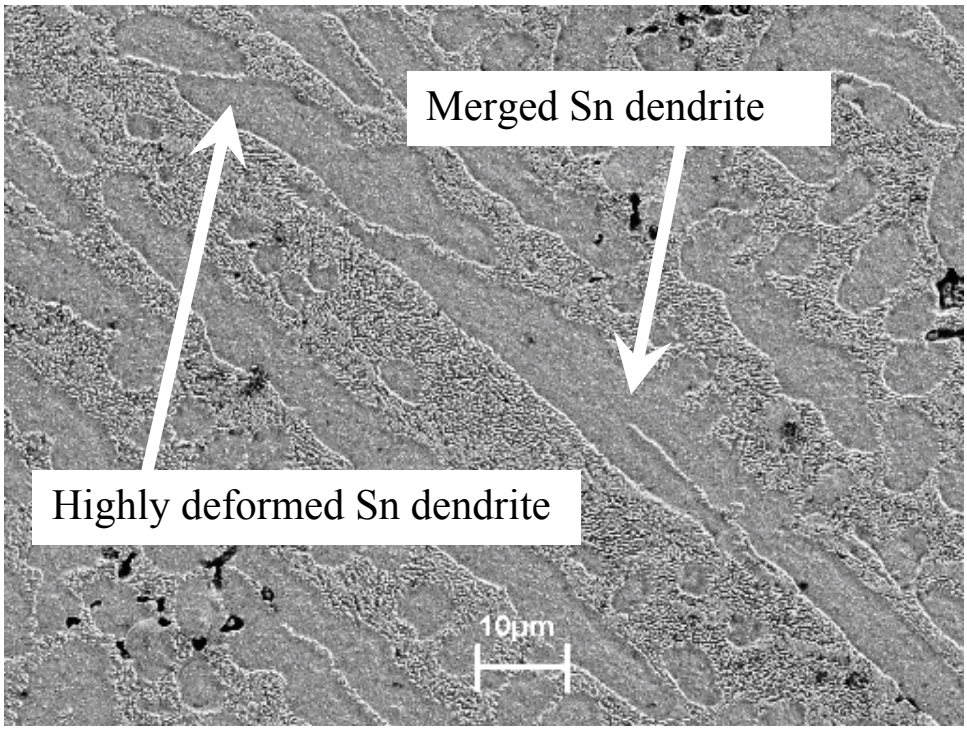

(b) 25wt% La, 1000 cycle, SEM, polished

Figure 75: SEM image of polished cross section of fatigue specimens at high deformation area. Sn dendrites were found to be highly deformed and sometimes merged after fatigue loading.

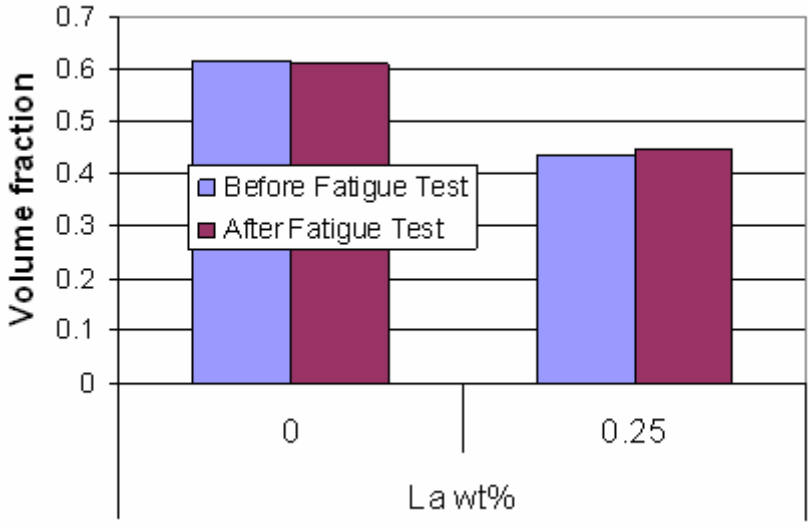

Figure 76: Dendrite volume fraction before and after fatigue test

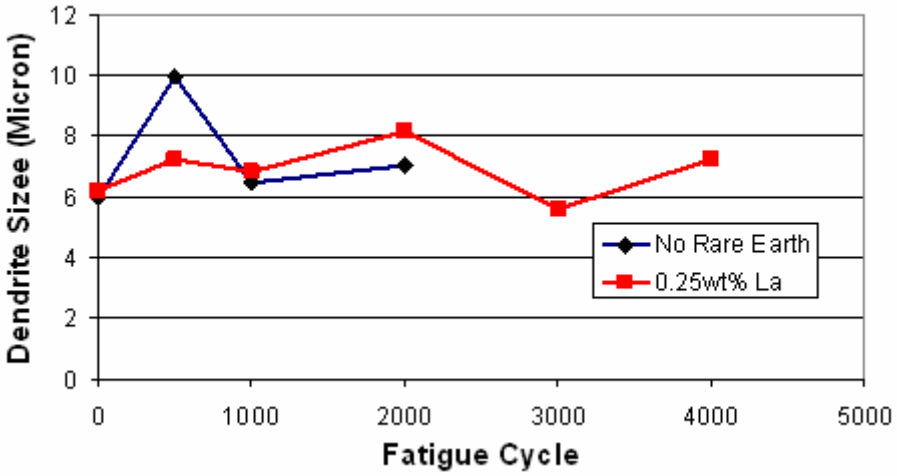

Figure 77: Dendrite size trend with fatigue loading

Summary

In this chapter, a fatigue study was performed on La doped solder material. La doping was found to be able to increase the fatigue life by approximately 5 times.

The deformation fields of the fatigue samples were simulated with a 3D FEM model. After validation, the inelastic strain and inelastic work at concentration point was used to fit fatigue model.

After fatigue loading, the Sn dendrites were found to merge along cluster directions and roughen the surface.

CHAPTER 9

CONCLUSION AND RECOMMENDATONS

This study is a systematic research focused on establishing the quantitative effects of La doping on the microstructure and mechanical behavior of the 96.5Sn3.5Ag alloy. The benefits of La doping in the lead-free solder are quantified, and can be predicted within the test range. The conclusions made from this study are briefly outlined below.

La doped samples have much smaller grain size than that of the un-doped (~ 0.3mm vs. >1.0mm). The optimal La doping to minimize grain size was found to be around 0.05%.

Similar to the un-doped solder alloys, the grains of La doped alloys do not coarsen with thermal aging, even though they are much smaller in size.

The Ag_3Sn particle size in the solder alloy was reduced with La doping, which can also reduce the particle coarsening rate. Using the power law particle coarsening model, it was found that La doping reduces the coarsening activation energy and reduces the pre-exponent constant drastically.

Inter-particle spacing remains relatively unaffected by the La doping amount. Because of stoichiometry, decreasing Ag_3Sn particle size increases the total number of Ag_3Sn particles. Therefore, a higher La doping level leads to a higher volume fraction of the eutectic region and a lower volume fraction of the Sn dendrite in the solder alloy.

La doping can increase the creep resistance of SnAg solder by about 15%. Within the range of 0.25% La doping, high doping percentage leads to high creep resistance.

La doping does not change the aging behavior of the solder material, and the strengthening effect of La doping still exists after thermal aging.

A particle size dependent Anand model was proposed and utilized on La doped solder alloys.

A hierarchal constitutive model was developed that considers the microstructure of SnAg solder as a composite material having two length scales: at the smaller scale, the SnAg eutectic region is first treated as a two-phase composite with the Ag_3Sn particles dispersed in Sn matrix; and at the larger length scale, the solder alloy is treated as a two-phase composite with the Sn dendrite embedded in SnAg eutectic matrix.

In the fatigue study, La doping was found to increase the fatigue life of bulk sample by approximately 5 times.

Recommendations for Future Work

Before RE doped lead-free solder can be used in industry, several more issues, including cost related issues and processing related issues need to be solved. One of the cost issues is the selection of RE element. With similar performance, the cost could be minimized with mixed RE elements because it is expensive to separate them. Systematic study comparing doping RE elements component was needed in the future for all the material properties of sold material, including wetting ability, microstructure and mechanical behaviors.

The biggest issues during the processing are manufacturing and reflow of solder powder and solder paste. The RE doped solder manufacturing process require high temperature vacuum or inert gas environments to mix the material and to atomize the solder into powder. The challenge on the reflow process is to ensure enough RE element remain in the bulk material afterwards. The control of the distribution of RE element in the solder material is the key to solving these problems. The RE element should be distributed on the material's surface and in bulk material depending on the request for the wetting ability and mechanical property.

The knowledge of the RE element distribution will also contribute to better understanding on RE doped material behavior. In this research, a systematic study quantitatively established the dependence of microstructure and mechanical behavior of

lead-free solder material to La doping percentage. Another approach to study the La doping effect is to study the effect of La atoms dispersed in material, as both the microstructure study and the creep test found that the La doping effect was applied through the dispersed La atoms. To more clearly understand the effect of La on solder material, two separate relations between La doping with solder properties are desired instead of building a direct relation between them: La doping vs. La dispersion and La dispersed atoms vs. solder properties. To build these two relations, atom level microstructure study is needed to identify and quantitatively study La atoms dispersed in bulk materials.

APPENDIX A

SUMMARIZED DATA OF Sn CYSTAL

The crystal structure of Sn is tetragonal with X=Y= 5.8318Å and Z= 3.1819Å [91]. In Figure 78, the crystal structure is rendered with Visual Molecular Dynamics software (VMD) [92]. The atoms are shown as yellow spheres, and the bonds between them are shown with dynamic bound method with cut off distance of 2.3 Å.

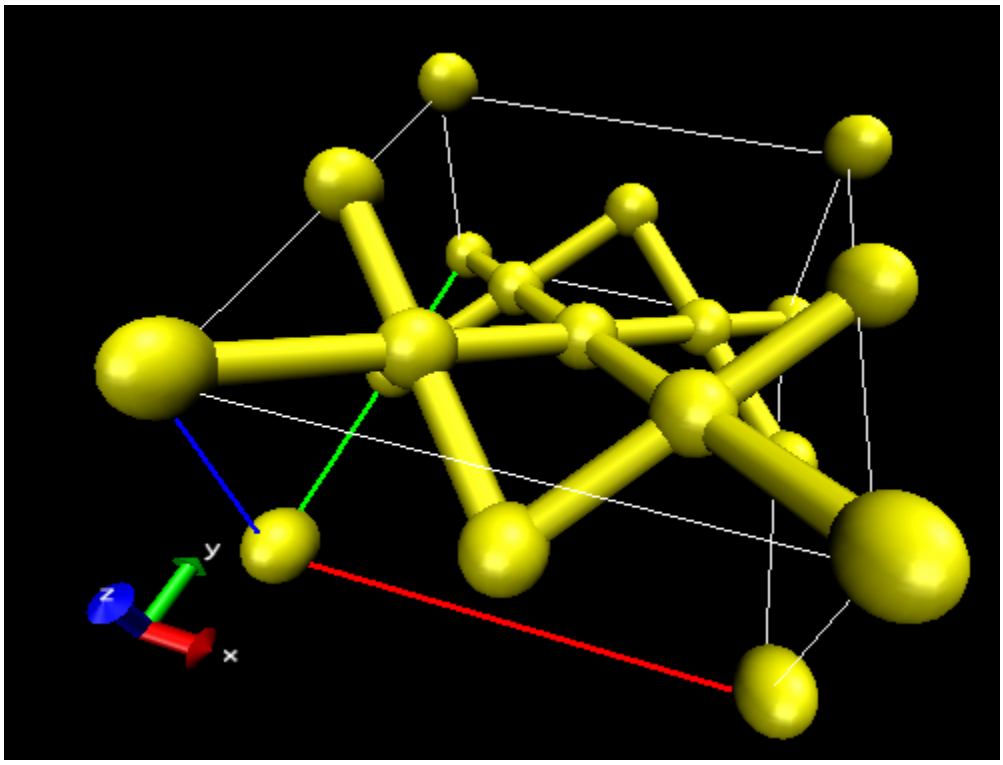

Figure 78: Sn crystal structure

Lee, *et al*, summarized some information in his 2002 papers [93]. Some will be copied as follows. The twinning plane is (301) and the twinning direction is $[\bar{3}01]$.

Table 10: Properties of single-crystal β-Sn with respect to different crystal directions [93]

Slip Plane	Slip Direction	T crss (MPa)
(100)	[001]	1.863

(110)	[00$\underline{1}$]	1.275
(101)	[10$\underline{1}$]	1.569
(121)	[101]	1.667
(100)	[011](?)	-

Table 11: Thermal and mechanical properties of single-crystal Sn [93]

Direction	Thermal Expansion Coefficient (ppm/°C)	Young's Modulus (GPa)	Hardness (GPa)
X, Y	15.4	85	0.98
Z	30.5	54	

Table 12: Calculated CTE and Young's modulus [93]

Direction	<100>	<101>	<103>	<001>	<113>	<112>	<111>	<110>
CTE (ppm/°C)	15.4	18.9	26.4	30.5	24.2	21.1	20.5	15.4
Modulus (GPa)	54.1	48.1	55.8	84.7	42.3	14.8	25.5	26.3

The elastic stiffness matrix for Sn at 300K is [94]:

$$C_{Sn} = \begin{bmatrix} 72.30 & 59.40 & 35.78 & 0 & 0 & 0 \\ 59.40 & 72.30 & 35.78 & 0 & 0 & 0 \\ 35.78 & 35.78 & 88.40 & 0 & 0 & 0 \\ 0 & 0 & 0 & 22.03 & 0 & 0 \\ 0 & 0 & 0 & 0 & 22.03 & 0 \\ 0 & 0 & 0 & 0 & 0 & 22.03 \end{bmatrix} \times 10^3 \text{ MPa}$$

The normal elastic stresses can be calculated for bi-crystal condition and the results can be found in are listed in [93]. Several other conditions considering finite grain

size are also calculated in the papers and the local CTE mismatch plays a critical role on damage accumulation/crack initiation during thermal-mechanical fatigue [93].

APPENDIX B

MELTING TEMPERATURE

The melting temperature of the materials is measured with a differential scanning calorimeter (DSC Q1000, TA Instruments).

A small piece of sample was put in an aluminum cup and heated at the rate of 5°C/min till 260°C. The heat flow per unit mass is shown in Figure 79 and the melting temperatures and melting heats are listed in Table 13. The melting temperatures of these three alloys are within 2°C of each other and the melting heat difference is very small.

One interesting observation on the heat flow chart is that the solidus temperatures are the same for all alloys, but the liquidus temperatures are different. Because the Sn3.5Ag solder is the eutectic alloy, its solidus and liquidus temperatures theoretically overlap. The other alloys are out of the eutectic point a little, so they have slightly higher liquidus temperatures.

Table 13: Melting temperature and melting heat of alloys

	SnAg No La	0.05%La	0.10%La	0.25%La
Melting T (°C)	224.09	226.18	225.16	225.04
Melting Heat (J/g)	63.97	64.55	63.32	64.30

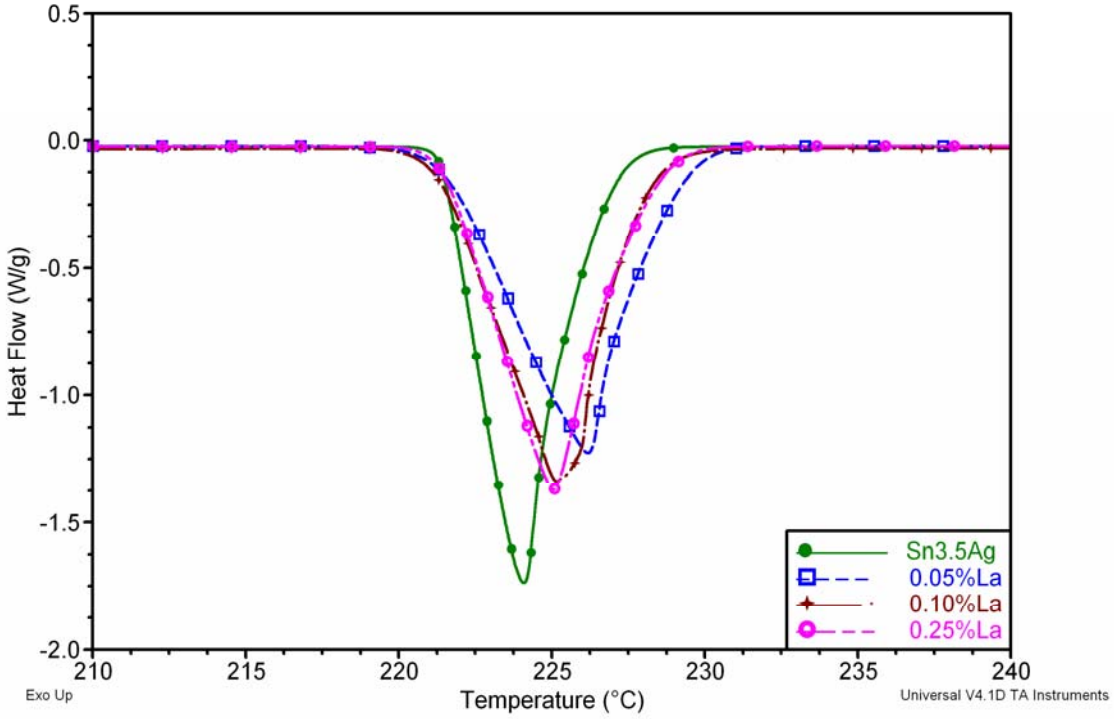

Figure 79: DSC unit heat flow of alloys

APPENDIX C

RESISTIVITY MEASUREMENT

Resistivity was obtained for the solder materials by measuring the resistance of tensile specimens at gage length. The geometry of the specimen was measured with a digital caliper and the resistance of the sample was measured using a Keithley® 2001Digital Multi Meter (DMM) with a Keithley® 1801 nano-volt Preamp. The four-point method of resistance measurement was used and the DMM was connected to the sample with twisted and shielded cable. Offset compensation was used to eliminate the thermocouple effect and every reading was averaged for more than 5 power supply cycles to reduce the noise effect.

In this measurement, the test range of 2mΩ was used in the DMM. From the Model 1801 Nanovolt Preamp specification sheet [95], the error at this range is ±(560 ppm of reading + 100 ppm of range). Given the reading at ~1mΩrange, the accuracy is ±(560 ppm x 1 + 100 ppm x 2) mΩ = ±0.76e-3 mΩ.

The resistivity of as-cast specimens and 170°C aged specimens are plotted in Figure 80 as functions of La percentage and in Figure 81 as the function of aging time, respectively. The resistivity of SnAg lead-free solder material is usually measured to be around 10-15μΩcm [25]. The results of this study show the resistivity readings to be well within this range. This demonstrates that the neither La doping, nor thermal aging could have an effect on the conductivity of SnAg solder material.

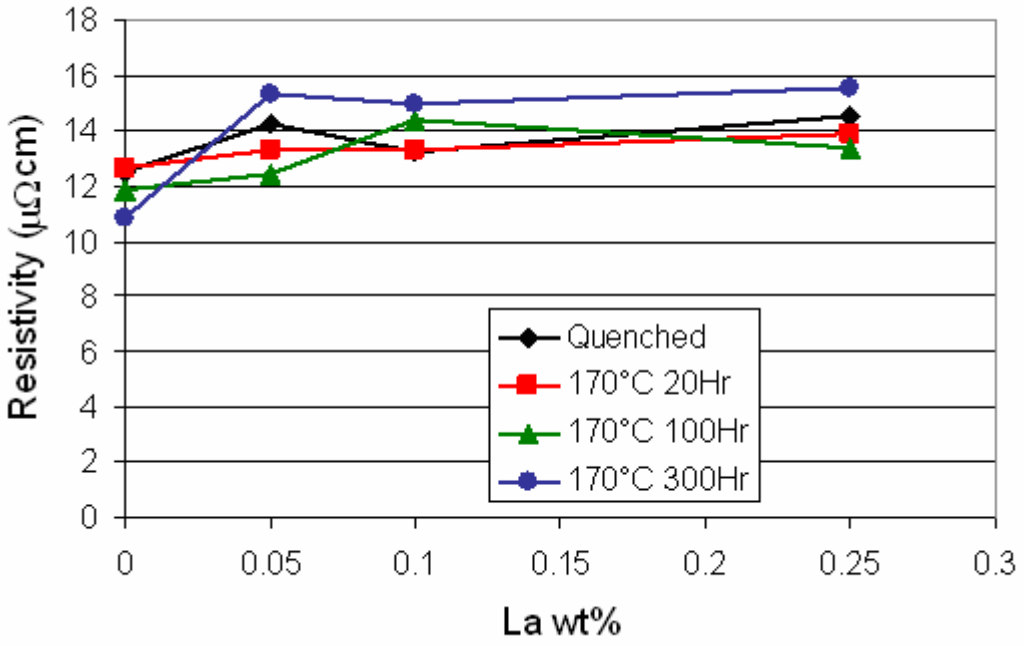

Figure 80: Resistivity as a function of La doping

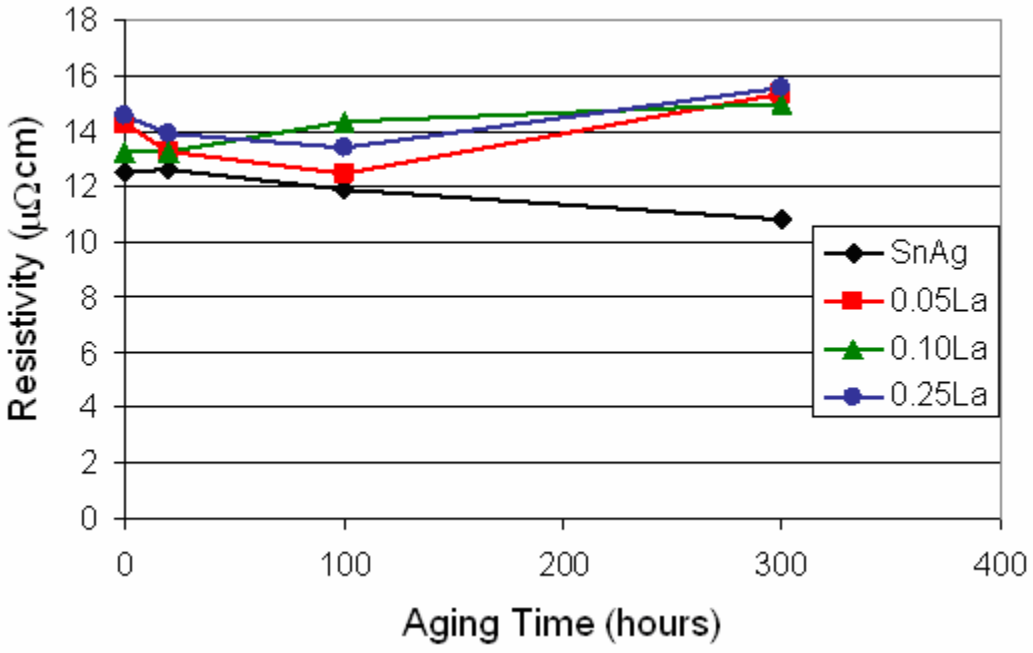

Figure 81: Resistivity as a function of aged time

APPENDIX D

NON-CONTACT STRAIN MEASUREMENT SYSTEM

Due to the soft nature and the small size of the specimen, a non-contact strain measurement method was used in this test. This non-contact method uses a CCD camera to capture the surface of the sample *in situ*. Image analysis software has been programmed to capture the images and to calculate the strain in real time.

Software Development

This non-contact strain measurement system is able to capture the image of the specimen into a computer during tensile tests, and to compare the images in pairs using image correlation software. To automate this process, software called "ImageStrain" was written by the author using Microsoft® Visual C++ 6.0. The ImageStrain software can capture the image from the CCD camera and, with a simple algorithm, can calculate the strain of sample being tested. A screen shot of the software is shown in Figure 82.

The image was captured and shown on a window of the software (label 1 in the screen shot). The operator needs to adjust the camera position to make the specimen parallel to the horizontal direction of the image, as shown in Figure 20. And adjustments are needed for the aperture of the camera and the light source in order to "white out" the metal specimen but to leave the two thin pieces of black tape dark. These tape pieces are served as markers of the gage length of the specimen and should be placed on the specimen before testing. The "Strain Position" can be changed to make the red line on the image (see label 2 in the figure) pass the specimen. The gray scale in the image along this line is recorded and value is plotted blow the sample image, as can be seen in the area near label 4. In that line, a higher brightness lower vertical value. So the two dark bands of the black tape will be seen as two peaks on the line marked with label 4. One small

problem of the plotted of the gray line is that the scale is not exactly the same as the image due to hardware limitations.

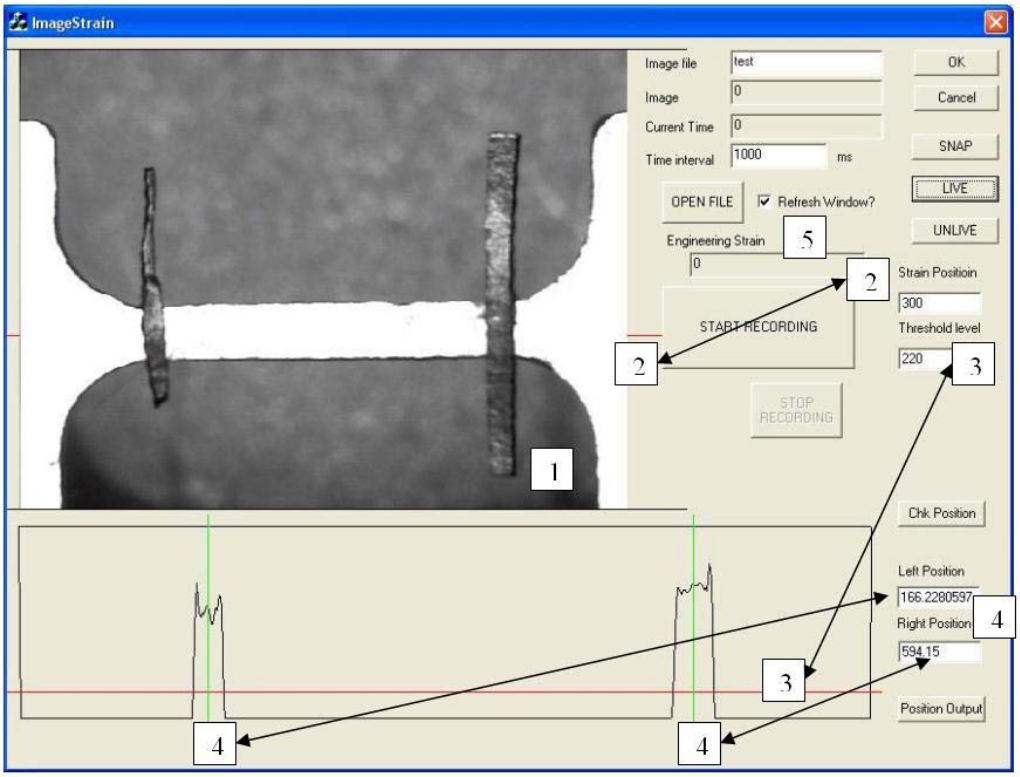

Figure 82: Screen shot of ImageStrain software for non-contact strain measurement

A threshold value is defined to help the software to recognize the peak position or the black tape position. This value is drawn with a red line on the chart in the gray scale display area. Adjusting the "Threshold level" edit box can change the red line cross the two peaks (label 3 in the figure) to make the threshold level low enough to block the noise from the top of the two peaks, and high enough to block the noise from below. The intersect position of the threshold level with the two peaks can be calculated and shown in the "Left Position" and "Right Position" edit boxes, with units of pixel, and marked with green lines as well (see the label 4 in the figure). In the recording condition, the distance of the two peaks at zero time will be used as initial length and the strain can be calculated based on measured distance between the peaks. The engineering strain will be

shown in the "Engineering Strain" edit box (label 5 in the figure) and out put to the data file as well, with the assigned frequency.

Calibration of the ImageStrain software

An aluminum specimen was made in order to calibrate the ImageStrain software. A strain gage was attached to the back side of the specimen to record the strain. The comparison of the strain measured by ImageStrain software and by the strain gage can be seen in Figure 83.

This test proved that the strain from ImageStrain software is close enough to the actual strain in small strain range. Comparing a caliper movement with pixel output confirms that this software is also capable of large strain measurement.

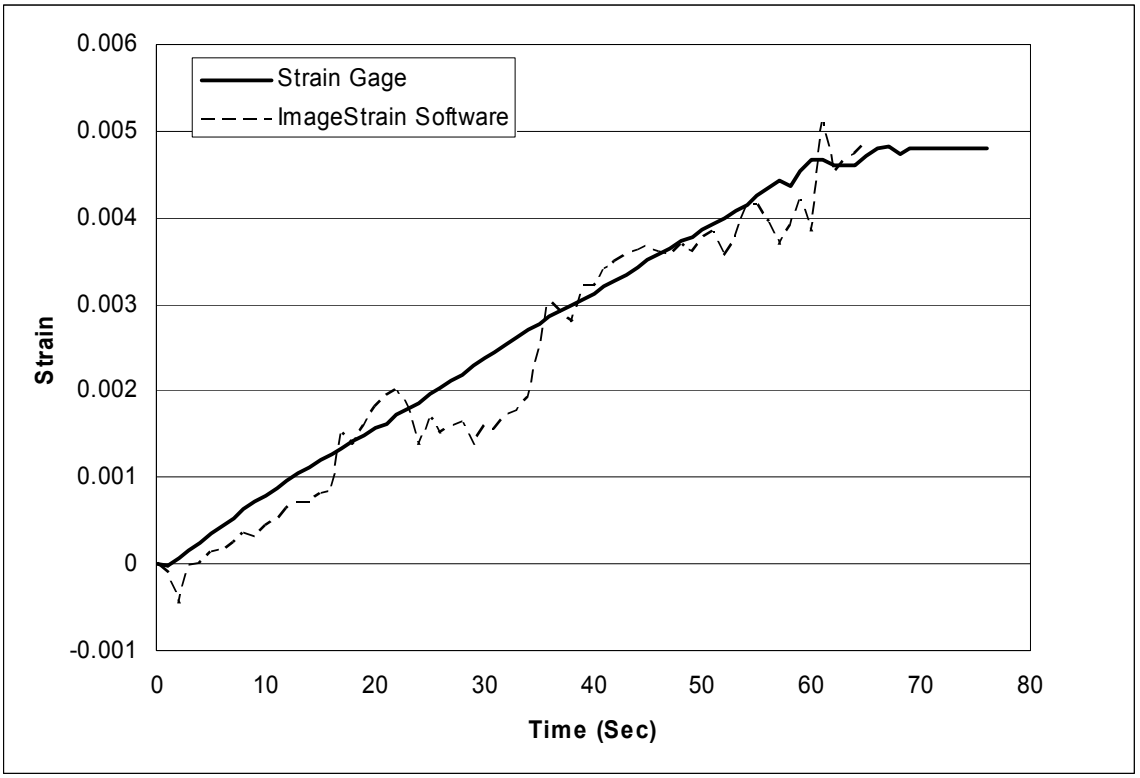

Figure 83: Calibration of non-contact strain measurement

As Figure 83 demonstrates, the strain output from ImageStrain software has some noise. This noise comes from the image digitalization of the CCD camera. The gray scale output of the CCD is always changing, sometimes at a level that cannot be detected by the human eye. This can cause strain output noise, in this case within 0.001. This will introduce some uncertainty on a Young's modulus measurement because the modulus measurement is dependent on small strain measurement.

One other limitation of the non-contact strain measurement is the data acquisition speed. The strain measurement is limited by the video frame refreshing speed. The experimental equipment uses the NTSC format, of which the quickest speed is 30 frames per second. However, the image capture card in the computer sometimes got an even lower capture rate due to different software/hardware load in the image capture card and the computer. The ImageStrain software can measure strain much faster than this but before the new frame comes in the software the software will output multiple strain readings from the one image in it. Tests have shown that the non-contact strain measurement used here is fast enough for this study.

APPENDIX E

STEADY STATE STRESS RESULT OF STRAIN RATE JUMP TEST

In Figure 40, the steady state stress measurements of the as-cast condition are plotted as a function of strain rate for different temperatures to compare the La doping effect. In Figure 41, the steady state stress measurements of as-cast condition are plotted as a function of temperature for different strain rates. The rest of thermal treatment conditions are shown in the following figures, from Figure 84 to Figure 95.

In Figure 42, the steady state stress measurements are shown as function of strain rate for different temperatures. And Figure 43 shows the steady state stress measurements as the function of temperature for differenct strain rates. These two figures show the steady state stress of SnAg solder without La doping. The creep data of other materials are shown from Figure 96 to Figure 101.

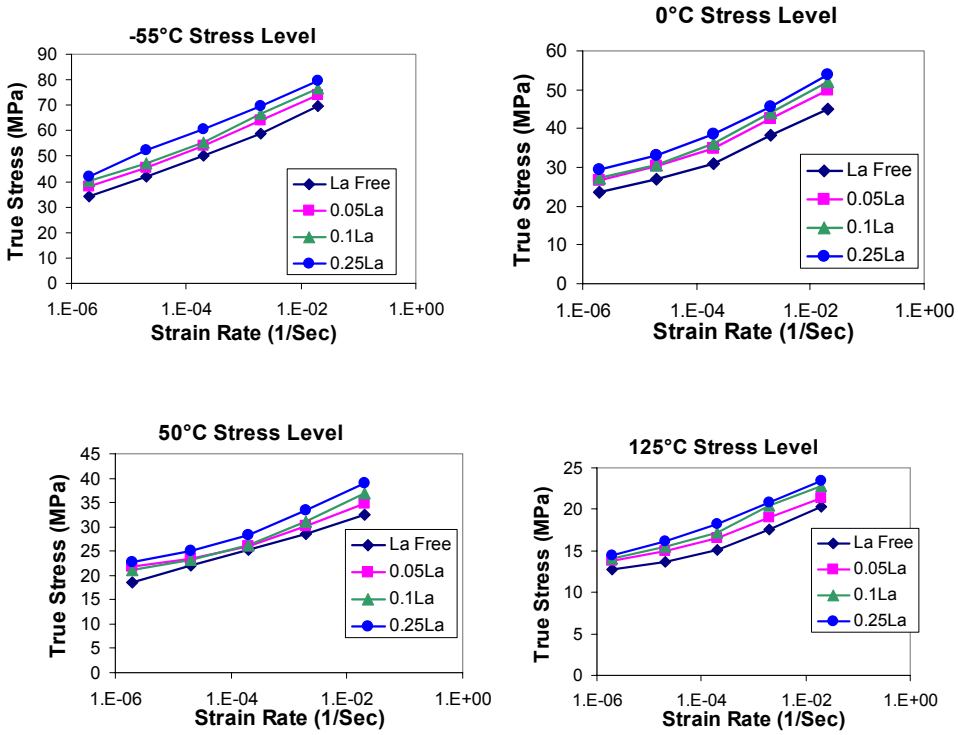

Figure 84: Steady state stresses of samples aged at 100°C for 20hours, listed by different temperatures

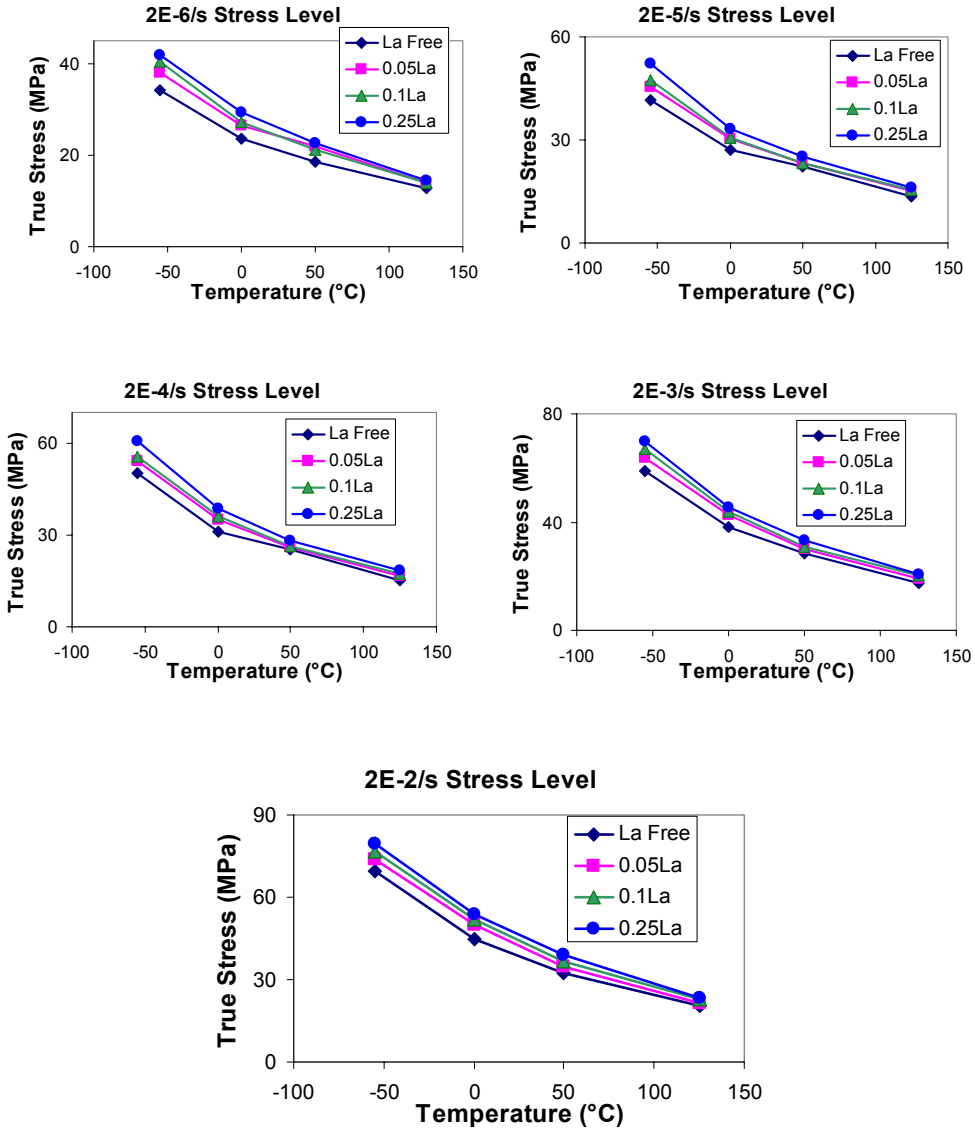

Figure 85: Steady state stresses of samples aged 100°C for 20hours, listed by different strain rates

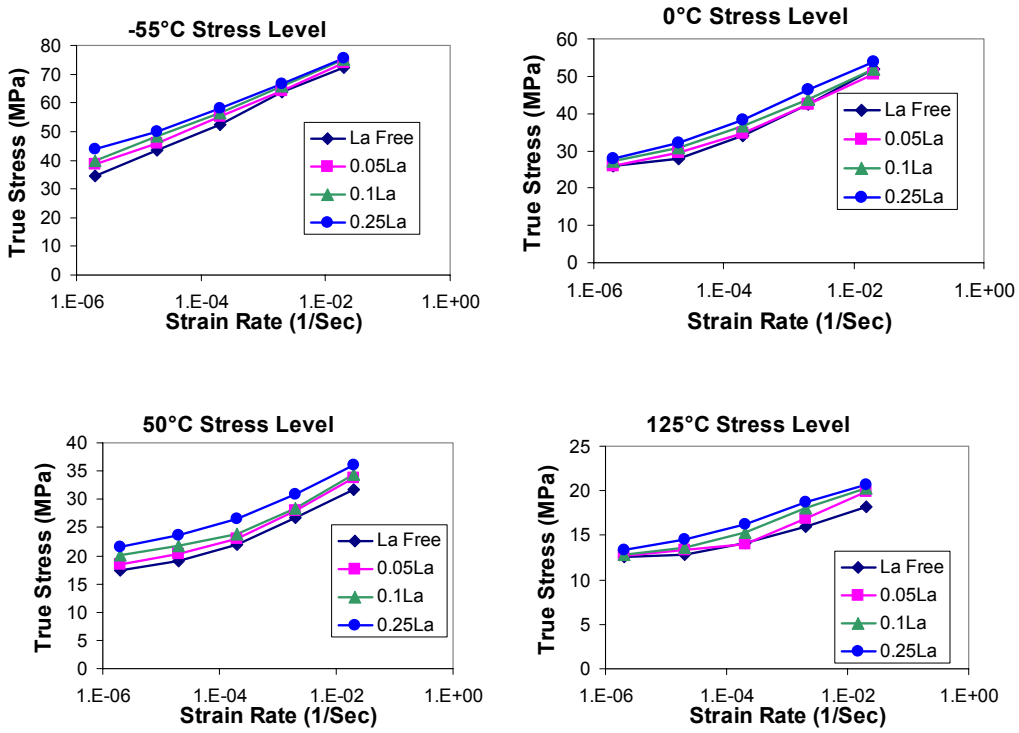

Figure 86: Steady state stresses of samples aged at 100°C for 100hours, listed by different temperatures

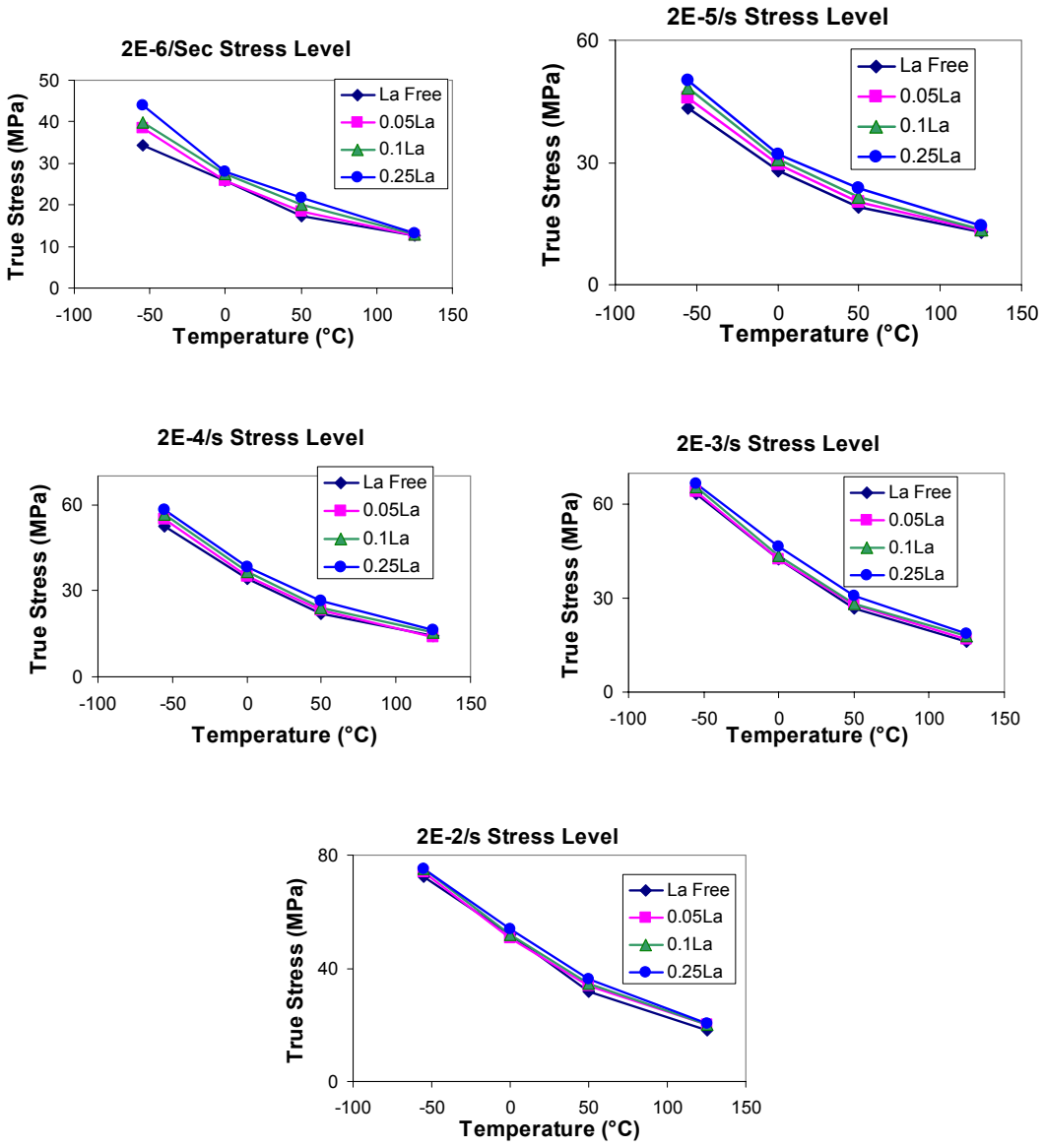

Figure 87: Steady state stresses of samples aged 100°C for 100hours, listed by different strain rates

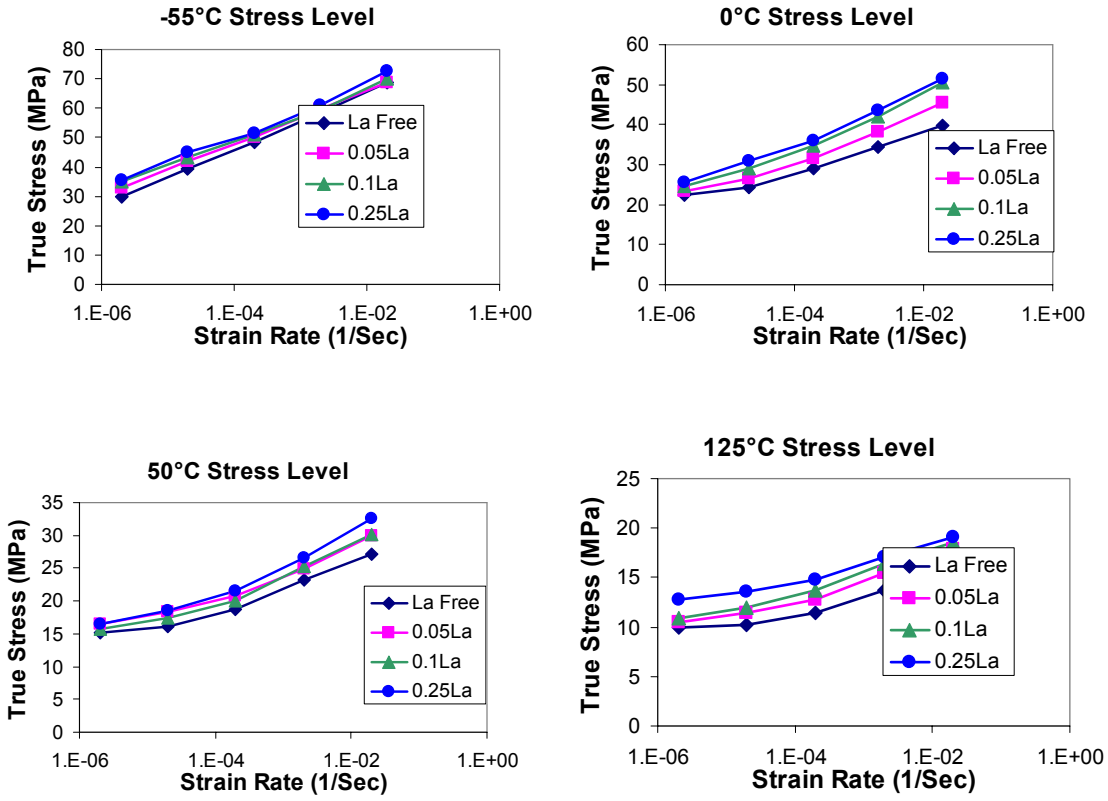

Figure 88: Steady state stresses of samples aged at 100°C for 300hours, listed by different temperatures

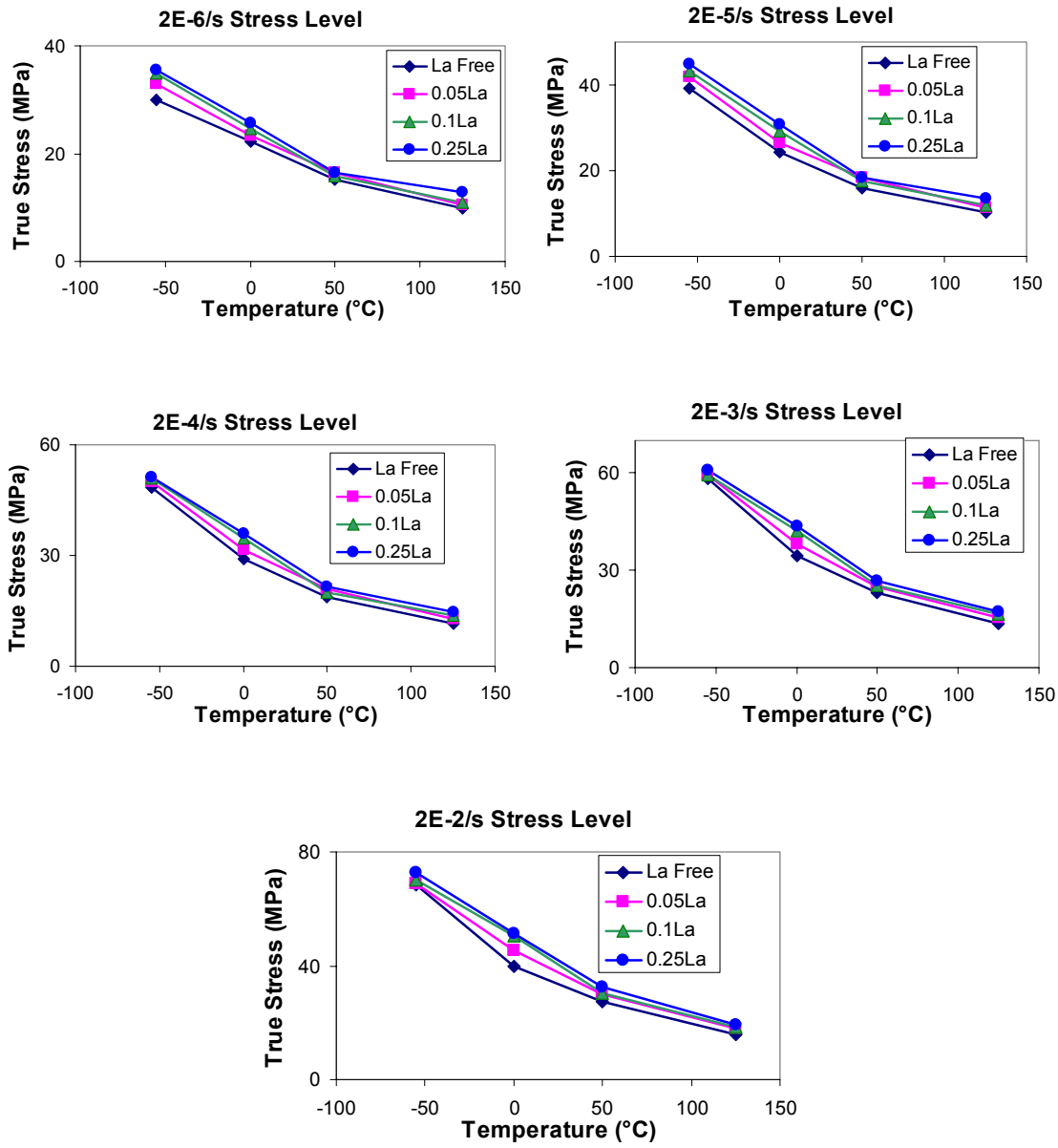

Figure 89: Steady state stresses of samples aged at 100°C for 300hours, listed by different strain rates

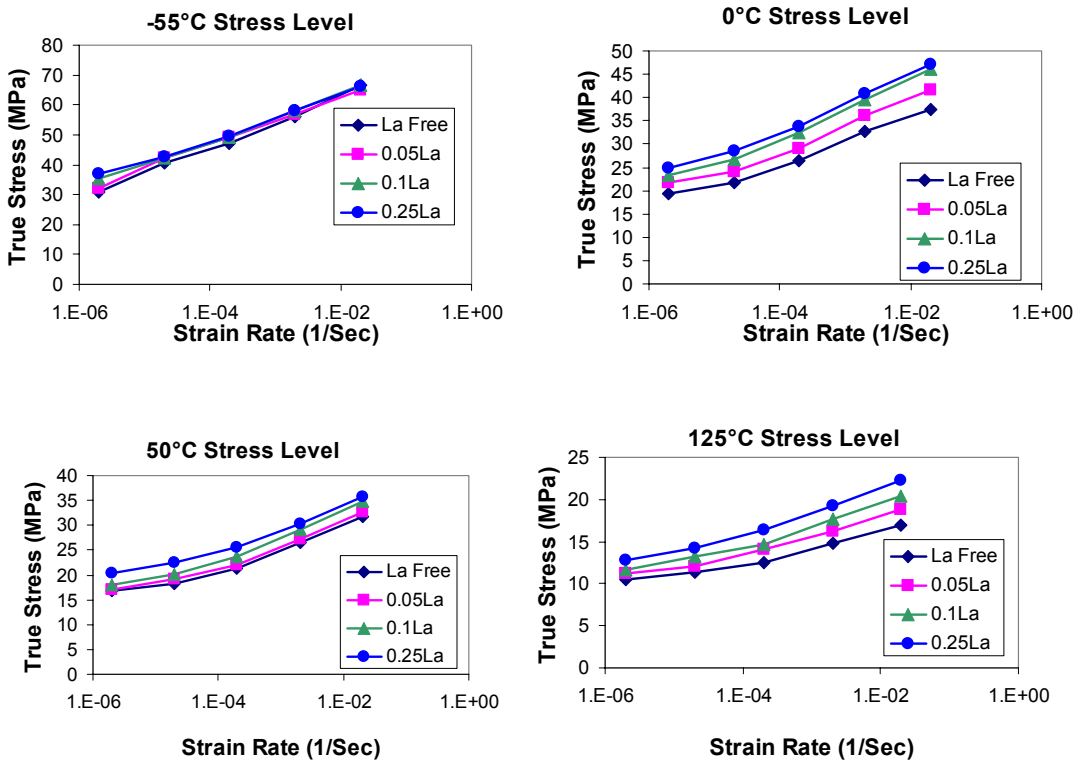

Figure 90: Steady state stresses of samples aged at 170°C for 20hours, listed by different temperatures

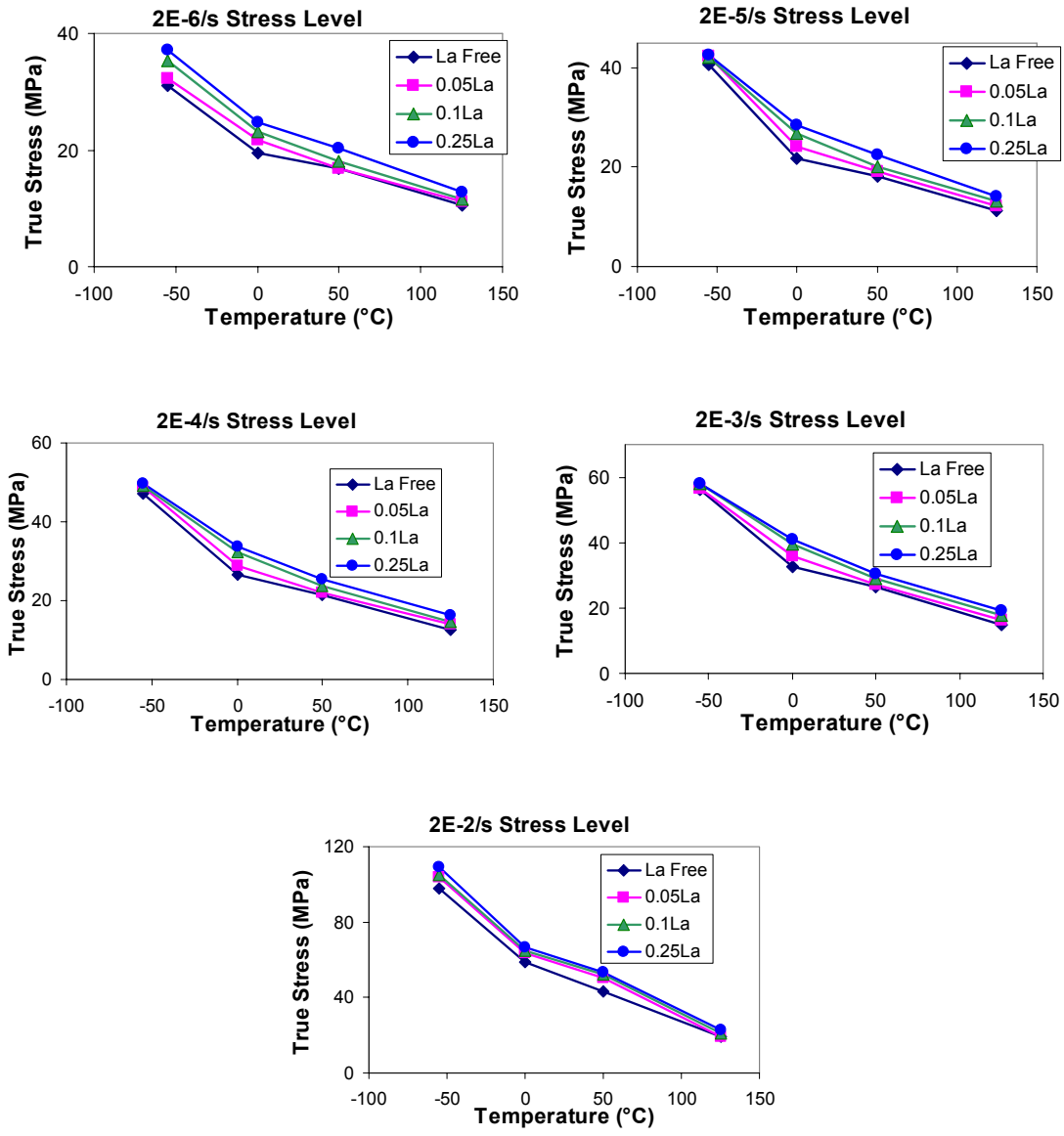

Figure 91: Steady state stresses of samples aged at 170°C for 20hours, listed by different strain rates

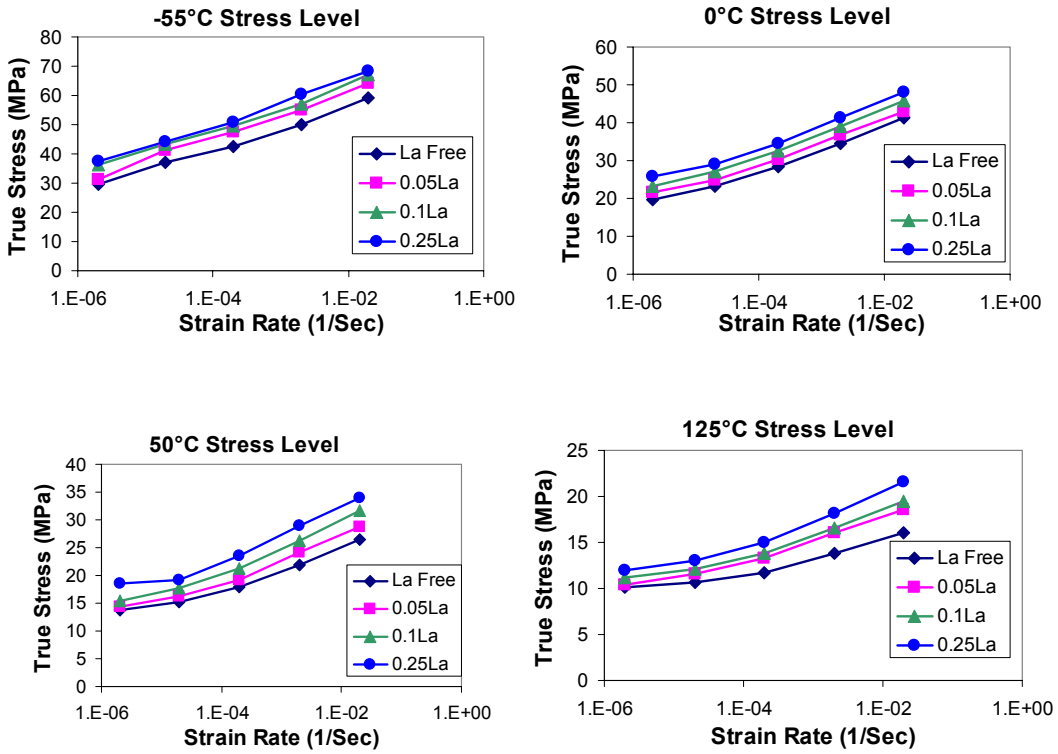

Figure 92: Steady state stresses of samples aged at 170°C for 100hours, listed by different temperatures

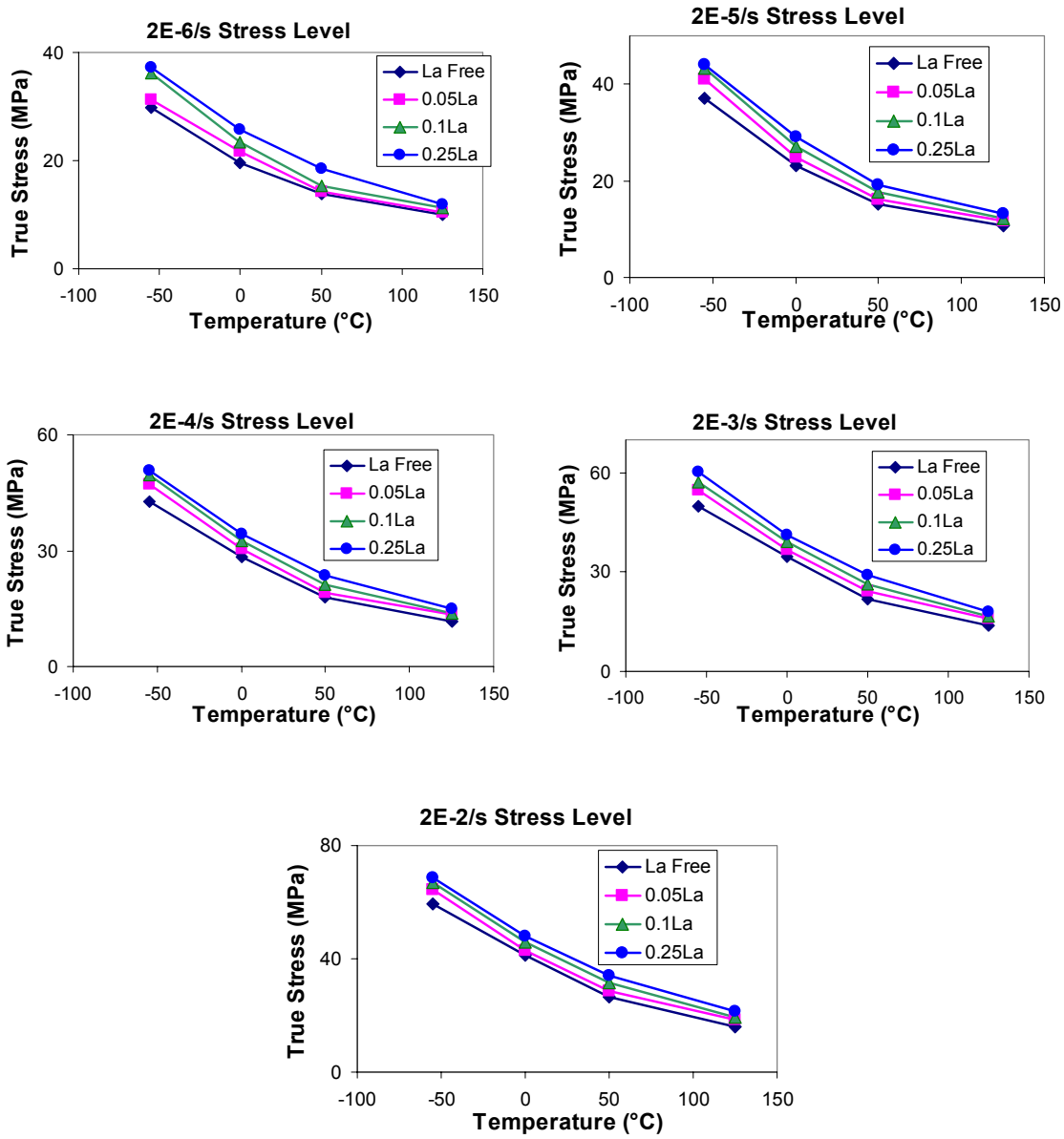

Figure 93: Steady state stresses of samples aged at 170°C for 100hours, listed by different strain rates

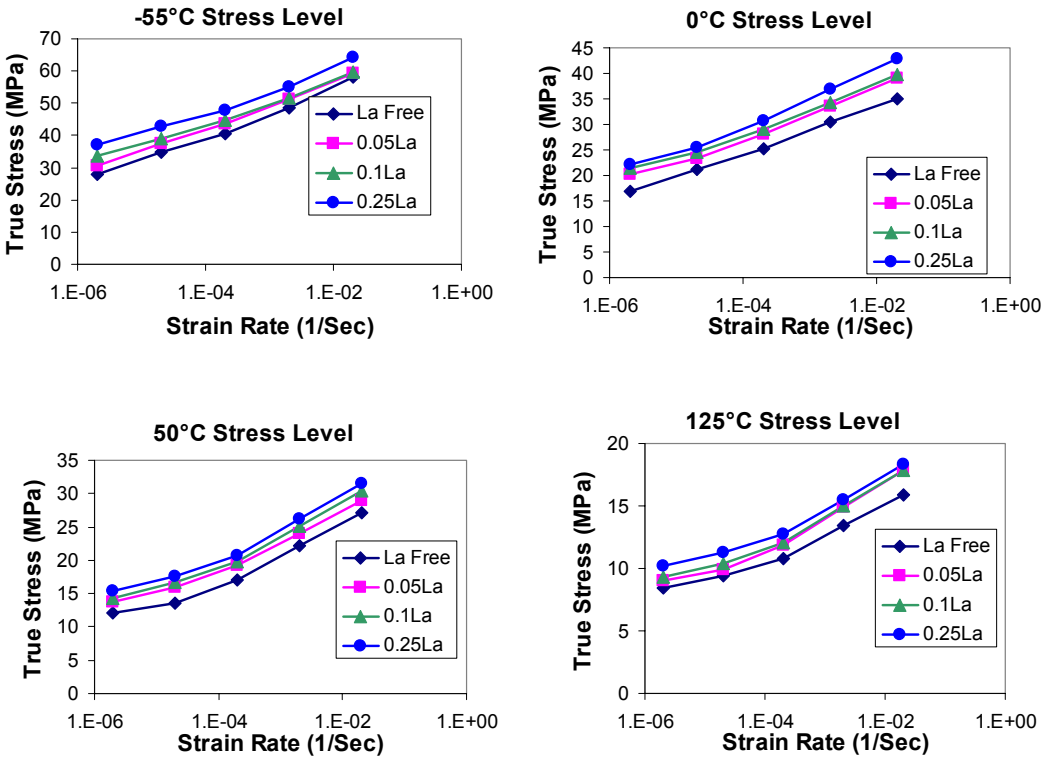

Figure 94: Steady state stresses of samples aged at 170°C for 300hours, listed by different temperatures

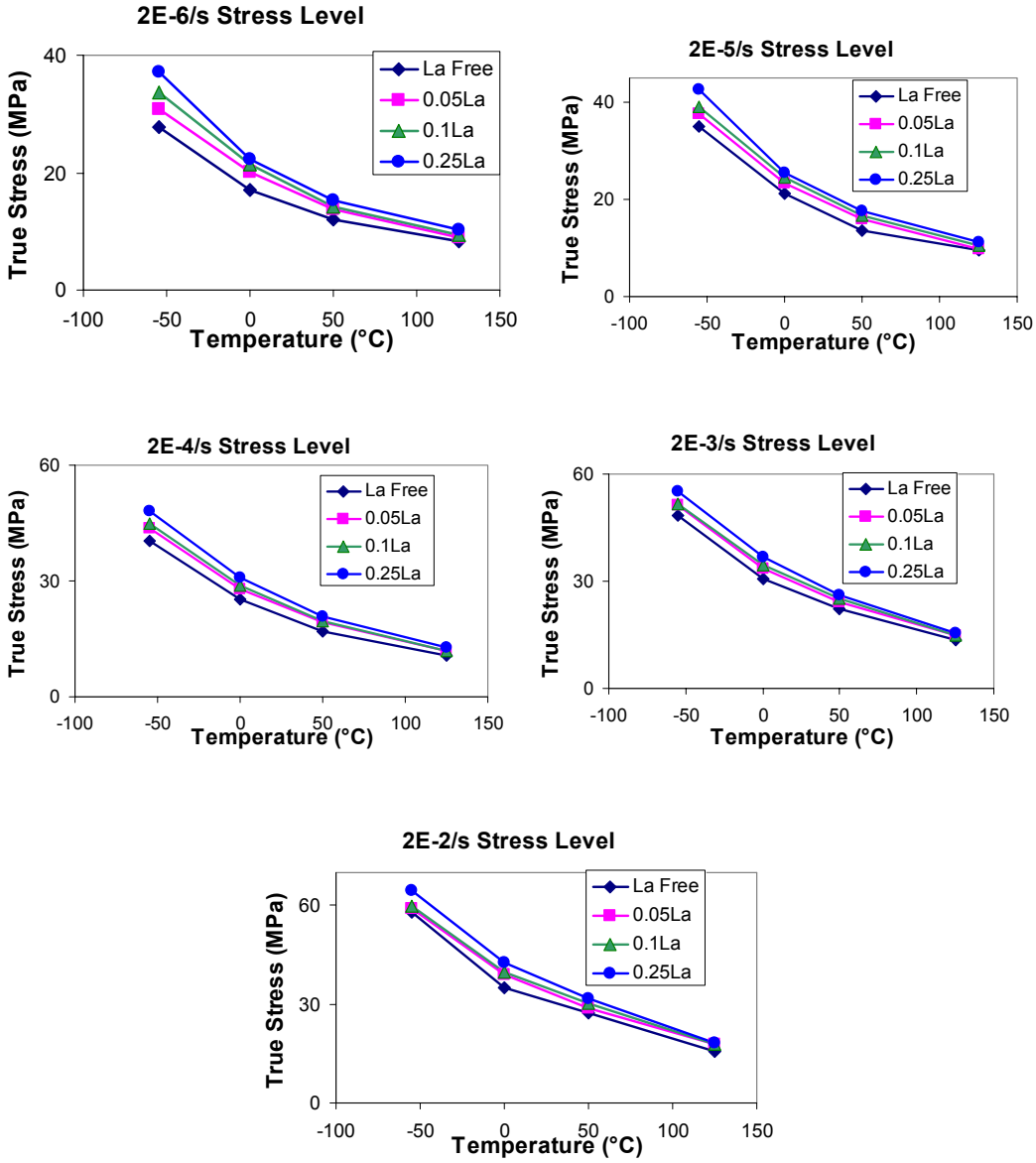

Figure 95: Steady state stresses of samples aged at 170°C for 300hours, listed by different strain rates

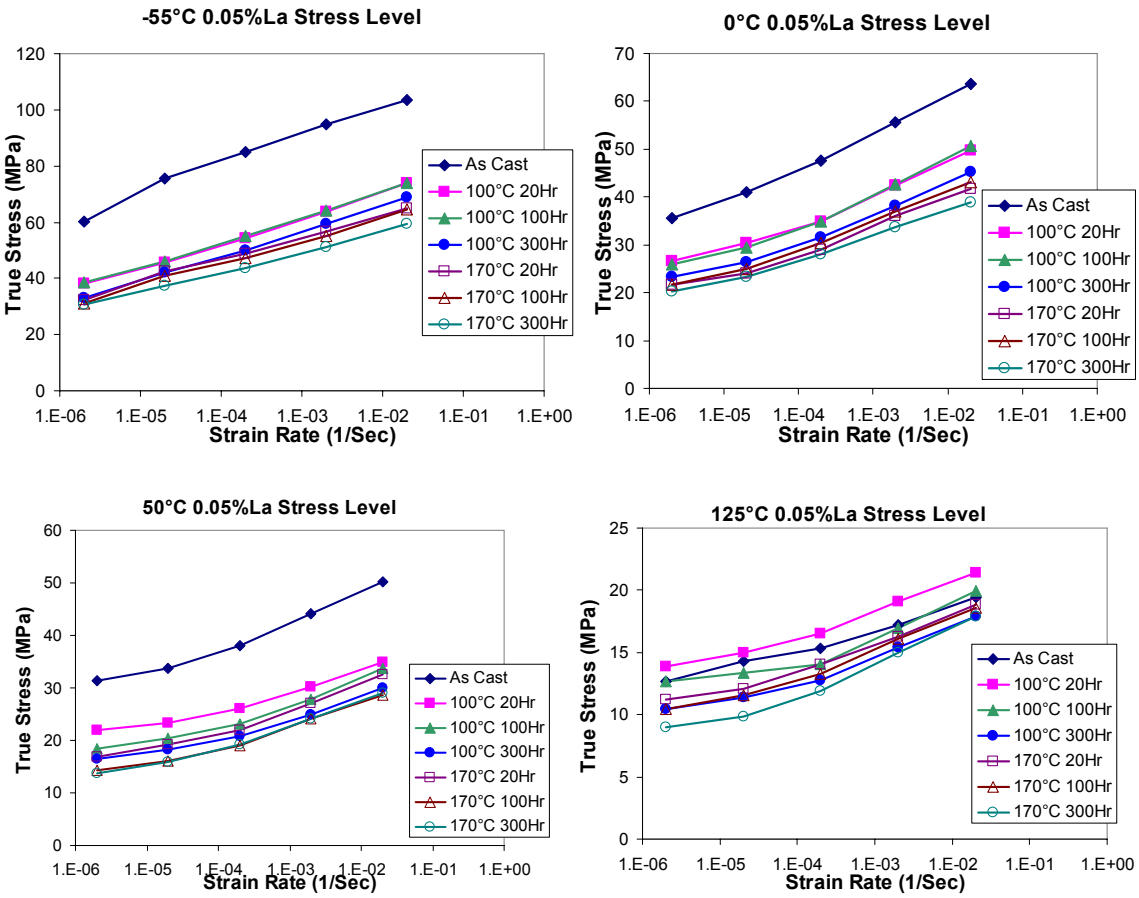

Figure 96: Steady state stresses of SnAg0.05La alloy, listed by different temperatures

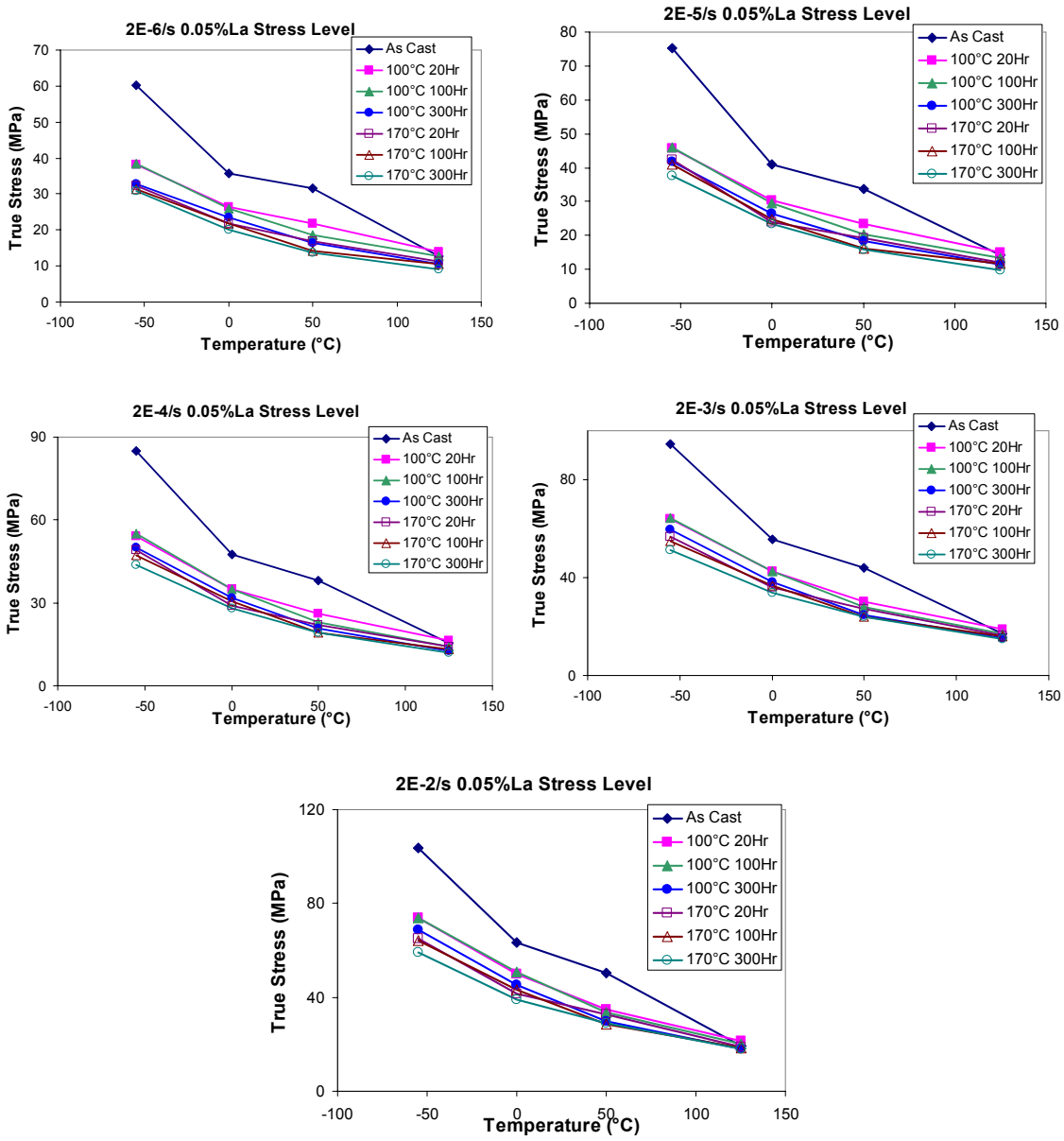

Figure 97: Steady state stresses of SnAg0.05La alloy, listed by different strain rates

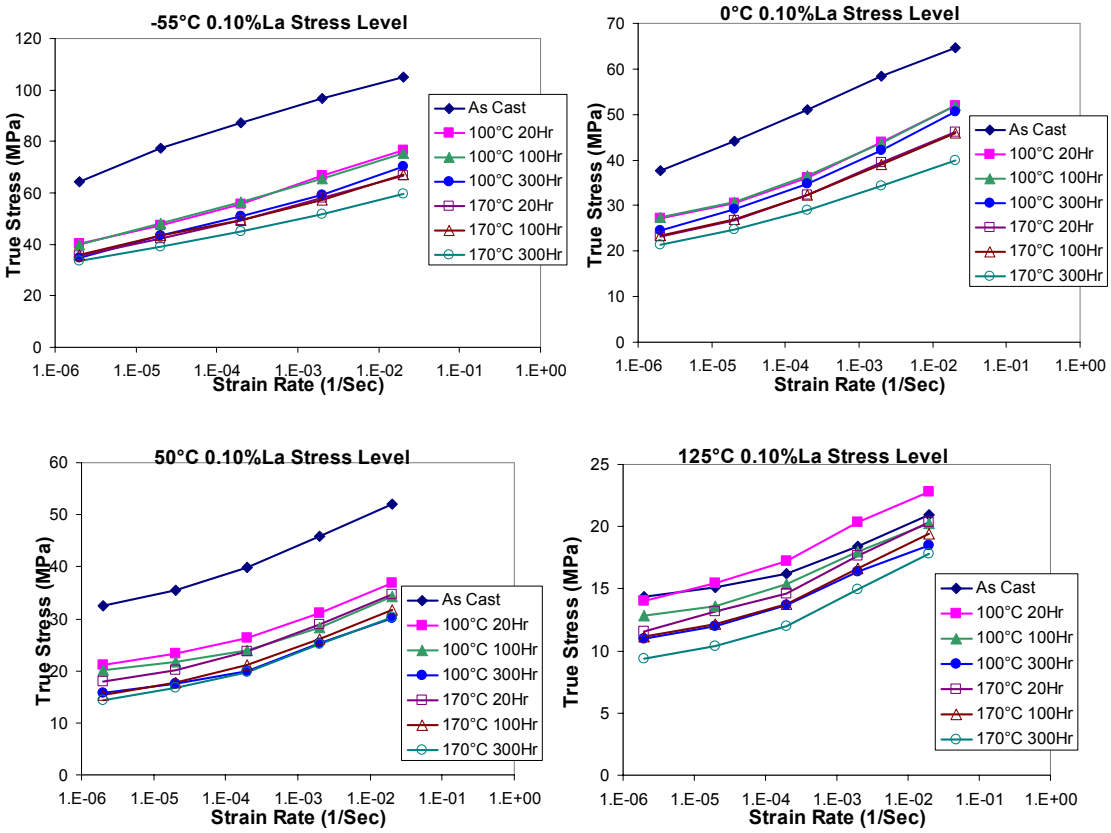

Figure 98: Steady state stresses of SnAg0.10La alloy, listed by different by temperatures

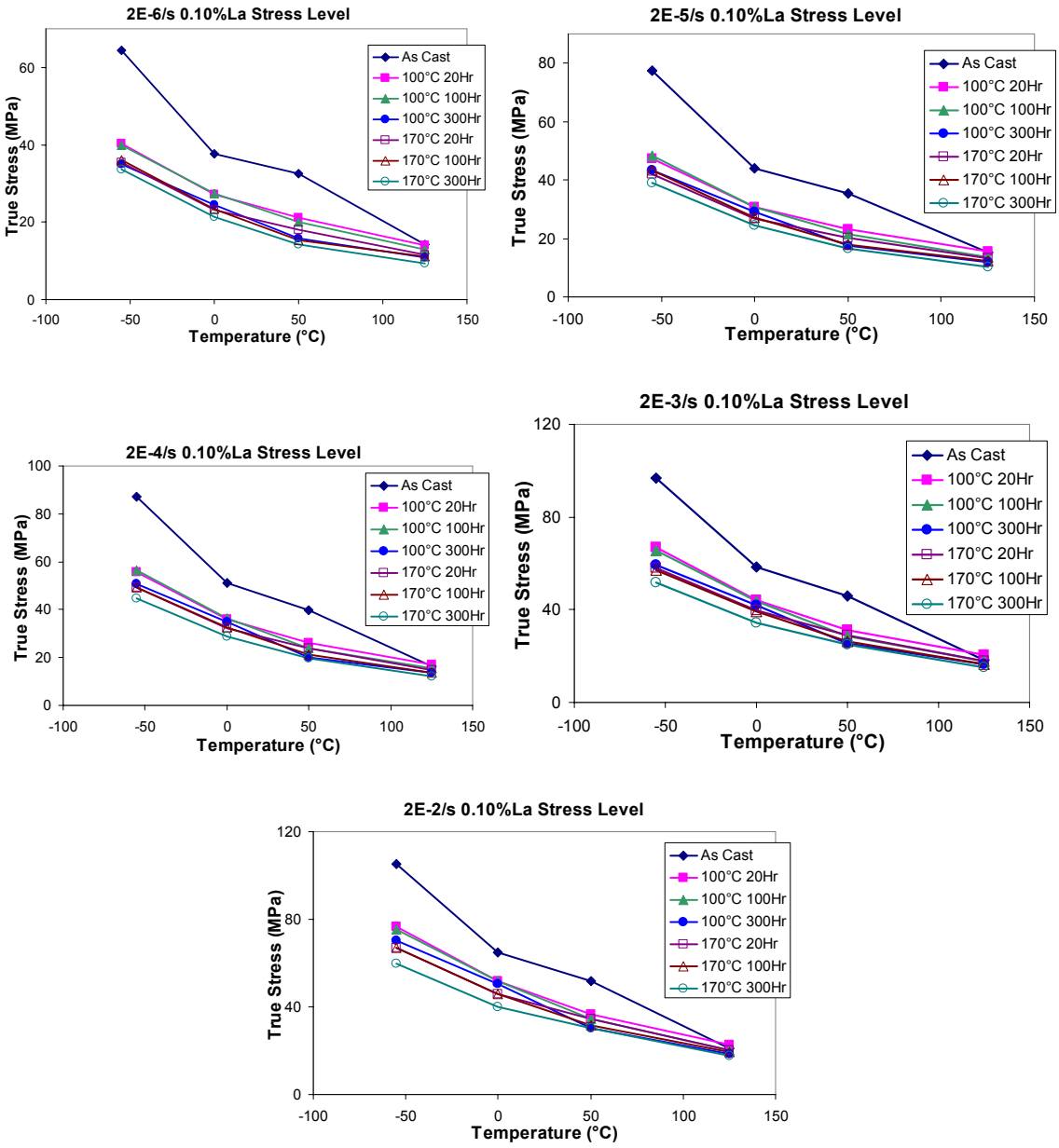

Figure 99: Steady state stresses of SnAg0.10La alloy, listed by different strain rates

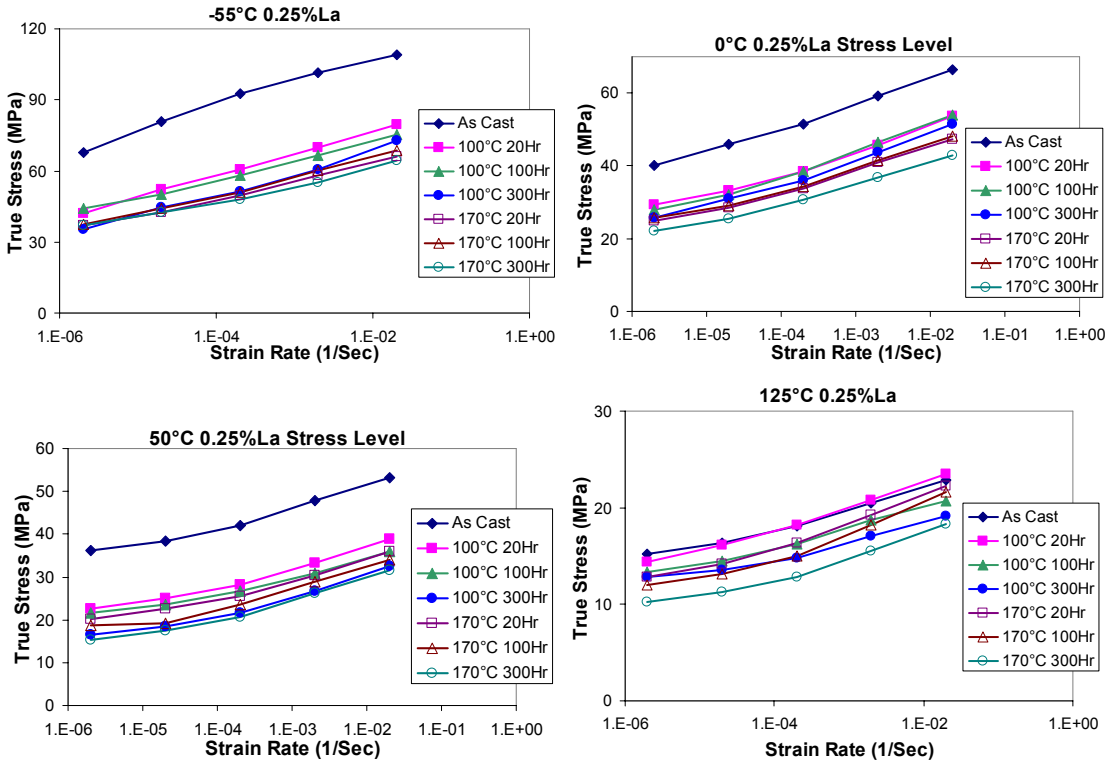

Figure 100: Steady state stresses of SnAg0.25La alloy, listed by different temperatures

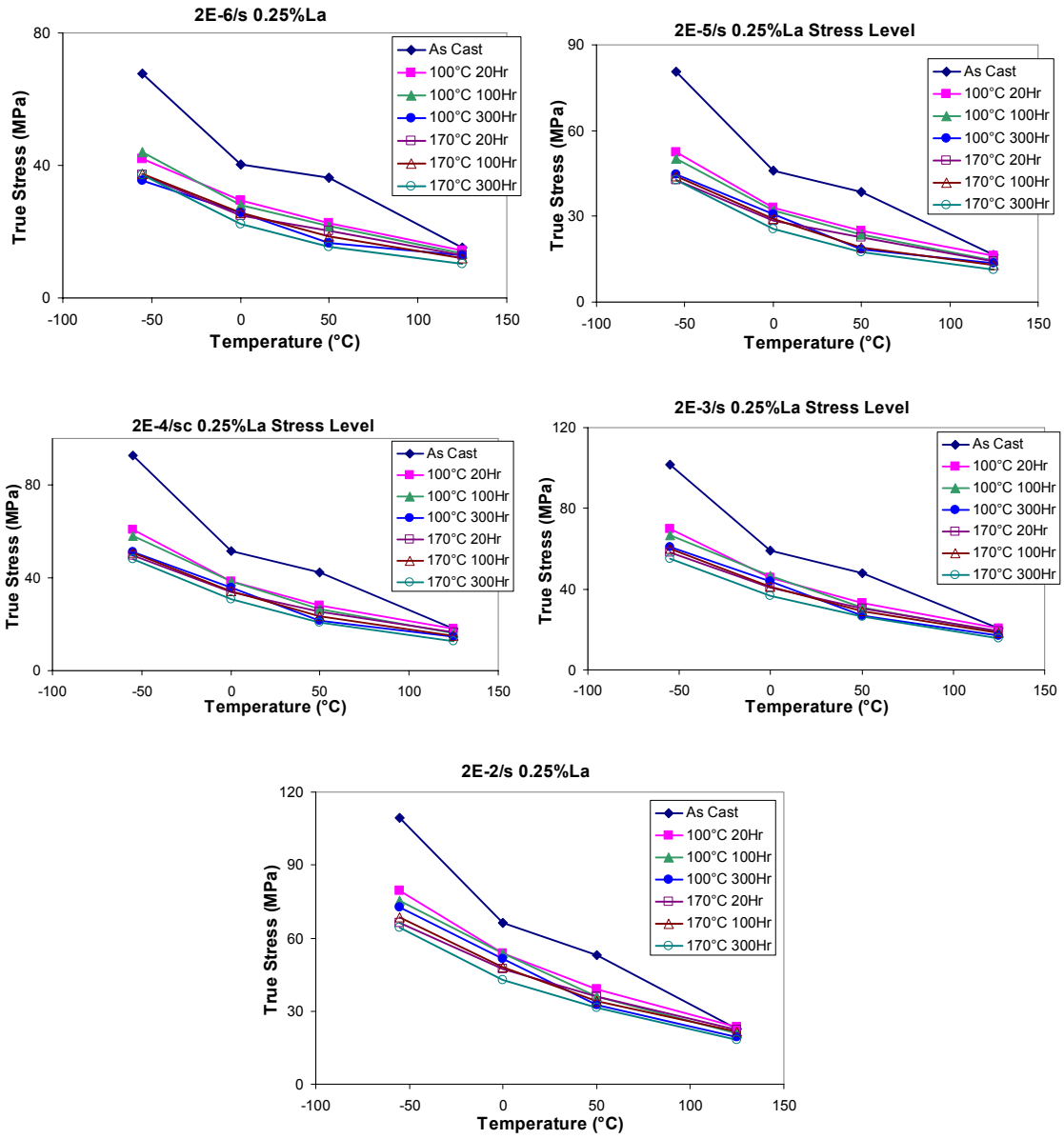

Figure 101: Steady state stresses of SnAg0.25La alloy, listed by different strain rates

APPENDIX F

PARTICLE SIZE DEPENDENT MODEL FITTING RESULT

The comparison of particle sized model result has been shown in Figure 45 and Figure 46 for as-cast condition and 170°C 300hours aged condition, respectively. In the section, the model comparisons with test result for the rest of the thermal conditions are shown in Figure 102 to Figure 106.

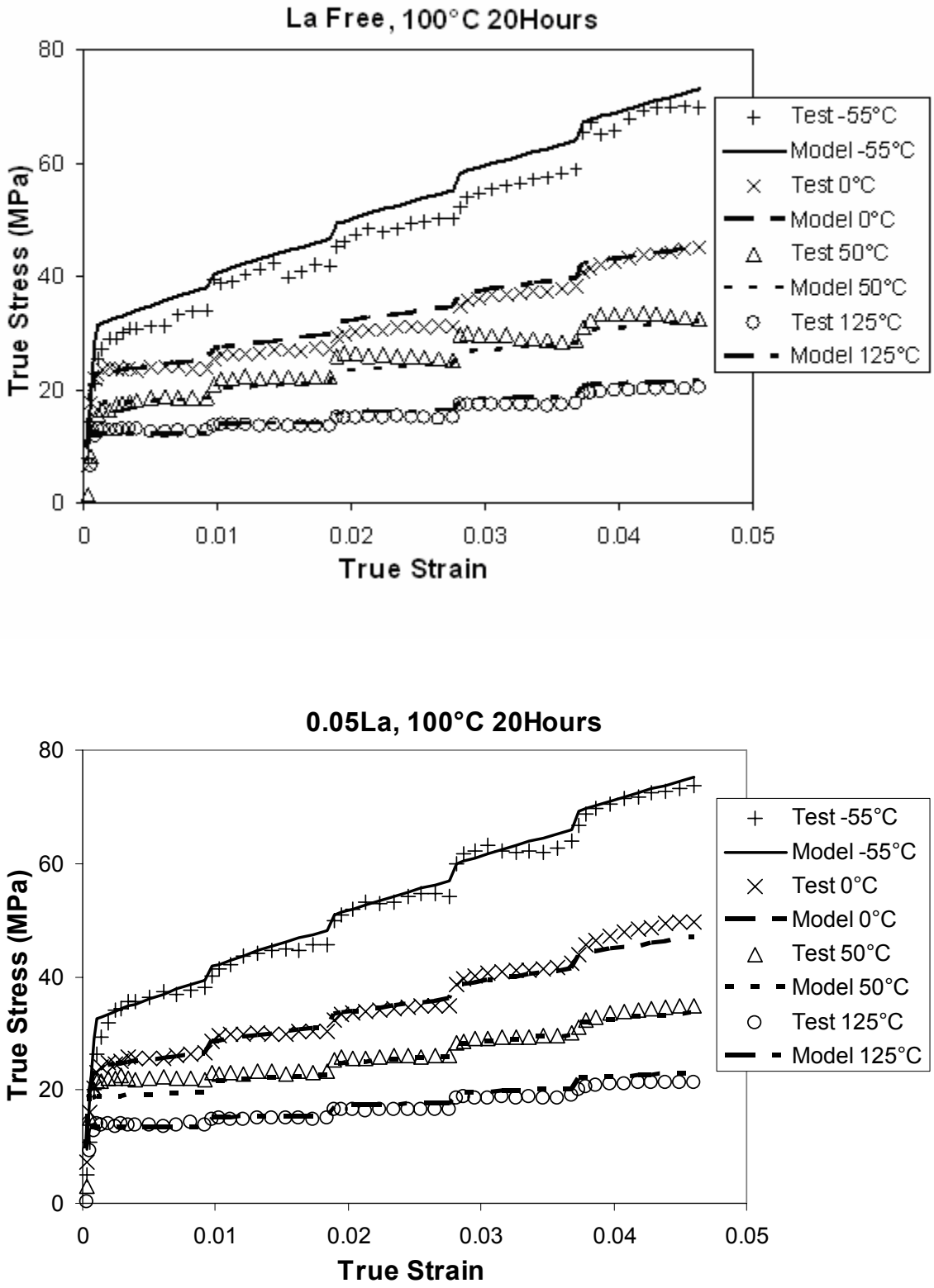

Figure 102: Modified Anand model fitting result of samples aged at 100°C for 20 hours

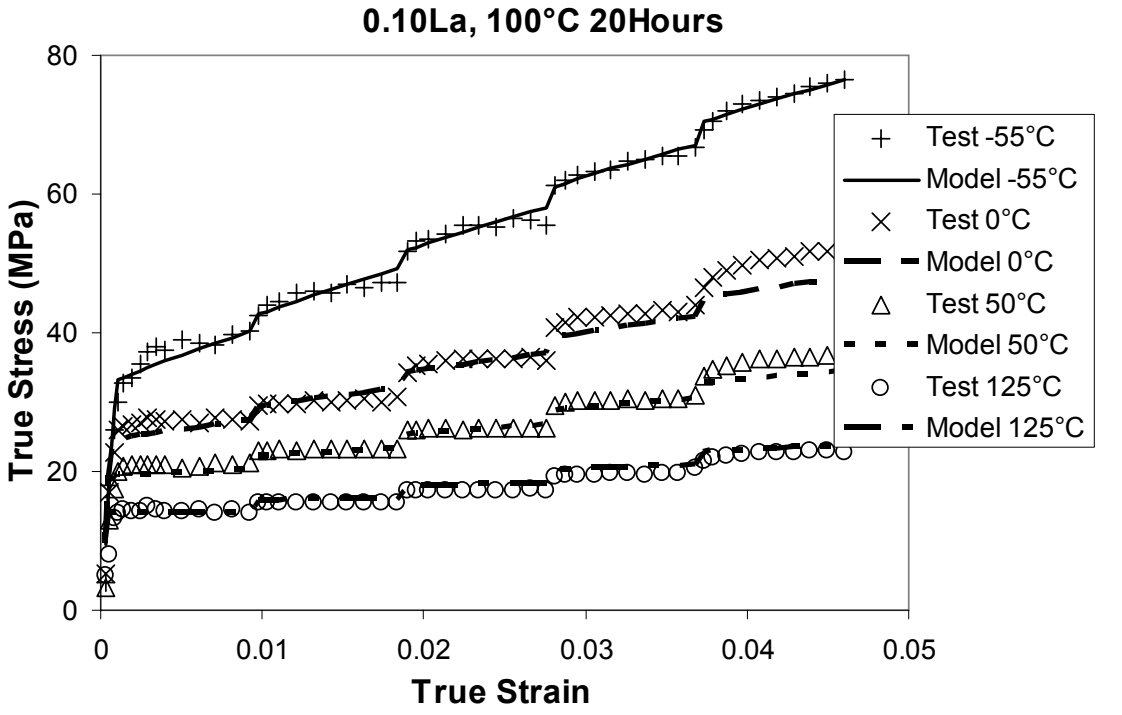

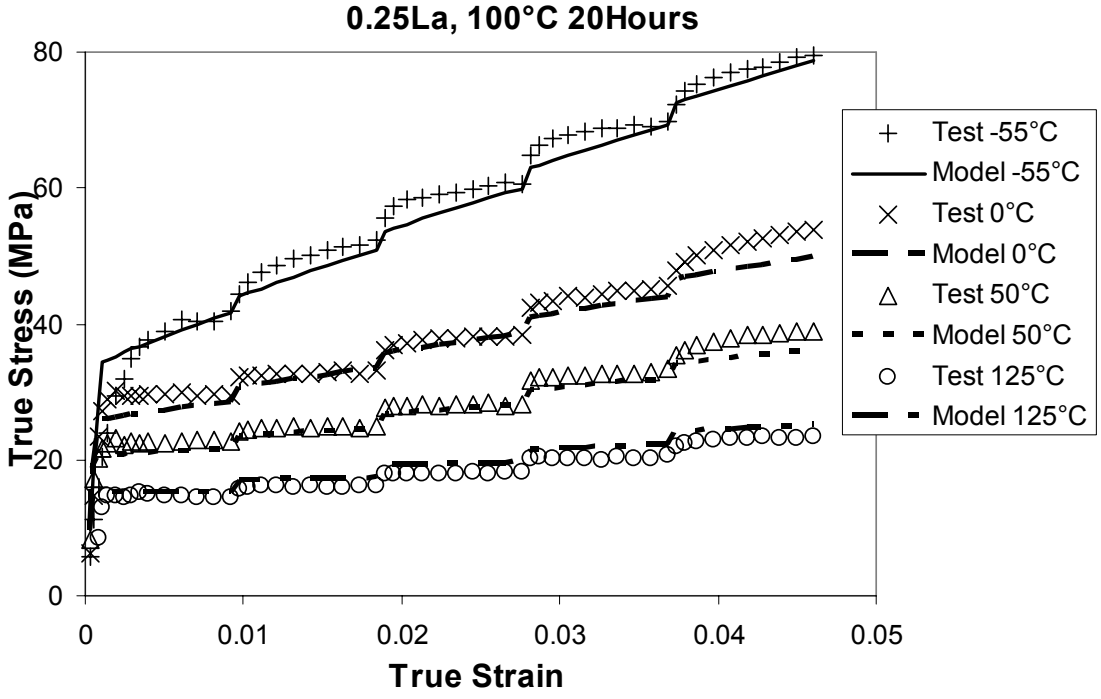

Figure 102: Modified Anand model fitting result of samples aged at 100°C for 20 hours (continue)

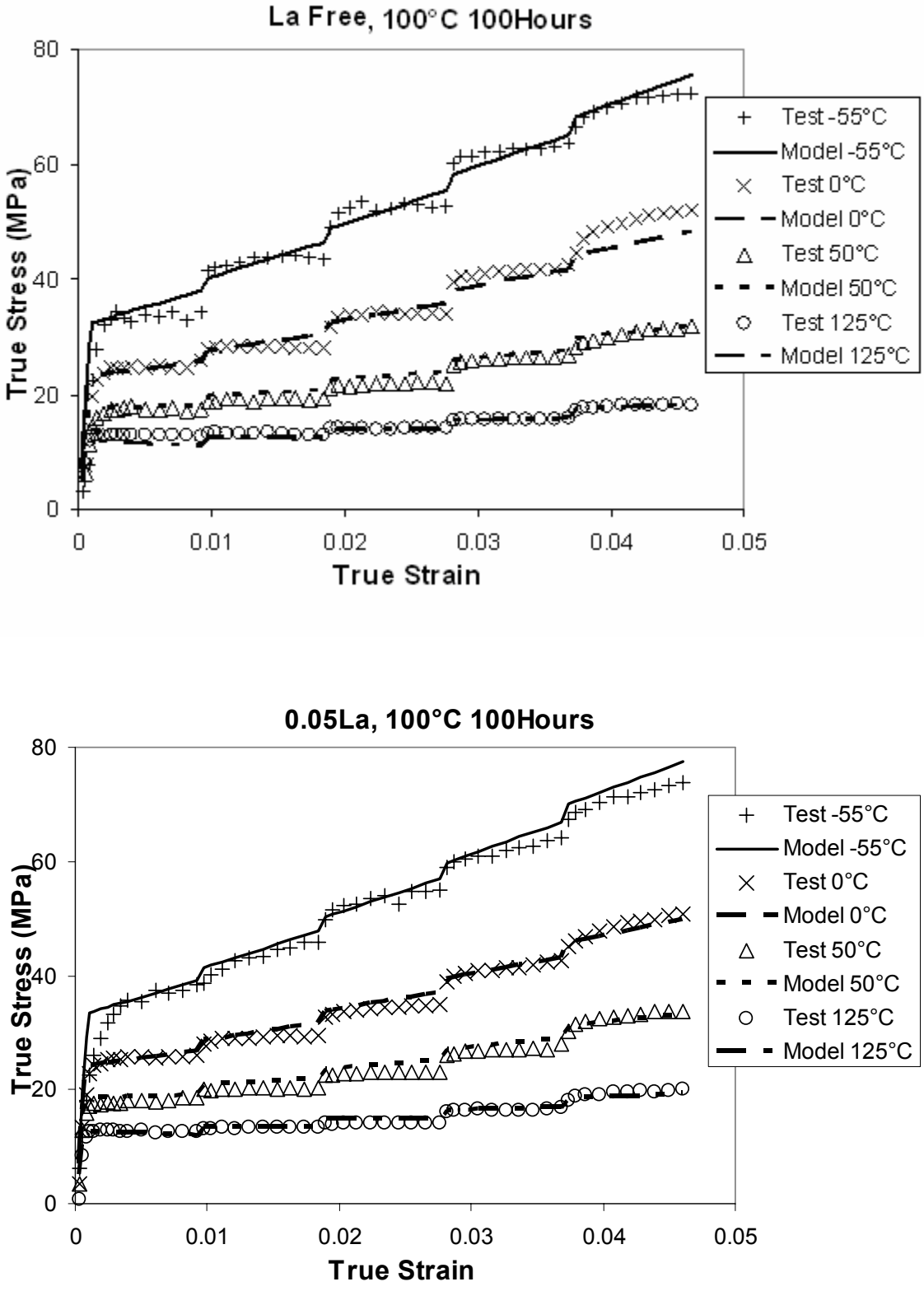

Figure 103: Modified Anand model fitting result of samples aged at 100°C for 100 hours

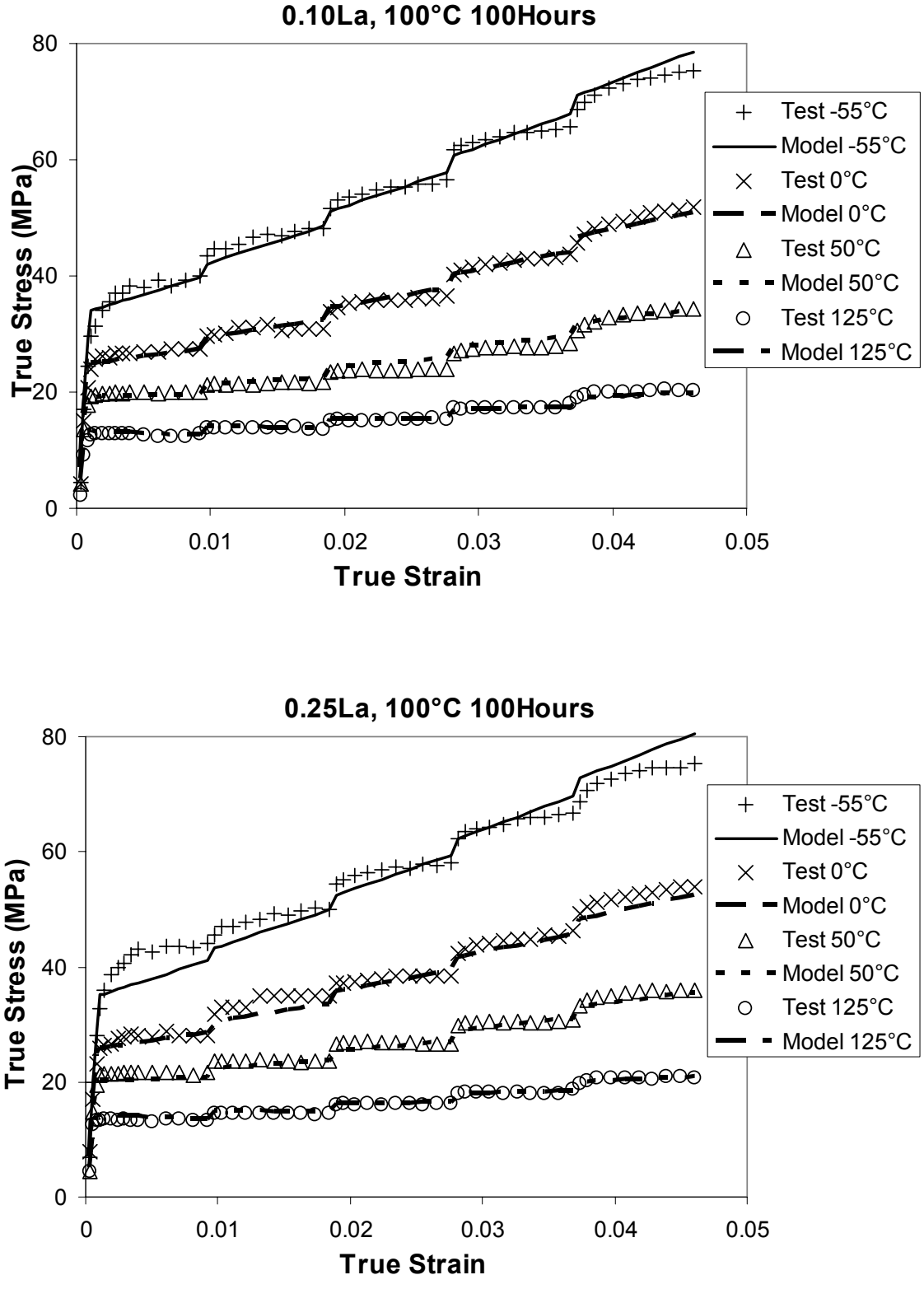

Figure 103: Modified Anand model fitting result of samples aged at 100°C for 100 hours (continue)

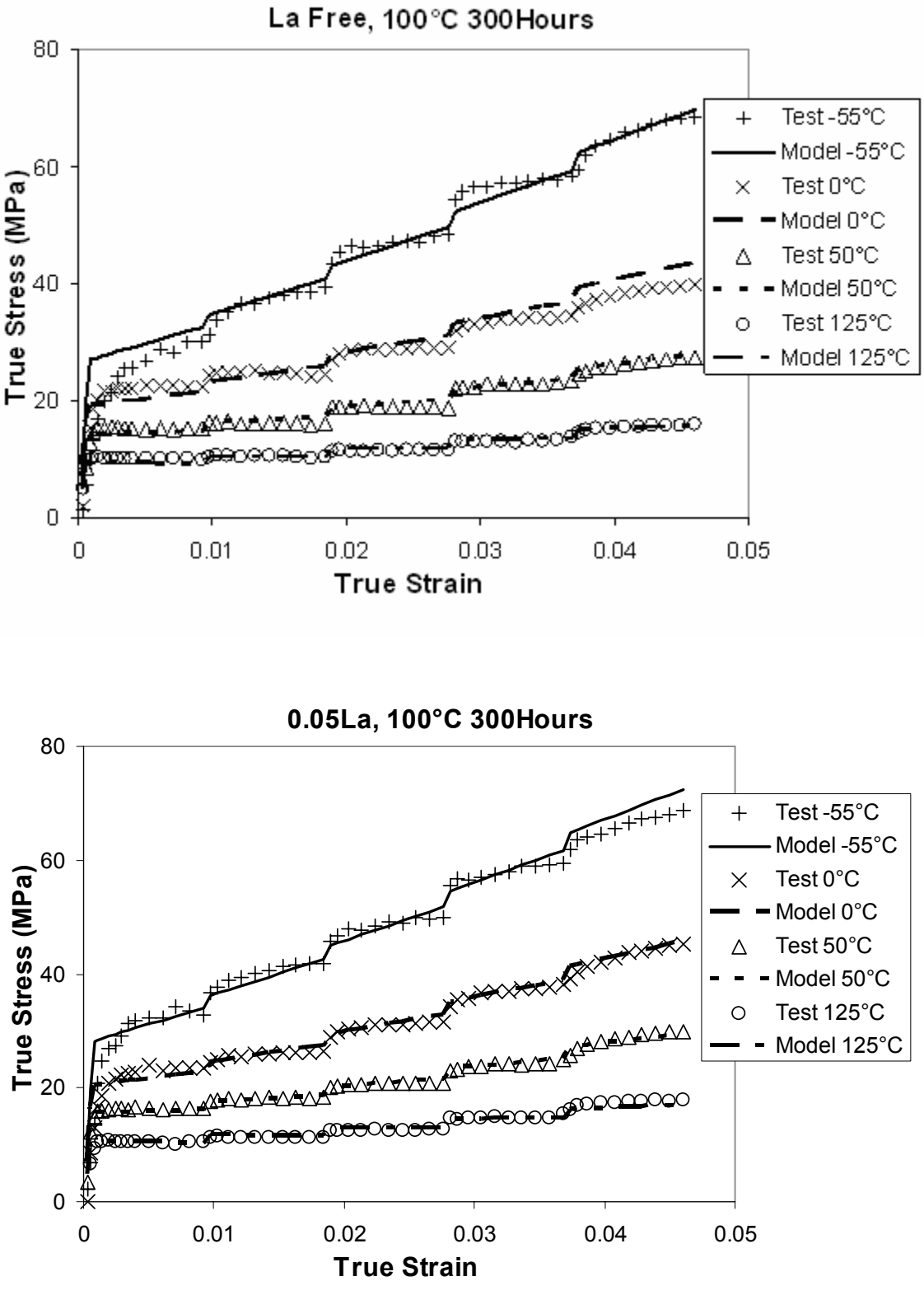

Figure 104: Modified Anand model fitting result of samples aged at 100°C for 300 hours

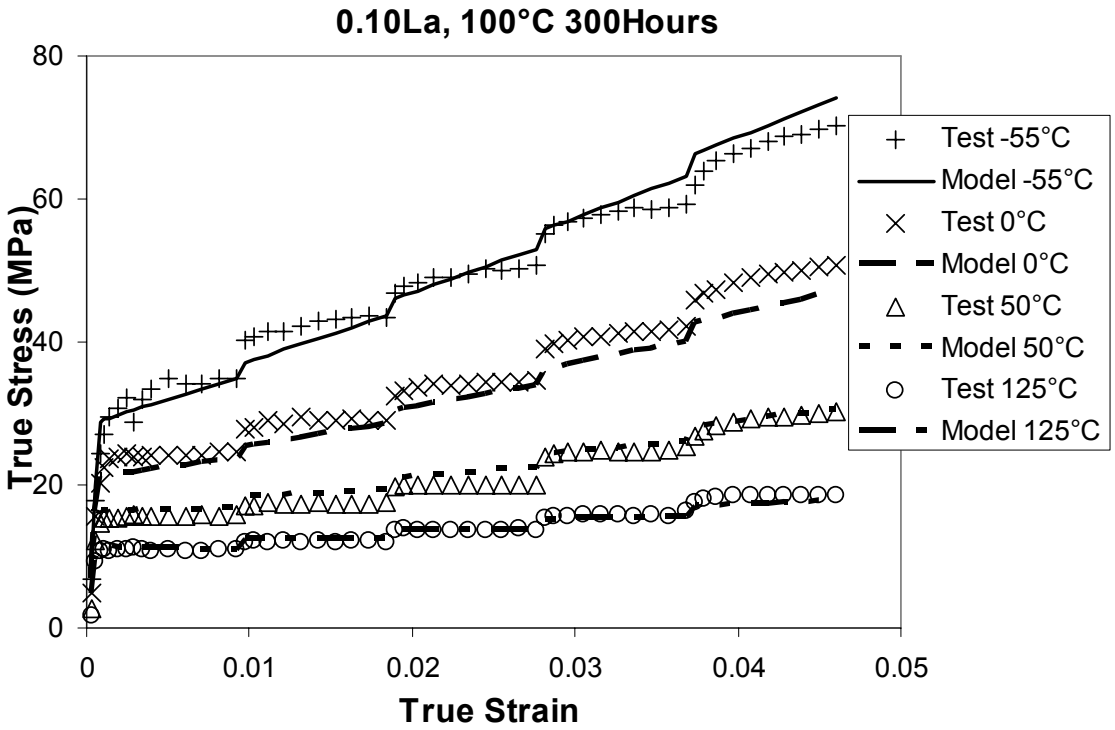

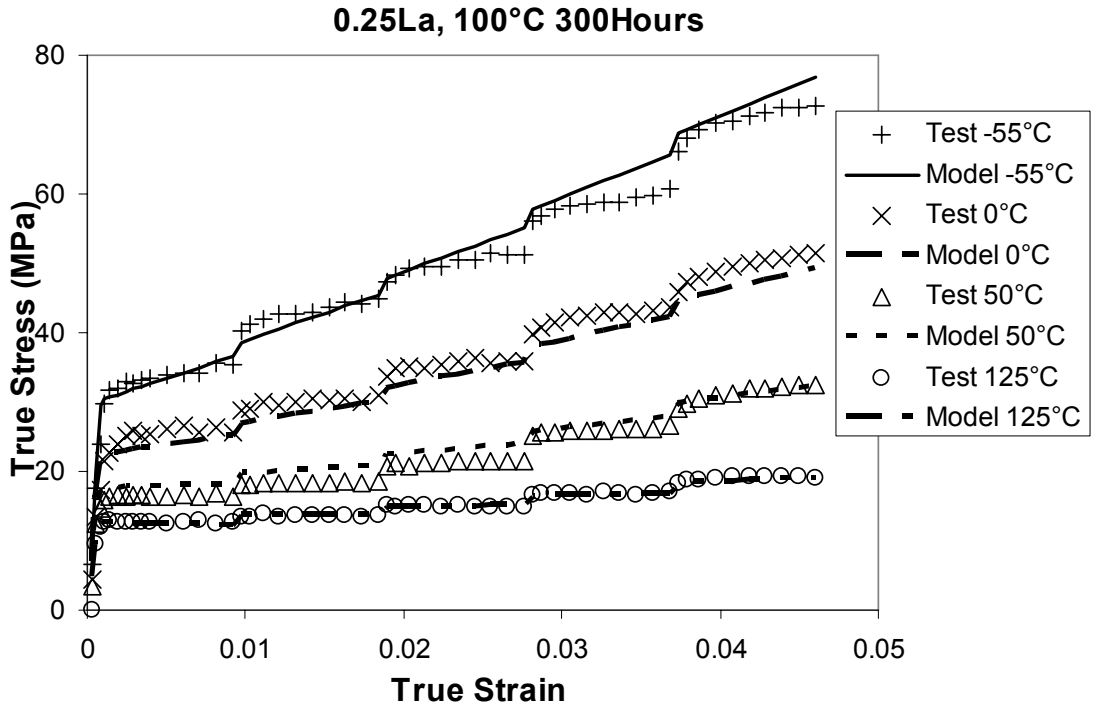

Figure 104: Modified Anand model fitting result of samples aged at 100°C for 300 hours (continue)

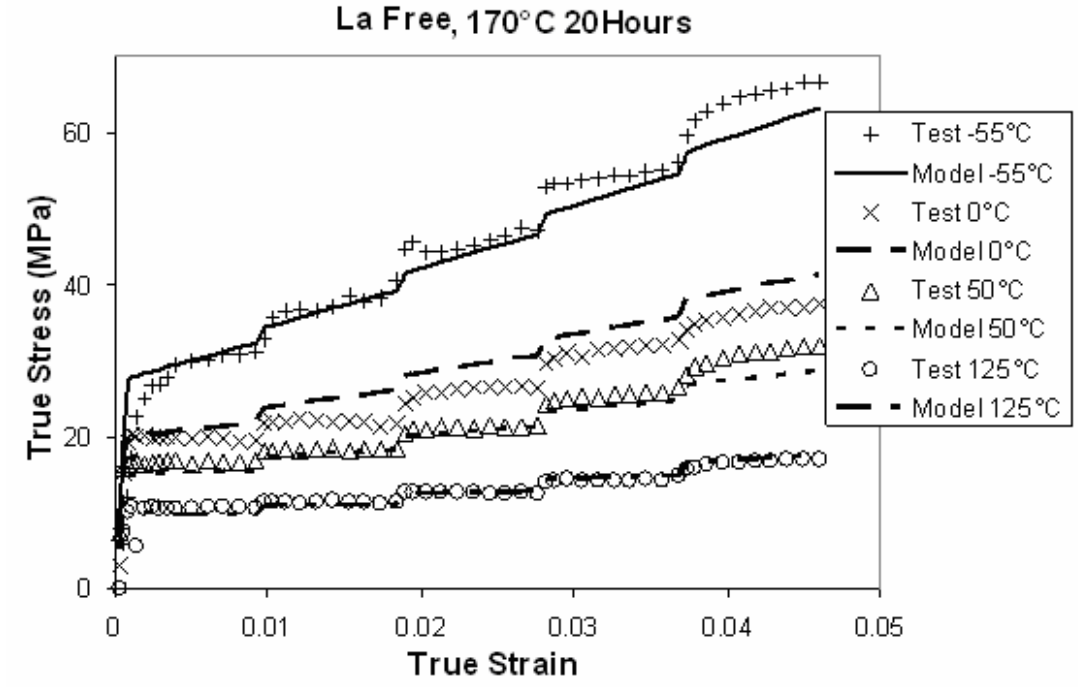

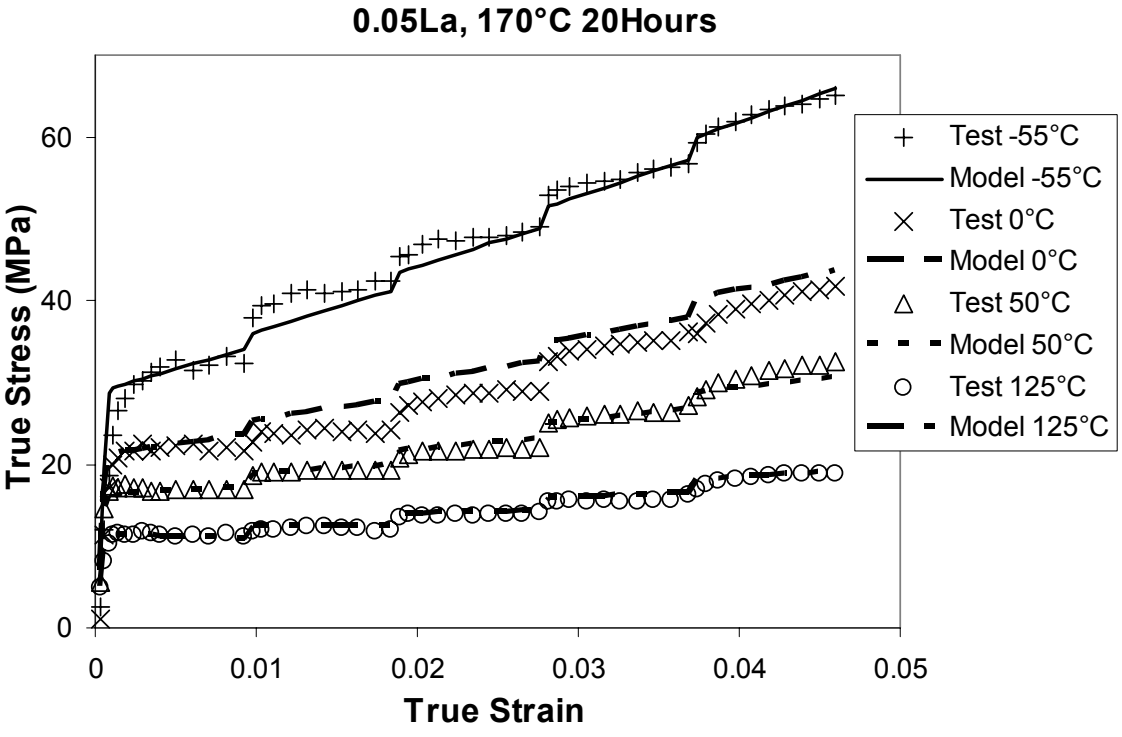

Figure 105: Modified Anand model fitting result of samples aged at 170°C for 20 hours

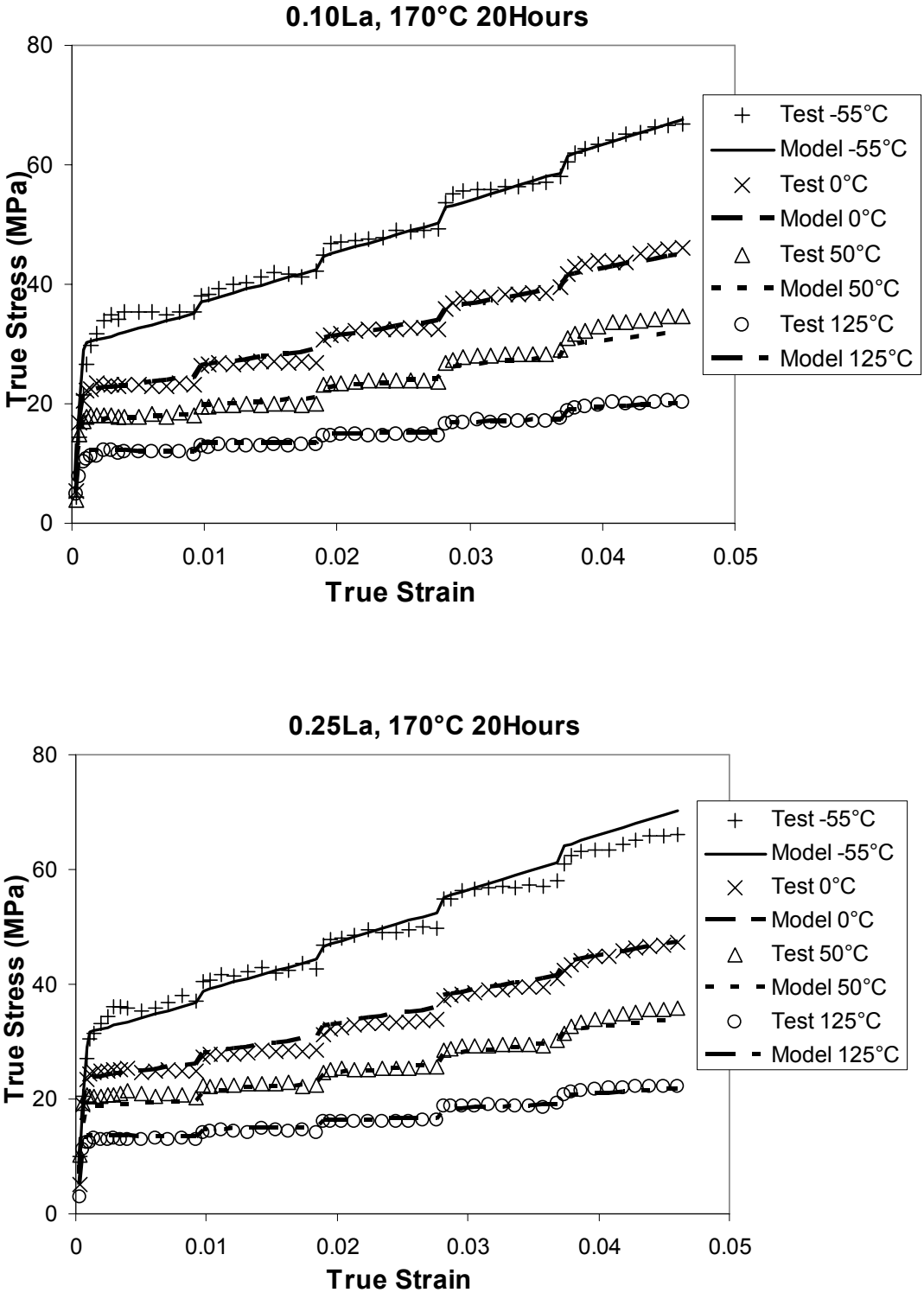

Figure 105: Modified Anand model fitting result of samples aged at 170°C for 20 hours (continue)

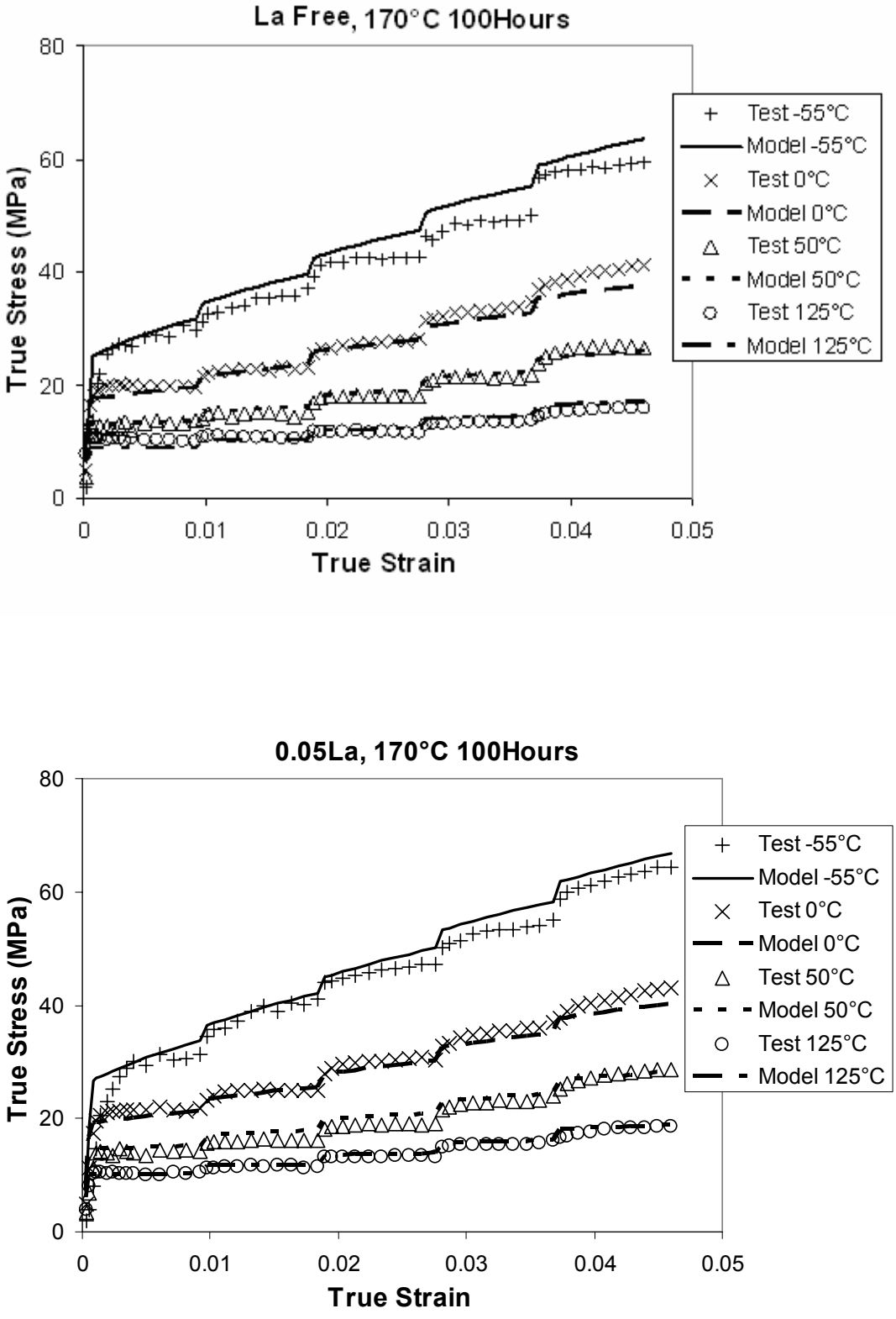

Figure 106: Modified Anand model fitting result of samples aged at 170°C for 100 hours

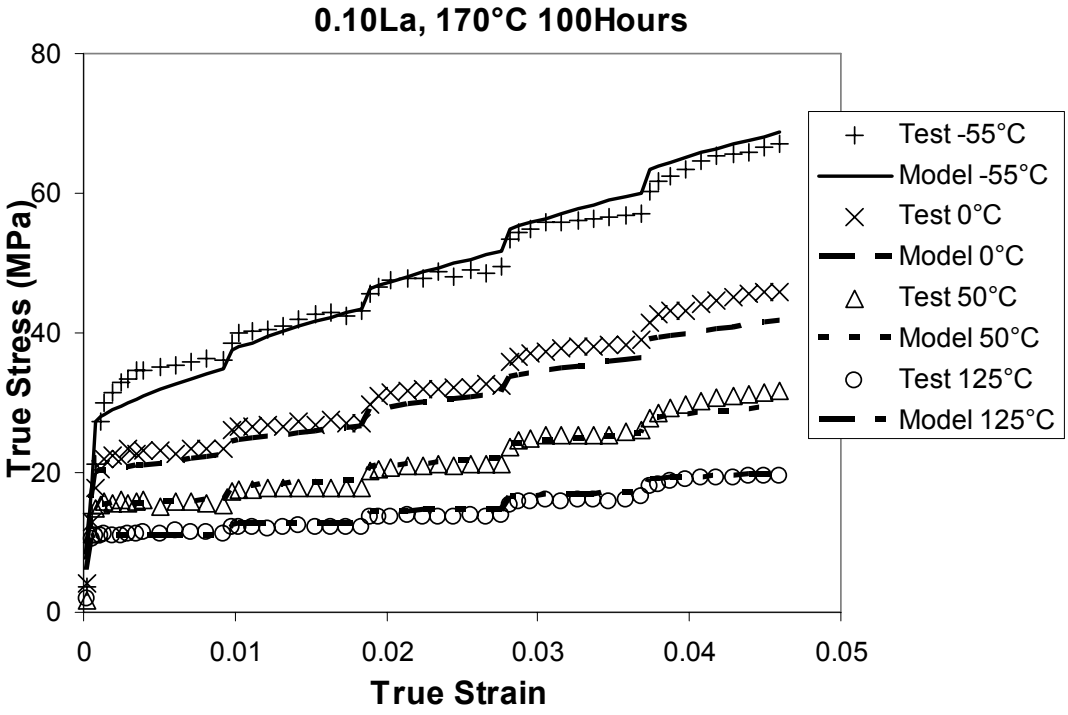

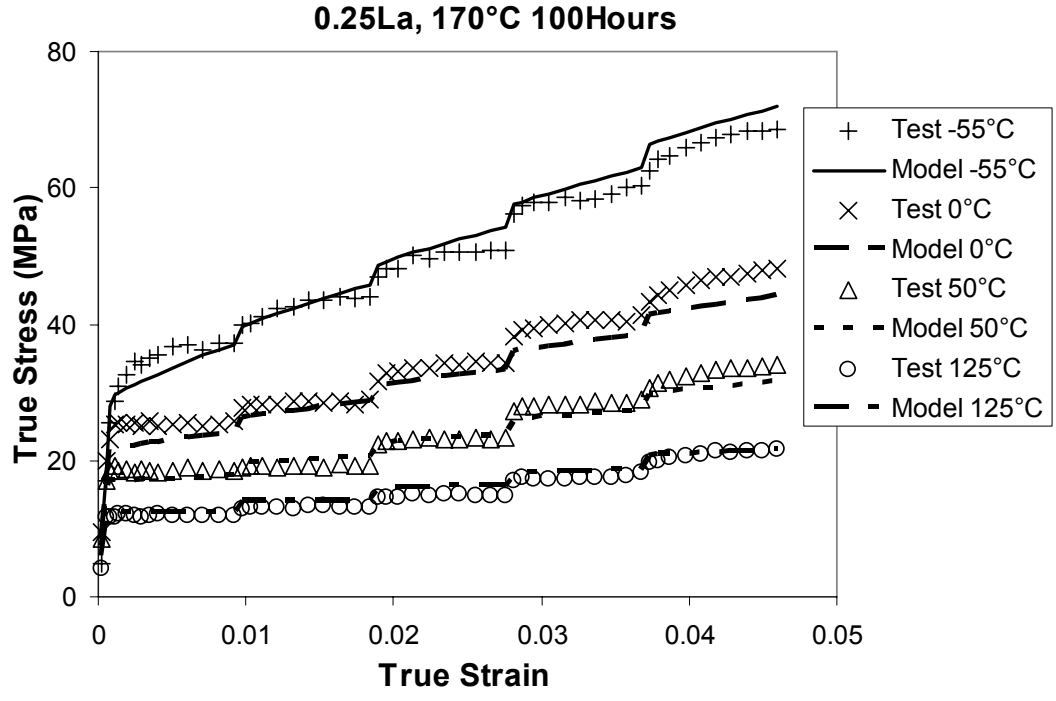

Figure 106: Modified Anand model fitting result of samples aged at 170°C for 100 hours (continue)

APPENDIX G

NANOINDENTATION TEST

Nanoindentation test was performed to study the creep property of Sn dendrite and eutectic regions in SnAg solder material. Nanoindentation has been used in solder materials before [96], but the existing tests consider the SnAg material as homogeneous material. As a result, a very small load was used to reduce the effected area and depth, in order to estimate the creep properties of Sn dendrite and eutectic region.

An un-doped sample and a 0.25%La doped sample were used in this study. The sample prepared is the same as in the microstructure study but no etching is necessary. A Berkovich type indenter is used with load control method. The indentation load was applied linearly to 8mN with the speed of 20mN/s and then held for 30 second. The typical load – displacement curve can be shown in Figure 107. With fixed loading level, the indented displacement will vary according to the pressed material. Indenter displacement on the softer Sn dendrite is much higher than that of test at eutectic region. Some data points of the indenter displacement at the end of holding period are shown in Figure 108. Note that the Y axis of final load is not start from 0. It can be seen that in general, doped solder is stiffer on both regions.

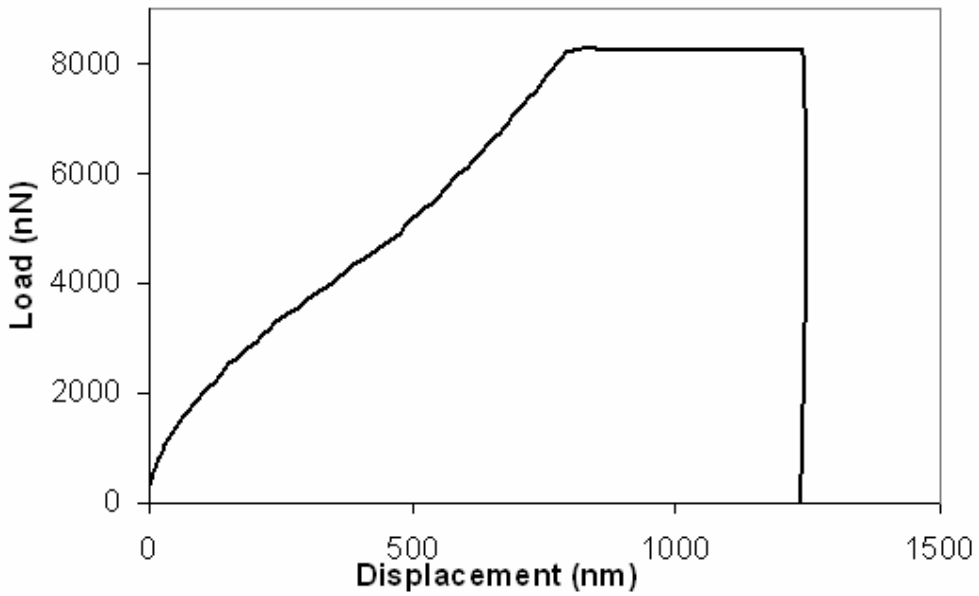

Figure 107: Typical nanoindentation loading curve

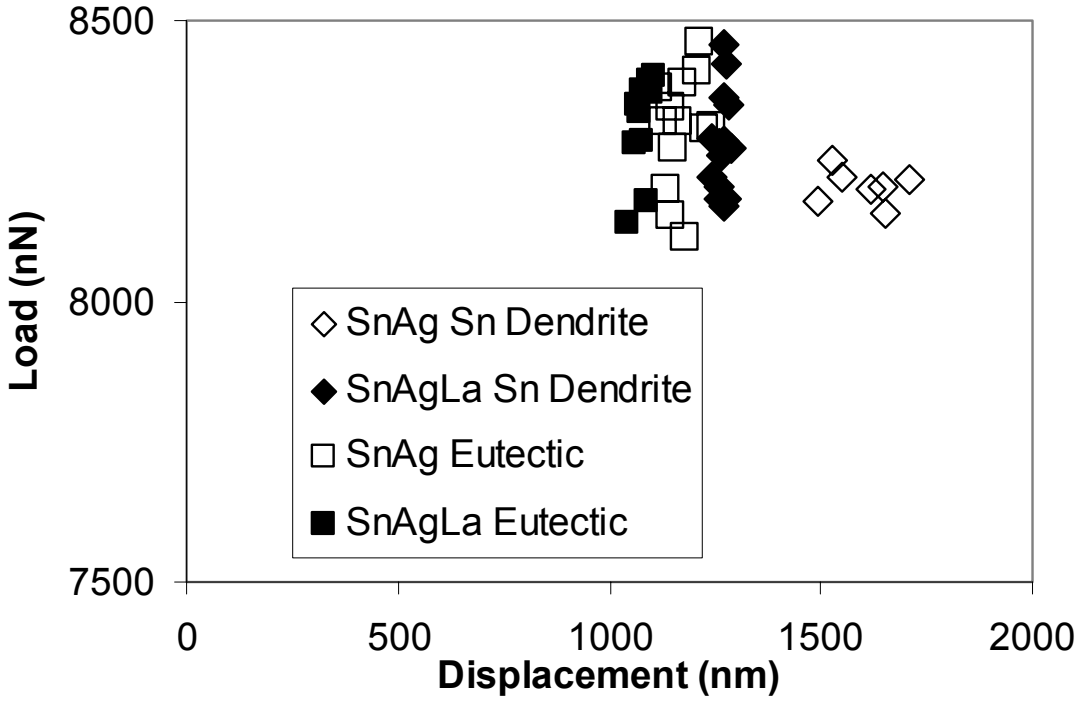

Figure 108: Final displacement of nanoindentation of two regions. Load axis not from zero

Currently there is no available method to extract creep property of indented material from test loading curves. A FEM model has to be used to simulate the nanoindentation test, as has been done in Gao *et al.*'s work [97], a 2D axisymmetric FEM model was established, as shown in Figure 109. Concentrated load was applied on the rigid body indenter to simulate the loading cure in nanoindentation test. By solving the contact problem in the FEM model, the indenter displacement can be obtained. A typical displacement field at the end of holding period is shown in Figure 109. At this load level, the effected indentation area is smaller than the character length scale of regions in the material.

As the nanoindentation test is only performed in room temperature, the power law creep model is simplified to be:

$$\dot{\varepsilon}^{cr} = A\sigma^{n} \quad \textbf{(33)}$$

To obtain the creep property of each region in the solder material, the FEM model result is fitted to the nanoindentation test. In the FEM model, by changing the creep constants A and n of the body material property, the indenter displacement was fit with the test curve. One example of a fit load-displacement curve compare with test curve is shown in Figure 110. The creep properties obtained from nanoindentation FEM fitting are show in Figure 111 and the constants are listed in Table 14.

Sn dendrite was found to be much stiffer than pure Sn. One possible reason is the solidus solution to serve as enforcement mechanism. In the alloy environment, the Sn phase contains 0.09at% of Ag in the form of solid solution [26]. The solid solute Ag exists in both the Sn dendrite region and the Sn matrix of eutectic structure.

It also can be noticed that La doped Sn dendrite is stiffer than that un-doped. The mechanism of La enforcing Sn phase is unknown at this point, but available models suggest that La atoms are able to stabilize the defects and serve as barrier for creep deformation [3].

It can be seen in Figure 111 that the La doped eutectic region is stiffer than that not doped. From conventional particle enforced metal model, La doped eutectic region should be softer because of relative low Ag_3Sn particle volume fraction. This conflict suggests that La doping provide enforcement on eutectic region.

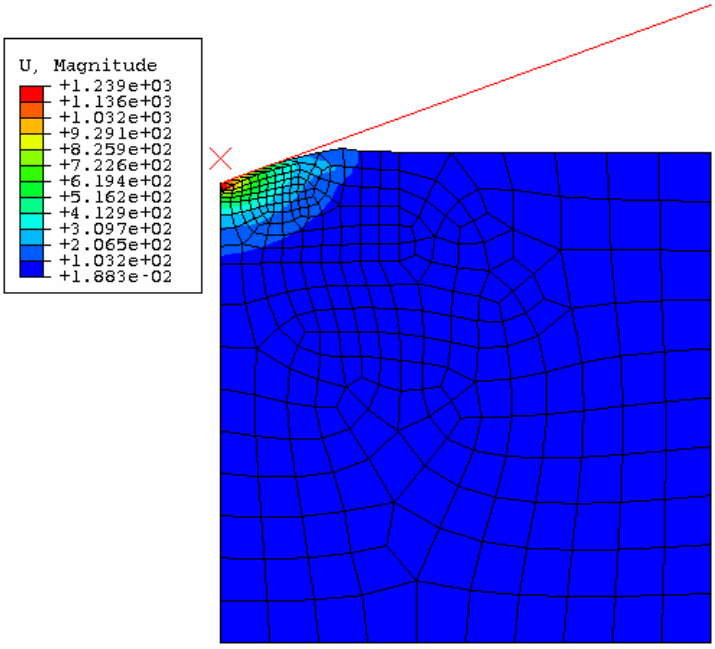

Figure 109: Typical FEM indentation model displacement field

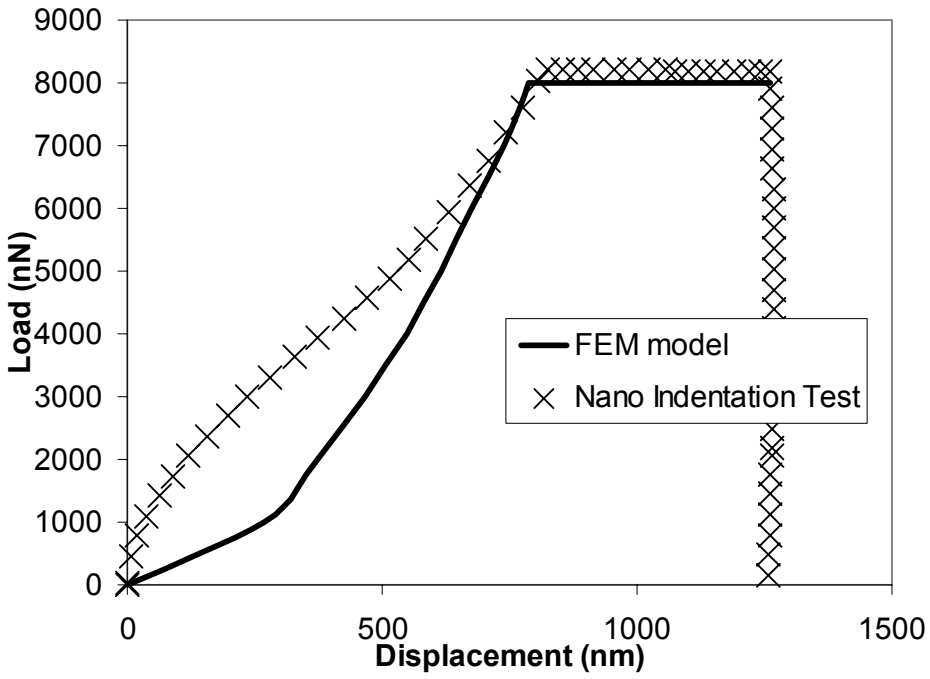

Figure 110: Nanoindentation study indenter displacement curve fitting example

Table 14: Power law creep model constants from nanoindentation test

	n	*A*
Sn dendrite in SnAg	15.5	4.3E-26
Sn dendrite in SnAg0.25La	17.0	6.8E-30
Eutectic region in SnAg	15.4	8.0E-29
Eutectic region in SnAgLa	12.9	1.5E-25

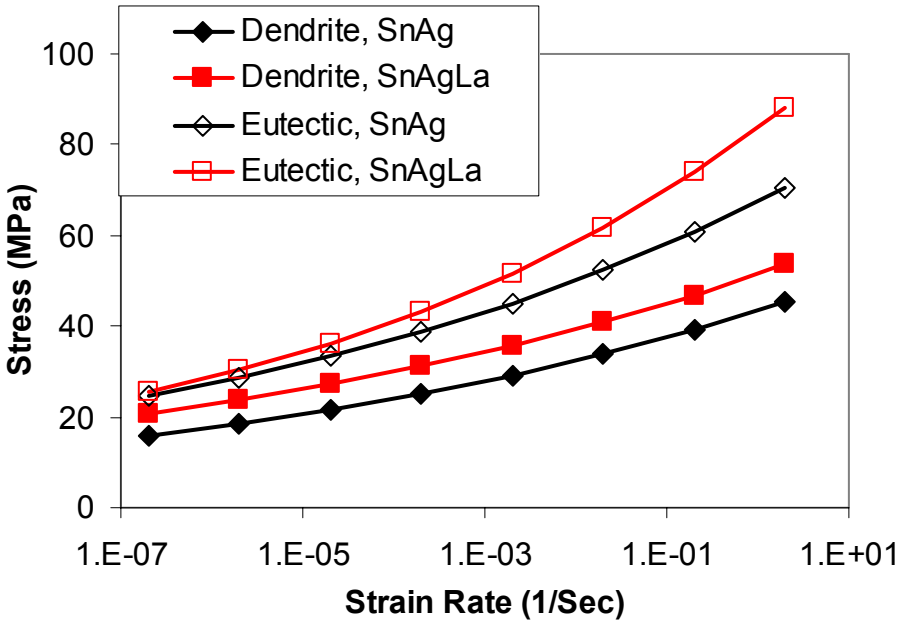

Figure 111: Region creep properties from nanoindentation test

APPENDIX H

MICROMECHANICAL COMPOSITE MATERIAL APPROACH

Composite material method was used to verify nanoindentation test result in the small length scale, and for creep behavior, classical method secant approach combined with Mori-Tanaka method is used. Through iteration of Mori-Tanaka method to calculate secant modulus of material, this method can solve inelastic behavior of composite materials.

Stress at 1% total strain was expected to be obtained from this model to serve as estimate of steady state creep stress. Iteration was needed to obtain this result. At the initial condition, the strain level of each phase is assumed to be at 1%. At this strain level, secant modulus of each phase can be calculated from power law creep model at given strain rate. At this point, a linear mean field theory can be used to calculate the effect secant modulus of the composite material. In this study, Mori-Tanaka method was used.

Mori-Tanaka method is a well established method to calculate the effective modulus of composite material. The derivation will not be listed here. In the final form, the effective stiffness tensor of the composite will be

$$\overline{\mathbf{L}} = \sum_{r=0}^{N} c_r \mathbf{L}_r \mathbf{T}_r \left[\sum_{n=0}^{N} c_n \mathbf{T}_n \right]^{-1} \quad \textbf{(34)}$$

where $\overline{\mathbf{L}}$ is the effective stiffness tensor for the composite material and $\mathbf{L}_i$ is the stiffness tensor of ith phase, with i=0 to be the matrix. c is the volume fraction of the phases. Tensor **T** depend on the geometry as defined as

$$\mathbf{T}_r = \left[\mathbf{I} + \mathbf{S}_r \mathbf{L}_0^{-1} \left(\mathbf{L}_r - \mathbf{L}_0 \right) \right]^{-1} \quad \textbf{(35)}$$

where **S** is the Eshelby tensor.

To use this model, the Ag_3Sn particles are considered to be in spherical shape and randomly dispersed through out Sn matrix. The matrix material is considered to be the Sn

dendrite material from nanoindentation and the particles are considered to be rigid material. With these assumptions, the composite material effective bulk modulus $\overline{K}$ and shear modulus $\overline{\mu}$ can be solved directly from moduli of each phase [71]:

$$\overline{K} = K_0 + \frac{c_1(K_1 - K_0)(3K_0 + 4\mu_0)}{3K_0 + 4\mu_0 + 3(1-c_1)(K_1 - K_0)} \quad (36)$$

$$\overline{\mu} = \mu_0 + \frac{5c_1\mu_0(\mu_1 - \mu_0)(3K_0 + 4\mu_0)}{5\mu_0(3K_0 + 4\mu_0) + 6(1-c_1)(\mu_1 - \mu_0)(K_0 + 2\mu_0)} \quad (37)$$

where subscript *0* is for matrix and *1* is for particles. c_1 is the volume fraction of the particles, and it is 0.180 for eutectic region in SnAg solder and 0.123 for that of SnAgLa solder. These values are calculated from microstructure study of phase volume in Chapter 3. In the model, secant modulus at given strain is used for Sn matrix and a large number is used for particle modulus.

After using Mori-Tanaka method to solve the composite material for the first step, effort was needed to remove the assumption that each phase strain level is equal to the target effective strain level. A classical method was used to estimate the averaged strain in each phase from effective strain [71]:

$$\begin{aligned}
&\tilde{\varepsilon}_m^{(0)} = A_m^{(0)}\bar{\varepsilon}_m, \quad \tilde{\varepsilon}_m^{(1)} = A_m^{(1)}\bar{\varepsilon}_m, \quad \tilde{\varepsilon}_{eq}^{(0)} = A_{eq}^{(0)}\bar{\varepsilon}_{eq}, \quad \tilde{\varepsilon}_{eq}^{(1)} = A_{eq}^{(1)}\bar{\varepsilon}_{eq}, \\
&A_m^{(0)} = \frac{1}{(1-c_1)}\frac{\overline{K} - K_1}{K_0 - K_1}, \quad A_m^{(1)} = \frac{1}{c_1}\frac{\overline{K} - K_0}{K_1 - K_0}, \\
&A_{eq}^{(0)} = \frac{1}{(1-c_1)}\frac{\overline{\mu} - \mu_1}{\mu_0 - \mu_1}, \quad A_{eq}^{(1)} = \frac{1}{c_1}\frac{\overline{\mu} - \mu_0}{\mu_1 - \mu_0}, \\
&\mu_0 = \mu_0^{Secant}\left(\tilde{\varepsilon}_{eq}^{(0)}\right), \qquad \mu_1 = \mu_1^{Secant}\left(\tilde{\varepsilon}_{eq}^{(1)}\right)
\end{aligned} \quad (38)$$

where equivalent total strain $\bar{\varepsilon}_{eq}$ was set to be 1% in this case. In equation (38), both phases can have inelastic deformation. For Sn matrix phase, the secant modulus will be re-calculated from the averaged phase strain $\tilde{\varepsilon}_{eq}^{(0)}$. But in this case, the particles are assumed stiff and elastic modulus is used, so their modulus does not need to be re-

calculated. These new modulus can be put in Mori-Tanaka method for next step of iteration. After iteration, the stress at targeted total strain can be obtained.

This procedure repeated for several strain rate conditions and the result is fit into the simple power law form in equation (33). The model constant is listed in Table 15 and the comparison of the model result with nanoindentation result is plot in Figure 47. Because this model only considered the particle enforcement but not the La atoms, the model underestimated the La doped eutectic region slightly. But these two methods get relative close result. To reduce the dependence to the experiment data, the composite material model result will be used in the large length scale.

Table 15: Creep model constant obtained with micromechanics composite model

	n	A
Eutectic region in SnAg	15.5	2.3E-29
Eutectic region in SnAgLa	15.5	4.3E-26

APPENDIX I

FEM PERIODIC BOUNDARY CONDITIONS

The Periodic boundary condition was applied to the 2D problem. The linear constraint equation function provided by ABAQUS [98] was used to apply the periodic boundary condition. Linear equations of the displacement can be input into ABAQUS and the displacement of the term appearing in the equation will be eliminated to impose the constraint. In our 2D case, the degrees of freedom of Edge 1, Edge 4 and of corner points C14, C24 will be eliminated.

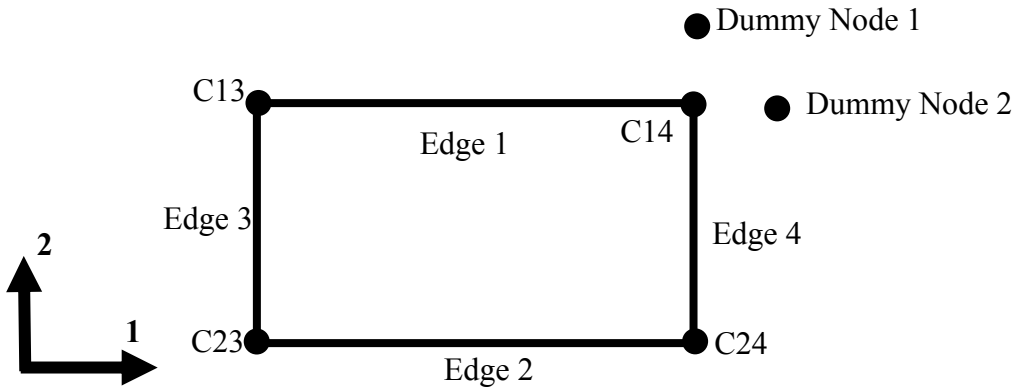

Figure 112: Edge and corner nomination for the periodic boundary condition

To provide the periodic boundary condition, two dummy nodes are added to the model. The location of the dummy node is not important. Dummy nodes also provided the ability to apply far field strain loading to the model. For the nodes pairs in Edge 1 & 4 excluding corner points, the constraint equations are:

$$u_i^{Edge1} = u_i^{Edge2} + u_i^{DummyNode1}$$
$$u_i^{Edge4} = u_i^{Edge3} + u_i^{DummyNode2} \qquad i = 1,2 \qquad \textbf{(39)}$$

where u_i is the displacement in different directions. The constraint equations for the corner points are:

$$u_i^{C14} = u_i^{C23} + u_i^{DummyNode1} + u_i^{DummyNode2}$$
$$u_i^{C24} = u_i^{C13} - u_i^{DummyNode1} + u_i^{DummyNode2} \qquad i = 1,2 \qquad \textbf{(40)}$$

Other than the periodic boundary conditions, some conventional boundary condition has to be applied to prevent rigid body movement of the model. One should bear in mind that degrees of freedom on the left hand side of the above equations have been eliminated so the boundary condition cannot be applied there. The boundary conditions are applied on the center points in this case, on the point C23:

$$u_i^{23} = 0 \qquad \textbf{(41)}$$

Displacement Loading

Displacement loading was applied to the model. Several load cases are applied including tensile loading on 1 and 2-directions and shear loading on both directions. To simulate the far field of displacement loading, moveable boundary conditions are applied to the dummy nodes. In all the cases, the initial boundary conditions are assigned to be zero and the final displacements were assigned to be equivalent to 1% total strain to the structure. The loading time is adjusted to achieve far field strain speed.

Tensile in 1-direction

In the tensile test, the distance between parallel edges will be assigned. The restrictions on the other pair of edges will be loosened to compensate for the shrinkage of Poission's ratio.

In the tensile loading in the 1-direction case, 1-direction of displacement was added on dummy node 2 to force the distance between edges 3 and 4 to become larger:

$$u_1^{DummyNode2} = u \qquad \textbf{(42)}$$

where u is the displacement applied. With the final strain of 1%, the u=1 %•(length of Edge1). Mean while, the restriction on the 2-direction of dummy node 1 will be removed for the surface condition:

$$u_2^{DummyNode1} = N / A \quad \textbf{(43)}$$

The other directions of the two dummy nodes are applied to ensure that the parallel edges keep parallel to each other.

$$\begin{aligned} u_2^{DummyNode2} &= 0 \\ u_1^{DummyNode1} &= 0 \end{aligned} \quad \textbf{(44)}$$

Tensile in 2-direction

Similar to the 1-direction, the displacement loading for tensile testing in the 1-direction are:

$$\begin{aligned} u_2^{DummyNode1} &= v \\ u_1^{DummyNode2} &= N / A \\ u_1^{DummyNode1} &= 0 \\ u_2^{DummyNode2} &= 0 \end{aligned} \quad \textbf{(45)}$$

where in this case the v=1 %•(length of Edge3) for 2-direction displacement loading.

Pure Shear

For pure shear loading, both pairs of parallel edges have relative shifting while their distance is kept constant. The equations will be:

$$\begin{aligned} u_1^{DummyNode1} &= u \\ u_1^{DummyNode2} &= 0 \\ u_2^{DummyNode1} &= 0 \\ u_2^{DummyNode2} &= v \end{aligned} \quad \textbf{(46)}$$

where in this case the u=1 %•(length of Edge1) and v=1 %•(length of Edge3)

APPENDIX J

DEFORMATION FILED OF SnAgLa ALLOY IN DIB MODEL

The result of digital image based (DIB) model study is listed in this section for SnAgLa model. The equivalent creep strain is shown in Figure 113. The displacement field is listed in Figure 114 and Figure 115 for 1 and 2-directions, respectively. The Von Mises stress field is shown in Figure 116.

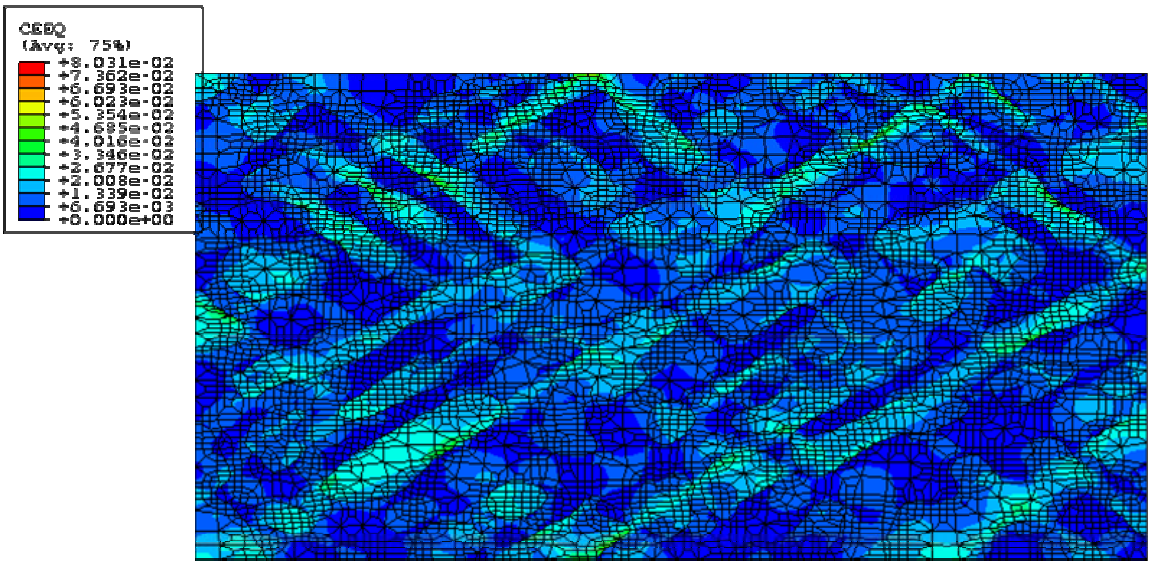

(a) 1-direction loading

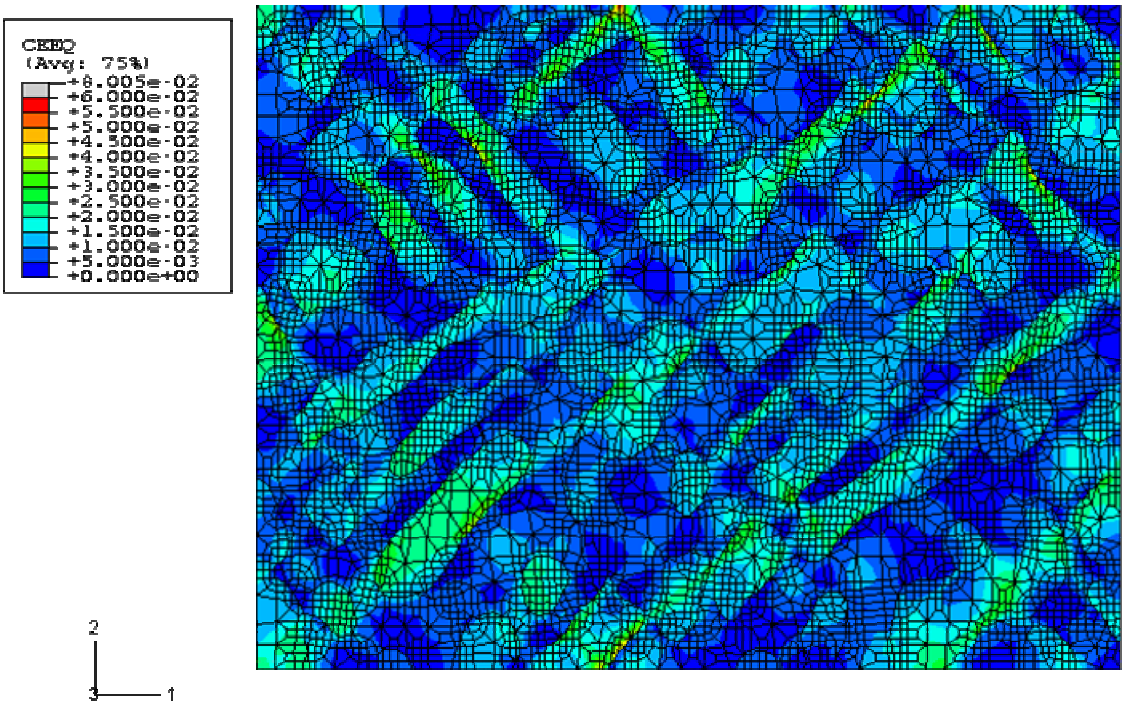

(b) 2-direction loading

Figure 113: Equivalent creep strain of La doped alloy DIB model

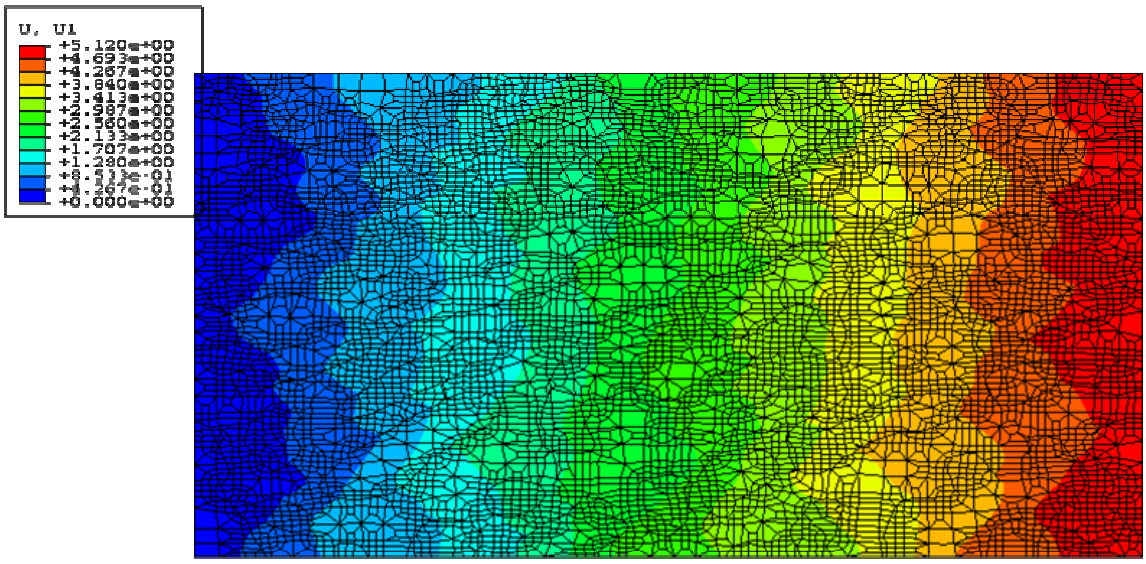

(a) 1-direction loading

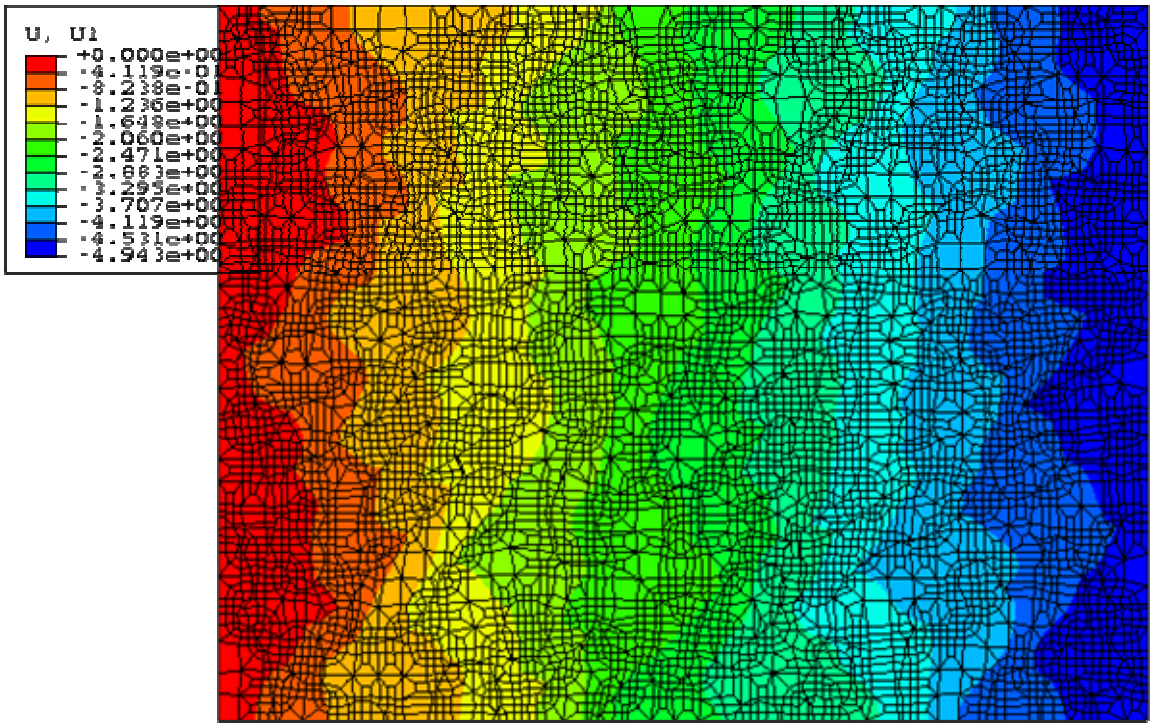

(b) 2-direction loading

Figure 114: 1-direction displacement field of La doped alloy DIB model

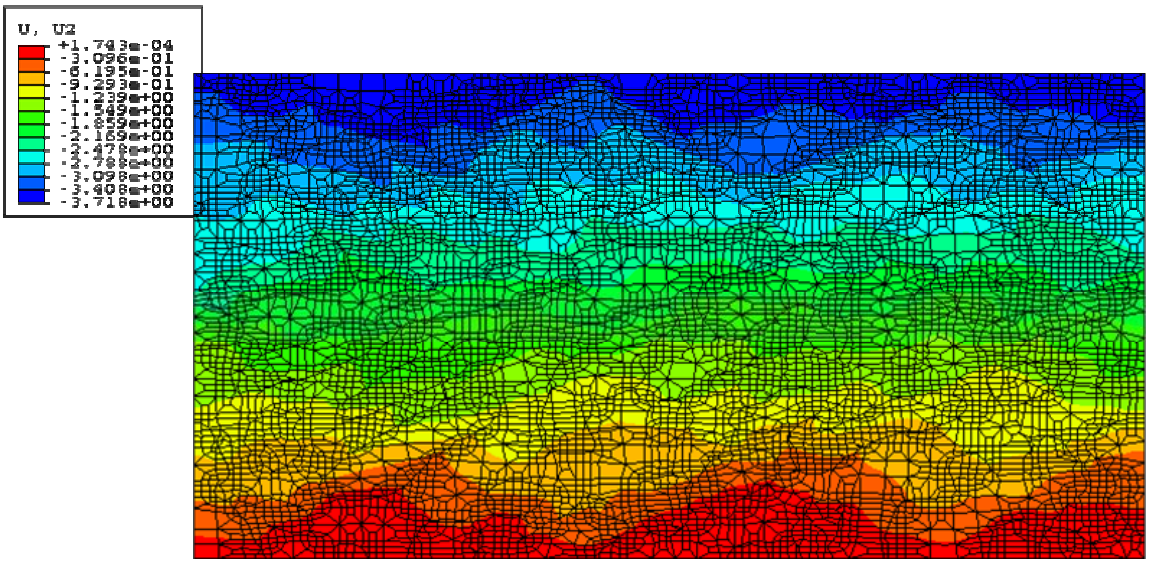

(a) 1-direction loading

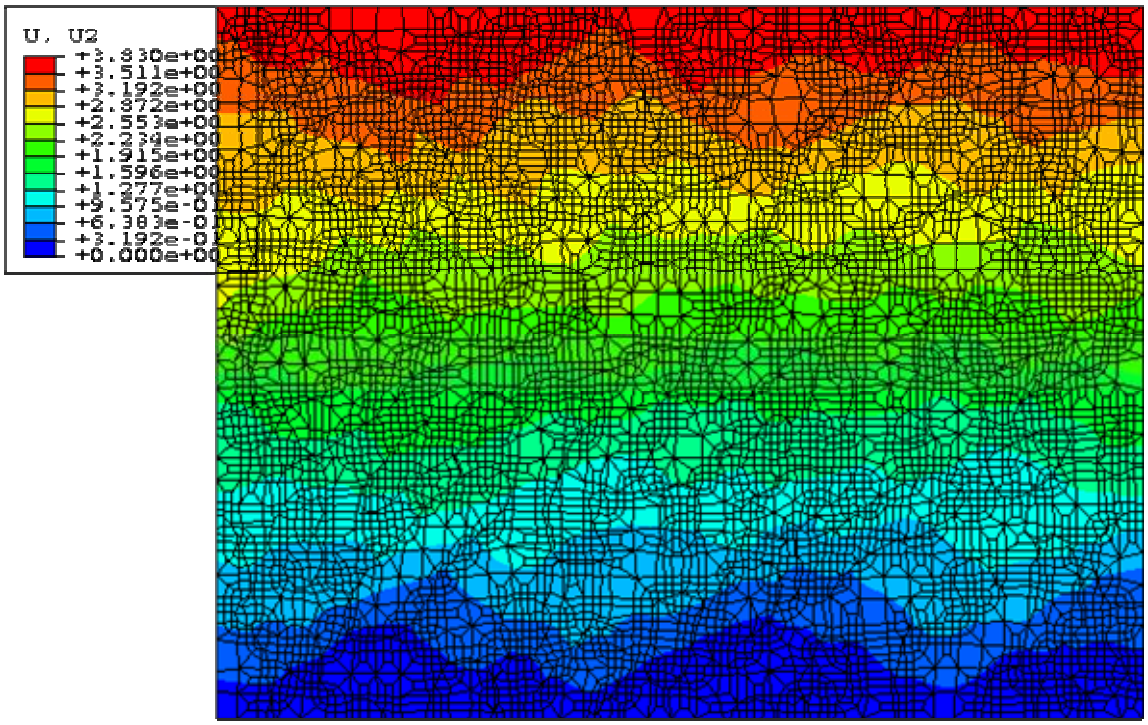

(b) 2-direction loading

Figure 115: 2-direction displacement field of La doped alloy DIB model

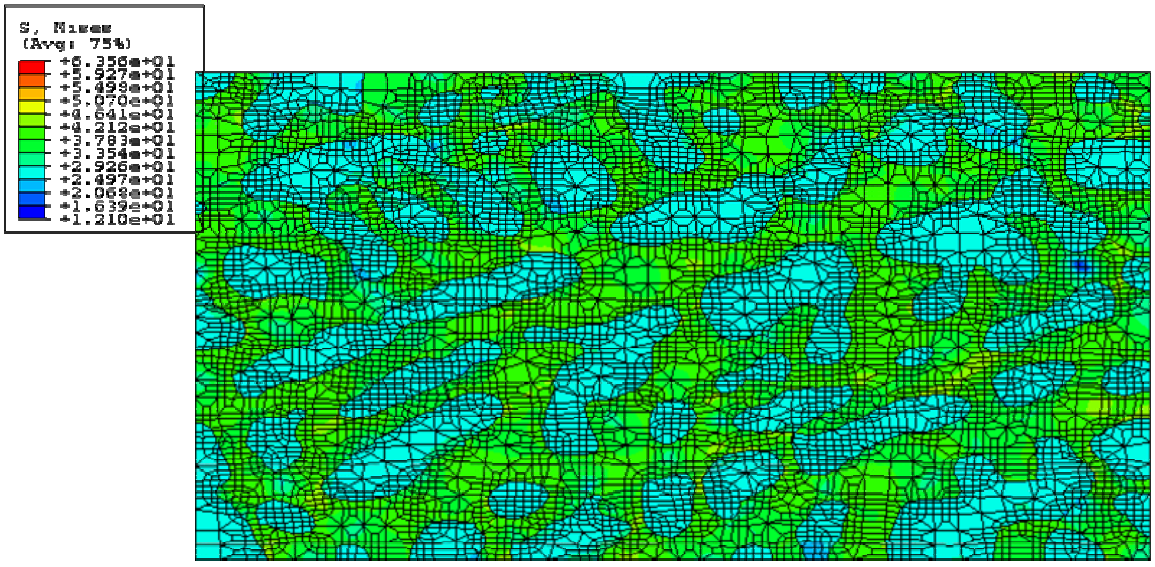

(a) 1-direction loading

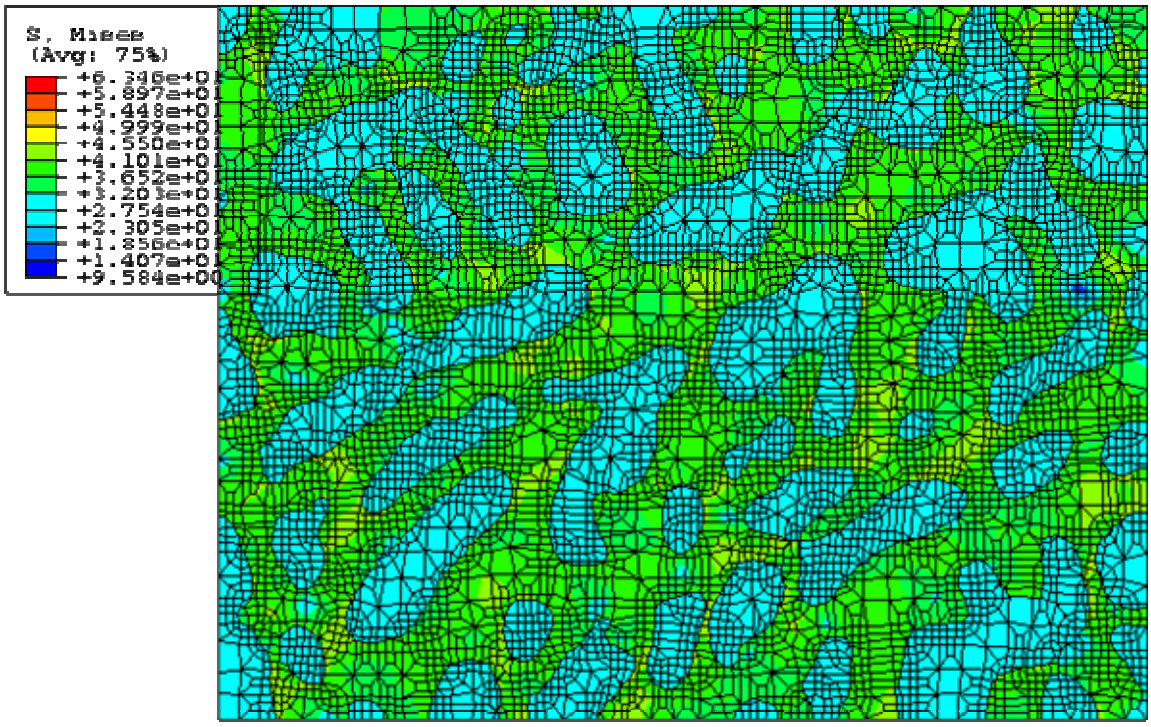

(b) 2-direction loading

Figure 116: Von Mises stress field of La doped alloy DIB model

REFERENCES

[1] Ku, A., Oetinscitan, O., Saphores, J.-D., Shapirod, A., Schoenunp, J.M., Lead-free solders. issues of toxicity, availability and impacts of extraction, Electronic Components and Technology Conference, 2003, pp 47 – 53.

[2] Bradley, E., Lead-free solder assembly: impact and opportunity, Electronic Components and Technology Conference, 2003, pp 41 – 46.

[3] Chen, Z.G., Shi, Y.W.; Xia, Z.D.; Yan, Y.F., Study on the microstructure of a novel lead-free solder alloy SnAgCu-RE and its soldered joints, Journal of Electronic Materials, v 31, n 10 SPEC., 2002, pp 1122-1128.

[4] Mavoori, H., Ramirez, A.G.; Jin, S., Lead-free universal solders for optical and electronic devices, Journal of Electronic Materials, v 31, n 11, 2002, pp 160-1165.

[5] Jin, S., Rare-Earth-Enabled Universal Solders for Microelectro-mechanical Systems and Optical Packaging, Journal of Electronic Materials, v 32, n 12, 2003, pp 1366-1370.

[6] Ramirez, A.G., Mavoori, H., Jin, S., Bonding nature of rare-earth-containing lead-free solders, Applied Physics Letters, v 80, n 3, 2002, pp 398.

[7] Ma, X.; Qian, Y, Yoshida, F., Effect of La on the Cu-Sn intermetallic compound (IMC) growth and solder joint reliability, Journal of Alloys and Compounds, 334, 2002, pp 224-2270.

[8] Yu, D.Q., Law, C.M.T., Wang, L., Wu, C.M.L., The properties of Sn-9Zn lead-free solder alloys doped with trace rare earth elements, Journal of Electronic Materials, v 31, n 9, 2002, pp 921-927

[9] Mavoori, H. , Jin, S., New, creep-resistant, low melting point solders with ultra fine oxide dispersions, Journal of Electronic Materials, v 27, n 11, 1998, pp 1216-1222.

[10] Choi, S., Lee, J.G., Guo, F., Bieler, T.R., Subramanian, K.N., Lucas, J.P., Creep properties of Sn-Ag solder joints containing intermetallic particles, JOM, June 2001, pp 22-26.

[11] Lee A.; Subramanian K.N.; Lee J.; Development of Nanocomposite Lead-Free Electronic Solders, IEEE/CPMT, 10th International Symposium on Advanced Packaging Materials: Processes, Properties and Interfaces, Mar, 16-18, 2005, pp 267-281

[12] http://en.wikipedia.org/wiki/Rare_earth, as of Mar. 2007

[13] Anon, Rare-Earth solders Make Better Bounds, Photonics Spectra, v36, n5, 2002, pp139.

[14] Yu, D.Q., Law, C.M.T.; Wang, L.; Wu, C.M. L, Microstructure and mechanical properties of new lead-free Sn-Cu-Re solder alloys, Journal of Electronic Materials, v 31, n 9, 2002, pp 928-932.

[15] Yu, D.Q., Zhao, J., Wang, L., Improvement on the microstructure stability, mechanical and wetting properties of Sn-Ag-Cu lead-free solder with the addition of rare earth elements, Journal of Alloys and Compounds, 376, 2004, pp 170-175.

[16] Wu, C.M.L., Yu, D.Q., Law, C.M.T., Wang, L., Improvements of microstructure, wettability, tensile and creep strength of eutectic Sn-Ag alloy by doping with rare-earth elements, Journal of Materials Research, v 17, n 12, 2002, pp 3146-3154.

[17] Chen, Z.; Shui, Y.; Xia, Z., Constitutive Relations on Creep for SnAgCuRE Lead-Free Solder Joints, Journal of Electronic Materials, v33, n9, 2004, pp 964-971.

[18] Wang, L., Yu, D.Q.; Huang, M.L.; Zhao, Jie, Improvement of wettability and tensile property in Sn-Ag-RE lead-free solder alloy, Materials Letters, v 56, n 6, 2002, pp 1039-1042.

[19] Ma, X.; Qian, Y.; Yoshida, F., Effect of La on the Sn-rich halo formation in Sn60-Pb40 alloy, Journal of Alloys and Compounds, v 327, n 1-2, 2001, pp 263-266.

[20] Zhu,Y., Fang, H., Qian, Y., Study of Sn-Pb-RE solder, Materials Research Society Symposium Proceedings, v 323, Electronic Packaging Materials Science VII, 1994, pp 137-143.

[21] Chen, Z.G., Shi, Y.W.; Xia, Z.D.; Yan, Y.F., Study on the microstructure of a novel lead-free solder alloy Sn-Ag-Cu-RE and its soldered joints, Journal of Electronic Materials, v 31, n 10 SPEC., 2002, pp 1122-1128.

[22] Xia, Z., Chen, Z.; Shi, Y.; Mu, N.; Sun, N., Effect of rare earth element additions on the microstructure and mechanical properties of tin-silver-bismuth solder, Journal of Electronic Materials, v 31, n 6, 2002, pp 564-567.

[23] Chen, Z,; Shi, Y.; Xia, Z.; Yan, Y., Properties of lead-free solder SnAgCu containing minute amounts of rare earth, Journal of Electronic Materials, v 32, n 4, 2003, pp 235-243.

[24] Wu, C.F.J, Hamada, M, Experiments Planning, Analysis, and Parameter Design Optimization, John Whiley & Sons, INC.2000

[25] http://www.boulder.nist.gov/div853/lead%20free/part2.html#%202.2.19 as in Dec. 2006.

[26] Karakaya, I., Thompson, W.T., Bulletin of Alloy Phase Diagrams, 8, 4, 1987, pp 340-347.

[27] Wiese, S.; Meusel, E.; Wolter, Klaus-Juergen, Microstructural dependence of constitutive properties of eutectic Sn-Ag and Sn-Ag-Cu solders, Proceedings - Electronic Components and Technology Conference, 2003, pp 197-206.

[28] Henderson, Donald W., Gosselin, Timothy; Sarkhel, Amit; Kang, Sung K.; Choi, Won-Kyoung; Shih, Da-Yuan; Goldsmith, Charles; Puttlitz, Karl J. , Ag3Sn plate formation in the solidification of near ternary eutectic Sn-Ag-Cu alloys, Journal of Materials Research, v 17, n 11, 2002, pp 2775-2778.

[29] Kang, S.K., Choi, W.K.; Shih, D.; Henderson, D.W.; Gosselin, T.; Sarkhel, A.; Goldsmith, C.; Puttlitz, K.J., Ag3Sn plate formation in the solidification of near-ternary eutectic Sn-Ag-Cu, JOM, v 55, n 6, 2003, pp 61-65.

[30] Kang, S.K., Choi, W.K.; Shih, D.; Henderson, D.W.; Gosselin, T.; Sarkhel, A.; Goldsmith, C.; Puttlitz, K.J., Formation of Ag3Sn plates in Sn-Ag-Cu alloys and optimization of their alloy composition, Proceedings - Electronic Components and Technology Conference, 2003, pp 64-70.

[31] Xiao, Q., Nguyen, L., Armstrong, W., 2004, Aging and Creep Behavior of Sn3.9Ag0.6Cu Solder Alloy, Electronic Components and Technology conference, 2004, pp 1325.

[32] Telang, A.U., Bieler, T.R., Choi, S., Subramanian, K.N., Orientation imaging studies of Sn-based electronic solder joints, Journal of Materials Research, v 17, n 9, 2002, pp 2294-2306.

[33] Dutta, I., A constitutive model for creep of lead-free solders undergoing strain-enhanced microstructural coarsening: A first report, Journal of Electronic Materials, v 32, n 4, 2003, pp 201-207.

[34] Kanchanomai, C., Yamamoto, S., Miyashita, Y., Mutoh, Y., McEvily, A.J., Low cycle fatigue test for solders using non-contact digital image measurement system, International Journal of Fatigue, v 24, n 1, 2002, pp 57-67.

[35] Kanchanomai, C.; Miyashita, Y.; Mutoh, Y.; Low-cycle fatigue behavior and mechanisms of a lead-free solder 96.5Sn/3.5Ag, Journal of Electronic Materials, v 31, n 2, 2002, pp 142-151.

[36] Kanchanomai, C.; Miyashita, Y.; Mutoh, Y.; Low-cycle fatigue behavior of Sn-Ag, Sn-Ag-Cu, and Sn-Ag-Cu-Bi lead-free solders, Journal of Electronic Materials, v 31, n 5, 2002, pp 456-465.

[37] Telang, A.U., Bieler, T.R., Mason, D.E., Subramanian, K.N., Comparisons of experimental and computed crystal rotations caused by slip in crept and thermomechanically fatigued Dual-shear eutectic Sn-Ag solder joints, Journal of electronic materials, Vol.32, No.12, 2003, pp 1455-1462.

[38] Zhao, J., Miyashita, Y., Mutoh, Y., Fatigue crack growth behavior of 96.5Sn-3.5Ag lead-free solder, International Journal of Fatigue, v 23, n 8, 2001, pp 723-731.

[39] Zhao, J.; Mutoh, Y.; Miyashita, Y.; Wang, L.; Fatigue crack growth behavior of Sn-Pb and Sn-based lead-free solders, Engineering Fracture Mechanics, v 70, n 15, 2003, pp 2187-2197.

[40] ASM Handbook, Vol. 9, Metallography and Microstructures, edited by G. F. VanderVoort, ASM International, 2004

[41] Dudek, M.A., Sidhu, R.S., Chawla, N., Novel Rare-Earth-Containing Lead-Free Solders with Enhancd Ductility, JOM, 58, 6, 2006, pp 57.

[42] Buban, J., Matsunaga, K. Chen, J., Shibata, N., Ching, W., Yamamoto, T., Ikuhara, Y., Grain Boundary Strengthening in Alumina by Rare Earth Impurities, Science, 311, 1, 2006, pp 212-215.

[43] Telang, A.U.; Bieler, T.R.; Lucas, J.P.; Subramanian, K.N.; Lehman, L.P.; Xing, Y.; Cotts, E.J., Grain-Boundary Character and Grain Growth in Bulk Tin and Bulk Lead-Free Solder Alloys, Journal of Electronic Materials 33, 12, 2004, pp 1412-1423.

[44] Callister, Jr., W., 1985, Materials Science and Engineering: An Introduction, Wiley, New York.

[45] Allen, S.L.; Notis, M.R.; Chromik, R.R.; Vinci, R.P., Microstructural evolution in lead-free solder alloys: Part I. Cast Sn-Ag-Cu eutectic, J. Mater. Res., Vol. 19, No. 5, 2004, pp 1417-1424.

[46] Senkov, O. N., and Myshlyaev, M. M., Grain Growth in a Superplastic Zn-22% Al Alloy, Acta metallurgica, 34, 1986, pp 97–106.

[47] Allen, S.L.; Notis, M.R.; Chromik, R.R.; Vinci, R.P.; Lewis, D.J.; Schaefer, R., Microstructural evolution in lead-free solder alloys: Part II. Directionally solidified Sn-Ag-Cu, Sn-Cu and Sn-Ag, J. Mater. Res., Vol. 19, No. 5, 2004, pp 1425-1431.

[48] Dutta, I., Park, C., Choi, S., Impression creep characterization of rapidly cooled Sn-3.5Ag solders, Materials Science and Engineering A 379,2004, pp 401-410.

[49] http://en.wikipedia.org/wiki/Aluminum, as of Mar. 2006

[50] Gibson, A.W. ; Choi, S.L. ; Subramanian, K.N. ; Bieler, T.R. Issues regarding microstructural coarsening due to aging of eutectic tin-silver solder, TMS Annual Meeting, Design Reliability of Solders and Solder Interconnections, 1997, pp 97-103.

[51] MICROELECTRONICS PACKAGING METERIALS DATABASE, Center for Information and Numerical Data Analysis and Synthesis(CINDAS), PURDUE UNIVERSITY, version 2.21

[52] Chen, Z.; Shi, Y.; Xia, Z.; Yan, Y., Properties of lead-free solder Sn-Ag-Cu containing minute amounts of rare earth, Journal of Electronic Materials, v 32, n 4, 2003, pp 235-243.

[53] Schubert, A., Walter, H., Dudek, R., Michel, B., Lefranc, G., Otto, J., Mitic, G., Thermo-mechanical properties and creep deformation of lead-containing and lead-free solders, Proceedings of the International Symposium and Exhibition on Advanced Packaging Materials Processes, Properties and Interfaces, 2001, pp 129-134.

[54] Darveaux, R., Banerji, K., Mawer, A., Dody, G., Reliability of Plastic Ball Grid Array Assembly, "Ball Grid Array Technology", edit by John H. Lau, 1995

[55] Schubert, A. , Dudek, R.; Auerswald, E.; Gollhardt, A.; Michel, B.; Reichl, H., Fatigue life models for Sn-Ag-Cu and Sn-Pb solder joints evaluated by experiments and simulation, Proceedings - Electronic Components and Technology Conference, 2003, pp 603-610.

[56] Zhang, Q.; Dasgupta, A.; Haswell, P., Viscoplastic constitutive properties and energy-partitioning model of lead-free Sn3.9Ag0.6Cu solder alloy, Proceedings - Electronic Components and Technology Conference, 2003, pp 1862-1868.

[57] Brown, S.B., Kim, K.H., Anand, L., An internal variable constitutive model for hot working of metals, International Journal of Plasticity, Vol. 5, 1989, pp 95-130.

[58] ANSYS theory manual, Version 7.1

[59] McDowell, D.L., Miller, M.P., Brooks, D.C., A unified creep-plastic theory for solder alloys, Fatigue of Electronic Materials, ASTM STP 1153, S.A. Scroeder and M.R. Mitchell, Eds., ASTM, Philadelphia, 1994, pp 42-59.

[60] Stolkarts, V.; Keer, L.M.; Keer, L.M. , Damage evolution governed by microcrack nucleation with application to the fatigue of 63Sn-37Pb solder, Journal of Mechanics and physics of solids, 47, 1999, pp 2451-2468.

[61] Wen, S.; Keer, L.M.; Mavoori, H., Constitutive and damage model for a lead-free solder , Journal of Electronic Materials, v 30, n 9, 2001, pp 1190-1196.

[62] Neu, R.W.; Scott, D.T.; Woodmansee, M.W., Measurement and modeling of back stress at intermediate to high homologous temperatures, International Journal of Plasticity, v 16, n 3, 2000, pp 283-301.

[63] Neu. R.W., Scott, D.T. and Woodmansee, M.W., Thermomechanical Behavior of 96Sn-4Ag and Casting Alloy, Journal fo Electronic Packaging, 123, 9, 2001, pp 238-246.

[64] Woodmansee, M.W.; Neu, R.W., The influence of prior strain rate on stress relaxation in solder alloys, Materials Science and Engineering A, v 322, n 1-2, 15, 2002, pp 79-88.

[65] Wang, G. Z.; Cheng, Z. N.; Becker K. and Wilde, J., Applying Anand model to represent the viscoplastic deformation behavior of solder alloys, Journal of Electronic Packaging, Transactions of the ASME, vol. 123, n3, 2001, pp 247-253.

[66] Wilde, J.; Becker, K.; Thoben, M.; Blum, W.; Jupitz, T.; Wang G. and Cheng, Z. N.; Rate dependent constitutive relations based on Anand model for 92.5Pb5Sn2.5Ag solder, IEEE Transactions on Advanced Packaging, v 23, n 3, 2000 pp 408-414.

[67] Chen, X.; Chen, G. and Sakane, M. , Modified Anand constitutive model for lead-free solder Sn-3.5Ag, ITherm 2004 - Ninth Intersociety Conference on Thermal and Thermomechanical Phenomena in Electronic Systems, Jun 1-4 2004, vol. 2, 2004 , pp 447-452.

[68] Matlab user manual, Version 7.3

[69] Ansell, G. S., Weertman, J., Creep of a Dispersion-Hardened Aluminum Alloy, Transactions of the Metallurgical Society of AIME 215, 1959, pp 838-843.

[70] Oliver, W.C., Nix, W.D., High temperature deformation of oxide dispersion strengthened Al and Al-Mg solid solution, Acta Metall., 30, 7, 1982, pp 1335-1347.

[71] Jianmin Qu, Mohammed Cherkaoui, Fundamentals of Micromechanics of Solids, John Wiley & Sons, Inc., Hoboken, New Jersey, 2006

[72] Mishnaevsky, L.L. Jr. and Schmauder, S., Continuum mesomechanical finite element modeling in materials development: A state-of-the-art review, Appl Mech Rev, 54, 1, 2001, pp 49-74.

[73] Schmauder, S., Computational Mechanics, Annu. Rev. Mater. Res. 2002. 32, pp 437-465.

[74] http://www.ctcms.nist.gov/oof/oof2/, Aug. 2006

[75] Glazer, J. Microstructure and mechanical properties of Pb-free solder alloys for low-cost electronic assembly. A review , Journal of Electronic Materials, v 23, n 8, 1994, pp 693-700.

[76] Vaynman, S., Mavoori, H., Fine, M.E., Comparison of isothermal fatigue of lead-free solders with lead-tin solders, American Society of Mechanical Engineers, EEP, v 10-2, Advances in Electronic Packaging, 1995, pp 657-662.

[77] Kanchanomai, C., Yamamoto, S., Miyashita, Y., Mutoh, Y., McEvily, A.J., Low cycle fatigue test for solders using non-contact digital image measurement system, International Journal of Fatigue, v 24, n 1, 2002, pp 57-67.

[78] Pang, J., Xiong, B.S., Low, T.H., 2004, Creep and Fatigue Characterization of Lead-free 95.5Sn-3.8Ag-0.7Cu Solder, 2004 Electronic Components and Technology conference, pp 1333.

[79] Schubert, A. , Dudek, R.; Auerswald, E.; Gollhardt, A.; Michel, B.; Reichl, H., Fatigue life models for Sn-Ag-Cu and Sn-Pb solder joints evaluated by experiments and simulation, Proceedings - Electronic Components and Technology Conference, 2003, pp 603-610.

[80] Zahn, B.A., Solder joint fatigue life model methodology for 63Sn37Pb and 95.5Sn4Ag0.5Cu materials, Electronic Components and Technology Conference, 2003 , pp 83 – 94.

[81] Syed, A., 2004, Accumulated Creep Strain and Energy Density Based Thermal Fatigue Life Prediction Models for Sn-Ag-Cu Solder Joints. 2004 Electronic Components and Technology conference, pp 737.

[82] Choi, S., Subramanian, K.N.; Lucas, J.P.; Bieler, T.R., Thermomechanical fatigue behavior of Sn-Ag solder joints, Journal of Electronic Materials, v 29, n 10, 2000, pp 1249-1257.

[83] Darveaux, R., Solder joint fatigue life model, Proceeding of the TMS Annual Meeting, 1997, pp 213-218.

[84] Guven, I.; Kradinov, V.; Madenci, E.; Tor, J.L., Solder joint life prediction model based on the strain energy density criterion, Electronic Components and Technology Conference, 2003, pp 214 – 220.

[85] Zhang, L.; Sitaraman, R.; Patwardhan, V.; Nguyen, L.; Kelkar, N., Solder joint reliability model with modified Darveaux's equations for the micro SMD wafer level-chip scale package family, Electronic Components and Technology Conference, 2003, pp 572 – 577.

[86] Kim, D.; Dias Filho, J.M.; Park, C; Mawer, A.; Moon, T.J.; Masada, G.Y., Crack length analysis of Sn-Pb and Sn-Ag solder joints in plastic ball grid array packages from dye penetration studies, Electronic Components and Technology Conference, 2003, pp 1746 – 1753.

[87] Chow, C.L.; Yang, F.; Fang, H.E., Damage mechanics characterization on the fatigue behaviour of a solder joint material, Proceedings of the Institution of Mechanical Engineers, Part C: Journal of Mechanical Engineering Science, v 215, n 8, 2001, pp 883-892.

[88] Tang, Hong; Basaran, Cemal, A damage mechanics-based fatigue life prediction model for solder joints, Journal of Electronic Packaging, Transactions of the ASME, v 125, n 1, 2003, pp 120-125.

[89] Basaran, Cemal; Tang, Hong, Implementation of a thermodynamic framework for damage mechanics of solder interconnects in microelectronics packaging , International Journal of Damage Mechanics, v 11, n 1, 2002, pp 87-108.

[90] Jian Zhang, In-Process Stress Analysis of Flip Chip Assembly and Reliability Assessment during Environmental and Power Cycling tests, Ph.D. Dissertation, 2003

[91] www.webelements.com, Dec. 2006

[92] Humphrey, W., Dalke, A. and Schulten, K., VMD - Visual Molecular Dynamics, J. Molec. Graphics, 14.1, 1996, pp 33-38.

[93] Lee, J.G.; Telang, A.; Subramanian, K.N.; Bieler, T.R., Modeling Thermomechanical Fatigue Behavior of Sn-Ag Solder Joints, Journal of Electronic Materials, 31, 11, 2002, pp 1152-1159.

[94] Allard, S., Metals: Thermal and Mechanical Data. Oxford: Pergamon Press, 1969

[95] 1801RevA_DocSpec.pdf from www.keithley.com

[96] Gao, F., Takemoto, T., Mechanical properties evolution of Sn-3.5Ag based lead-free solders by nanoindentation, Materials Letters 60, 2006, pp 2315-2318.

[97] Gao, F., Takemoto, T., The Evolution of Plastic Deformation of Sn3.5Ag-Based Lead-Free Solders, ECTC 2006, pp 269-274.

[98] ABAQUS Manual, version 6.6